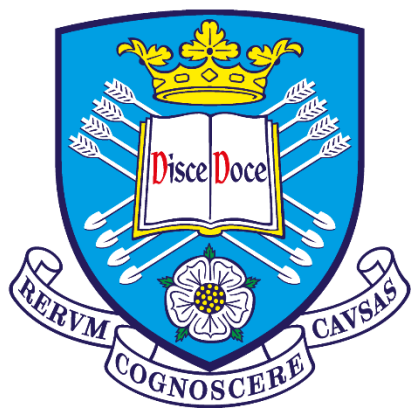


# The Ultrafast Excited States Dynamics of Pt(II) Organometallic Compounds



The  
University  
Of  
Sheffield.

Guanzhi WU

*A thesis submitted to the University of Sheffield in partial fulfilment of the  
requirements for the degree of Doctor of Philosophy*

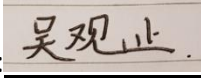
Department of Chemistry

University of Sheffield

August 2022

# Acknowledgement of Collaborative Work within the Thesis

The work described in this thesis was undertaken at the University of Sheffield under the supervision of Professor Julia A. Weinstein from September 2018 to September 2022 and has not been submitted, either wholly or in part, for this or any other degree at this, or any other, university. All the work is the original work of the author, except where acknowledged.

Signature: 

Name: Guanzhi WU

Date: September 2022

# Contents

<b>Abstract</b> .....	4
<b>Acknowledgements</b> .....	6
<b>Abbreviations</b> .....	8
<b>1. Chapter 1-Introduction</b> .....	10
<b>1.1 Motivation</b> .....	10
<b>1.2 Solar Energy Harvesting and Photo-Catalysed Reaction</b> .....	12
<b>1.2.1 Concentrating Solar Power (CSP) Plants</b> .....	13
<b>1.2.2 Photovoltaic Power Station</b> .....	14
<b>1.2.3 Artificial Photocatalyzed Reaction</b> .....	16
<b>1.3 Donor-Bridge-Acceptor Systems and Formation of a Charge Separated State</b> .....	18
<b>1.3.1 Organic Donor-Bridge-Acceptor Molecular Photocatalyst</b> .....	20
<b>1.3.2 Transition Metal Complex Donor-Bridge-Acceptor Photocatalysts</b> .....	22
<b>1.3.3 Jablonski Diagram</b> .....	24
<b>1.4 Intersystem Crossing Process in Transition Metal Complexes</b> .....	25
<b>1.4.1 ISC in Transition Metal Complexes</b> .....	26
<b>1.4.2 Ultrafast ISC Process in Heavy-Atom Free Organic Molecules</b> .....	32
<b>1.5 Ultrafast Time-Resolved Spectroscopy Techniques</b> .....	33
<b>1.5.1 A Brief History</b> .....	33
<b>1.5.2 Femtosecond Transient Absorption (TA) Spectroscopy</b> .....	36
<b>1.5.3 Transient Emission Spectroscopy</b> .....	39
<b>1.5.4 Transient Infrared Spectroscopy</b> .....	51
<b>1.5.5 IR Control Spectroscopy</b> .....	52
<b>1.6 Global Analysis and Target Analysis</b> .....	53
<b>1.7 Research Aims</b> .....	58
<b>1.8 Reference</b> .....	58
<b>2. Chapter 2-Ultrafast Dynamics in NAP-(B)-Pt-(B)-NAP Complexes</b> .....	64
<b>2.1 Introduction</b> .....	64
<b>2.3 Results and Discussion</b> .....	66

2.3.1	Fourier transform Infrared (FTIR) Spectra .....	66
2.3.2	Time Resolved Transient Infrared Spectroscopy .....	69
2.3.3	Femtosecond Broadband Fluorescence Up-conversion Spectroscopy (FLUPs) 80	
2.3.4	Femtosecond Transient Absorption Spectroscopy in DCM .....	83
2.3.5	Density Functional Theory (DFT) .....	89
2.4	Conclusion .....	92
2.5	Reference .....	93
2.SI.	Supplementary Information for Chapter 2 .....	94
	S11. Global Analysis Result of Pt-0 .....	94
	S12. Global Analysis Result of Pt-1 .....	97
	S13. Global Analysis Result of Pt-2 .....	99
3.	Chapter 3-Solvent Effect on Acceptor-Bridge-Acceptor Complexes .....	109
3.1.	Introduction .....	109
3.2.	Chapter Aims .....	110
3.3.	Results and Discussion .....	111
	3.3.1. UV-Vis Absorption Spectra, Steady-state emission Spectra and Time- Resolved fluorescence Spectra .....	112
3.4.	Conclusion .....	149
3.5.	Future Work .....	150
3.6.	Reference .....	151
4.	Chapter 4- Pt A-B-A Complex IR Control .....	152
4.1	Introduction .....	152
4.2	Chapter Aims .....	158
4.3	Results and Discussion .....	158
	4.3.1 Transient 2DIR of Pt-0 .....	161
	4.3.2 Transient 2DIR of Pt-1 .....	163
	4.3.3 Transient 2DIR of Pt-2 .....	175
4.4	Conclusion .....	177
4.5	Reference .....	178
4.SI.	Supplementary Information for Chapter 4 .....	180

<b>5. Chapter 5- The Influence of the <i>Trans</i>-Ligand L (the “opposite” ligand) on The Photophysics of L-Pt-C≡C-NAP Complexes</b> .....	182
<b>5.1. Introduction</b> .....	182
<b>5.2. Chapter Aims</b> .....	184
<b>5.3. Results and Discussion</b> .....	184
<b>5.3.1. UV-Vis Absorption and Emission Spectra</b> .....	184
<b>5.3.2. Transient Absorption Spectra and Fluorescence Up-Conversion Spectra</b> ....	186
<b>5.3.3. Summary and Conclusion</b> .....	197
<b>5.4. Future Work</b> .....	199
<b>5.5. Reference</b> .....	200
<b>6. Conclusion</b> .....	201
<b>7. Experimental</b> .....	203
<b>7.1 Ultrafast Time-Resolved Spectroscopies</b> .....	203
<b>7.1.1 Femtosecond Fluorescence Up-Conversion Spectroscopy (FLUPS)</b> .....	203
<b>7.1.2 Time-Resolved Transient UV-vis Absorption Spectroscopy (TA)</b> .....	205
<b>7.1.3 Time-Resolved Infrared Spectroscopy (TRIR)</b> .....	206
<b>7.1.4 Frequency Domain Two-Dimensional Infrared (2DIR) and Transient Two-Dimensional Infrared Spectroscopy (T-2DIR)</b> .....	206
<b>7.2 Density Functional Theory (DFT) Calculation</b> .....	207
<b>7.3 Steady State Absorption Spectra</b> .....	207
<b>7.3.1 UV-vis Absorption Spectroscopy</b> .....	207
<b>7.3.2 Steady State Fourier-transform Infrared Spectroscopy (FTIR)</b> .....	208
<b>7.3.3 Steady State Emission Spectroscopy</b> .....	208
<b>7.3.4 Data Analysis</b> .....	208
<b>7.4 Reference</b> .....	208

## Abstract

Artificial photosynthesis and photocatalysis has attracted a lot of interest as this approach could convert solar energy into fuel to replace currently widely used fossil fuels, and prevent emission of the green-house gases. Donor-bridge-acceptor (D-B-A) structures are a core part of this approach, hence a lot of research has been done on different molecular architectures.

Transition metal complexes with D-B-A structure can form charge separated state (CSS) which is the key intermediate in photosynthesis and photocatalysis. As D and A components are usually too far separated to engage in a direct electron transfer, the first populated excited state is usually a charge transfer (CT) state. Consequent electron transfer in the CT state reaches the desired CSS. The D-B-A complexes can also undergo fast intersystem crossing (ISC) process to generate triplet states, which are usually long lived, and therefore important in artificial photosynthesis and photocatalysis, where often a bimolecular step is involved. However, the back electron transfer process in a CT state can also happen that inhibits the formation of CSS state by quenching the CT state formed. Thus we need to further our understanding on the kinetics of back electron transfer process in the CT state, so in the future this process could be prevented and the yield of the CSS state increased. To answer this question, a series of Pt based Acceptor-Bridge-Acceptor (A-B-A) systems – that could be seen as an analog to the D-B-A systems, but without a donor, have been characterised by multiple ultrafast spectroscopy techniques and their photophysical properties such as excited state energy, excited state lifetimes and ISC rate have been investigated in this research. We find that with the increase of bridge length between Pt centre and NAP acceptor, back electron transfer rate decreases, and the bridge itself starts to trap positive charge on the bridge.

The solvent effect on the dynamics in A-B-A Pt(II) complexes, and especially on the rate of ISC process are also investigated which provides more details on the nature and decay kinetics of CT state forms in A-B-A complex after excitation. We found that the solvent effect on different A-B-A complexes are different from each other, this result may be caused by the difference in excited states' nature of the A-B-A complexes investigated here.

Previously, the research in our group established that excitation of bridge-localised vibrational mode of the CT state formed in D-B-A complexes can influence the CT state decay routine and the formation of a charge-separated state. In this thesis, IR control experiments on the A-B-A complexes were performed. We found that with the excitation of vibrations on the bridge, back electron transfer process of CT state is accelerated.

ISC process is also important in photosynthesis and in our group's previous research, a massive acceleration of ISC rate was observed by simply changing the ligand opposite to an electron acceptor in Pt complexes. Further research is also done by characterising ISC rate of a series NAP-Pt-R complexes with fluorescence up-conversion spectroscopy (FLUPS). We recognized strong correlation between the structure of the "opposite" ligand and ISC rate and this phenomenon is explained in the framework of spin-orbit charge transfer intersystem crossing (SOCT-ISC) mechanism.

## Acknowledgements

First, I want to acknowledge my supervisor, Professor Julia Weinstein for giving me the opportunity to undertake this project in her group. I am grateful for Julia's fabulous guidance in science and her great academic achievements. I am very grateful for her patience and unwavering support in the face of any difficulties.

I am also grateful for Professor Niko Ernsting for the development of FLUPS, the amazing ultrafast fluorescence spectroscopy technique. I am grateful for his teaching and generous help with any problems I faced during the development and running of FLUPS, here in Sheffield.

I also want to thank Dr. George Farrow for his all help, teaching, and training on FLUPS and all other academic questions. Without his help, I would not be able to fully understand FLUPS and operate it perfectly in such a short time.

I want to acknowledge Dr. Dimitri Chekulaev for his great work in laser systems. Without his help and hard work, the high quality ultrafast spectroscopy experiments featured in this thesis could not have been achieved.

Additionally, many thanks to Dr. Igor Sazanovich for his great work in the Central Laser Facility, research complex at Harwell, Rutherford Appleton Laboratories. The amazing TRIR spectroscopy setup there has helped to answer a great number of questions in my PhD project.

I am thankful for all colleagues in Julia Weinstein's group from past to present. I am especially thankful for the help of Dr. Alex Auty in data processing and analysis and Dr. Tao Cheng, for synthesising massive amounts of amazing Pt complexes.



Thanks to all other people I have ever met in the group during the past four years:  
Andy, Heather, Samantha, Martin, Catherine, Rory, Ricardo, and Iona.

I would like to thank my parents for their continual support and trust.

Last but not least, I want to thank the China Scholarship Council (CSC) for funding my  
PhD study during the past four years.

## Abbreviations

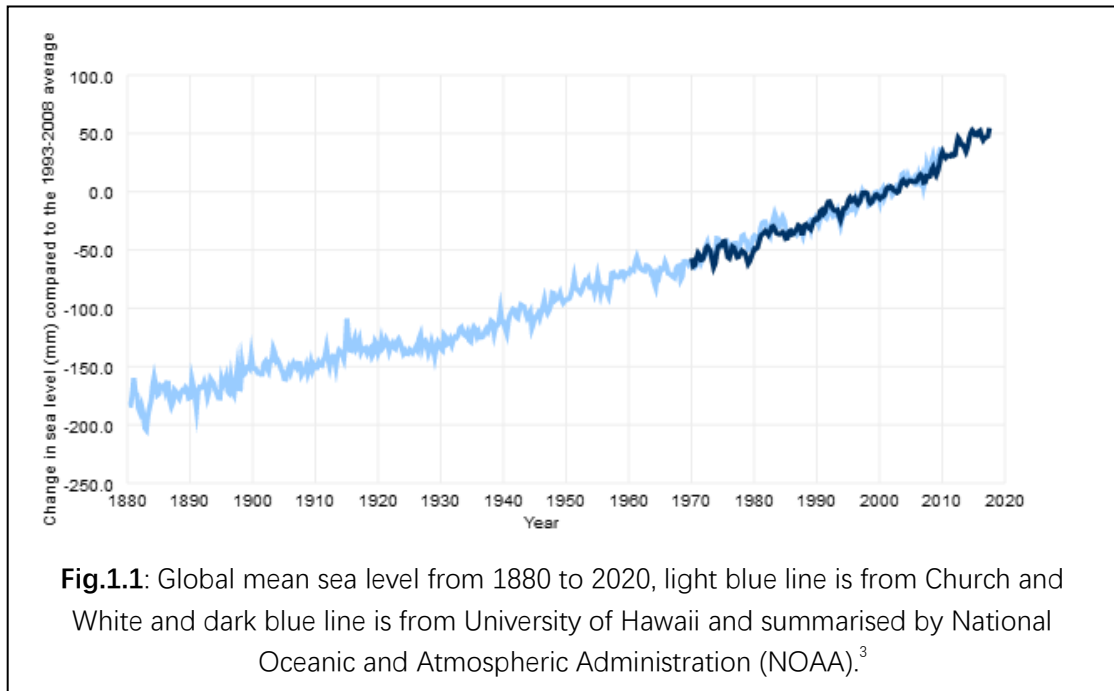
2D	Two dimensional
BBO	Beta Barium Borate
BO	Born-Oppenheimer
CCD	Charge-Coupled Device
CO	Carbon monoxide
CR	Charge Recombination
CSS	Charge Separation State
CT	Charge Transfer
DAS	Decay Associated Spectra
DCA	9,10-dicyanoanthracene
DCM	Dichloromethane
DFT	Density Functional Theory
DM	Deformable Mirror
DMF	N,N-Dimethylformamide
DMJ	Dimethyl julolidine
DMJ-An	Dimethyl julolidine-anthracene
EAS	Evolution Associated Spectra
EJ	Exajoule
FC	Franck-Condon
FLUPS	Femtosecond Fluorescence Up-Conversion Spectroscopy
FTIR	Fourier Transform Infrared Spectroscopy
FWHM	Full Width Half Maximum
GHG	Greenhouse Gas
GLA	Global Analysis
HF-TRIR	High Frequency Transient Infrared Spectroscopy
IC	internal conversion
ILCT	Intraligand Charge Transfer
IR	Infrared
IRF	Instrument Response Function
ISC	Intersystem Crossing
LF-TRIR	Low Frequency Transient Infrared Spectroscopy
MLCT	Metal to Ligand Charge Transfer
MMLLCT	Mixed Metal-Ligand to Ligand Charge Transfer
NAP	Naphthalene-Mono-Imide
PES	Potential Energy Surfaces
Ph	Phenyl
SAS	Species Associated Spectra
SE	Stimulate Emission

SF	Sum Frequency Generation
SHG	Second Harmonic Generation
SOCT-ISC	Spin-Orbit Coupling Charge Transfer Intersystem Crossing
T-2DIR	Transient Two-Dimensional Infrared Spectroscopy
TA	Transient Absorption Spectroscopy
TCA	2,6,9,10-tetracyanoanthracene
THF	Tetrahydrofuran
	Travelling-Wave Optical Parametric Amplifier of
TOPAS	Superfluorescence
trEPR	transient electron spin resonance
TRIR	Transient Time Resolved Infrared Spectroscopy
$\mu$	dipole moment

# 1. Chapter 1-Introduction

## 1.1 Motivation

In 2020, the concentration of  $CO_2$  in atmosphere reached its new high at  $413.2 \pm 0.2 \text{ ppm}$  which is about 1.5 times compared with pre-industrial levels, together with other two primary greenhouse gases  $CH_4$  ( $1889 \pm 2 \text{ ppb}$ ) and  $N_2O$  ( $333.2 \pm 0.1 \text{ ppb}$ ) according to the World Meteorological Organization's report.<sup>1</sup> The increase of greenhouse gas concentration in atmosphere leads to global warming which made the temperature in 2020  $1 \text{ }^\circ\text{C}$  higher than 1951-1980 average, and  $1.25 \text{ }^\circ\text{C}$  higher than in the preindustrial age (AD1750-1850).<sup>2</sup> Global warming further induces sea ice melting, and sea level rise rate reaches  $3 \text{ mm/yr}$ , with the resulting change of sea level from 1880 to 2020 illustrated in **Fig.1.1**.<sup>3</sup> The increase of carbon dioxide concentration also leads to a phenomenon named 'Ocean Acidification', which is caused by absorption of  $CO_2$  from the atmosphere by the ocean, generating carbonic acid. The average ocean pH is about 0.11 lower in 2000 compared with 1770, this change in acidity also leads to the change of ocean's chemistry.<sup>4</sup>



The exceeded carbon dioxide emission is mainly caused by the wide use of fossil fuels<sup>5</sup> including coal, oil and natural gas. In 2021, global primary energy consumption reaches its new height at 595.15 exajoules (EJ,  $1 \text{ EJ} = 1 \times 10^{18} \text{ J}$ ), to which 82% were contributed by fossil fuels: coal produced 160.1 EJ (contributed 26.7%), oil produced 184.21 EJ (contributed 30.96%), and natural gas produced 145.35 EJ (24.42%). Also, solar energy, wind energy and other renewables only account for 6.7% in energy consumption, with 39.91 EJ in 2021.<sup>6</sup> Renewable energy consumption increased by around 5.11 EJ compared with 34.8 EJ consumption in 2020. However, this does not change the perilous conditions of climate change, and does not slow down the carbon dioxide emission to offset the emission from other sources. CO<sub>2</sub> emission from energy consumption increased 1805.6 million tonnes to 33884.1 million tonnes in 2021 compared with 32078.5 million tonnes in 2020 and which is close to 34095.8 million tons emission in 2019 before covid pandemic. This is not the end of the story, considering world's population is expected to reach 8 billion on 15 November 2022 and the United Nations (UN) projects that this number will reach 8.5 billion in 2030 and 9.7 billion in 2050.<sup>7</sup> Because of the increase of global population and economic growth, by 2050, the world is predicted to consume 80% more energy than in 2014, which would lead

to 50% more global greenhouse gas (GHG) emission.<sup>8</sup> The excess of CO<sub>2</sub> will further increase global temperature and with the CO<sub>2</sub> concentration in atmosphere increasing, carbons stored in the soil will also be released so current carbon cycle equilibrium will break down, the released CO<sub>2</sub> will cause further warming to the earth: this is a vicious circle.<sup>9</sup>

To prevent this vicious circle, 193 parties (192 countries and European Union) joined the Paris Agreement on 22<sup>th</sup> April 2016. The Agreement aims to keep the global average temperature no more than 2 °C above the pre-industrial levels and reduce the risk of climate change to the world.<sup>10</sup> For this purpose, carbon neutrality, a state with net zero CO<sub>2</sub> emissions is targeted to be achieved by 2050. To achieve this target, renewable energy technologies such as solar energy, wind energy and so on should be further developed: these technologies potentially can supply 3000 times more energy than the global energy consumption today.<sup>11</sup> Apart from using renewable energy, CO<sub>2</sub> capture, utilization, and storage techniques are also important, and can be used to decrease 95% carbon dioxide emission and also capture CO<sub>2</sub> that has been released into the atmosphere.<sup>12</sup>

Even though renewable energy is free of CO<sub>2</sub> emission, so is friendly to the environment, it is still facing challenges in developing countries with 6.69 billion population, 85.33% of the world's population. These challenges include high price of renewable energy technologies and lack of skilled labour in these developing countries.<sup>13</sup> In order to make the target set in Paris Agreement,<sup>10</sup> new renewable energy techniques with less cost that are easy to use need to be developed, so renewable energy could expand in developing countries, and so together we can prevent irreversible climate change and break the vicious circle caused by GHG emission.

## **1.2 Solar Energy Harvesting and Photo-Catalysed Reaction**

One of the types of renewable energy is solar energy. It is produced by the star located in the centre of our system,  $1.49 \times 10^8 \text{ km}$  away from the earth,<sup>14</sup> via nuclear fusion reaction.<sup>15</sup> Solar energy is treated as a kind of inexhaustible energy source on the earth. The amount of solar energy that arrives at the top of the atmosphere of the earth is about 175 petawatts ( $PW$ ,  $1 PW = 1 \times 10^{15} W$ ).<sup>16</sup> solar energy arriving at earth in 3400 seconds is sufficient to cover the global energy usage in 2021. The solar energy arriving at earth is still only a tiny amount of the energy emitted from the Sun, the Sun's luminosity is about  $3.8 \times 10^{26} W$ ,  $2.17 \times 10^9$  times of the solar energy arriving at the earth.<sup>17</sup> Even the energy that comes from burning fossil fuels is also originating from the Sun, as 'ancient' solar energy is stored in ancient plants and then converted into fossil fuels in the end.<sup>18</sup> However, most of the solar energy is not efficiently used by the society, so new methods of harvesting solar energy are attracting attention of researchers.

### 1.2.1 Concentrating Solar Power (CSP) Plants

Concentrating solar power method is a kind of solar-thermal conversion system which focuses (concentrates) sunlight by a concentrator: normally, a series of reflectors focussing onto a much smaller receiver. The focused sunlight on the receiver is converted into heat and then transferred and stored in the thermal energy storage by using heat transfer liquid (HTF). The heat stored is then converted into electric power via electrical generator.<sup>19</sup> A photo of CSP plant is given in **Fig.1.2**. In 2021, global CSP plant capacity is 6 gigawatts ( $GW$ ,  $1 GW = 1 \times 10^9 W$ ), and another 1  $GW$  capacity was under construction in Chile, China, the United Arab Emirates and South Africa.<sup>20</sup>



**Fig.1.2:** The CSP plant located in Andalusia (Spain).

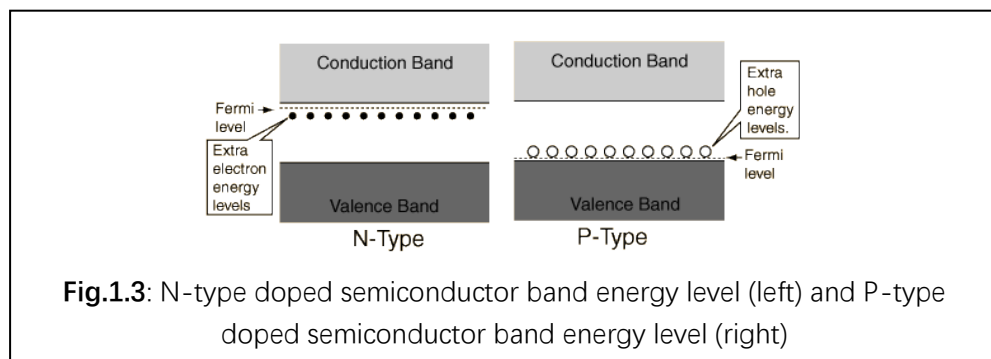
However, current CSP plants are suffering low efficiency problem with annual efficiency only 10-20%, and high construction costs which could be improved by doubling current annual efficiency, or reducing the current construction costs by half.<sup>19,21</sup> By using high temperature receiver (output temperature  $>700\text{ }^{\circ}\text{C}$ ), different heat transfer medium such as molten salt and new power cycle method, next generation CSP plants can achieve annual efficiency 25 – 30% which may make CSP more competitive with traditional energy sources such as fossil fuels.<sup>19,22,23</sup>

### **1.2.2 Photovoltaic Power Station**

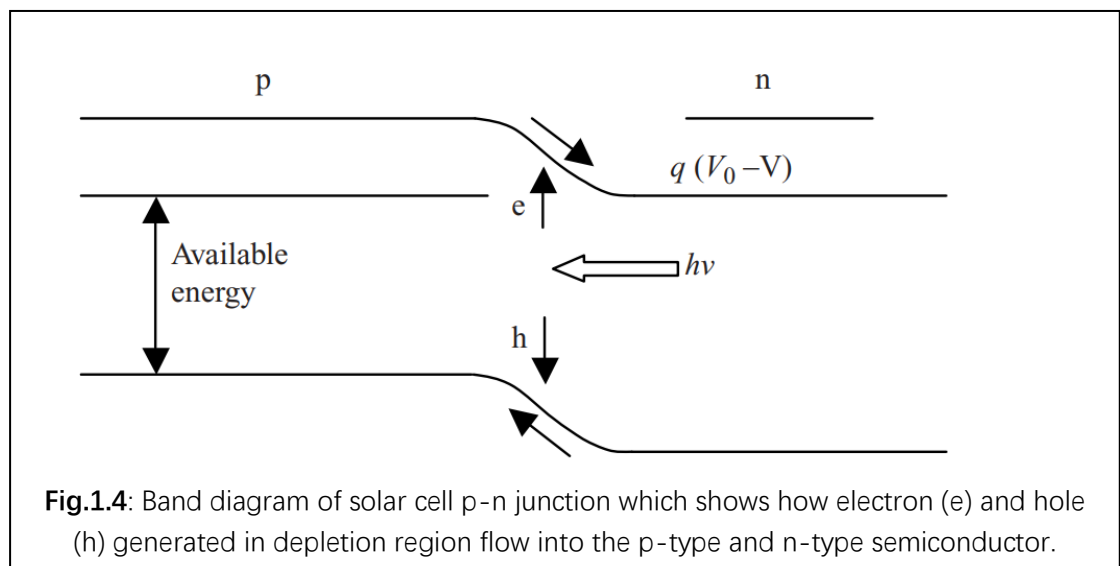
Photovoltaic phenomenon finding could be dated back to 1839, when Alexandre-Edmond Becquerel reported the first observation of photovoltaic effect.<sup>24,25</sup> Today, photovoltaic effect is the basis of a lot of technological advances. To achieve photovoltaic effect, in such solar cells, an n-type semiconductor and a p-type semiconductor are joined together to generate a structure called p-n junction. Here the n-type semiconductor is a kind of semiconductor doped with electron donor impurities (creating an excess of



“electrons” – hence “n”=negative) and the p-type semiconductor is doped with electron acceptor impurities (additional “holes”). This imbalance of charges results in new energy levels between the valence band and the conduction band of the semiconductor, as shown in **Fig.1.3**. A new energy level filled with electrons with energy just below than the conduction band appears in an n-type doped semiconductor and a new unoccupied energy level with the energy slightly higher than the valence band appears in a p-type doped semiconductor.<sup>26</sup>



In solar cells, photons from the Sun are absorbed by the so-called depletion region, a region formed at the interface of p-type and n-type semiconductor in p-n junction. The absorbed photons generate electron-hole pairs in the depletion region. The holes generate flow into p-type semiconductor region, and the electrons generate flow into n-type semiconductor region, so the voltage difference is created as shown in **Fig.1.4**.<sup>27</sup>



The first photovoltaic (PV) solar cell generated by p-n junction method was produced in 1954 with only 6% efficiency.<sup>28</sup> Three generations of PV solar cells have been developed since then. The first generation is single-junction silicon wafer solar cells which are built with single-crystal silicon and multi-crystalline silicon with efficiency about 13-14%. The second generation PV solar cells are thin-film devices to avoid unnecessary cost by reducing the amount of the material used. In these PV solar cells, the semiconductor used is no longer single crystal and multi-crystalline silicon, but other semiconductor materials such CdTe, CuIn(Ga)Se<sub>2</sub> which are more able to absorb solar photons compared with first generation solar cells, hence less materials could be used to achieve higher efficiency.<sup>29</sup> The third generation PV solar cells are based on semiconductive organic macromolecules or inorganic nanostructures that are promising to achieve large-scale solar energy to electric energy transfer, with lower cost.<sup>30</sup> Instead of single junction PV solar cells, to further increase the solar cell efficiency, a technique called multi-junction solar cells is also developed. Instead of using only one p-n junction, multiple p-n junctions are used in the solar cell which has the potential to achieve over 50% efficiency.<sup>31</sup> With so many years' effort, the silicon single junction solar cell till May 2022 achieved efficiency 26.7% and III-V cells achieved 29.1% efficiency. Multijunction cells efficiency record till May 2022 is 47.1% which is very close to the 50% efficiency limit.<sup>32</sup>

In 2021, global PV solar cells capacity increased 175 GW and reached a new record around 942 GW which occupies 30% of renewable power capacity, that is only second to hydropower capacity (38%).<sup>20</sup>

### **1.2.3 Artificial Photocatalyzed Reaction**

The previous two techniques introduced are focused on how to convert solar energy into electric energy in order to replace current fossil fuels. However,

electric power is not easy to store on a large scale and cannot replace fossil fuels such as petrol totally.<sup>33</sup> Take electric car as an example, to fully charge a battery electric vehicle (BEV) requires two hours with fast-charging technique, and the time could be further reduced to 30 min if faster charging technique is used. Instead of 2 hours or 30 min, filling in a traditional internal combustion engine vehicle (ICEV) fuel tank only takes 5 min. To achieve charging times as low as 5 min on a BEV, ultra-fast charging techniques are required,<sup>34,35</sup> which have not been developed as yet.

Instead of converting solar energy into electricity, alternative option is converting solar energy into fuel directly via a photosynthetic process or a photocatalytic process. There are two major photocatalysis fuel generation methods that are attracting as lot of research: 1). Water splitting to produce H<sub>2</sub>, 2). Reducing CO<sub>2</sub> to fuels. The processes behind these two methods are similar to each other and include: 1). absorption of light, 2). Separation of positive charge and negative charge, 3). Redox reactions happen with the positive charge and negative charge.<sup>36</sup>

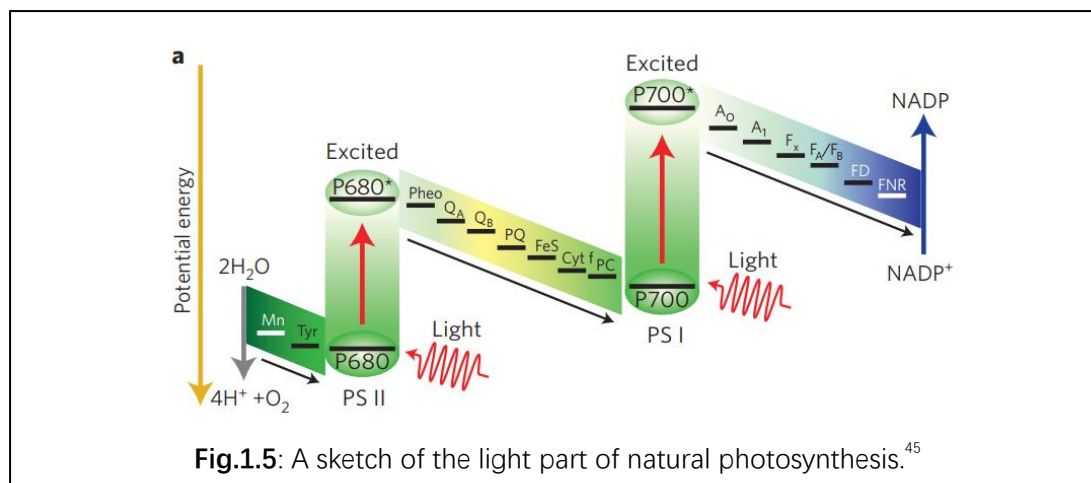
As a carbon-free fuel, H<sub>2</sub> is an ideal fuel for future as when it is burnt only water is produced and no greenhouse gas is emitted. However, today's H<sub>2</sub> fuel is mainly produced from fossil fuels via cracking or reforming process and in this process, CO<sub>2</sub> is generated and emitted which makes hydrogen produced in these ways no longer carbon free fuel.<sup>37</sup> To produce carbon free hydrogen, photocatalytic water splitting technique is an option.<sup>38</sup> The first example of an artificial photocatalytic water splitting reaction is reported by Fujishima in 1972, in which TiO<sub>2</sub> semiconductor electrode is used to absorb sun light and react with water to generate O<sub>2</sub> and the electron is transported to the platinum electrode on which proton is reduced to produce H<sub>2</sub>.<sup>39</sup>

Another option to produce fuel and fulfil the net-zero CO<sub>2</sub> emission (carbon-neutral) target is producing fuel via photocatalytic carbon dioxide reduction reaction. Fuels produced in this way are generated from CO<sub>2</sub> and after their use the same amount of CO<sub>2</sub> is emitted, so no extra CO<sub>2</sub> released into atmosphere. The research on efficient artificial CO<sub>2</sub> reduction photocatalysts could be dated back to 1982, before that the systems on photocatalysis CO<sub>2</sub> reduction were very inefficient. In 1982, Jean- Marie Lehn et al reported Ru(bpy)<sub>3</sub><sup>2+</sup>/Co<sup>2+</sup> system which can reduce CO<sub>2</sub> in aqueous solution to generate CO and H<sub>2</sub> gas mixture.<sup>40</sup> Apart from CO as reduction product, other photoreduction processes such as CO<sub>2</sub> reduce to CH<sub>4</sub>,<sup>41</sup> methanol,<sup>42</sup> and HCOOH are also reported.<sup>43</sup> The latter two product mentioned are liquid fuels which are much easier to store and use compared with the gas fuel product CO, H<sub>2</sub> and CH<sub>4</sub>. This may not be the end of the story, as recently Tao Cai et al. reported a cell-free synthesis of amylopectin (food) from carbon dioxide and hydrogen<sup>44</sup>. In future, artificial photosynthesis of food may become real.

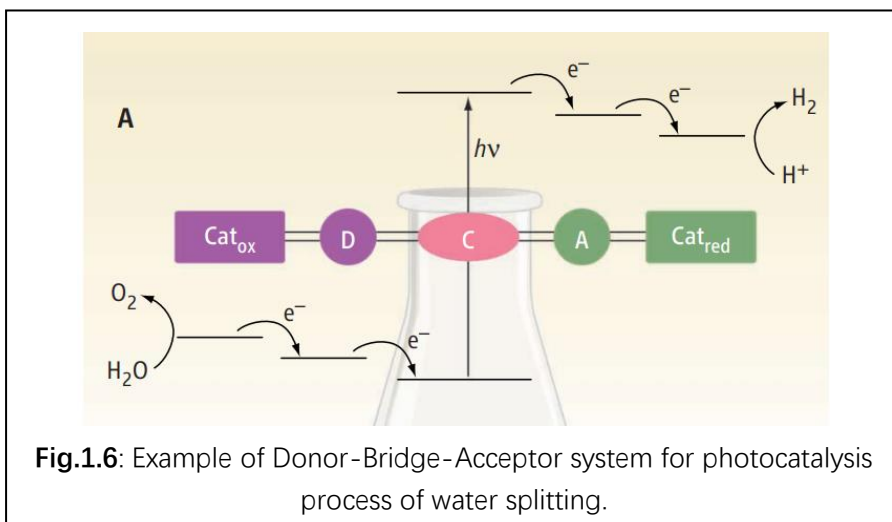
### 1.3 Donor-Bridge-Acceptor Systems and Formation of a Charge Separated State

The process of natural photosynthesis (NPS) includes two parts, light reactions and dark reactions. The light reaction, also known as “Z-scheme”, is shown in **Fig.1.5**.<sup>45</sup> It includes two photosystems: photosystem I (PSI) and photosystem II (PSII). These two photosystems are membrane protein complexes including multiple units.<sup>46,47</sup> In photosystem I, the solar energy (light) is harvested by an antenna system, then the energy is transferred to the so-called P700 (“pigment 700, a chlorophyll dimer with an absorption maximum at 700 nm).<sup>47</sup> In photosystem II, solar energy is absorbed by various pigments in the PSII reaction center then the excitation energy is transferred to P680 (another chlorophyll dimer, which absorbs at 680 nm); the P680 in its singlet excited state can work as an electron donor for an electron transport chain.<sup>48</sup> Historically, PSI was discovered first, but it is PSII that acts first. Chlorophyll in the reaction center, being promoted into <sup>1</sup>C\*, undergoes electron

transfer to the primary electron acceptor, pheophytin, generating a charge-separated state in PSII. The consequent steps include hole transfer to a “Manganese cluster” – a catalyst for water oxidation to oxygen; and an electron transfer to PSI, to replenish an electron transferred by  $^1\text{P700}^*$  (a singlet excited state of the chlorophyll in the special pair in PSI) to ferredoxin where  $\text{NADP}^+$  is reduced to  $\text{NADPH}$  used to power dark reaction.<sup>45</sup> In dark reactions,  $\text{CO}_2$  is reduced into carbohydrates with the energy provided by  $\text{NADPH}$  and  $\text{ATP}$  generated in light reaction, electrons and protons provided by water oxidation.<sup>49</sup>



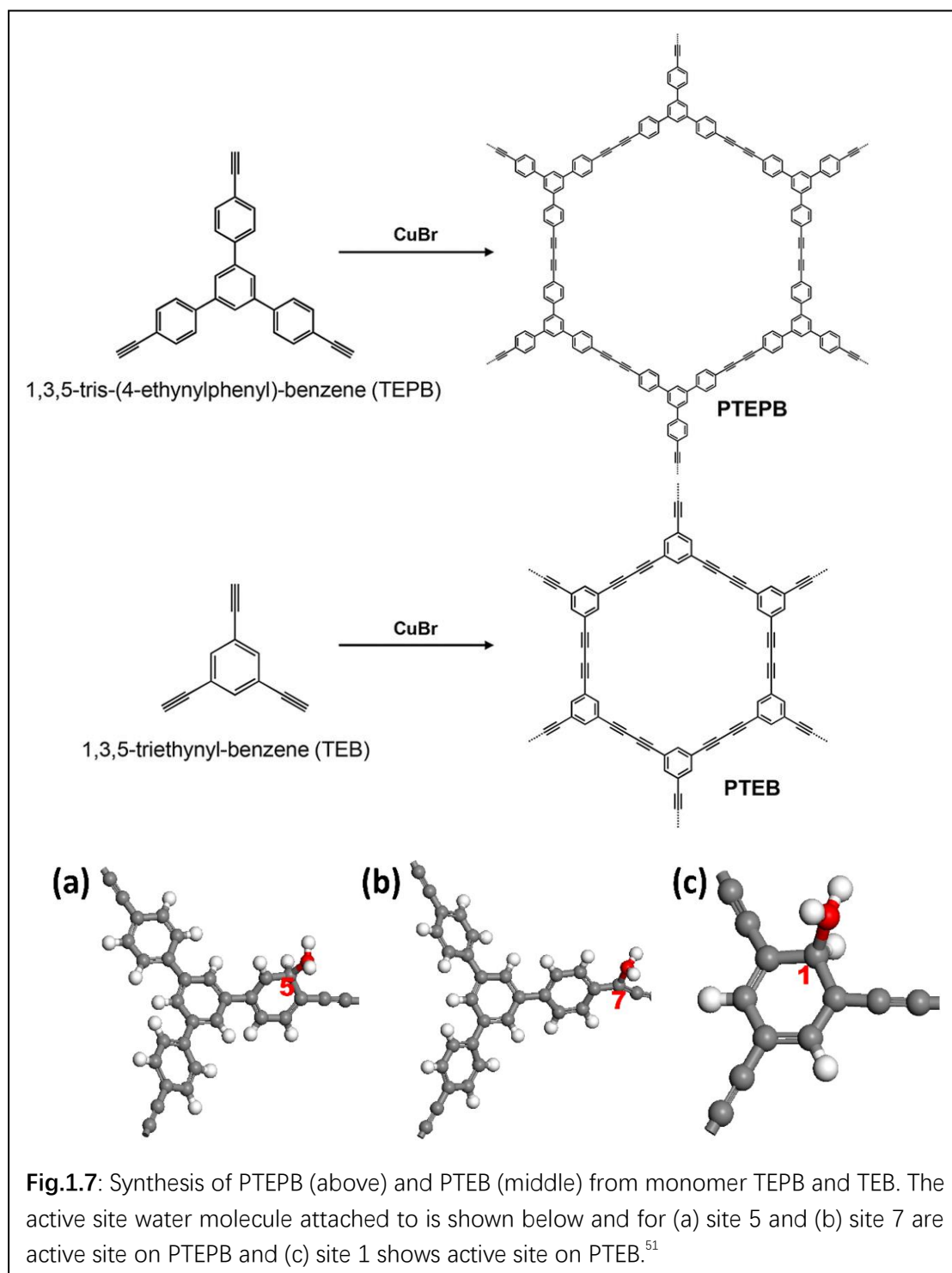
Photocatalysis processes, including natural and artificial photosynthesis, could be divided into three elementary steps: 1). Light Harvesting, 2). Charge separation, and 3). Catalysis reaction.<sup>45</sup> An artificial system which can perform a photocatalytic process normally includes 1). An electron donor (D), 2). An electron acceptor (A) and 3). A bridge linking the donor and acceptor, or 3'). A chromophore replaces the bridge to improve light harvesting ability. Then the hole and the electron are transferred to the oxidation catalyst and reduction catalyst respectively, in separate steps as shown in **Fig.1.6**.<sup>50</sup>



### 1.3.1 Organic Donor-Bridge-Acceptor Molecular Photocatalyst

#### 1.3.1.1 PTEPB and PTEB

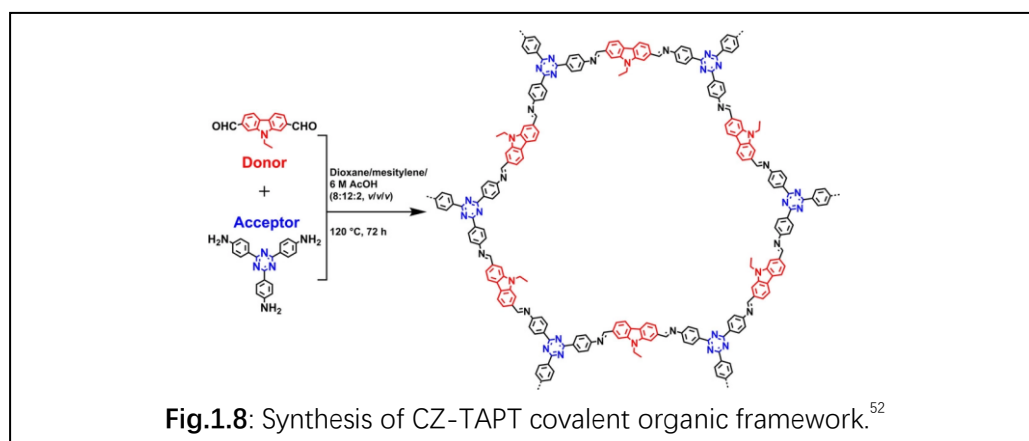
The first reported fully organic molecular photocatalyst for water splitting is - conjugated polymer/covalent organic framework, constructed by 1,3,5-tris-(4-ethynylphenyl)-benzene (TEPB) and 1,3,5-triethynylbenzene (TEB) units with the structure show in **Fig.1.7**.<sup>51</sup> In these two polymers, the phenyl group in TEPB and TEB unit works as an electron donor, generates multiple positive charge holes and the triple bonds works as electron acceptor which accept electrons generated after photoexcitation. Then a water molecule attached to active sites which are also shown in **Fig.1.7** on the photoexcited PTEPB and PTEB can be split to produce H<sub>2</sub> and O<sub>2</sub>.



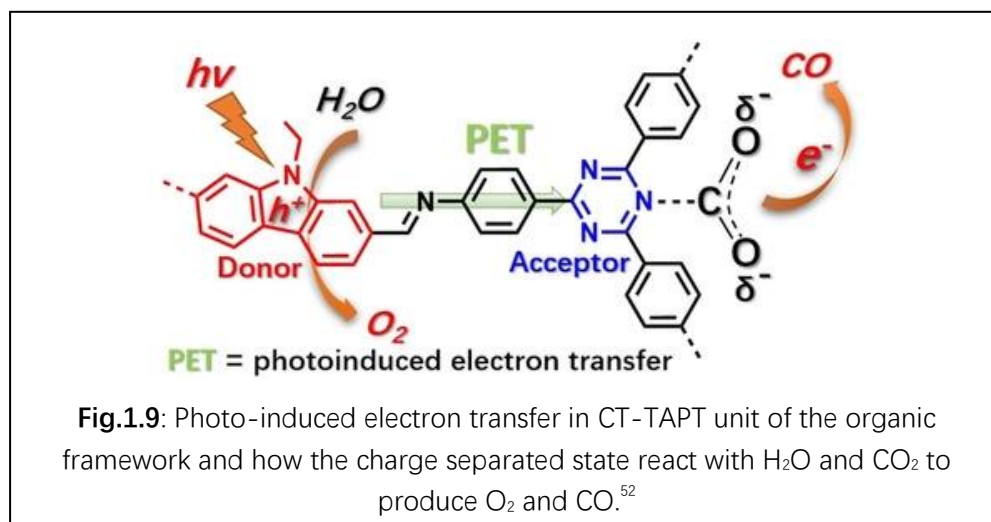
### 1.3.1.2 CZ-TAPT Covalent Organic Framework

Based on the PTEPB and PTEB mentioned above, a novel CO<sub>2</sub> reduction organic photocatalyst is synthesized by using 9-ethyl-9Hcarbazole-2,7-dicarboxaldehyde (CZ) as electron donor and tris-(4-aminophenyl) triazine

(TAPT) as electron acceptor, whose structure is given in **Fig.1.8**.<sup>52</sup>



When this organic framework is excited by visible light, photo-induced electron transfer from CZ to TAPT happens to form a charge separated state. This leaves a positive charge on CZ, which can react with water oxidizing it to generate oxygen. The electron on TAPT will be used to reduce  $\text{CO}_2$  associated with it to produce CO as show in **Fig.1.9**.



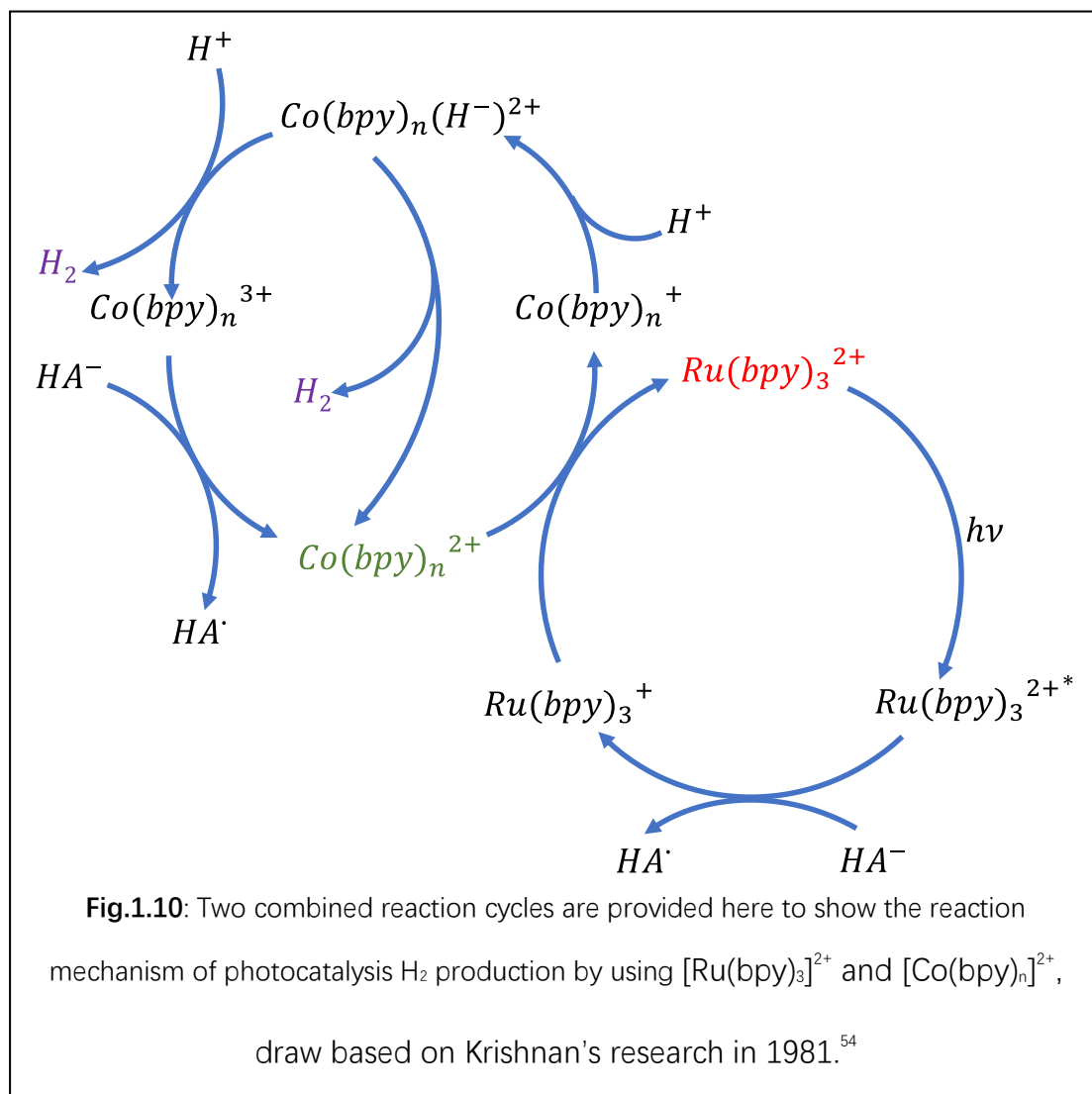
### 1.3.2 Transition Metal Complex Donor-Bridge-Acceptor Photocatalysts

#### 1.3.2.1 Tris(2,2'-bipyridine)ruthenium(II)-Cobalt(II) Bipyridine System

This is a type of homogeneous catalyst of photocatalysis water reduction by absorbing visible light. In this system,  $[\text{Ru}(\text{bpy})_3]^{2+}$  is used as photosensitizer which forms  $^1\text{MLCT}$  state undergoes sub-picosecond intersystem crossing (ISC) process<sup>53</sup> to generate  $^3\text{MLCT}$  state which react with ascorbate (electron donor)



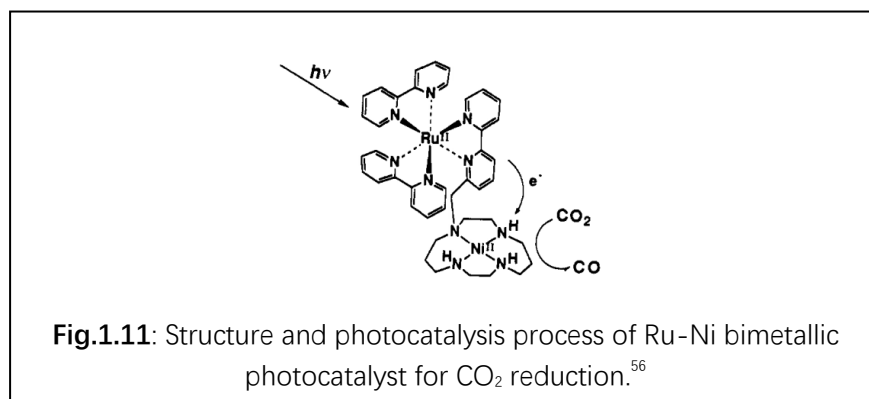
to produce reactive  $[\text{Ru}(\text{bpy})_3]^+$ , then  $[\text{Ru}(\text{bpy})_3]^+$  react with  $[\text{Co}(\text{bpy})_n]^{2+}$  to produce  $[\text{Co}(\text{bpy})_n]^+$  which can further react with  $\text{H}^+$  to reduce it and generate  $\text{H}_2$ .<sup>54</sup> The structure of  $[\text{Ru}(\text{bpy})_3]^{2+}$  and  $[\text{Co}(\text{bpy})_n]^{2+}$  are shown in **Fig.1.10**.



### 1.3.2.2 Bimetallic Photocatalyst for $\text{CO}_2$ Reduction – covalent systems

Instead of the previously mentioned  $[\text{Ru}(\text{bpy})_3]^{2+}/[\text{Co}(\text{bpy})_3]^{2+}$  bimolecular mixture, a system which links the photosensitizer  $[\text{Ru}(\text{bpy})_3]^{2+}$  with the reduction active center covalently is reported as shown in **Fig.1.11**. In this system, the  $[\text{Ru}(\text{bpy})_3]^{2+}$  center harvest visible light to generate MLCT state, then the electron on bipyridine ligand is transferred to the  $\text{Ni}^{2+}$  reduction catalyst center where it reduces  $\text{CO}_2$  into  $\text{CO}$ . However, this process lacks

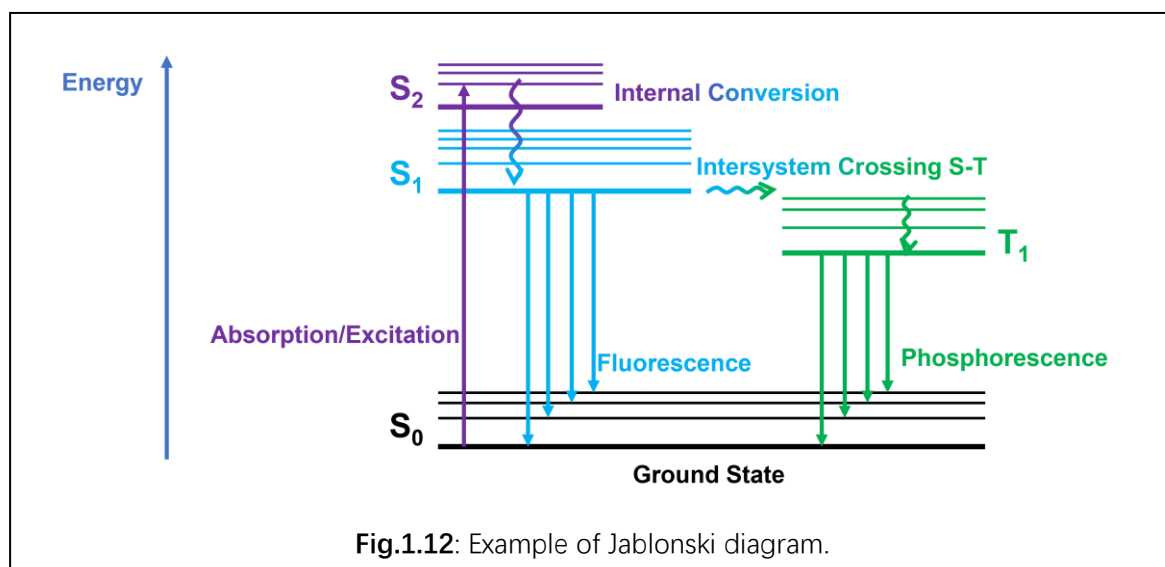
selectivity in CO and H<sub>2</sub> production, in other word, this kind of bimetallic photocatalyst cannot selectively reduce CO<sub>2</sub> or H<sub>2</sub>O.<sup>55,56</sup>



Further research on the metal complex photocatalysts for water splitting or CO<sub>2</sub> reduction is still ongoing to improve conversion efficiency, product selectivity, and to decrease the cost by using earth-abundant elements.<sup>57,58</sup>

Notwithstanding current limitations of metal complexes as photocatalysts such as metal centers include expensive and toxic heavy metal elements,<sup>54-56</sup> they allowed for a tremendous progress in the field. To make the next steps, one needs to understand the mechanism by which such catalysts operate, and this starts from the very event of light absorption.

### 1.3.3 Jablonski Diagram



To describe excited states and ultrafast dynamics process clearly, Jablonski diagram is introduced. As shown in an example of the Jablonski diagram (Fig.1.12), excited states are labelled according to their multiplicity (for example S for singlet state and T for triplet state), the number at lower right indicates the consecutive number of the excited state in a singlet or a triplet manifold. The solid arrow pointing from the ground state to an excited state indicates an absorption (or excitation) process and the solid arrow pointing from the excited state to the ground state indicates a radiative process. If the radiative transition is between the states with the same multiplicity, it is called fluorescence; if it is between states with different multiplicity, it is called phosphorescence. The isoenergetic process between states with different multiplicity is an ISC process and is draw with curved arrow. The curved arrow point from high energy state to lower energy state indicates the radiationless relaxation called “internal conversion”.

## 1.4 Intersystem Crossing Process in Transition Metal Complexes

The intersystem crossing (ISC) process is defined as an isoenergetic transition process between two electronic states with different multiplicities<sup>59</sup> which corresponds with electron spin orientation change such as transition from singlet state (all electron spins paired) to triplet state (with two electrons spin parallel to each other) which also could be from doublet state to quartet state such as Cr(III) complexes.<sup>60</sup>

Intersystem crossing (ISC) process is the basis of many phenomena and applications such as phosphorescence,<sup>61,62</sup> singlet oxygen generation,<sup>63</sup> phototherapy,<sup>64</sup> and thermally activated delayed fluorescence (TADF).<sup>65</sup> We are interested in intersystem crossing process because the excited triplet state (take  $T_1$  state as an example) is much longer lived compared with a singlet state. This is

because a  $T_1 \rightarrow S_0$  transition is spin-forbidden, so its transition probability is only  $10^{-6}$  of the transition probability of the spin-allowed transition such as  $S_1 \rightarrow S_0$ .<sup>66</sup> The lifetime of the excited state is important, because the photocatalytic process of water splitting or CO<sub>2</sub> reduction includes a step that H<sub>2</sub>O/CO<sub>2</sub> react with the charge-separated excited state or with an electronically excited reductant as introduced above. This process could be treated as a simple bimolecular reaction whose rate is diffusion-controlled with the rate coefficient  $10^9 - 10^{10} M^{-1}s^{-1}$ ,<sup>67</sup> or in other words, the excited reductant should live long enough to react with the substrate, and the lifetime should be longer than tens of nanoseconds – usually unachievable with singlet excited states.

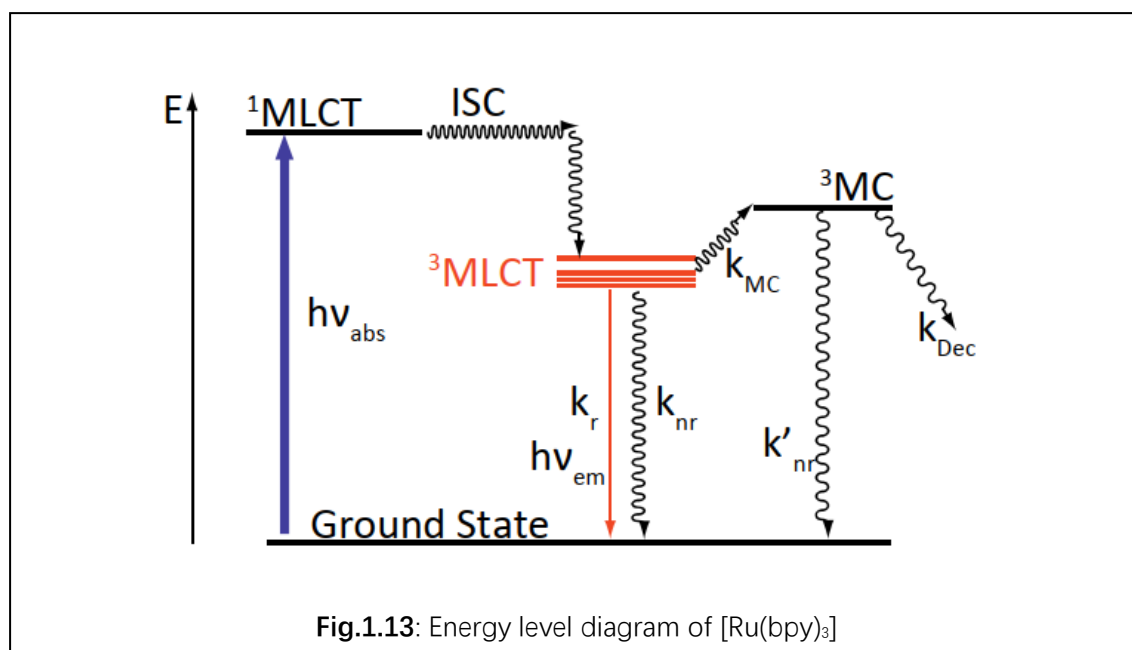
To achieve high yield of a triplet state, acceleration of ISC process is required. The ISC process could be strongly accelerated by introducing heavy atoms into the molecule structure which is known as ‘heavy-atom effect’. This effect was first observed by DS McClure in 1949<sup>68</sup> and first stated by EL-Sayed et al, here the ‘heavy’ means high atomic number.<sup>69</sup> Heavy atom effect could be explained by a relativistic effect called spin-orbit coupling (SOC),<sup>70</sup> it is caused by the interaction between electron spin magnetic moment in the magnetic field generated by relative motion of the nucleus, the higher the nucleus’ atomic number, the higher its nuclear charge and the stronger the magnetic field generated.<sup>71</sup> This also indicates that transition metal complexes should undergo fast ISC process because the metal included is a heavy atom. Based on SOC, the strong phosphorescence of nitrogen heterocycles and its very efficient ISC process:  $S_{(n,\pi^*)} \rightarrow T_{(\pi,\pi^*)}$ , and  $S_{(\pi,\pi^*)} \rightarrow T_{(n,\pi^*)}$  is explained by El-Sayed: this explanation is known as El-Sayed rule which is stated that if the ISC process involves orbital type change then the ISC rate is relatively high,<sup>72</sup> in which the spin forbidden transition becomes partially allowed because of spin-orbit coupling.

#### 1.4.1 ISC in Transition Metal Complexes

### 1.4.1.1 Ruthenium Trisbipyridine, $[Ru(bpy)_3]^{2+}$

An archetypal photosensitizer,  $[Ru(bpy)_3]^{2+}$  was one of the first to be used in photocatalytic processes of  $H_2O$  splitting and  $CO_2$  reduction. Consequently, its photochemical properties and photo-induced dynamics attracted a lot of attention.

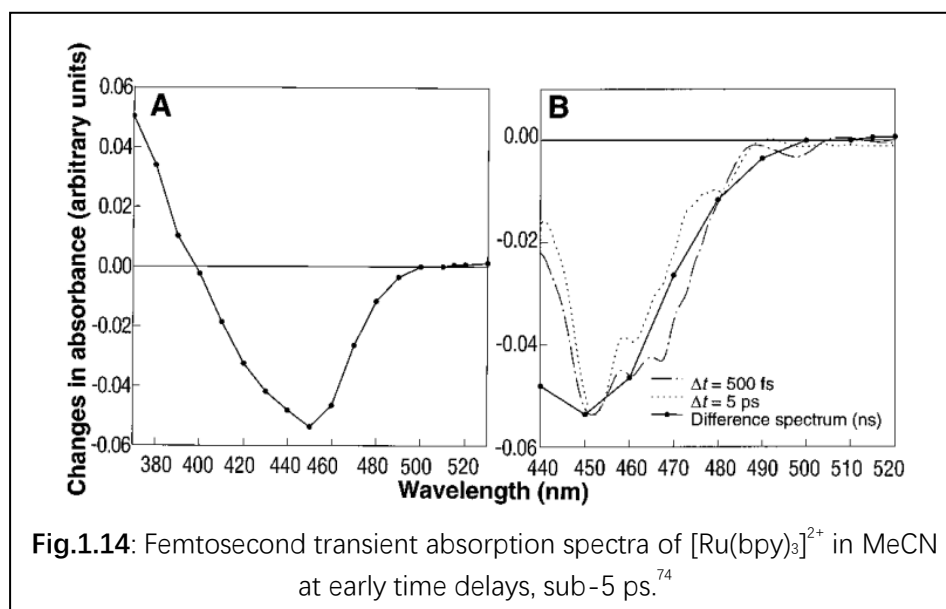
One of the most powerful techniques to investigate dynamics of excited states and extract lifetime of the excited states is called ultrafast spectroscopy. Ultrafast spectroscopy is an umbrella term which includes multiple different techniques that will be introduced in detail later.



The energy level diagram of  $[Ru(bpy)_3]^{2+}$  is shown in **Fig.1.13**; it shows the ISC process from  $^1MLCT$  to  $^3MLCT$  state.<sup>73</sup> To measure the rate of this process, a lot of work has been done by using different ultrafast spectroscopy techniques in the past decades.

In early research, the ultrafast (sub-picosecond) ISC process of  $[Ru(bpy)_3]^{2+}$  was suggested based on femtosecond time resolved transition absorption spectroscopy (Shown in **Fig.1.14**)<sup>74</sup> (which can detect absorption spectra corresponding to the excited state) together with the assumed near unity

quantum yield of the  $^3\text{MLCT}$  phosphorescent state.<sup>75</sup> Later research indicates that  $^1\text{MLCT}$  fluorescence quantum yield is indeed very low, only around  $9 \times 10^{-5}$ .<sup>76</sup>



In the spectra shown in **Fig.1.14**, the bleach at 400 to 500 nm is a combination of  $^3\text{MLCT}$  state absorption (positive signal) together with the loss of the ground state  $^1\text{MLCT}$  absorption (negative signal). With careful analysis of single-wavelength kinetic traces, the half-life of the  $^3\text{MLCT}$  state formation is extracted, of the order of 100 fs.<sup>74</sup>

However, the transient absorption research of  $[\text{Ru}(\text{bpy})_3]^{2+}$  does not extract absorption signal directly from the short lived  $^1\text{MLCT}$  state. Direct observation of signal from  $^1\text{MLCT}$  state is achieved with another technique called fluorescence up-conversion spectroscopy, FLUP. FLUP is a technique used to collect time-resolved emission spectra, and the reported spectra of  $[\text{Ru}(\text{bpy})_3]^{2+}$  are given in **Fig.1.15**.<sup>53</sup> Here, the emission signal collected at  $15500\text{-}19500\text{ cm}^{-1}$  (512-645 nm) is assigned to fluorescence from  $^1\text{MLCT}$  state of  $[\text{Ru}(\text{bpy})_3]^{2+}$  with lifetime shorter than the instrument response function; and by deconvolution of the emission kinetic trace the lifetime of  $^1\text{MLCT}$  is

suggested as  $15 \pm 10$  fs which is much shorter than the lifetime suggested by transient absorption spectroscopy study mentioned above.

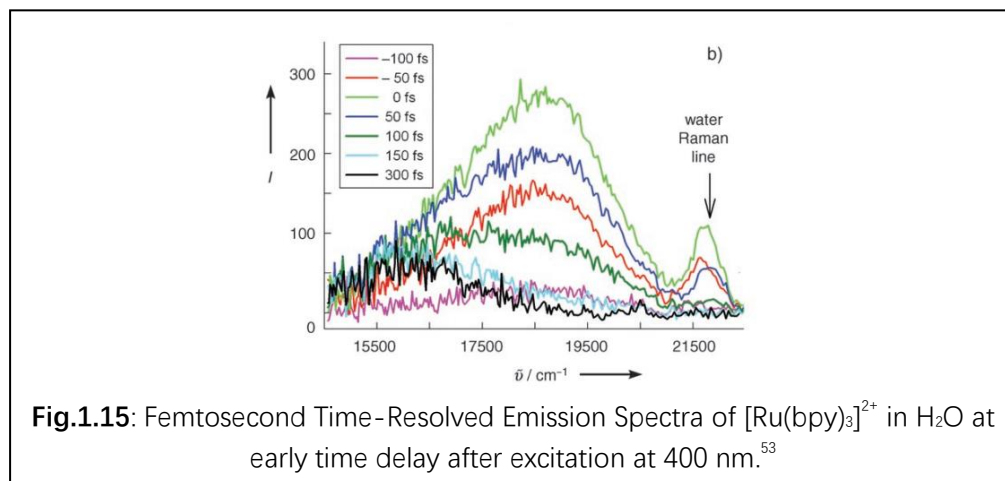
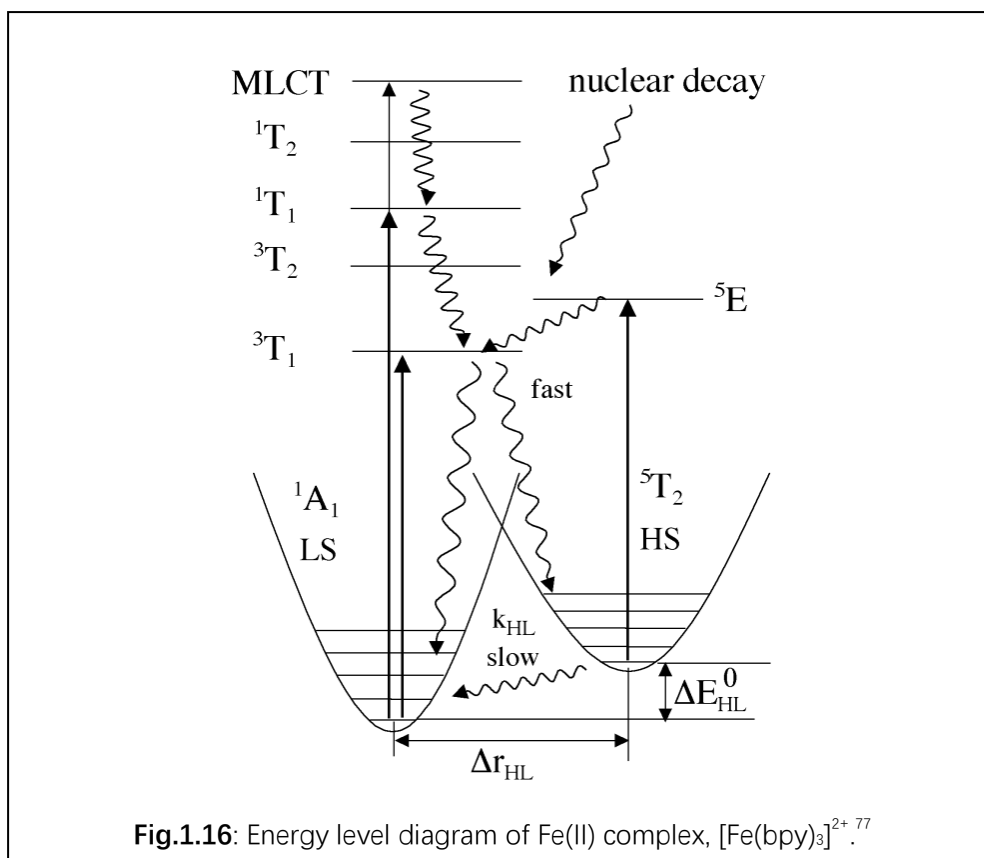


**Fig.1.15:** Femtosecond Time-Resolved Emission Spectra of  $[\text{Ru}(\text{bpy})_3]^{2+}$  in  $\text{H}_2\text{O}$  at early time delay after excitation at 400 nm.<sup>53</sup>

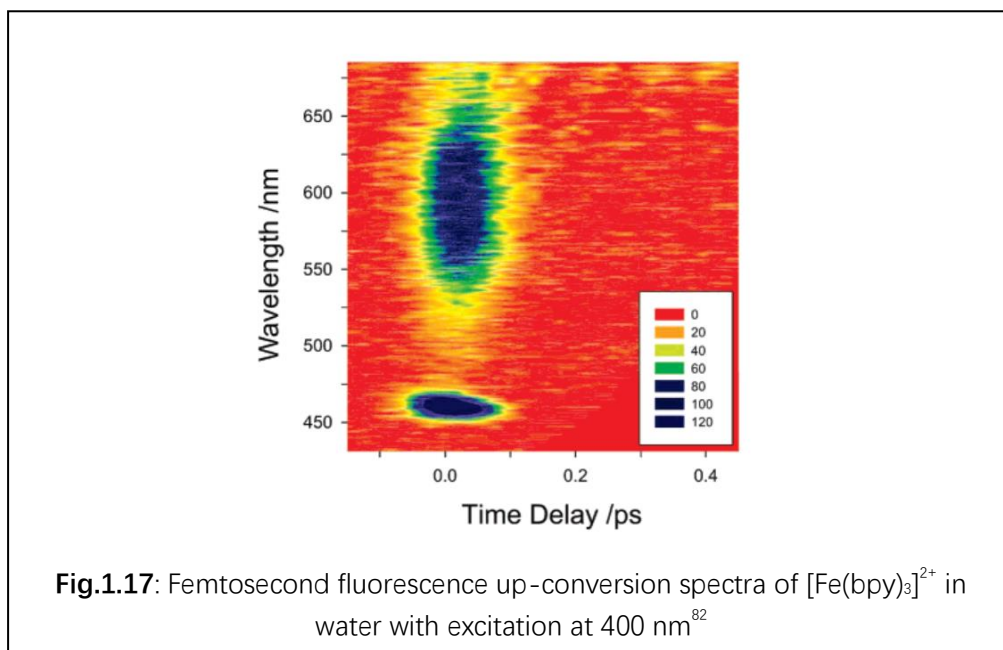
#### 1.4.1.2 Iron Trisbipyridine, $[\text{Fe}(\text{bpy})_3]^{2+}$

An obvious difficulty with using Ru-complexes as photosensitisers is the cost, and the fact that Ruthenium is rare. A replacement photosensitisers using more available, cheaper metals have been sought for decades. One of those is an iron analog of  $[\text{Ru}(\text{bpy})_3]^{2+}$ ,  $[\text{Fe}(\text{bpy})_3]^{2+}$ . However, energy levels and the nature of the excited states in  $[\text{Fe}(\text{bpy})_3]^{2+}$  are different from those of  $[\text{Ru}(\text{bpy})_3]^{2+}$ . In  $[\text{Fe}(\text{bpy})_3]^{2+}$  photoexcitation populates an <sup>1</sup>MLCT state, which undergoes fast decays into a high-spin metal centered quintet state (<sup>5</sup>T) as show in **Fig.1.16**.<sup>77</sup> This decay process from singlet state to quintet state of Fe(II) complexes is also known as spin crossover (SCO).



Research on the spin crossover process of  $[\text{Fe}(\text{bpy})_3]^{2+}$  could be dated back to 1981. In early research work, SCO was assigned to direct intersystem crossing  $^1\text{MLCT} \rightarrow ^5\text{T}$  because of lack of suitable ultrafast spectroscopy techniques with sufficient time resolution.<sup>78–81</sup> Further study based on femtosecond fluorescence up-conversion spectroscopy revealed an ultrashort emission signal centered at 600 nm, and the other emission signal centered at 660 nm as shown in **Fig.1.17**.<sup>82</sup>





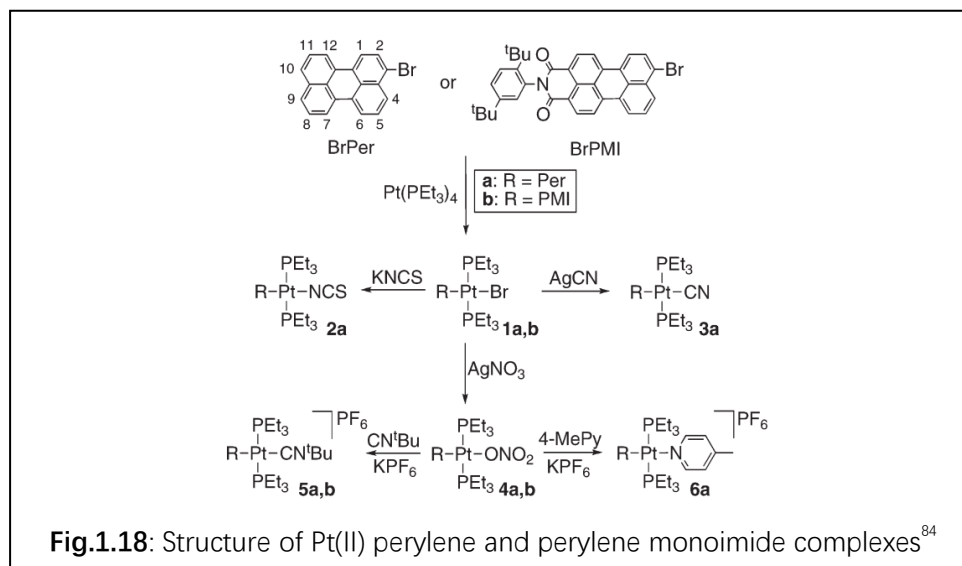
In this research, the 600 nm centered emission was attributed to  $^1\text{MLCT}$  and the emission at 660 nm is attributed to  $^3\text{MLCT}$ , the observation of emission from the ultrashort lived  $^3\text{MLCT}$  state indicates the spin crossover process of  $[\text{Fe}(\text{bpy})_3]^{2+}$  is  $^1\text{MLCT} \rightarrow ^3\text{MLCT} \rightarrow ^5\text{T}$  with two ultrafast intersystem crossing processes, from  $^1\text{MLCT}$  to  $^3\text{MLCT}$  to  $^5\text{T}$ .<sup>82</sup> Further research on the lifetimes of  $^1\text{MLCT}$  state and  $^3\text{MLCT}$  state was done by transition absorption method with time resolution  $\sim 40 \text{ fs}$ , the result implies the  $^5\text{T}$  state is populated within 50 fs after excitation.<sup>83</sup>

The problem with Fe(II) complex discussed here is the extremely short lifetime, which makes it unsuitable as photosensitizer.

#### 1.4.1.3 Platinum (II) Perylene and Perylene Monoimide Complexes

However, not all transient metal complexes undergo ultrafast (sub-picosecond) ISC process, there are several examples of transition metal complexes with nanosecond intersystem crossing. An example here is Pt(II) perylene and perylene monoimide complexes, whose structures are given in **Fig.1.18**. The fluorescence lifetime of these complexes in dichloromethane are varied from 1.88 ns to 5.02 ns with excitation at 510 nm, which is  $10^6$  times longer than the sub-picosecond lifetime introduced before.<sup>84</sup> The strong fluorescence of

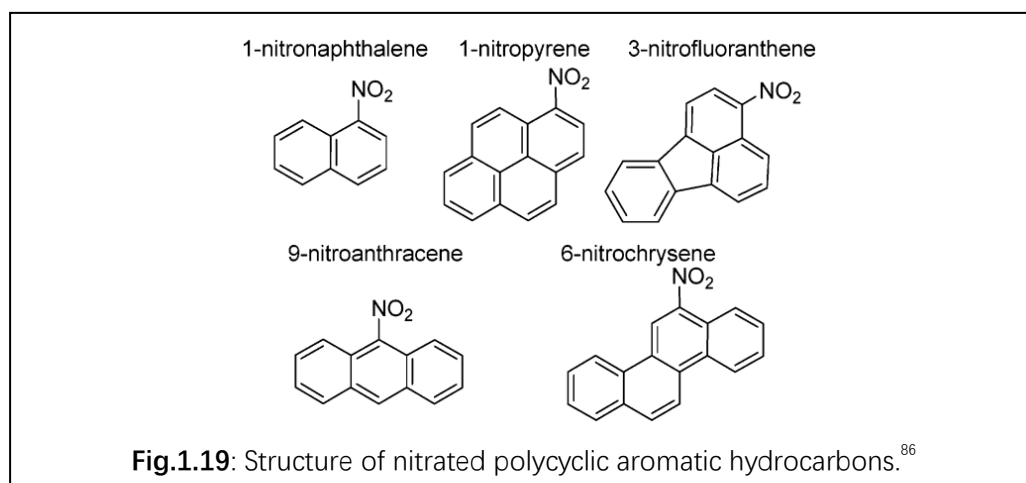
transition metal complexes is explained as the fluorescence decay rate is fast and competitive with the slow ISC process caused by poor interaction between metal (the heavy atom) and ligands.<sup>85</sup>



## 1.4.2 Ultrafast ISC Process in Heavy-Atom Free Organic Molecules

### 1.4.2.1 Nitrated Polycyclic Aromatic Hydrocarbons (NPAHs)

Intersystem crossing process in heavy-atom free organic molecules can also be ultrafast and even as fast as sub-picosecond. Nitrated polycyclic aromatic hydrocarbons are one of the kinds of molecules with ultrafast ISC, their structure is given in **Fig.1.19**.<sup>86</sup> All of these molecules undergo ISC within 5 ps; and it is worth to note that fluorescence lifetime of 1-nitronaphthalene is measured as 70 fs by fluorescence up-conversion technique.<sup>86</sup> The sub-picosecond ISC process in 1-nitronaphthalene after excitation is explained by the existence of a higher-lying triplet excited state ( $T_n$ ) with more  $\pi - \pi$  character and so stronger spin-orbit coupling compared with the first triplet excited state ( $T_1$ ).<sup>86</sup> The ISC process becomes  $S_1 \rightarrow T_n \rightarrow T_1$  and the nature of this process is  $^1(n - \pi^*) \rightarrow ^3(\pi - \pi^*) \rightarrow ^3(n - \pi^*)$ , the transition between  $^1(n - \pi^*) \rightarrow ^3(\pi - \pi^*)$  being allowed according to El-Sayed's rule.<sup>87</sup>



Based on the cases introduced above, the influence of the heavy atom effect on spin-orbit coupling and on the rate of the ISC process is not so reliable as the systems including 'heavy' transition metals can be strongly fluorescent, whilst the molecules that only include 'light' atoms can undergo sub-picosecond ISC (such as 1-nitronaphthalene). Also, there are other intersystem crossing processes which we did not mention here, such as thermal activated delayed fluorescence which is caused by reverse ISC process from triplet state back to singlet state.<sup>88</sup> The rate of ISC could be influenced by many factors apart from the heavy atoms: for example, is the molecule rigid or not, or are the electronic states localized or delocalized. For the molecules with more flexibility, the spin, vibrational, and electronic degrees of freedom are interacting with each other and may lead to spin-vibronic coupling which may enhance ISC process.<sup>89-91</sup> In other words, there are still lots of things that need to be investigated on the mechanism of ISC processes.

## 1.5 Ultrafast Time-Resolved Spectroscopy Techniques

### 1.5.1 A Brief History

The first time resolved 'spectra' could be dated back to 1894, which is a series of photographs of a falling cat taken by Étienne-Jules Marey (**Fig.1.20**) with chrono-photography technique at 12 Hz frequency that gave dynamics of a

falling cat.<sup>92</sup> From these photographs, the state of a cat at certain time delay after being thrown down is recorded.

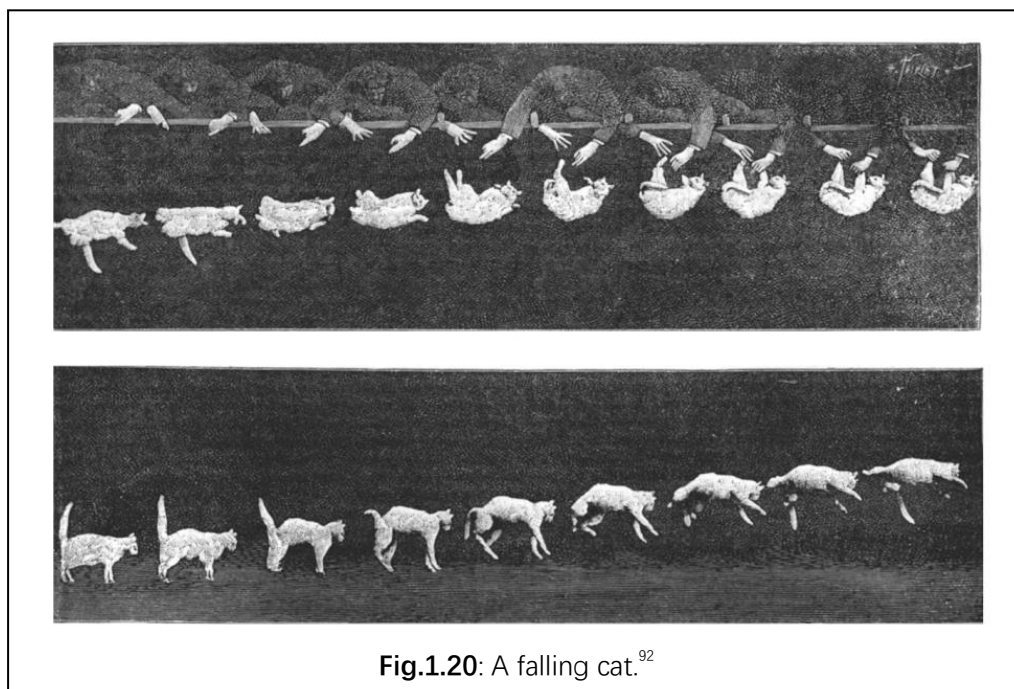


**Fig.1.20:** A falling cat.<sup>92</sup>

Fifty-six years later, a technique called flash photolysis spectroscopy was developed by George Porter and Ronald Norrish, to monitor the dynamics of photoinduced free radical reactions, a discovery that led to them, along with Manfred Eigen, being awarded Nobel Prize in Chemistry in 1967. The first flash photolysis spectrometer is shown in **Fig.1.21**.<sup>93</sup> This setup includes two flash lamps: one is photolysis flash (excitation flash), the other is spectro-flash (probe flash), the flash duration is around  $50 \mu s$ . The time delay is controlled by two contacts on a rotating wheel, by changing the distance between the two contacts.<sup>94</sup> This setup could be treated as the very first form of the pump-probe setup of ultrafast transient absorption spectroscopy later.

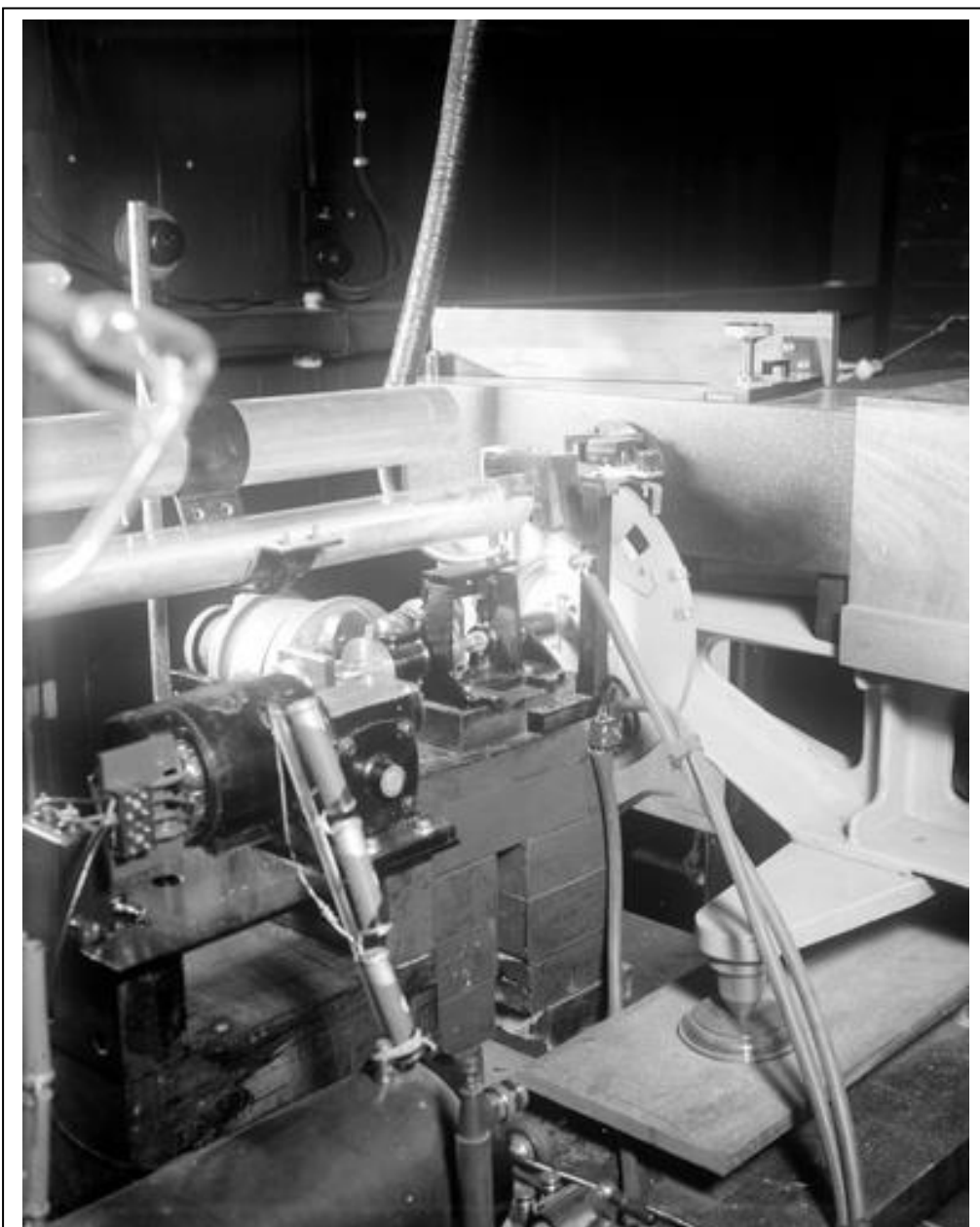
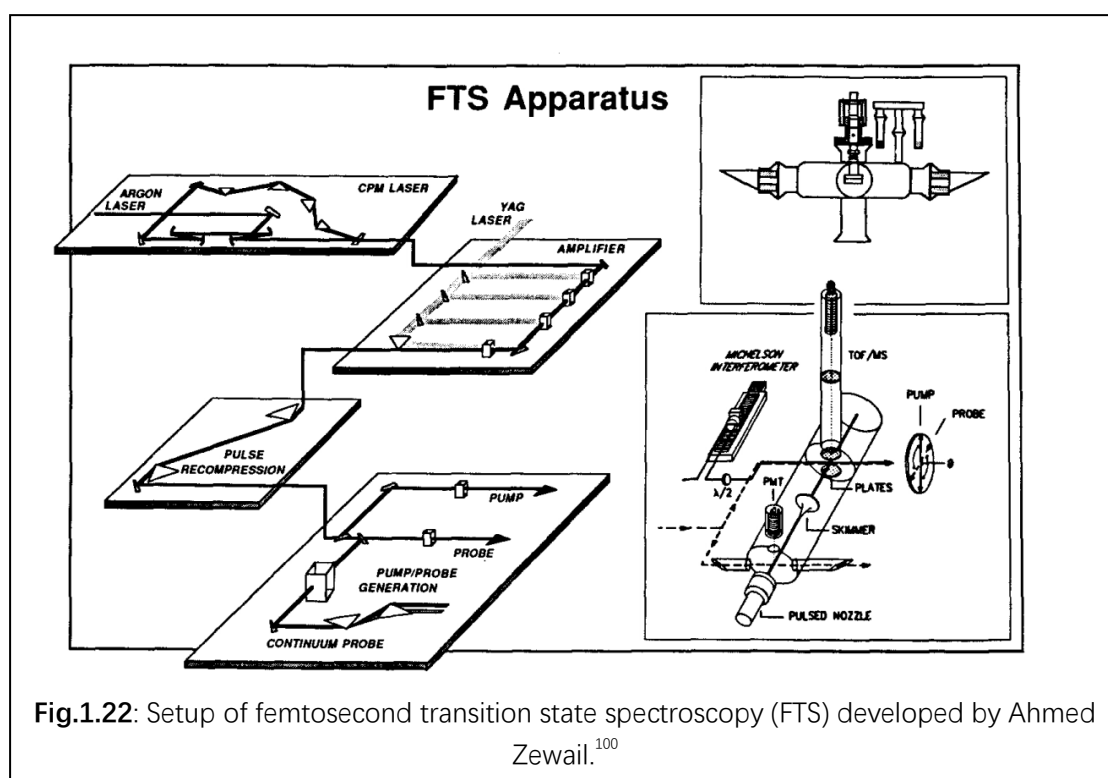


**Fig.1.21:** The first flash photolysis spectrometer.<sup>93</sup>

In 1960, ten years after the first flash photolysis spectrometer was invented, the first laser system was developed by Theodore Maiman by using Ruby as a gain medium.<sup>95</sup> With the development of laser techniques, especially mode-locking method applications, laser pulse duration has been decreased to femtoseconds.<sup>96</sup> Today, laser pulse duration has been further compressed to attosecond scale.<sup>97,98</sup> The development of laser techniques provided the opportunity to substitute the flash lamps (duration  $50 \mu s$ ) with ultrafast lasers,

dramatically improving time resolution.

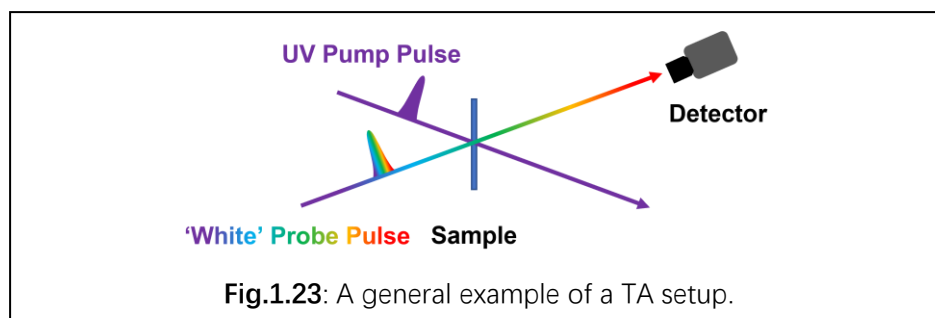
In the 1980s, Ahmed Zewail et al reported a new technique, whereby they applied an ultrafast ( $\sim 100$  fs) laser pulse as the pump pulse to induce photoreaction and used the second femtosecond ( $\sim 100$  fs) laser pulse as the probe pulse to detect the absorption change induced by the pump pulse.<sup>99,100</sup> The time delay between the pump and probe pulse is controlled by a linear precision actuator as show in **Fig.1.22**. Zewail's attribution in research of transition states of chemical reaction by using femtosecond spectroscopy led to an award of the Nobel Prize in Chemistry in 1999.



### 1.5.2 Femtosecond Transient Absorption (TA) Spectroscopy

A general TA setup is shown in **Fig.1.23**. There, a UV pump pulse and a 'white' probe pulse are directed onto the sample and the spot of pump and probe pulse are overlapped with each other, after the white probe pulse passes

through the sample, it is directed into the detector to be detected.



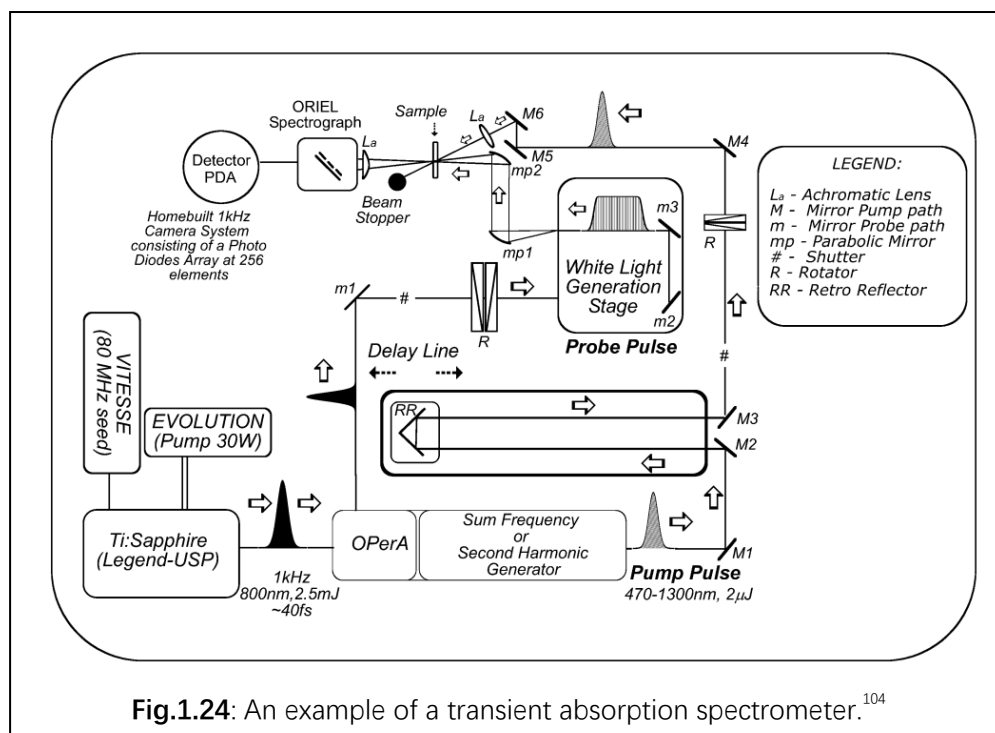
### 1.5.2.1 Supercontinuum Generation

Supercontinuum generation is a key step in femtosecond transient absorption (TA) spectroscopy setup, which is used to generate broadband white light probe pulse with femtosecond time resolution. This phenomenon was first reported by Alfano et al.: when they excited borosilicate glass with strong 530 nm picosecond laser pulse, continuous broadband emission with wavelength 400-700 nm was generated.<sup>101</sup> This phenomenon is caused by the plasma formed in the medium when excited with a high power laser pulse, the free electrons generated change the nonlinear behavior of the medium so continuous white pulse is generated. Other mechanisms such as self-phase modulation and retardation behavior of the medium may also contribute to the supercontinuum generation.<sup>102,103</sup>

### 1.5.2.2 Femtosecond Transient Absorption Setup

Femtosecond TA is a type of pump-probe method. An example setup is given in **Fig.1.24**. There, the pump pulse and probe pulse are generated from the laser source and the pump (excitation) pulse beam is introduced into optical delay stage used to control the time delay between the pump and probe pulses in the example setup.<sup>104</sup> The optical delay stage can change the path length of the laser pulse so it changes the time laser pulse arrive at the sample, it does not matter which beam is on the delay stage - it could be a pump beam or a probe beam.<sup>105</sup> In the pump pulse beam line before the sample, there is a

chopper which will chop half of the pump pulses in the pulse train. After the pump beam passes through the sample, it is directed to a beam stopper and absorbed so it would not hit the detector as the pump beam is too strong and may damage the detector and influence the detection of transient absorption signal.



The probe generated from the laser source is first directed into a white light generation stage to generate the femtosecond white probe beam by supercontinuum generation, this stage could be a crystal such as CaF<sub>2</sub> or as in early setups, water could also be used.<sup>106</sup> The generated white light probe pulse is focused onto the sample and then collected into the detector.

The process of TA spectra collection is as follows. First, the time delay between the pump and probe pulses is fixed. Secondly, because the chopper in pump pulse beam line chopped half of the pump pulse, the probe beam absorption measured could be separated as signal from excited sample ( $I(\lambda)_{ex}$ ) and ground state sample ( $I(\lambda)_{gr}$ ), and the absorbance of the excited state ( $\Delta A(\lambda)$ )



is given in **Equation 1**.<sup>104</sup>

$$\Delta A(\lambda) = -\lg \left( \frac{I(\lambda)_{ex}}{I(\lambda)_{gr}} \right) \quad \text{Equation 1}$$

### 1.5.3 Transient Emission Spectroscopy

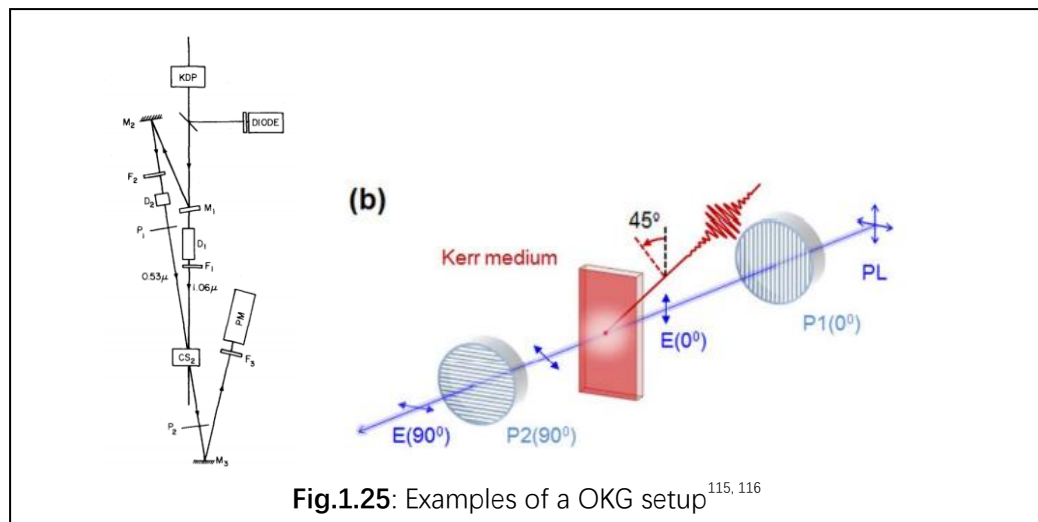
As introduced in the “intersystem crossing” part above, transient emission spectroscopy has its own advantages. Transient emission spectroscopy technique is sensitive to fluorescent states of the molecules because this technique focus on the detection of absolute emission signal instead of absorbance change such as in TA, so it is widely used in detection of sub-picosecond fluorescent states and to extract the corresponding intersystem crossing rate.<sup>53,82</sup> Also, emission spectra including time-resolved emission spectra and steady-state emission spectra contain information of the energy gap between the ground state and the corresponding (emissive) excited state which cannot be extracted with other techniques.<sup>107</sup> However, once the emissive state of the sample is populated, the photons start to emit, so the question becomes how to extract and detect photons emitted at certain time delay with ultrashort time scale in time resolved emission spectroscopy. There are many methods to obtain time resolved emission spectra which will be introduced in the following part.

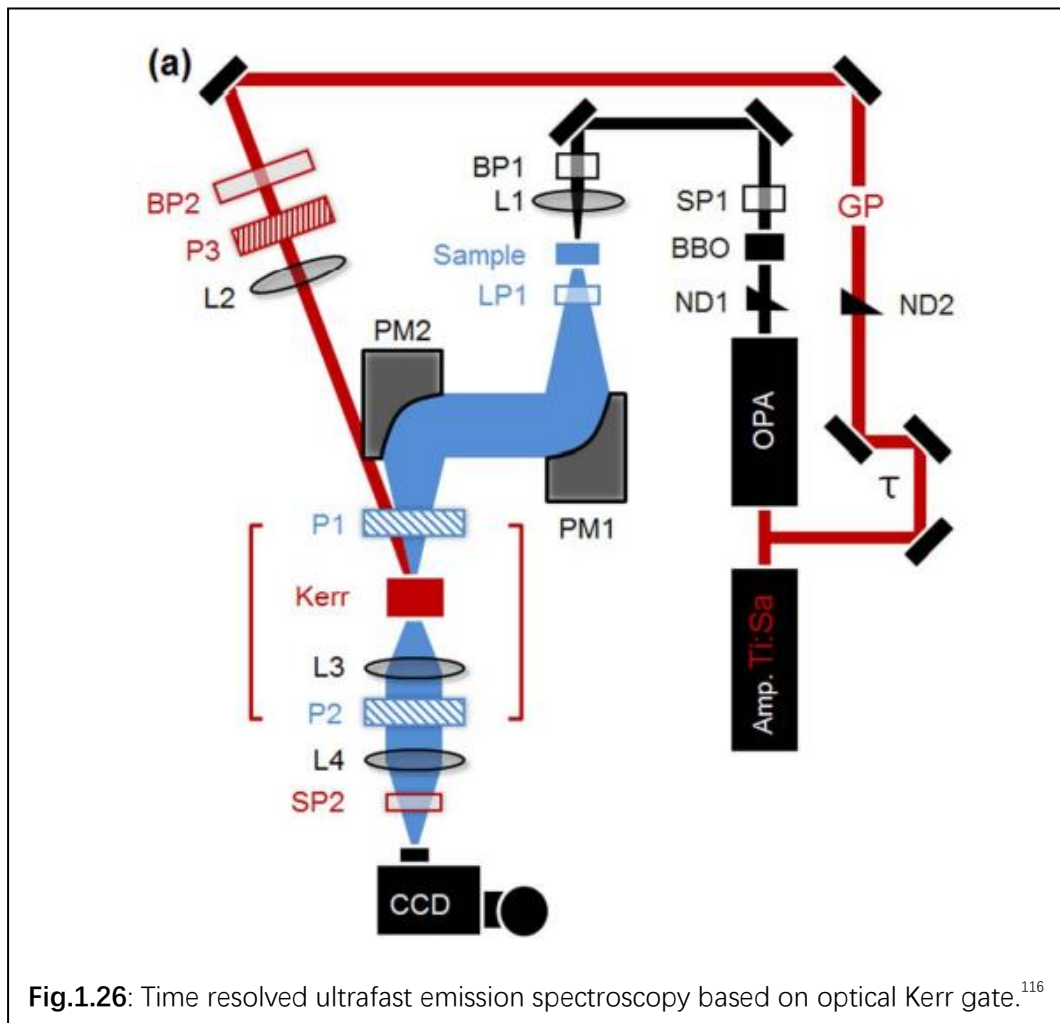
#### 1.5.3.1 Kerr Gate Method

Kerr gate method is based on a phenomenon called optical Kerr effect. It was first proposed in theory by Buckingham in 1955,<sup>108</sup> which predicted that with strong light incident into an isotropic medium, the medium will become temporarily birefringent. This is different from Kerr effect observed by John Kerr in 1875 in which the electric field is generated by a voltage source but in optical Kerr effect it is generated by a strong field of electromagnetic wave.<sup>109,110</sup> This predicted phenomenon was later observed by Maker et al in 1964.<sup>111</sup> Just like birefringent crystal is widely used in producing waveplates<sup>112-</sup>

<sup>114</sup> which could change light polarization, the optical Kerr medium could be made into laser controlled transient waveplate or in other words, into an optical Kerr gate (OKG).

A OKG setup is shown in **Fig.1.25** for the test of ultrafast optical gate.<sup>115</sup> Here the optical Kerr medium used is CS<sub>2</sub>, the CS<sub>2</sub> cell is put in between the two optical polarizers, their orientation is set perpendicular to each other in the 530 nm beam line. The 1060 nm laser beam is used to induce optical Kerr effect of the CS<sub>2</sub> cell. In this setup, when the 1060 nm laser pulse is not passing through the CS<sub>2</sub> cell, the optical Kerr medium would not show birefringence and the 530 nm beam that passes through the first polarizer cannot pass through the second polarizer because the polarization of 530 nm is perpendicular to the second polarizer's orientation. When the intense 1060 nm laser pulse passes through the CS<sub>2</sub> cell, the CS<sub>2</sub> becomes birefringent and can change the polarization of the light that passes through it, so if the 530 nm pulse passes through the CS<sub>2</sub> cell at the same time as the strong 1060 nm pulse, the polarization of the 530-nm pulse will be changed and is allowed to pass through the second polarizer and then be detected by the detector.<sup>115</sup>





One of the applications of OKG is ultrafast time resolved emission spectroscopy, a typical setup based on optical Kerr gate method is given in **Fig.1.26**.<sup>116</sup> This setup also includes two laser beams: one is an excitation beam, which is focused on the sample to excite the substance and the emitted photons are collected by parabolic mirrors and then pass through the optical Kerr gate setup and focused on the CCD camera, the detector. The other beam is the gate beam, unlike the probe beam in TA setup, this beam is focused on the Kerr medium instead of the sample to control the Kerr gate opening and closing. The gate beam used is 800 nm with pulse duration 100 fs, and only when the 100 fs duration gate laser pulse pass through the Kerr medium the Kerr gate is open and the emission could pass and get detected, the rest of the emission is blocked by the Kerr gate.<sup>116</sup> The time difference between the pump and gate beam is controlled by a delay stage which is similar to TA setup introduced

before. Thus, by controlling the pump-gate time delay, one can control at what time after the pump emission from the sample can pass through the Kerr gate – in this way, spectra at different delays are collected, and the kinetics reconstructed afterwards from the spectral data.

An interesting application of the Kerr-gated set-up is detection of time-resolved Raman spectra from highly emissive substances.<sup>117</sup>

### 1.5.3.2 Up-Conversion Method

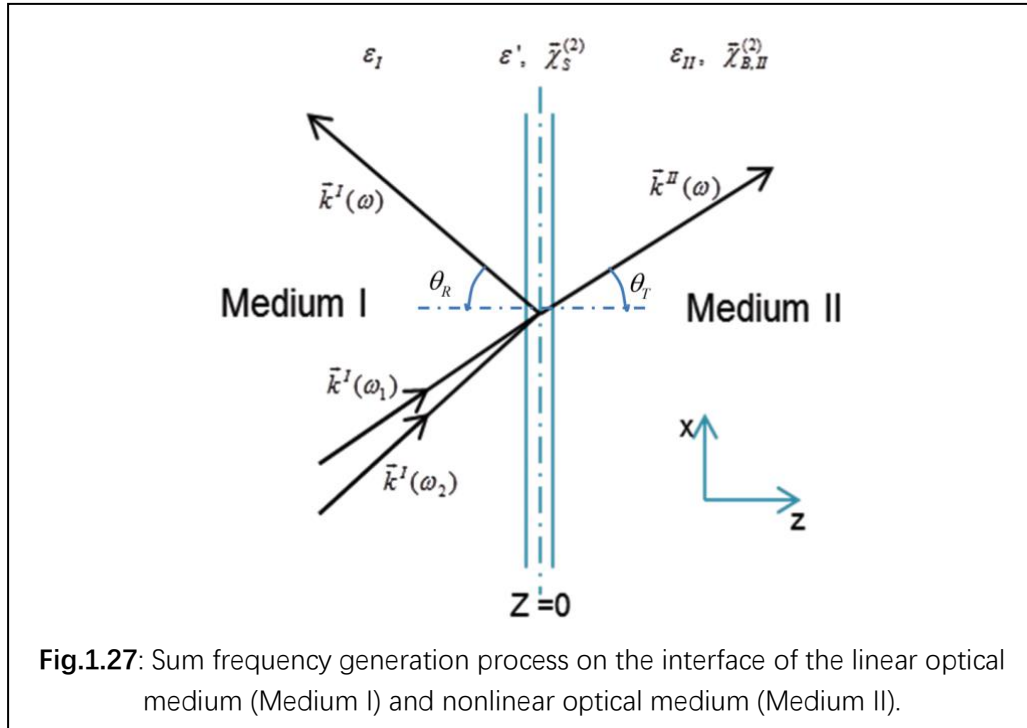
Up-conversion method is based on the phenomenon called sum-frequency generation (SFG) process. With the development and application of ruby laser systems, from 1960<sup>95</sup> non-linear optical phenomenon could be observed. In 1961, Franken et al reported that when 694.3 nm Ruby laser beam pass through quartz crystal, another light with wavelength 347.2 nm is generated, this phenomenon is called second harmonic generation (SHG) the generated photon with energy equal to two incident photons from Ruby laser.<sup>118</sup> One year later, in 1962, Braslau et al reported another non-linear optical phenomenon that when the ruby laser (694.3 nm) together with mercury lamp lights are focussed into potassium dihydrogen phosphate (KDP) crystal together, signal lines with energy equal to the sum of mercury lamp lines and the ruby laser is observed. This is the first reported observation of SFG process.<sup>119</sup> One year later, in 1963, Braslau et al reported another non-linear optical phenomenon, in which when they focus 694.3 nm Ruby laser and 311.5 nm light from a mercury lamp together into the KDP crystal, the signal at 565 nm was observed which was equal to the energy difference between 694.3 nm ruby laser and 311.5 nm mercury lamp. This phenomenon is known as difference frequency generation (DFG).<sup>120</sup>

The sum frequency generation non-linear optical mediums such as KDP mentioned before, contains a nonzero second order optical susceptibility ( $\chi^{(2)}$ )

in the following equation of polarization  $P$  and electric field  $E$  shown in **Equation.2**. Here the  $\alpha$  is linear susceptibilities and  $\chi^{(2)}, \chi^{(3)}, \dots, \chi^{(n)}$  are corresponding nonlinear optical susceptibilities. The nonzero  $\chi^{(2)}$  of sum frequency generation medium is caused by asymmetric electron density distribution in the medium according to theoretical calculation. This asymmetric electron density distribution could be achieved with a distorted anion group in the crystal such as  $B_3O_6^{3-}$  anion in  $\beta - BaB_2O_4$  (BBO) crystal.<sup>121</sup>

$$P = \alpha E + \chi^{(2)} E^2 + \chi^{(3)} E^3 + \dots + \chi^{(n)} E^n \quad \text{Equation.2}$$

To achieve efficient SFG, phase matching also needs to be taken into consideration as shown in **Fig.1.27**. In this figure, the two incident photons with energy  $\omega_1$  and  $\omega_2$  generate a photon via SFG with energy  $\omega = \omega_1 + \omega_2$  (to meet the energy conservation law). Apart from energy conservation, momentum conservation law also should be met, so the transmitted up-converted photon's wavevector should satisfy the following equation  $\vec{k}^{II}(\omega) = \vec{k}^I(\omega_1) + \vec{k}^I(\omega_2)$ , where the  $\vec{k}^I(\omega_1)$  and  $\vec{k}^I(\omega_2)$  are wavevectors of the two incident photons.<sup>122</sup> There are two different types of the second order SFG process: Type I uses the two incident light beams with the same polarization and Type II uses the two incident light beams with orthogonal polarization.<sup>123,124</sup>

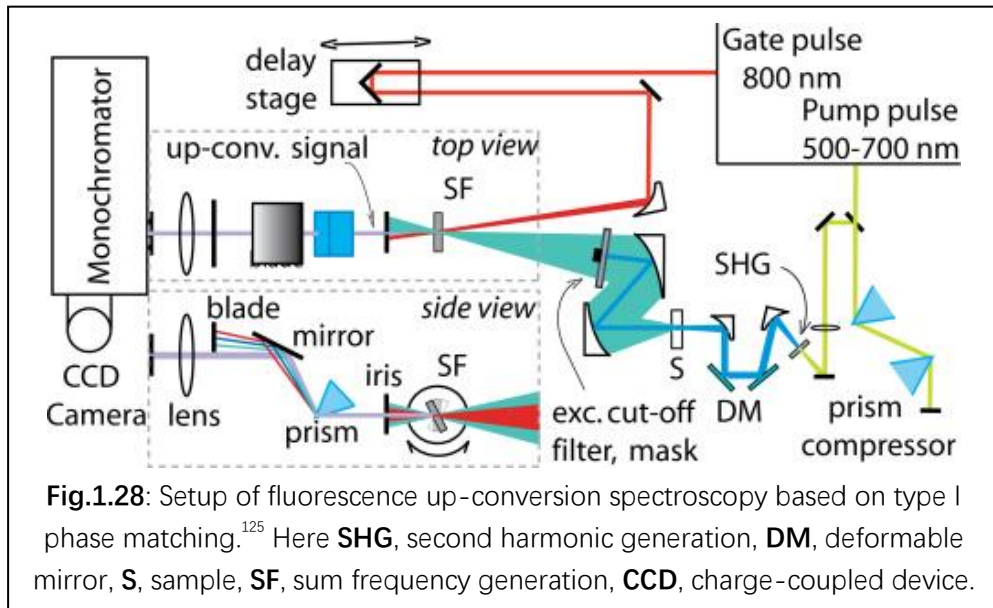


### 1.5.3.2.1 Femtosecond Fluorescence Upconversion (FIUC) Spectroscopy Setup

Based on the sum-frequency generation phenomenon, the time resolved fluorescence up-conversion spectroscopy can be setup as shown in **Fig.1.28**.<sup>125</sup> This setup, similar to the Kerr-gate method, includes two laser beams, one is the tunable (500-700 nm) narrowband pump pulse, the other is 800 nm gate pulse with 50 fs pulse duration used to up-convert the emission signal at the nonlinear optical crystal. The pump beam is focused on the sample and the emission generated is collected and focused into the sum frequency crystal. The time delay between the pump and probe pulse is controlled by sending either beam on a delay stage.

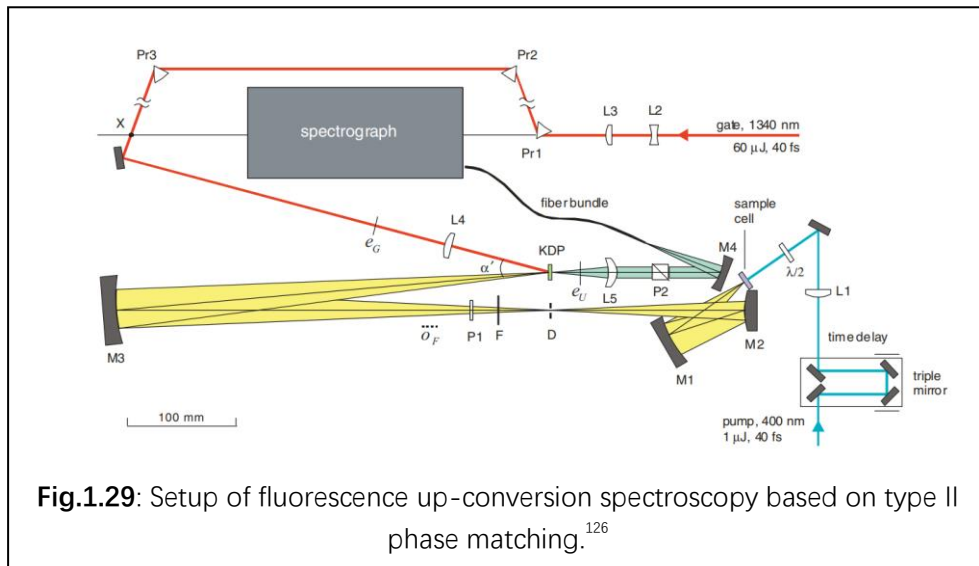
At the nonlinear optical medium (BBO crystal) only the emitted photons that arrive at the same time as the gate pulse could be upconverted and separated out from the background emission. The up-converted emission signal is then refracted into another direction by a prism, because it is shorter in wavelength compared with the background emission, and

directed into a detector. The detector is made of a spectrometer combined with a charge-coupled device (CCD) camera. In this setup type I phase matching is used. To achieve efficient broadband up-conversion to cover the whole emission wavelength range the sum frequency crystal is continuously rotating from  $-23^\circ$  to  $+5^\circ$  at constant angular speed,<sup>125</sup> as the phase matching depends on the wavelength of the photon and the incident angle.



### 1.5.3.2.2 Femtosecond Broadband Fluorescence Upconversion Spectroscopy (FLUPS)

To achieve broadband fluorescence upconversion range, one method is to continuously rotate the crystal in type I sum frequency phase matching. The other method is to use type II phase matching instead as it covers broader wavelength range. An example setup is given in **Fig.1.29**.<sup>126</sup>

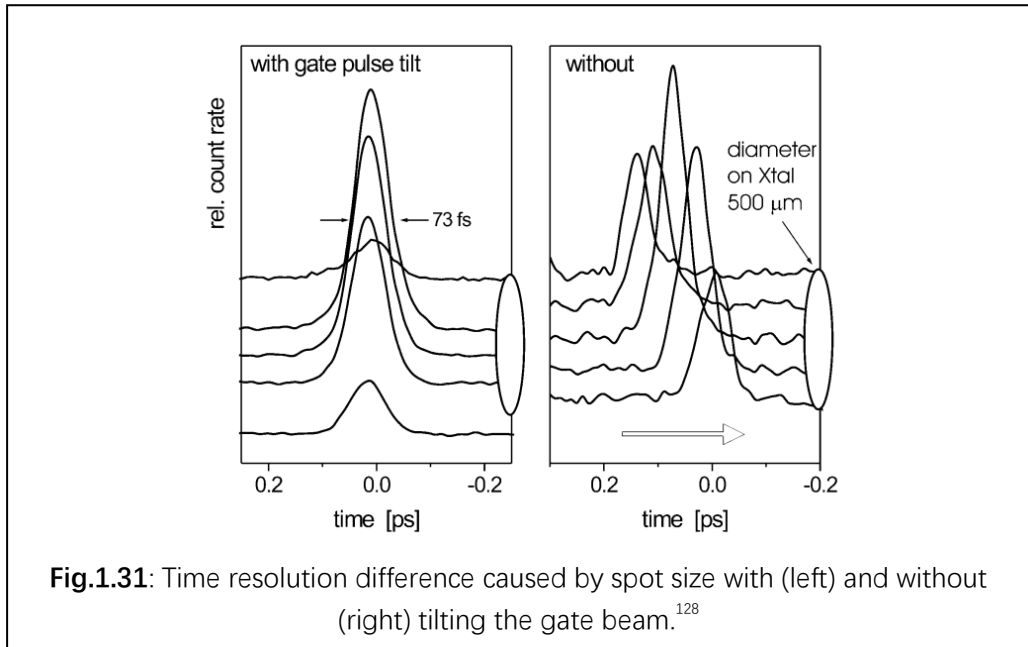
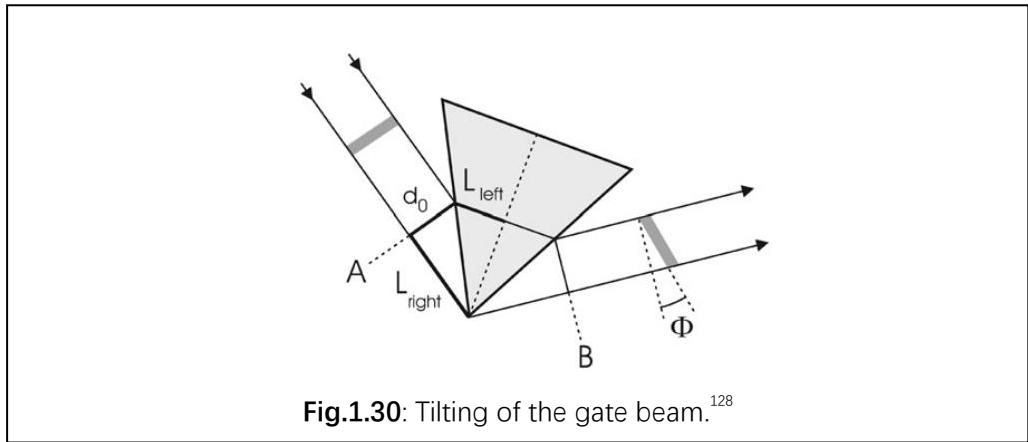


In this setup, the pump pulse is 400 nm with the FWHM 40 fs, and the gate beam used is 1340 nm, also 40 fs FWHM. The time delay is also controlled by the delay stage with the 400 nm pump beam on the delay stage (because 1340 nm gate beam loses power faster with the increase of path length). The pump beam is focused into the sample and the emission is collected and focused into the nonlinear optical medium, a potassium dihydrogen phosphate (KDP) crystal<sup>126</sup> or a BBO crystal.<sup>127</sup> At the sum frequency crystal, the emission signal is upconverted by the 1340 nm gate beam with type II phase matching to gain efficient upconversion in a broad range, and the crystal is fixed at a specific angle during the experiment. The upconverted emission signal propagates in different direction to the background emission, then the upconverted emission is reflected into a fiber and sent into the spectrograph which is made by combining a spectrometer with a CCD camera.

With a fixed sum frequency generation crystal, the time resolution of this setup could be further improved by tilting the gate pulse wavefront to achieve optimal timing with fluorescence. As shown in **Fig.1.29**, there are only three prisms inserted in the gate beam line. The first two prisms are used to compress the gate beam to improve time resolution and the third

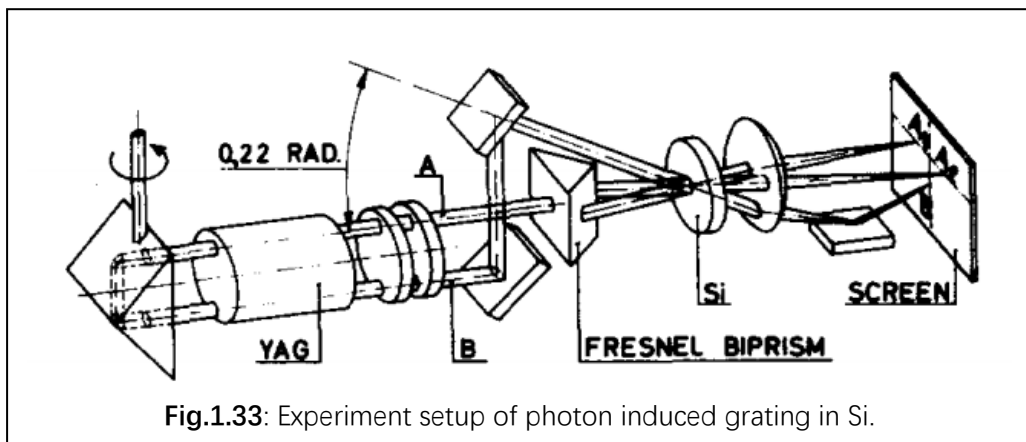
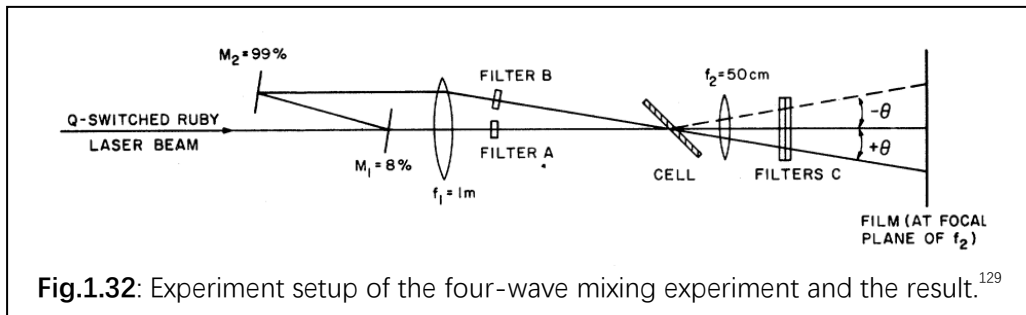


beam is used to tilt the gate beam as shown in **Fig.1.30**.<sup>128</sup> In this setup, to achieve broadest upconversion range, the gate beam and the fluorescence beam are set at an angle of  $14^\circ$ . The spot size of both beams are around  $300\ \mu\text{m}$  FWHM so the outer side rays will arrive at the upconversion crystal and interact with each other earlier compared with the inner side, and this limits the overall time resolution to around 250 fs as shown in **Fig.1.31**. The tilting of the gate beam can improve the time resolution to 80 fs.<sup>128</sup>



### 1.5.3.3 Transient Grating Method

Transient grating method is based on the phenomenon called transient grating phenomenon which is a four-wave mixing (FWM) non-linear optical processes. This phenomenon was first reported in 1966 by Kelley et al,<sup>129</sup> when two ruby laser beams at a specific angle were focused into a cell with nitrobenzene. The forward laser hit in the center and the other beam is refracted into direction with angle  $+\theta$  to the forward laser, whilst an additional beam in  $-\theta$  direction is generated, **Fig.1.32**.



In 1969, similar phenomenon was also observed in Si by Bolger et al with the setup shown in **Fig.1.33**. The result is given in **Fig.1.34**, in which when the beam  $A_1$  and  $A_2$  are incident, equidistant spots appear to the left of  $A_1$  and to the right of  $A_2$  spot. When the beam  $B$  is introduced, similar spots also arise near the  $B$  spot. With an increase in the angle  $\theta$ , the number of the refracted spots decreased. If the beam  $A$  was blocked, the refracted spots corresponding to beam  $B$  also vanished.<sup>130</sup>

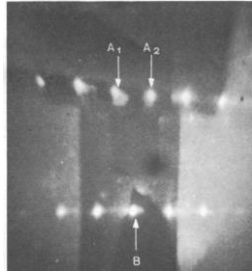


**Fig.1.34:** Refracted spots from beam A and B caused by laser induced grating process.<sup>130</sup>

Based on this phenomenon, a type of femtosecond broadband fluorescence spectroscopy named transient grating photoluminescence spectroscopy (TGPLS) was proposed. The setup of this method is given in **Fig.1.35**.<sup>131</sup>

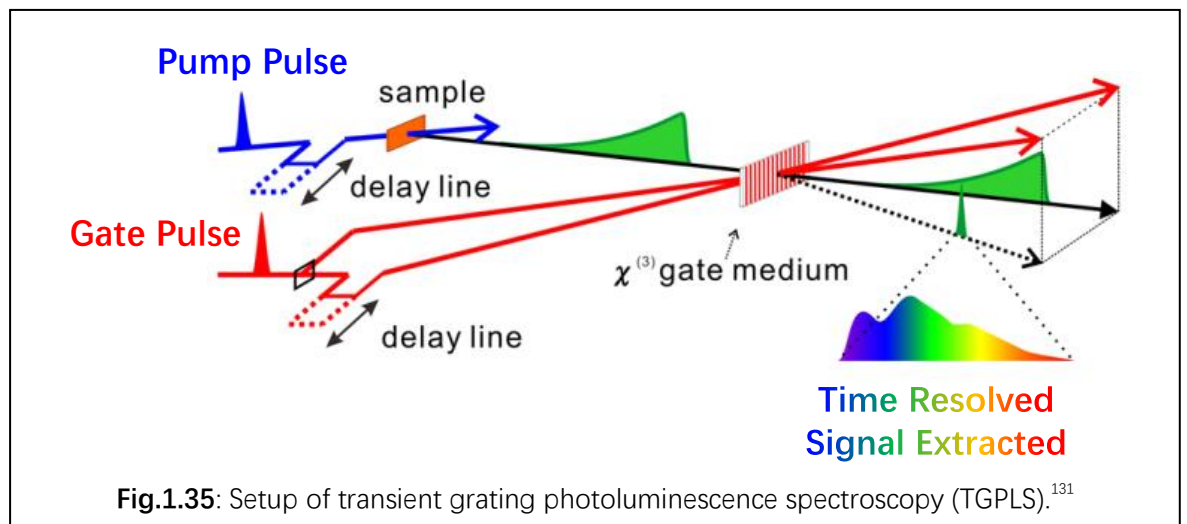


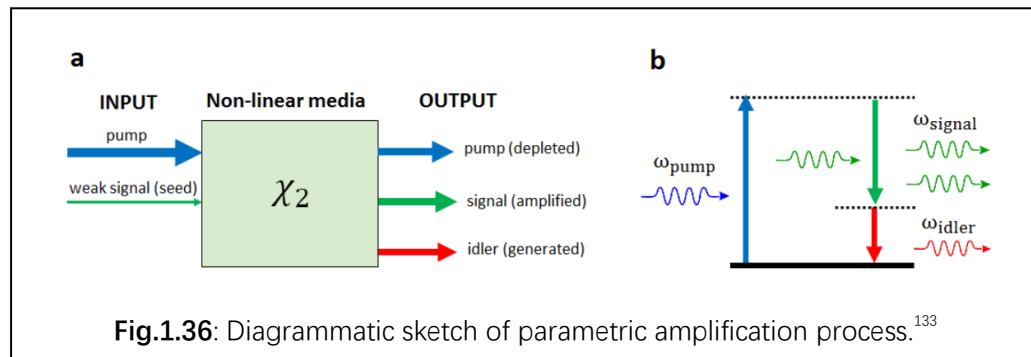
**Fig.1.35:** Setup of transient grating photoluminescence spectroscopy (TGPLS).<sup>131</sup>

In this setup, apart from the pump beam line used to excite the sample to induce emission, two 800 nm, 100 fs gate beams lines are introduced to control the third order nonlinear gate medium ( $\chi^{(3)}$ ). The time delay between pump pulse and gate pulses is controlled by the delay stage in pump pulse beam line. Here the  $\chi^{(3)}$  gate medium is 1 mm thick fused silica and can only be activated when both 800 nm laser pulses pass through it. Once the gate is activated, the emission passing through is refracted into a different direction from the background emission and detected separately as shown in **Fig.1.35**.<sup>131</sup>

#### 1.5.3.4 Optical Parametric Amplification Method

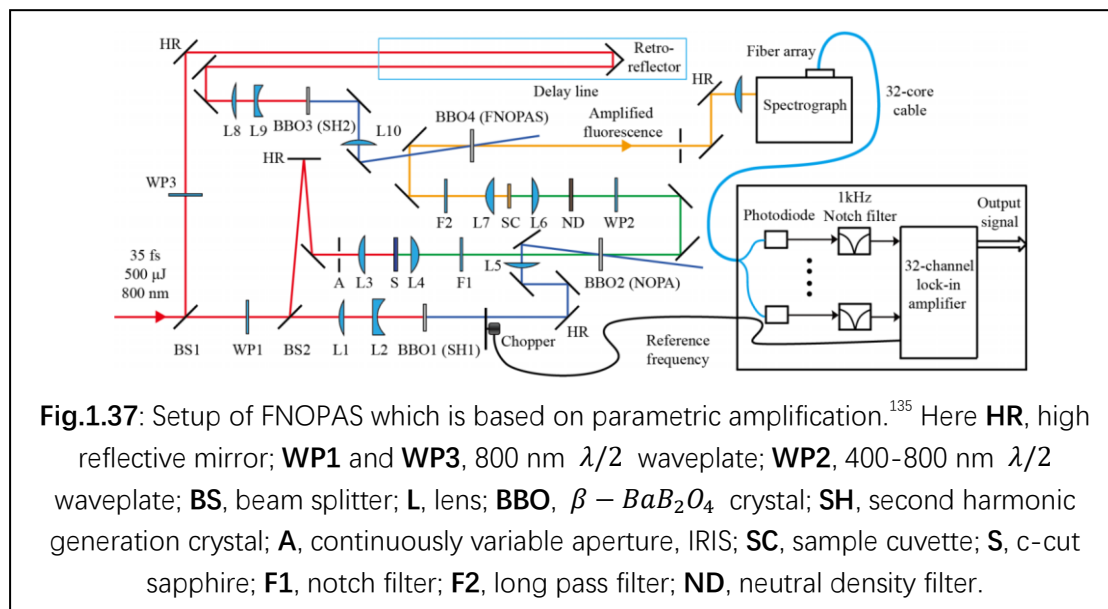
Optical parametric amplification was first achieved in 1965. There, the second

harmonic of a ruby laser with the wavelength 346.9 nm was used to amplify 632.8 nm light beam generated from HeNe laser in ADP ( $\text{NH}_4\text{H}_2\text{PO}_4$ ) crystal.<sup>132</sup> The diagrammatic sketch of parametric amplification process is shown in **Fig.1.36**.<sup>133</sup> Here, the pump beam has higher energy than the weak signal beam (seed), and when they pass through a second order non-linear media ( $\chi^{(2)}$ ) together, the pump beam power will be used to generate much more seed beam photons so the signal beam intensity is amplified a lot. This nonlinear optical process is the fundamental process of ultrafast optical parametric amplifiers.<sup>134</sup>



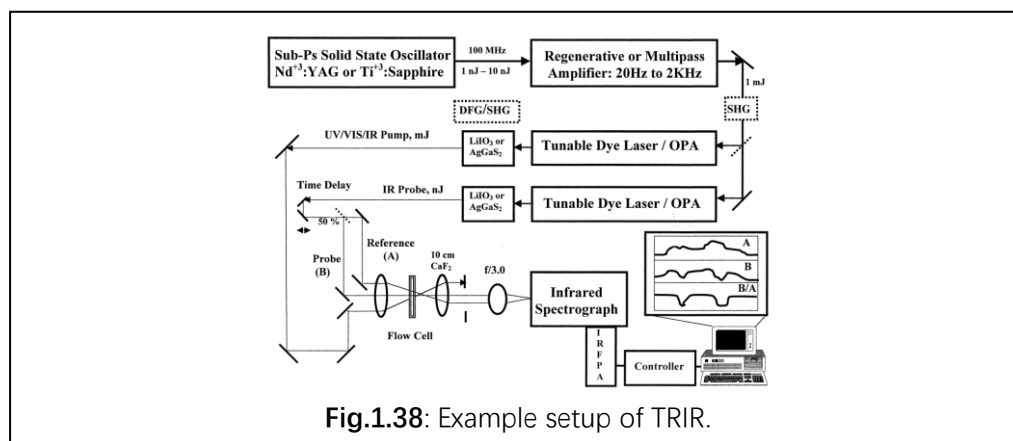
Since the amplification process requires weak seed signal and the pump pulse pass through the nonlinear optical media at the same time to amplify the seed signal, it could be used to build time resolved fluorometer. A fluorescence non-collinear optical parametric amplification spectroscopy (FNOPAS) setup is shown in **Fig.1.37**.<sup>135</sup> In this setup, the pump beam is generated by a non-collinear optical parametric amplification (NOPA) whose output is tunable from 460 to 1150 nm. The gate beam is generated by the second harmonic generation process at BBO3 with 800 nm, 35 fs laser pulse to get 400 nm beam pulse. This gate beam is used as pump beam in optical amplification. Time delay is controlled with a delay stage in the gate beam line before second harmonic generation BBO3. The emission from the sample is collected and focused into the BBO4 where the fluorescence parametric amplification happens together with the 400 nm gate beam. Only the emission photons that pass through together with the 400 nm gate pulse (femtosecond timescale)

could be amplified, so femtosecond time resolution is achieved. The amplified fluorescence is much more intense compared to the background fluorescence, so in the detector the amplified fluorescence can mask the background fluorescence.<sup>135</sup>



#### 1.5.4 Transient Infrared Spectroscopy

Transient infrared spectroscopy (TRIR) is also classified as pump-probe method which is similar to the electronic transient absorption. The difference is that the probe beam is changed to broadband mid-infrared (IR) (with wavenumber from 1000 to 4000  $cm^{-1}$ ) which could be generated via nonlinear difference frequency generation introduced above.<sup>136</sup>



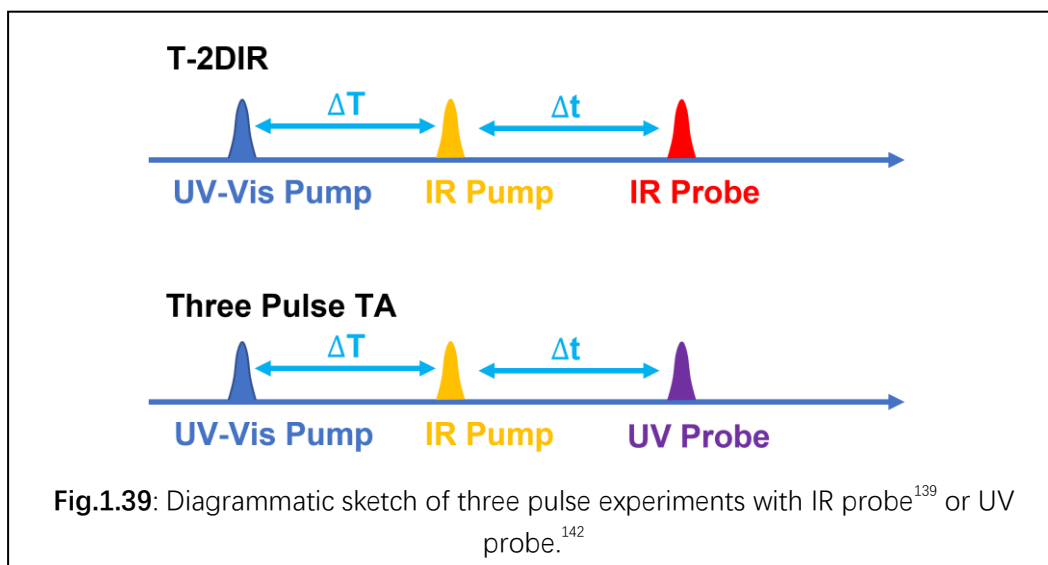
An example setup of TRIR is given in **Fig.1.38**. In this setup, the pump pulse is

generated by the SHG process in nonlinear optical medium and then focused on the sample. The probe IR pulse is generated via difference frequency generation and the probe beam is sent into a delay stage to control the time delay between the pump and the probe pulses.<sup>137</sup>

With probe pulse in mid-IR range, the vibration from IR-active fragments, for example –CC-triple bonds, -CN or carbonyl groups in the excited state could be detected, as vibrational modes are sensitive to the change of electron density distribution. This method thus provides bond-specific information, and could be used in detecting the formation and decay of charge transfer state and charge separated state more clearly. Lifetimes of these excited states can also be extracted from TRIR spectra.<sup>138</sup>

### **1.5.5 IR Control Spectroscopy**

In the recent research on charge transfer states, it was found that when a certain vibrational mode in the excited state is additionally excited by a narrow-band IR-pump, the excited state decay kinetics and in some cases the population ratio of excited states is influenced by the presence of the IR-pump.<sup>139–142</sup> This phenomenon is known as ‘IR control’ which is caused by the ultrafast nature of the transitions between close in energy of the excited states so Born-Oppenheimer approximation breaks down, and the change in nuclear center position (vibration) can influence the decay routine of the excited states.<sup>143,144</sup>



To investigate the IR pump influence on excited state dynamics, IR control spectroscopy is performed by introducing a narrow band IR pump pulse between the UV/vis pump pulse and a probe pulse, thus becoming a UV pump-IR pump-Probe sequence as shown in **Fig.1.39**. In this setup, a tunable narrow band IR pump pulse targets a specific vibration mode in the excited state. The probe pulse could be an IR-probe, which is the same pulse sequence as in transient two-dimensional infrared spectroscopy (T-2DIR). Or, the probe pulse could be a UV/vis-probe, which will be a three-pulse TA. Two delay stages are used to control the time delay between UV pump and IR pump, and time delay between IR pump and probe pulse. The final spectra are obtained by recording the absorption difference with IR pump on and off, so the influence of the IR pump introduced is recorded.<sup>139,142</sup>

## 1.6 Global Analysis and Target Analysis

The time resolved spectra is a type of two-dimensional spectra as shown in **Fig.1.15**<sup>53</sup> and **Fig.1.17**,<sup>82</sup> in which one axis is time delay, the other is the spectra at certain time delay (and the 3<sup>rd</sup> axis is intensity of the signal). To extract useful information about the excited states such as lifetime and spectra of each individual excited state, global analysis is required. Global analysis is a mathematics concept which is defined as 'the study of differential equations, both ordinary and partial, on manifolds and vector space bundles.'<sup>145</sup> In time resolved spectroscopy, global

analysis is defined as simultaneous analysis of all experimental data.<sup>146</sup>

Let's think about what happens during the time-resolved experiment. First, the sample is excited into certain excited state(s), then the excited state(s) decays into other excited state or ground state, and the other excited state continuous decay into other excited state or ground state. At the end, all the excited states decay into ground state so no signal is detected. And at a given time delay ( $t$ ), only limited types of excited states ( $l$ ) are populated in different concentrations ( $c_l(t)$ ). Each type ( $l$ ) of excited states will have its own spectra with certain absorption (or emission) coefficient ( $\varepsilon_l(\lambda)$ ) at a given wavelength  $\lambda$  (or wavenumber for TRIR,  $\varepsilon_l(\tilde{\nu})$ ) according to Beer-Lambert law. The absorption (or emission) spectra of the system at certain time delay could be write as in **Equation 3** for TA and emission spectra ( $\psi(t, \lambda)$ ), or as in **Equation 3'** for TRIR spectra ( $\psi(t, \tilde{\nu})$ ).<sup>146</sup>

$$\psi(t, \lambda) = \sum_l^{n_{comp}} c_l(t) \cdot \varepsilon_l(\lambda) \quad \text{Equation 3}$$

$$\psi(t, \tilde{\nu}) = \sum_l^{n_{comp}} c_l(t) \cdot \varepsilon_l(\tilde{\nu}) \quad \text{Equation 3'}$$

The decay process of the excited state could be treated as unimolecular elementary reaction for femtosecond time resolved experiment, so the reaction rate is given in **Equation 4** and the excited state concentration  $c_l(t)$  change with time could be written as in **Equation 5** here  $k_l$  is rate constant of excited state  $l$  decay process.

$$r_l = k_l \cdot c_l(t) \quad \text{Equation 4}$$

$$c_l(t) = c_l^{start} \cdot e^{-k_l t} \quad \text{Equation 5}$$

Here we assume the excited state population signal is directly induced by laser pump. The laser pump profile together with the detection pulse profile gives an instrument response function (IRF),  $i(t)$  which could be written by Gaussian distribution and if we assume that the peak of the IRF is at a time delay  $a$ , we can describe the IRF using Gaussian distribution as shown in **Equation 6**, here  $\sigma$  is standard deviation. The change in the concentration of the excited state with time

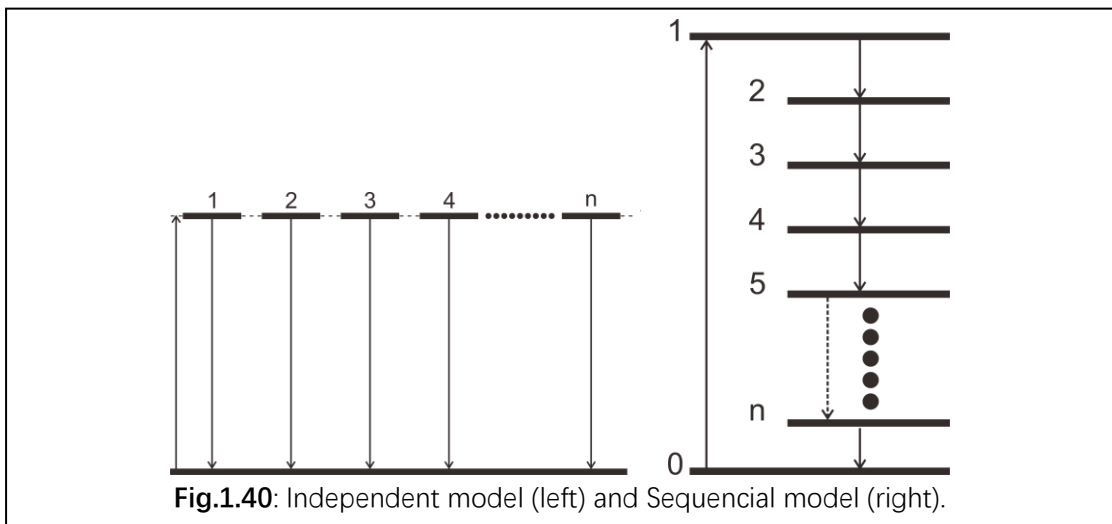


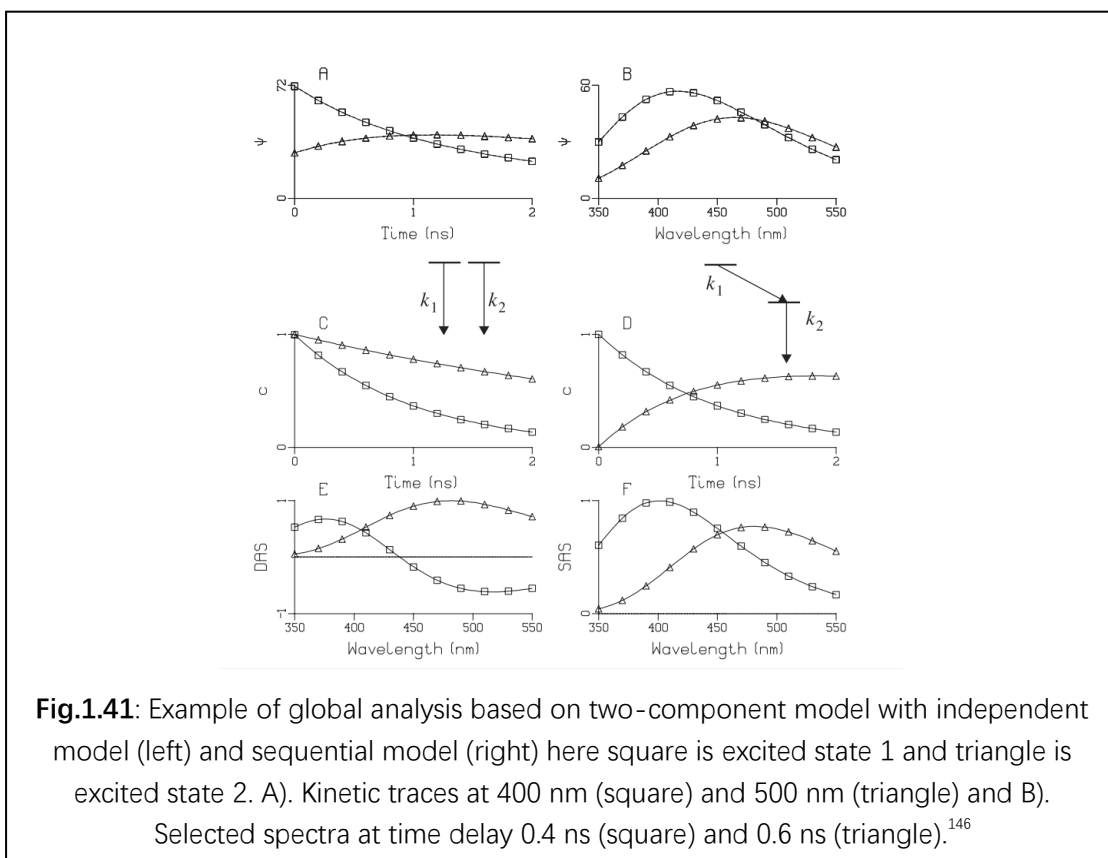
$c_l(t)$  could be written as a convolution of the exponential decay with the IRF function as shown in **Equation 7** here  $\oplus$  stands for convolution operation and  $erf$  stands for error function.<sup>146</sup>

$$i(t) = \frac{1}{\sigma\sqrt{2\pi}} e^{-\frac{(t-a)^2}{2\sigma^2}} \quad \text{Equation 6}$$

$$c_l(t) = i(t) \oplus e^{-k_l t} = \frac{1}{2} e^{-k_l \left[ (t-2a) - \frac{\sigma^2 k_l}{2} \right]} \left[ 1 + erf \left( \frac{[(t-2a) - \sigma^2 k_l]}{\sqrt{2}\sigma} \right) \right] \quad \text{Equation 7}$$

By combining **Equation 3 (or 3')**, **5** and **7** plus suitable kinetic models with suitable parameters, the time resolved spectra could be reconstructed. The most often used models are sequential model and an independent (parallel) model shown in **Fig.1.40**. The independent model assumes all excited states are independently populated and independently decay into ground state. The sequential model assumes that laser excitation populates only one excited state, which sequentially decays into lower energy excited states, and then finally to the ground state, without any branching.

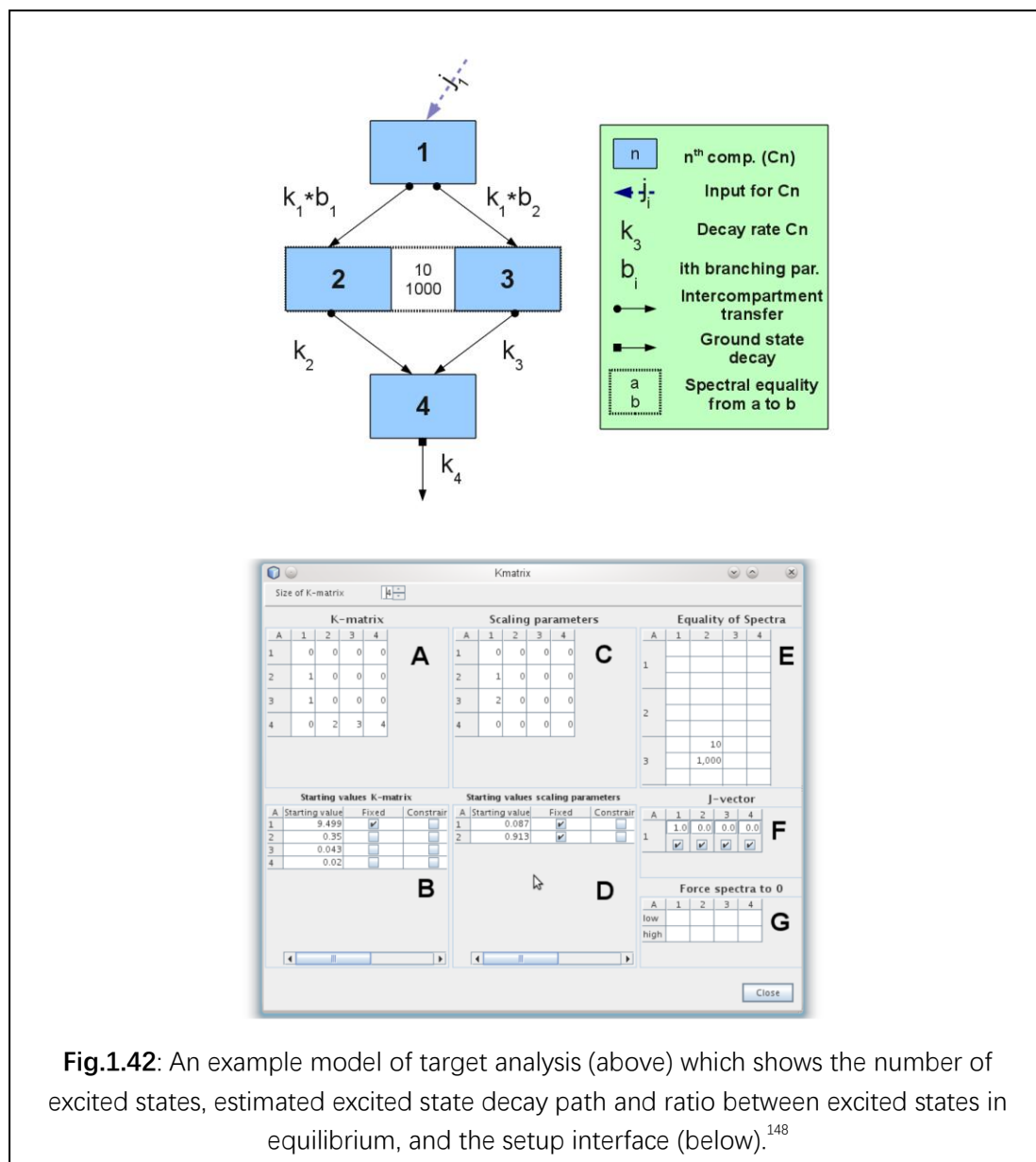




By applying different kinetic models, the result of the global analysis could be different as shown in **Fig.1.41**.<sup>146</sup> Applying independent model gives decay associated spectra (DAS) in **Fig.1.41(E)** which shows a bleach at 500 nm in the DAS of the excited state 1, which is caused by the decay from excited state 1 to excited state 2. In the result obtained by a sequential model, the evolution-associated spectra (EAS) show no bleaches which could be treated as spectra of the corresponding excited states, and from the kinetic traces extracted the lifetimes of the excited states could be established.

Either a sequential model or an independent model are usually sufficient to deal with most of the conditions of the excited state decay. But the condition of the excited state decay could be complicated by for example including branching decay from one state to another two excited states.<sup>138</sup> Under these conditions, target analysis based on a given model becomes important.<sup>147</sup> This could be done by using a software based on R package TIMP called Glotaran,<sup>148</sup> which can do global

analysis or target analysis with given model as shown in **Fig.1.42**; the target analysis will give associated spectra named species associated spectra (SAS) together with the corresponding lifetimes.



Glutaran works in the following steps, first, it takes the model and experimental data together with other starting parameters such as the excitation pulse duration, decay rate constant and a starting point of excitation to construct a theoretical set of data. Then the theoretical data is compared with the experimental data, and if they meet with each other (within the limit established) then the parameters are

acceptable; if not Glotaran will modify the parameters to construct another theoretical data which is again compared with the experimental data. This loop will keep cycling until the reasonable parameters are found or the software crashes, which indicates the starting parameters or the model are not suitable and need to be reconsidered. Once the acceptable parameters are found, Glotaran yields the associated spectra and corresponding lifetimes based on these parameters.<sup>148</sup>

## 1.7 Research Aims

The aims of this research are stated below.

1. Apply various ultrafast spectroscopy techniques to characterise excited states dynamics of Pt based organometallic compounds.
2. Apply various spectroscopy techniques including static and ultrafast methods to characterise solvent influence on excited state energies and dynamics of Pt based organometallic compounds.
3. Apply ultrafast three-pulse transient two-dimensional IR spectroscopy technique to investigate the influence of transient IR-excitation on excited states dynamics and establish if these compounds are subjectable to IR-control.
4. Apply fluorescence upconversion spectroscopy, in combination with ultrafast TA and TRIR to establish the influence of the opposite ligand influence on the rate of intersystem crossing in a series of NAP-Pt-L organometallic compounds.
5. Combine the results from 1-4 to derive factors influencing the rate of ISC, and the propensity of the NAP-Pt-L to IR-control.

A further aim was to establish, optimise, and add variable excitation wavelengths to the FLUPs set-up.

## 1.8 Reference

- 1 L. Barrie and G. Braathen, *WMO GREENHOUSE GAS BULLETIN The State of Greenhouse Gases in the Atmosphere Based on Global Observations through 2020*, .
- 2 P. Voosen, *Science (1979)*, 2021, **371**, 334–335.
- 3 R. Lindsey, *Available online: Climate.gov (accessed on 14 August 2020)*.

- 4 L. Q. Jiang, B. R. Carter, R. A. Feely, S. K. Lauvset and A. Olsen, *Sci Rep*, ,  
DOI:10.1038/s41598-019-55039-4.
- 5 T. M. Gür, *Prog Energy Combust Sci*, 2022, **89**, 100965.
- 6 bp, *Statistical Review of World Energy 2022*, .
- 7 U. Photo and E. Debebe, *World Population Prospects 2022 Summary of Results*, .
- 8 K. Rabaey and A. J. Ragauskas, *Curr Opin Biotechnol*, 2014, **27**, 5–6.
- 9 P. M. Cox, R. A. Betts, C. D. Jones, S. A. Spall and I. J. Totterdell, *Nature*, 2000, **408**,  
184–187.
- 10 C. A. Horowitz, *International Legal Materials*, 2016, **55**, 740–755.
- 11 O. Ellabban, H. Abu-Rub and F. Blaabjerg, *Renewable and Sustainable Energy Reviews*,  
2014, **39**, 748–764.
- 12 IEA, *World Energy Model Documentation*, 2021.
- 13 C. A. Gabriel, *Renewable and Sustainable Energy Reviews*, 2016, **64**, 362–371.
- 14 K. Wilhelm and B. N. Dwivedi, *Astrophys Space Sci*, 2013, **347**, 41–45.
- 15 G. Fiorentini, B. Ricci and F. L. Villante, *Nuclear Fusion in the Sun Downloaded from*,  
2004, vol. 154.
- 16 T. R. Karl and K. E. Trenberth, *Science (1979)*, 2003, **302**, 1719–1723.
- 17 K. H. Schatten, *J Geophys Res Space Phys*, 1993, **98**, 18907–18910.
- 18 J. S. Dukes, *Clim Change*, 2003, **61**, 31–44.
- 19 L. A. Weinstein, J. Loomis, B. Bhatia, D. M. Bierman, E. N. Wang and G. Chen, *Chem  
Rev*, 2015, **115**, 12797–12838.
- 20 *RENEWABLES 2022 Global Status Report*, .
- 21 B. Milow, F. Tellez and J. Karni, *Concentrating Solar power plants-How to Achieve  
Competiveness SOLAR-THERMAL POWER GENERATION*, .
- 22 Y. L. He, Y. Qiu, K. Wang, F. Yuan, W. Q. Wang, M. J. Li and J. Q. Guo, *Energy*, ,  
DOI:10.1016/j.energy.2020.117373.
- 23 M. Mehos, C. Turchi, J. Vidal, M. Wagner, Z. Ma, C. Ho, W. Kolb, C. Andraka and A.  
Kruizenga, *Concentrating Solar Power Gen3 Demonstration Roadmap*, 2017.
- 24 L. el Chaar, L. A. Lamont and N. el Zein, *Renewable and Sustainable Energy Reviews*,  
2011, **15**, 2165–2175.
- 25 R. Williams, *J Chem Phys*, 1960, **32**, 1505–1514.
- 26 In *Principles of Solar Cells, LEDs and Diodes: The role of the PN junction*, John Wiley  
& Sons, Ltd, 2011, pp. 1–67.
- 27 In *Principles of Solar Cells, LEDs and Diodes: The role of the PN junction*, John Wiley  
& Sons, Ltd, 2011, pp. 159–213.
- 28 D. M. Chapin, C. S. Fuller and G. L. Pearson, *J Appl Phys*, 1954, **25**, 676–677.
- 29 D. M. Bagnall and M. Boreland, *Energy Policy*, 2008, **36**, 4390–4396.
- 30 J. Yan and B. R. Saunders, *RSC Adv*, 2014, **4**, 43286–43314.
- 31 M. Yamaguchi, T. Takamoto, K. Araki and N. Ekins-Daukes, *Solar Energy*, 2005, **79**, 78–  
85.
- 32 M. A. Green, E. D. Dunlop, J. Hohl-Ebinger, M. Yoshita, N. Kopidakis, K. Bothe, D.  
Hinken, M. Rauer and X. Hao, *Progress in Photovoltaics: Research and Applications*,  
2022, **30**, 687–701.
- 33 B. Zhang and L. Sun, *Chem Soc Rev*, 2019, **48**, 2216–2264.

- 34 G. L. Zhu, C. Z. Zhao, J. Q. Huang, C. He, J. Zhang, S. Chen, L. Xu, H. Yuan and Q. Zhang, *Small*, 2019, 15.
- 35 C. Chen, Z. Wei and A. C. Knoll, *IEEE Transactions on Transportation Electrification*, , DOI:10.1109/TTE.2021.3135525.
- 36 S. R. Lingampalli, M. M. Ayyub and C. N. R. Rao, *ACS Omega*, 2017, **2**, 2740–2748.
- 37 F. Dawood, M. Anda and G. M. Shafiullah, *Int J Hydrogen Energy*, 2020, 45, 3847–3869.
- 38 C. Kranz and M. Wachtler, *Chem Soc Rev*, 2021, 50, 1407–1437.
- 39 A. FUJISHIMA and K. HONDA, *Nature*, 1972, **238**, 37–38.
- 40 J.-M. Lehn and R. Ziessel, *Proceedings of the National Academy of Sciences*, 1982, **79**, 701–704.
- 41 Z. W. Wang, Q. Wan, Y. Z. Shi, H. Wang, Y. Y. Kang, S. Y. Zhu, S. Lin and L. Wu, *Appl Catal B*, , DOI:10.1016/j.apcatb.2021.120000.
- 42 J. C. S. Wu and H.-M. Lin, *Photo reduction of CO 2 to methanol via TiO 2 photocatalyst*, 2005, vol. 07.
- 43 R. Cauwenbergh and S. Das, *Green Chemistry*, 2021, **23**, 2553–2574.
- 44 T. Cai, H. Sun, J. Qiao, L. Zhu, F. Zhang, J. Zhang, Z. Tang, X. Wei, J. Yang, Q. Yuan, W. Wang, X. Yang, H. Chu, Q. Wang, C. You, H. Ma, Y. Sun, Y. Li, C. Li, H. Jiang, Q. Wang and Y. Ma, *Science (1979)*, 2021, **373**, 1523–1527.
- 45 Y. Tachibana, L. Vayssieres and J. R. Durrant, *Nat Photonics*, 2012, **6**, 511–518.
- 46 J. Barber, *Q Rev Biophys*, 2003, 36, 71–89.
- 47 P. Fromme, P. Jordan and N. Krauß, *Biochimica et Biophysica Acta (BBA) - Bioenergetics*, 2001, **1507**, 5–31.
- 48 S. R. Greenfield and M. R. Wasielewski, *Excitation energy transfer and charge separation in the isolated Photosystem II reaction center\**, Kluwer Academic Publishers, 1996, vol. 48.
- 49 D. Heineke and R. Scheibe, in *eLS*, Wiley, 2009.
- 50 R. Eisenberg, *Science (1979)*, 2009, **324**, 44–45.
- 51 L. Wang, Y. Wan, Y. Ding, S. Wu, Y. Zhang, X. Zhang, G. Zhang, Y. Xiong, X. Wu and J. Yang, *Advanced Materials*, 2017, **29**, 1702428.
- 52 K. Lei, D. Wang, L. Ye, M. Kou, Y. Deng, Z. Ma, L. Wang and Y. Kong, *ChemSusChem*, 2020, **13**, 1725–1729.
- 53 A. Cannizzo, F. van Mourik, W. Gawelda, G. Zgrablic, C. Bressler and M. Chergui, *Angewandte Chemie*, 2006, **118**, 3246–3248.
- 54 C. v Krishnan and N. Sutin, *J Am Chem Soc*, 1981, **103**, 2141–2142.
- 55 E. Kimura, S. Wada, M. Shionoya and Y. Okazaki, *New Series of Multifunctionalized Nickel(II)-Cyclam (Cyclam = 1,4,8,11-Tetraazacyclotetradecane) Complexes. Application to the Photoreduction of Carbon Dioxide*, 1994, vol. 33.
- 56 E. Kimura, X. Bu, M. Shionoya, S. Wada and S. Maruyama, *A New Nickel(II) Cyclam (Cyclam = 1,4,8,11-Tetraazacyclotetradecane) Complex Covalently Attached to Ru(phen)32+ (phen = 1,10-Phenanthroline). A New Candidate for the Catalytic Photoreduction of Carbon Dioxide*, 1992, vol. 31.
- 57 R. Reithmeier, C. Bruckmeier and B. Rieger, *Catalysts*, 2012, 2, 544–571.
- 58 P. Du and R. Eisenberg, *Energy Environ Sci*, 2012, 5, 6012–6021.
- 59 In *The IUPAC Compendium of Chemical Terminology*, International Union of Pure and

- Applied Chemistry (IUPAC), 2008.
- 60 J. N. Schrauben, K. L. Dillman, W. F. Beck and J. K. McCusker, *Chem Sci*, 2010, **1**, 405–410.
- 61 M. Kasha, *Chem Rev*, 1947, **41**, 401–419.
- 62 G. N. Lewis and M. Kasha, *J Am Chem Soc*, 1944, **66**, 2100–2116.
- 63 A. Krieger-Liszka, in *Journal of Experimental Botany*, 2005, vol. 56, pp. 337–346.
- 64 H. Ma, S. Long, J. Cao, F. Xu, P. Zhou, G. Zeng, X. Zhou, C. Shi, W. Sun, J. Du, K. Han, J. Fan and X. Peng, *Chem Sci*, 2021, **12**, 13809–13816.
- 65 Y. Tao, K. Yuan, T. Chen, P. Xu, H. Li, R. Chen, C. Zheng, L. Zhang and W. Huang, *Advanced Materials*, 2014, **26**, 7931–7958.
- 66 M. Kasha, *Discuss Faraday Soc*, 1950, **9**, 14–19.
- 67 D. Shoup, G. Lipari and A. Szabo, *Biophys J*, 1981, **36**, 697–714.
- 68 D. S. McClure, *J Chem Phys*, 1949, **17**, 905–913.
- 69 S. K. Lower and M. A. El-Sayed, *Chem Rev*, 1966, **66**, 199–241.
- 70 P. A. M. Dirac, *Proceedings of the Royal Society of London. Series A, Containing Papers of a Mathematical and Physical Character*, 1928, **117**, 610–624.
- 71 J. C. Koziar, S. P. McGlynn, M. J. Reynolds, G. W. Daigre and N. D. Chris, *Elements of Organic Photochemistry*, American Chemical Society, 1976, vol. 98.
- 72 M. A. El-Sayed, *J Chem Phys*, 1963, **38**, 2834–2838.
- 73 L. Troian-Gautier and C. Moucheron, *Molecules*, 2014, **19**, 5028–5087.
- 74 N. H. Damrauer, G. Cerullo, A. Yeh, T. R. Boussie, C. v Shank and J. K. McCusker, *Science (1979)*, 1997, **275**, 54–57.
- 75 G. A. Crosby and J. N. Demas, *J Am Chem Soc*, 1971, **93**, 2841–2847.
- 76 A. C. Bhasikuttan, M. Suzuki, S. Nakashima and T. Okada, *J Am Chem Soc*, 2002, **124**, 8398–8405.
- 77 A. Hauser, *Spin crossover in transition metal compounds II*, 2004, 155–198.
- 78 M. Bergkamp, B. Brunschwig, P. Gütllich, T. L. Netzel and N. Sutin, *Chem Phys Lett*, 1981, **81**, 147–150.
- 79 J. K. McCusker, K. N. Walda, R. C. Dunn, J. D. Simon, D. Magde and D. N. Hendrickson, *J Am Chem Soc*, 1992, **114**, 6919–6920.
- 80 E. A. Juban, A. L. Smeigh, J. E. Monat and J. K. McCusker, *Coord Chem Rev*, 2006, **250**, 1783–1791.
- 81 J. K. McCusker, K. N. Walda, R. C. Dunn, J. D. Simon, D. Magde and D. N. Hendrickson, *J Am Chem Soc*, 1993, **115**, 298–307.
- 82 W. Gawelda, A. Cannizzo, V. T. Pham, F. van Mourik, C. Bressler and M. Chergui, *J Am Chem Soc*, 2007, **129**, 8199–8206.
- 83 G. Auböck and M. Chergui, *Nat Chem*, 2015, **7**, 629–633.
- 84 S. Lentijo, J. A. Miguel and P. Espinet, *Inorg Chem*, 2010, **49**, 9169–9177.
- 85 Y. Y. Chia and M. G. Tay, *Dalton Transactions*, 2014, **43**, 13159–13168.
- 86 R. Morales-Cueto, M. Esquivelzeta-Rabell, J. Saucedo-Zugazagoitia and J. Peon, *Journal of Physical Chemistry A*, 2007, **111**, 552–557.
- 87 J. S. Zugazagoitia, C. X. Almora-Díaz and J. Peon, *Journal of Physical Chemistry A*, 2008, **112**, 358–365.
- 88 H. Uoyama, K. Goushi, K. Shizu, H. Nomura and C. Adachi, *Nature*, 2012, **492**, 234–238.

- 89 S. Perun, J. Tatchen and C. M. Marian, *ChemPhysChem*, 2008, **9**, 282–292.
- 90 L. Mewes, R. A. Ingle, S. Megow, H. Böhnke, E. Baranoff, F. Temps and M. Chergui, *Inorg Chem*, 2020, **59**, 14643–14653.
- 91 R. M. van der Veen, A. Cannizzo, F. van Mourik, A. Vlček and M. Chergui, *J Am Chem Soc*, 2011, **133**, 305–315.
- 92 *Nature*, 1894, **51**, 80–81.
- 93 B. A. Thrush, *Photochemical and Photobiological Sciences*, 2003, **2**, 453–454.
- 94 G.-N. Porter, *Proc R Soc Lond A Math Phys Sci*, 1950, **200**, 284–300.
- 95 T. H. MAIMAN, *Nature*, 1960, **187**, 493–494.
- 96 P. M. W. French, *Reports on Progress in Physics*, 1995, **58**, 169.
- 97 M. Hentschel, R. Kienberger, Ch. Spielmann, G. A. Reider, N. Milosevic, T. Brabec, P. Corkum, U. Heinzmann, M. Drescher and F. Krausz, *Nature*, 2001, **414**, 509–513.
- 98 P.-M. Paul, E. S. Toma, P. Breger, G. Mullot, F. Augé, P. Balcou, H. G. Muller and P. Agostini, *Science (1979)*, 2001, **292**, 1689–1692.
- 99 M. J. Rosker, M. Dantus and A. H. Zewail, *Science (1979)*, 1988, **241**, 1200–1202.
- 100 M. J. Rosker, M. Dantus and A. H. Zewail, *J Chem Phys*, 1988, **89**, 6113–6127.
- 101 R. R. Alfano and S. L. Shapiro, *Phys Rev Lett*, 1970, **24**, 584.
- 102 A. M. Zheltikov, *Physics-Uspexhi*, 2006, **49**, 605.
- 103 F. Silva, D. R. Austin, A. Thai, M. Baudisch, M. Hemmer, D. Faccio, A. Couairon and J. Biegert, *Nat Commun*, , DOI:10.1038/ncomms1816.
- 104 R. Berera, R. van Grondelle and J. T. M. Kennis, *Photosynth Res*, 2009, **101**, 105–118.
- 105 P. M. Norris, A. P. Caffrey, R. J. Stevens, J. M. Klopff, J. T. McLeskey and A. N. Smith, in *Review of Scientific Instruments*, 2003, vol. 74, pp. 400–406.
- 106 N. Tamai and H. Masuhara, *Chem Phys Lett*, 1992, **191**, 189–194.
- 107 M. Iwamura, S. Takeuchi and T. Tahara, *Acc Chem Res*, 2015, **48**, 782–791.
- 108 A. D. Buckingham, in *Optical, Electric and Magnetic Properties of Molecules*, Elsevier, 1997, pp. 264–269.
- 109 J. Kerr, *The London, Edinburgh, and Dublin Philosophical Magazine and Journal of Science*, 1875, **50**, 337–348.
- 110 J. Kerr, *The London, Edinburgh, and Dublin Philosophical Magazine and Journal of Science*, 1875, **50**, 446–458.
- 111 P. D. Maker, R. W. Terhune and C. M. Savage, *Phys Rev Lett*, 1964, **12**, 507.
- 112 M. Cheng, W. Jin, Z. Yang and S. Pan, *Inorg Chem*, 2020, **59**, 13014–13018.
- 113 C. J. Yang, J. Li, J. Lehmann, N. Strkalj, M. Trassin, M. Fiebig and S. Pal, *Appl Phys Lett*, , DOI:10.1063/5.0043216.
- 114 R. Ishikawa, R. Kano, T. Bando, Y. Suematsu, S. N. Ishikawa, M. Kubo, N. Narukage, H. Hara, S. Tsuneta, H. Watanabe, K. Ichimoto, K. Aoki and K. Miyagawa, *Appl Opt*, 2013, **52**, 8205–8211.
- 115 M. A. Duguay and J. W. Hansen, *Appl Phys Lett*, 1969, **15**, 192–194.
- 116 K. Appavoo and M. Y. Sfeir, *Review of Scientific Instruments*, , DOI:10.1063/1.4873475.
- 117 P. Matousek, M. Towrie, A. Stanley and A. W. Parker, *Appl Spectrosc*, 1999, **53**, 1485.
- 118 P. A. Franken, A. E. Hill, C. W. el Peters and G. Weinreich, *Phys Rev Lett*, 1961, **7**, 118.
- 119 A. W. Smith and N. Braslau, *IBM J Res Dev*, 1962, **6**, 361–362.
- 120 A. W. Smith and N. Braslau, *J Appl Phys*, 1963, **34**, 2105–2106.

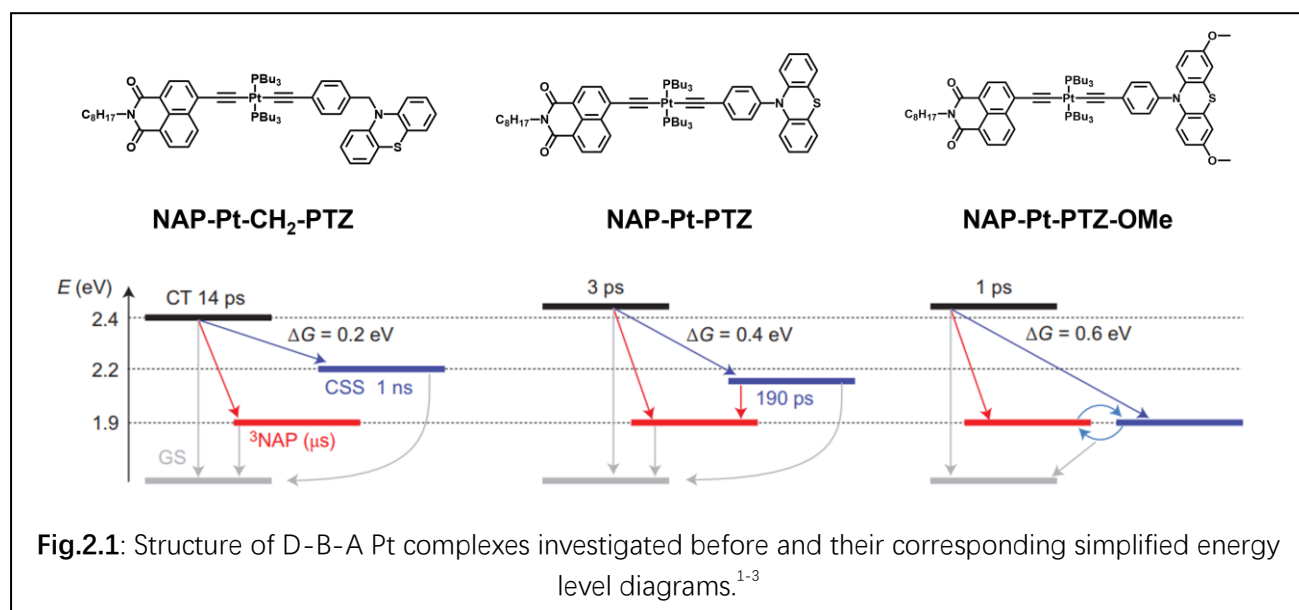


- 121 R.-K. Li and C.-T. Chen, *Acta Phys. Sin.*, 1985, **34**, 823–827.
- 122 Y. R. Shen, *Journal of Physical Chemistry C*, 2012, **116**, 15505–15509.
- 123 J. E. Midwinter and J. Warner, *British Journal of Applied Physics*, 1965, **16**, 1135.
- 124 M. v. Hobden, *J Appl Phys*, 1967, **38**, 4365–4372.
- 125 A. Cannizzo, O. Bräm, G. Zgrablic, A. Tortschanoff, A. A. Oskouei, F. van Mourik and M. Chergui, *Opt Lett*, 2007, **32**, 3555–3557.
- 126 X.-X. Zhang, C. Würth, L. Zhao, U. Resch-Genger, N. P. Ernsting and M. Sajadi, *Review of Scientific Instruments*, 2011, **82**, 063108.
- 127 M. Gerecke, G. Bierhance, M. Gutmann, N. P. Ernsting and A. Rosspeintner, *Review of Scientific Instruments*, , DOI:10.1063/1.4948932.
- 128 L. Zhao, J. L. P. Lustres, V. Farztdinov and N. P. Ernsting, *Physical Chemistry Chemical Physics*, 2005, **7**, 1716–1725.
- 129 R. L. Carman, R. Y. Chiao and P. L. Kelley, *Phys Rev Lett*, 1966, **17**, 1281.
- 130 J. P. Woerdman and B. Bölger, *Phys Lett A*, 1969, **30**, 164–165.
- 131 K. Chen, J. K. Gallaher, A. J. Barker and J. M. Hodgkiss, *Journal of Physical Chemistry Letters*, 2014, **5**, 1732–1737.
- 132 C. C. Wang and G. W. Racette, *Appl Phys Lett*, 1965, **6**, 169–171.
- 133 A. G. Ciriolo, M. Negro, M. Devetta, E. Cinquanta, D. Faccialà, A. Pusala, S. de Silvestri, S. Stagira and C. Vozzi, *Applied Sciences (Switzerland)*, 2017, **7**.
- 134 G. Cerullo and S. de Silvestri, *Review of Scientific Instruments*, 2003, **74**, 1–18.
- 135 P. Mao, Z. Wang, W. Dang and Y. Weng, *Review of Scientific Instruments*, 2015, **86**, 123113.
- 136 E. J. Heilweil, *Ultrashort-pulse multichannel infrared spectroscopy using broadband frequency conversion in LiIO<sub>3</sub>*, 1989, vol. 14.
- 137 T. A. Heimer and E. J. Heilweil, *Bull Chem Soc Jpn*, 2002, **75**, 899–908.
- 138 P. A. Scattergood, M. Delor, I. v. Sazanovich, O. v. Bouganov, S. A. Tikhomirov, A. S. Stasheuski, A. W. Parker, G. M. Greetham, M. Towrie, E. S. Davies, A. J. H. M. Meijer and J. A. Weinstein, *Dalton Transactions*, 2014, **43**, 17677–17693.
- 139 M. Delor, P. A. Scattergood, I. v Sazanovich, A. W. Parker, G. M. Greetham, A. J. H. M. Meijer, M. Towrie and J. A. Weinstein, *Science (1979)*, 2014, **346**, 1492–1495.
- 140 M. Delor, T. Keane, P. A. Scattergood, I. v. Sazanovich, G. M. Greetham, M. Towrie, A. J. H. M. Meijer and J. A. Weinstein, *Nat Chem*, 2015, **7**, 689–695.
- 141 M. Delor, S. A. Archer, T. Keane, A. J. H. M. Meijer, I. v. Sazanovich, G. M. Greetham, M. Towrie and J. A. Weinstein, *Nat Chem*, 2017, **9**, 1099–1104.
- 142 Z. Lin, C. M. Lawrence, D. Xiao, V. v. Kireev, S. S. Skourtis, J. L. Sessler, D. N. Beratan and I. v. Rubtsov, *J Am Chem Soc*, 2009, **131**, 18060–18062.
- 143 M. Baer, *INTRODUCTION TO THE THEORY OF ELECTRONIC NON-ADIABATIC COUPLING TERMS IN MOLECULAR SYSTEMS*, 2002, vol. 358.
- 144 G. A. Worth and L. S. Cederbaum, *Annu Rev Phys Chem*, 2004, **55**, 127–158.
- 145 S. Smale, in *The Collected Papers of Stephen Smale: Volume 2*, World Scientific, 2000, pp. 544–549.
- 146 I. H. M. van Stokkum, D. S. Larsen and R. van Grondelle, *Biochim Biophys Acta Bioenerg*, 2004, **1657**, 82–104.
- 147 C. Hippus, I. H. M. van Stokkum, E. Zangrando, R. M. Williams and F. Würthner, *Journal*

## 2. Chapter 2-Ultrafast Dynamics in NAP-(B)-Pt-(B)-NAP Complexes

### 2.1 Introduction

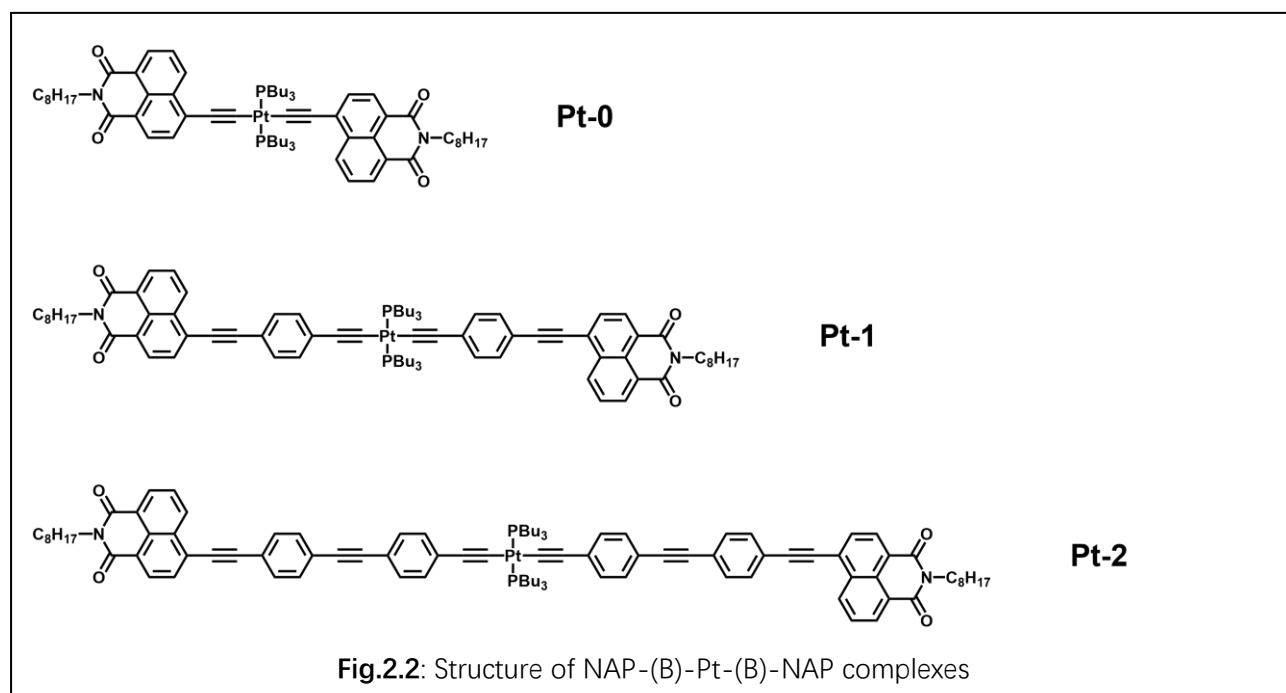
As discussed in the introduction, the key steps in photocatalysis process includes three steps: 1). Light harvesting, 2). Charge separation, and 3). Catalysis reaction. To achieve such charge separated state (CSS), a *Donor – Bridge – Acceptor* (D-B-A) system is required. In our previous research, a series of (D-B-A) systems based on Pt complexes (shown in **Fig.2.1**) are synthesised and characterized by ultrafast spectroscopy and corresponding energy level diagrams are suggested in **Fig.2.1**.<sup>1-3</sup>



In these complexes, the Pt metal centre works as the light harvesting chromophore in visible range and NAP ligand is the acceptor and PTZ ligand is the electron donor. With photon excitation of these complexes, a photo-induced charge transfer process happens with electron transfer from Pt metal centre to the NAP acceptor and that the metal-to-ligand charge transfer (MLCT) state be populated. Then there are two possible states that the CT state decays into, one is form the targeted CSS state by

electron transfer from the PTZ electron donor to the Pt cation formed in MLCT state or a competing back electron transfer process can happen by the electron on the NAP<sup>-</sup> anion of the MLCT state transfer to the Pt cation centre and form an excited NAP ligand localised state <sup>3</sup>NAP as shown in the energy level diagrams.<sup>1-3</sup> In the **NAP-Pt-CH<sub>2</sub>-PTZ** complex, the yield of <sup>3</sup>CSS state from initial MLCT state is about 10% and the yield of <sup>3</sup>NAP state is around 57%.

To reduce the yield of competing back electron transfer process, one of the methods is to increase the distance between the positive and negative charge centre formed, similar phenomenon has been observed in many other D-B-A systems where the back electron transfer process kills the CSS state formed.<sup>4,5</sup> However, in the **NAP-Pt-PTZ** systems discussed here, the CSS state is not formed directly after photon excitation but the MLCT state and the back electron transfer process is competing with the formation process of CSS state. To investigate the influence with the increase of bridge length between Pt centre and NAP acceptor and provide guidelines in high yield CSS formation systems, the Pt complexes (Structure Shown in **Fig.2.2**) are synthesised and characterised by ultrafast spectroscopies and the result is discussed in this chapter. In these complexes, there are only NAP acceptor together with bridge included alkyne and phenyl groups are included and no electron donor ligand which makes these complexes good model to investigate bridge length dependence of back electron transfer process of CT state.



## 2.2 Chapter Aim

1. Investigate excited states dynamics of NAP-(B)-Pt-(B)-NAP complexes shown in **Fig.2.2** by combining different ultrafast spectroscopies. Establish the rates of intersystem crossing, charge separation, and charge recombination in each complex.
2. Use the knowledge of the dynamics, combine it with electrochemical and steady-state emission and absorption data, to create an energy level diagram for each complex.
3. Compare the dynamics and energetics of the 3 complexes as a function of bridge length, and deduce the role of the bridge.

## 2.3 Results and Discussion

### 2.3.1 Fourier transform Infrared (FTIR) Spectra

The structures of **Pt-0**, **Pt-1** and **Pt-2**, and their ground state FTIR spectra in DCM in the wavenumber region from  $1450\text{ cm}^{-1}$  to  $2250\text{ cm}^{-1}$  are shown in **Fig.2.3**. The absorption band at  $1583\text{ cm}^{-1}$  for **Pt-0** is attributed to NAP ring breathing modes  $\nu(\text{NAP})$ , the same attribution is made to the band in **Pt-1** at  $1588\text{ cm}^{-1}$  and in **Pt-2** at  $1589\text{ cm}^{-1}$

based on previous **NAP-Pt** complexes research done by Paul et al.<sup>1</sup> In **Pt-0**, the bands at 1653 cm<sup>-1</sup> and 1693 cm<sup>-1</sup> are attributed to asymmetric ( $\nu(\text{CO})_a$ ) and symmetric ( $\nu(\text{CO})_s$ ) combinations of the carbonyl groups stretching vibrations of the each of the NAP units which can be considered independent from one another. These asymmetric/symmetric combinations are observed at 1656 cm<sup>-1</sup> and 1698.5 cm<sup>-1</sup> for **Pt-1** and 1658.5 cm<sup>-1</sup> / 1700 cm<sup>-1</sup> for **Pt-2**. The IR-absorption bands in the region from 2000 cm<sup>-1</sup> to 2250 cm<sup>-1</sup> correspond to the stretching vibrations of the alkyne 'bridge' between the Pt metal centre and NAP acceptor. For **Pt-0**, a single band at 2084 cm<sup>-1</sup> is observed, which is attributed to the closely overlapping asymmetric ( $\nu(\text{CC})_a$ ) and a very weak symmetric ( $\nu(\text{CC})_s$ ) combinations of the alkyne group stretching vibrations, this band occurs at the same frequency as reported previously for Pt(II) complexes containing a Pt – C  $\equiv$  C – NAP fragment.<sup>1</sup> For **Pt-1** and **Pt-2**, which possess two or three alkyne groups on each ligand side, resp., the spectra contain multiple IR absorption bands in the 2000 – 2250 cm<sup>-1</sup> region. For **Pt-1**, the absorption band at 2096 cm<sup>-1</sup> is attributed to the asymmetric and symmetric vibrations combinations from the alkyne group bound directly to the Pt centre ( $\nu(\text{CC}_{\text{Pt}})_{a+s}$ ), and the band at 2199 cm<sup>-1</sup> is attributed to the asymmetric/symmetric combinations of the alkyne group bound directly to the NAP group ( $\nu(\text{CC}_{\text{NAP}})_{a+s}$ ). For **Pt-2**, the absorption band at 2110 cm<sup>-1</sup> is attributed to vibration modes  $\nu(\text{CC}_{\text{Pt}})_{a+s}$  and the band at 2203 cm<sup>-1</sup> is attributed to vibration modes  $\nu(\text{CC}_{\text{NAP}})_{a+s}$  combined with  $\nu(\text{CC}_{\text{mid}})_{a+s}$ , the vibration from the triple bonds in between of the two phenyl groups and close to NAP ligand. The  $\nu(\text{CC}_{\text{Pt}})_{a+s}$  absorption band in **Pt-2** is much weaker than the corresponding absorption band in **Pt-1**, and weaker than the  $\nu(\text{CC})_{a+s}$  in **Pt-0**, likely due to an increase in the bridge length causing a reduction in the change in the dipole moment upon vibration. All assignments are supported by DFT calculations as shown in support information (SI) **Fig.2.S8** and all of the DFT calculation on **Pt-0**, **Pt-1** and **Pt-2** are done by Dr. Heather Carson with Gaussian View 09.

To investigate the ultrafast excited state dynamics of **Pt-0**, **Pt-1** and **Pt-2**, transient

infrared (TRIR), electronic transient absorption (TA) and broadband fluorescence up-conversion spectroscopy (FLUPs) have been used.

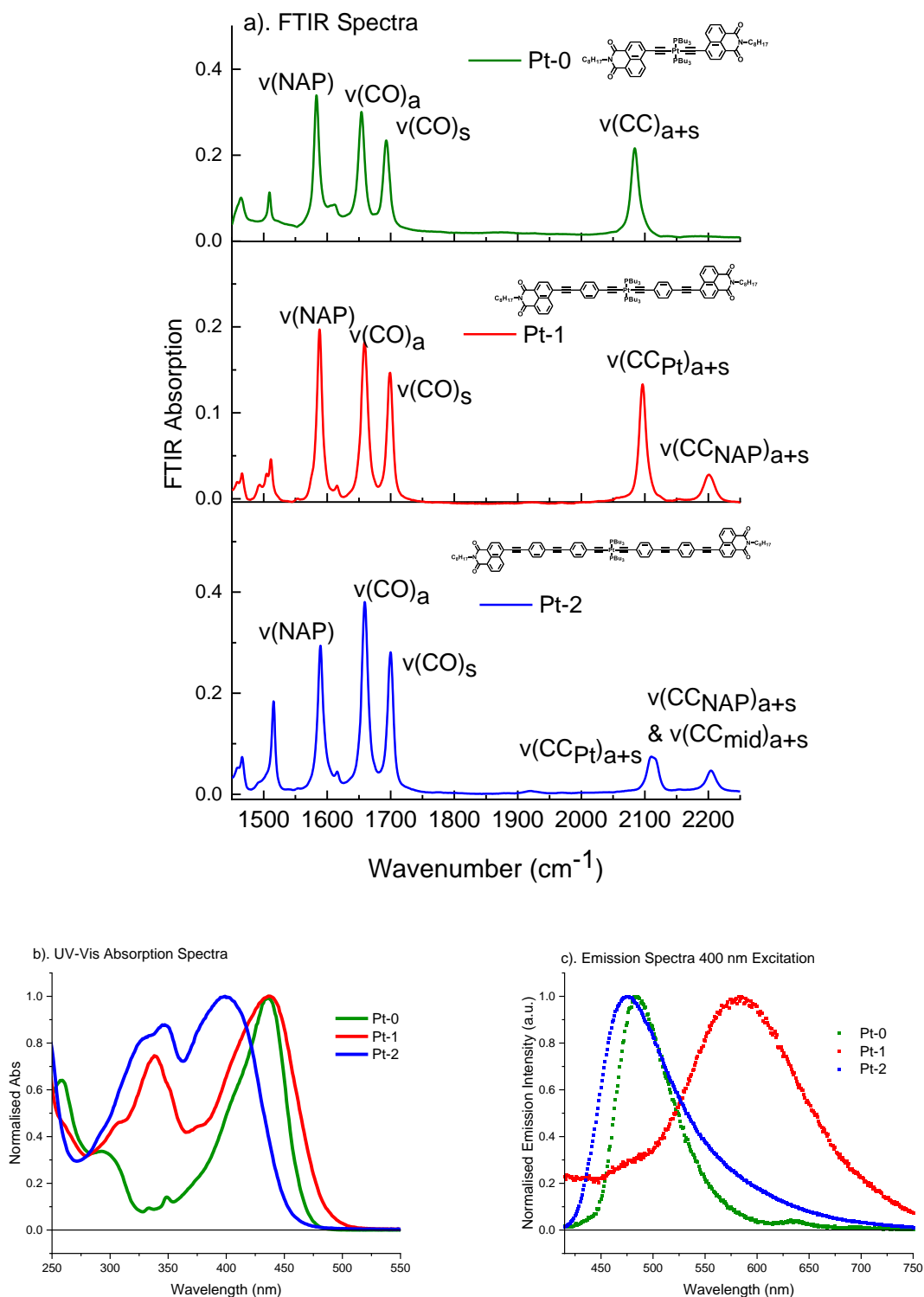


**Fig.2.3:** a). Fourier Transform infrared (FTIR) spectra for **Pt-0** (green), **Pt-1** (red) and **Pt-2** (blue) in DCM shown in the region between  $1450 \text{ cm}^{-1}$  and  $2250 \text{ cm}^{-1}$ . b). Normalised UV-Vis absorption spectra and Emission spectra with excitation at 400 nm of **Pt-0** (green), **Pt-1** (red) and **Pt-2** (blue)

### 2.3.2 Time Resolved Transient Infrared Spectroscopy

TRIR studies have been conducted in DCM solutions, under excitation with a 400 nm,

40 fs full width at half maximum (FWHM) laser pulse. After the excitation, the samples were probed by a broad-band mid-IR laser pulse generated from the same seed source (see Experimental for the information on how probe pulses were generated). For discussion, the TRIR data are called either low-frequency TRIR (LF-TRIR) in probe region from 1450  $\text{cm}^{-1}$  to 1750  $\text{cm}^{-1}$ , or as a high-frequency TRIR (HF-TRIR) in the probe region from 1800  $\text{cm}^{-1}$  to 2250  $\text{cm}^{-1}$  as show in **Fig.2.4**. Original data are processed by using `ultra_view` provided by central laser facility (CLF), Rutherford Appleton Laboratory (RAL).<sup>6</sup>

Global analysis or target analysis were performed on the TRIR spectra to extract component (excited state) spectra and corresponding excited state decay constants using Glotaran.<sup>7</sup>

### 2.3.2.1 TRIR of Pt-0

Excitation of **Pt-0** in DCM with the 400 nm laser pulse, negative signals corresponding to the bleaching of the ground state absorbencies across the spectrum have been observed, along with a rise of an extremely broad absorption feature that covers the entire HF-TRIR and LF-TRIR probe region from 1450  $\text{cm}^{-1}$  to 2200  $\text{cm}^{-1}$ , **Fig.2.4**. This broadband absorption is attributed to a 'tail' of the transient electronic absorption band of the charge transfer (CT) state, similar to that observed in other Pt(II) acetylide complexes reported by Weinstein's group.<sup>1,8,9</sup> In the high frequency region, the decay of the broadband CT-state electronic absorption is accompanied by a growth of the peak at 1947  $\text{cm}^{-1}$  which persists on the time-scale of the experiment as shown in **Fig.2.4 (b)**. This feature is characteristic of the long-lived intra-ligand triplet state (<sup>3</sup>NAP), as are the bands at 1596  $\text{cm}^{-1}$  and 1641  $\text{cm}^{-1}$  observed in LF-TRIR at later times as shown in **Fig.2.4 (a)**.<sup>1</sup> Global analysis of the HF-TRIR (show in Fig.2.5) by a sequential model required two exponential components with the lifetime of 1.2 ps, 9.5 ps and a long-lived component modelled as a constant, which represents the <sup>3</sup>NAP state. The 1.2 ps and 9.5 ps components are attributed to the Franck-Condon (FC) state and the singlet mixed metal-ligand-to-ligand charge transfer (<sup>1</sup>MMLLCT) state where the



electron density shift from the Pt centre and alkyne fragment to the NAP fragment – see **Fig.2.S10-11** and the **SI**, for the DFT calculations.

The LF-TRIR of **Pt-0** in DCM at early time after the excitation (shown in **Fig.2.4(a)**) also features a very broad “offset-like” tail of the broadband electronic absorption of the CT state. The bands at around  $1568\text{ cm}^{-1}$  and  $1618\text{ cm}^{-1}$  are attributed to  $\nu(\text{NAP})$  and  $\nu(\text{CO})$  modes in NAP-anion ( $\text{NAP}^-$ ), localised on either of the NAP-groups, which decay with the lifetime 8.4 ps as extracted by global analysis based on a sequential model with 3 components. The peak at  $1599\text{ cm}^{-1}$  is assigned to the combination of  $\nu(\text{NAP})$  and  $\nu(\text{CO})_a$  modes in the  $^3\text{NAP}$  state, and the  $1641\text{ cm}^{-1}$  band is assigned to the  $\nu(\text{CO})_s$  mode of  $^3\text{NAP}$  state and the kinetic traces and corresponding fitting at these two wavenumber are shown in **Fig.2.4 (g)**, which does not significantly decay on the time-scale of the experiment.

Global analysis required three components to satisfactorily fit the LF-TRIR spectra of **Pt-0** in DCM, with the lifetimes of 0.02 ps, 8.4 ps and a constant. Instead of the 1.2 ps and 9.5 ps components observed in HF-TRIR data, only one, 8.4 ps component, is necessary to describe the LF-TRIR. On the basis of EAS/DAS spectral profiles (**Fig.2.5**, **Fig.2.S1** and **Fig.2.S2** in SI), 0.02 and 1.2 ps components correspond to vibrationally hot singlet states.

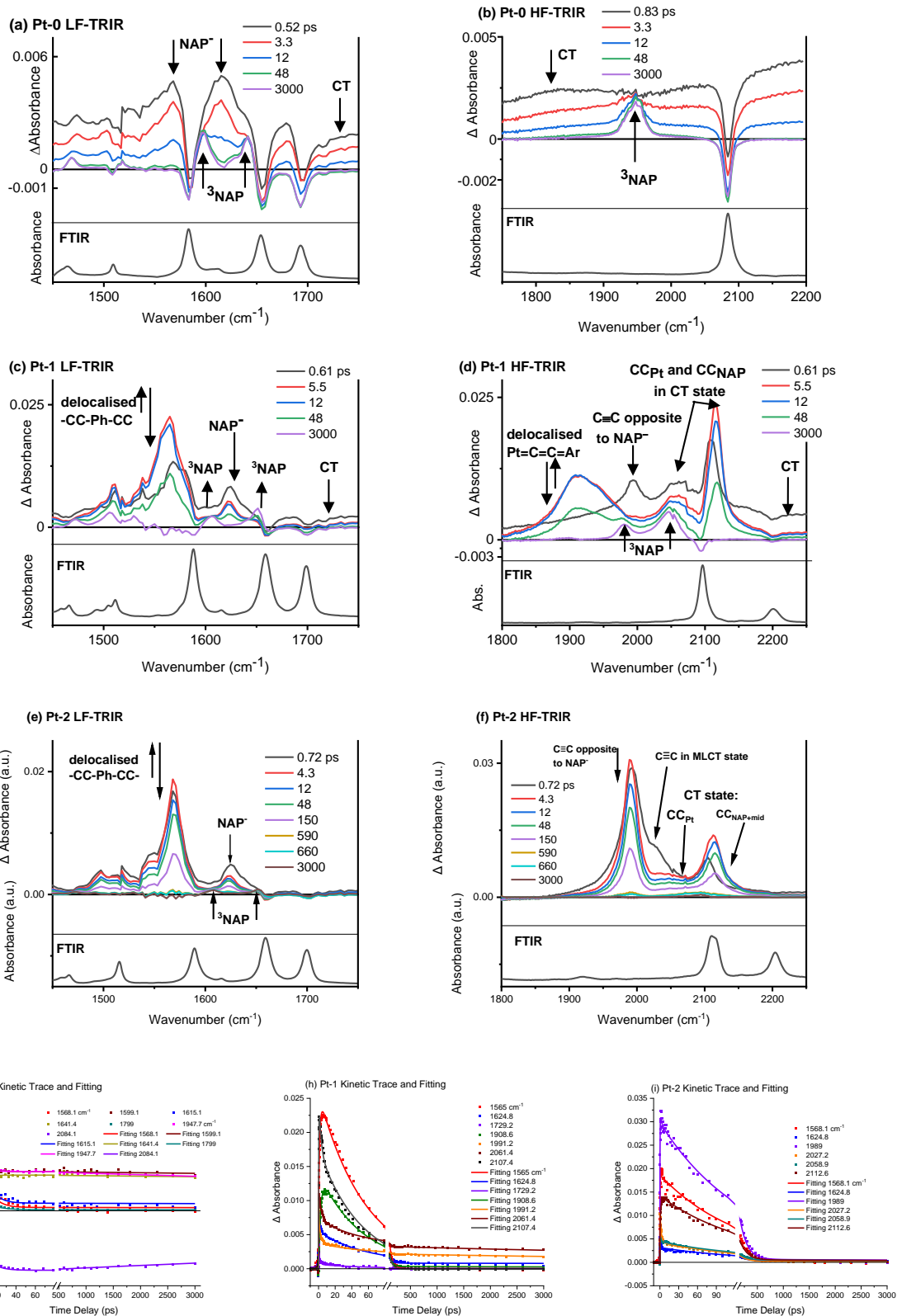
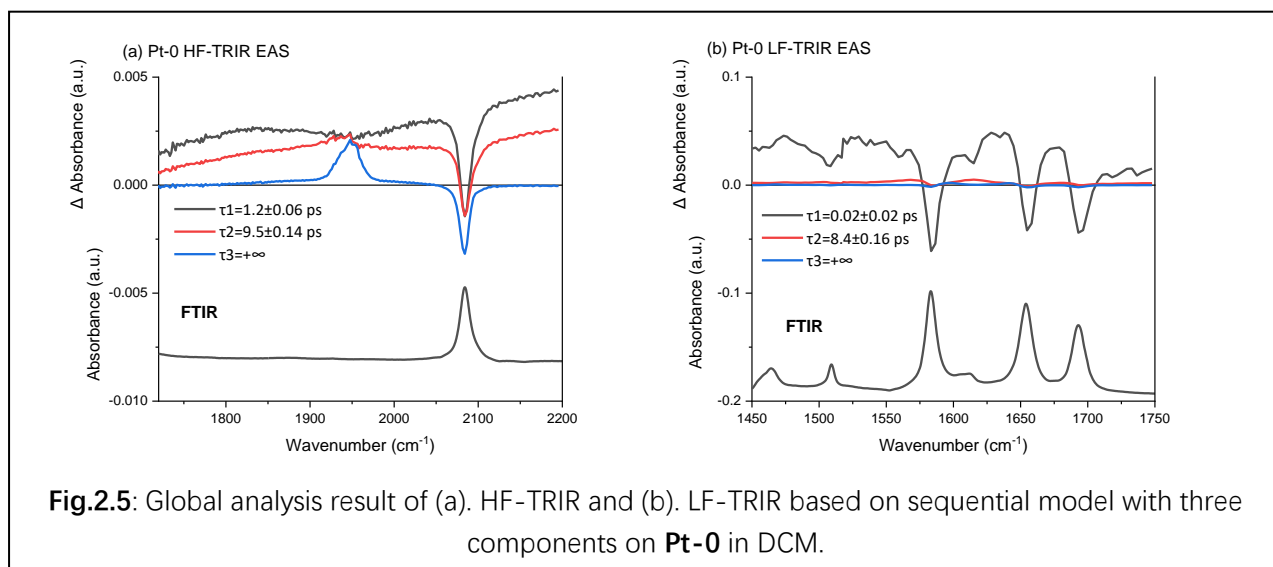


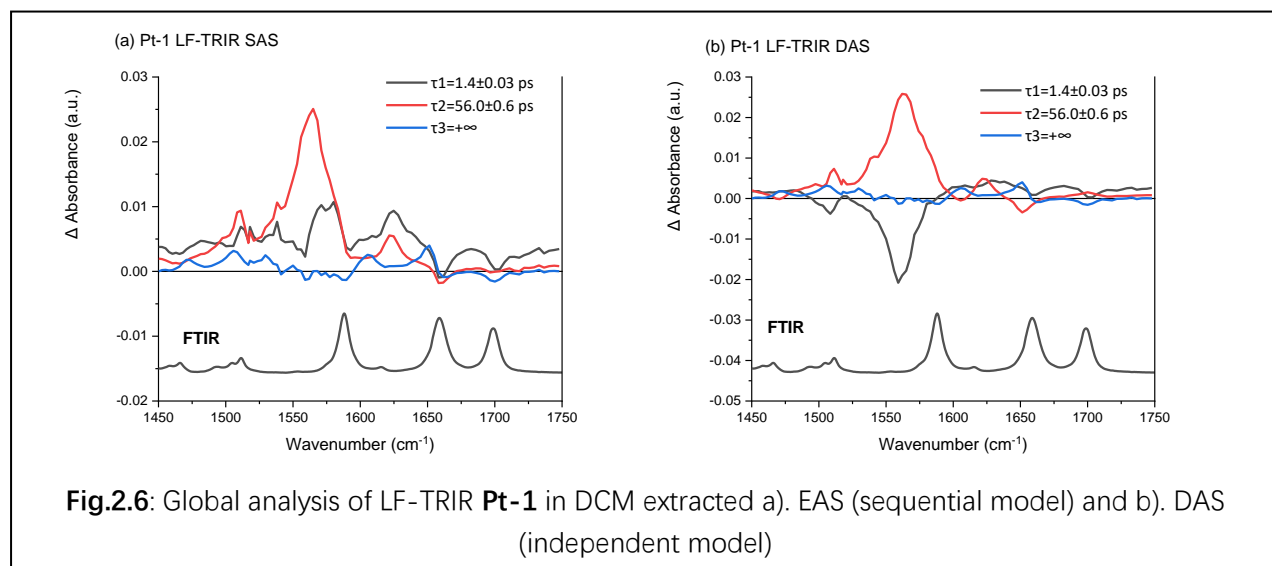
**Fig.2.4:** Time Resolved IR (TRIR) spectra collected under 400-nm excitation of **Pt-0** (a, b), **Pt-1**(c, d) and **Pt-2**(e, f) in DCM solutions at room temperature, in the low-frequency and high-frequency (LF-TRIR and HF-TRIR) regions of the spectrum. Together with kinetic traces and global analysis fitting at selected wavenumber of g). **Pt-0**, h). **Pt-1** and i). **Pt-2**.



### 2.3.2.2 TRIR of Pt-1

The LF-TRIR of **Pt-1** (shown in **Fig.2.4 (c)**) following the 400 nm excitation show formation of an offset-like tail of the broadband electronic absorption attributed to a CT state and of the transients at 1580  $\text{cm}^{-1}$  and 1625  $\text{cm}^{-1}$  attributed to  $\nu(\text{NAP})$  and the  $\nu(\text{CO})$  modes of the  $\text{NAP}^-$  anion. Both these observations indicate that 400-nm excitation populates a CT-state in **Pt-1**. However, the nature of the CT state is slightly different to that in **Pt-0**. According to the DFT calculation (shown in **Fig.2.S12** in **SI**, all of the DFT calculation is done by Heather Carson<sup>10</sup>), the CT state populated in **Pt-1** is also MMLLCT state but with less electron density donated from Pt metal centre, which makes it more like an ‘intraligand charge transfer’ (ILCT) with an admixture of Pt state in which electron density shifts from the  $\text{C} \equiv \text{C} - \text{Ph} - \text{C} \equiv \text{C}$  fragment to the NAP fragment of the same ligand. (Details of this MMLLCT state will be discussed later). With time, the broadband absorption and the peak at 1625  $\text{cm}^{-1}$  decay, and 1580  $\text{cm}^{-1}$  peak shifts to 1565  $\text{cm}^{-1}$  as shown in **Fig.2.4 (c, h)**. The band at 1565  $\text{cm}^{-1}$  which is much more intense than a shoulder observed for NAP-anion spectrum, is attributed to delocalised  $-\text{CC} - \text{Ph} - \text{CC} -$  fragment vibration mode formed in CT state, but the slightly lower frequency indicates that the initially populated MMLLCT state decays into a CT state of different nature (the shift to lower frequency rules out cooling effect). This 1565  $\text{cm}^{-1}$  band could be attributed to the double bond vibration on phenyl group after isomerisation breaks the aromatic system (shown in **Fig.2.7**), which meets well

with FTIR of quinones which has similar structure as the isomerised phenyl group where the C = C vibrational mode region is reported from 1560 to 1620  $\text{cm}^{-1}$ .<sup>11</sup>



Global analysis of the LF-TRIR data of **Pt-1** in DCM required a sequential model with three components with the lifetimes of 1.3 ps, 56.0 ps and a long-lived component. The EAS and DAS extracted are given in **Fig.2.6**.

The HF-TRIR immediately after 400-nm excitation shows a broad absorption feature (caused by a tail of the electronic absorption of a CT state), and positive signals peaked at 1993  $\text{cm}^{-1}$ , 2061  $\text{cm}^{-1}$  and 2107  $\text{cm}^{-1}$  as show in **Fig.2.4(d)**. The band at 1993  $\text{cm}^{-1}$  decays within 5 ps whilst a new, extremely intense absorption band with a maximum at 1909  $\text{cm}^{-1}$  grows in, and the peak at 2107  $\text{cm}^{-1}$  blue-shift to 2115  $\text{cm}^{-1}$ . These observations can be explained by a decay of the initially populated CT-to-NAP state into a new excited state, which according to the LF-TRIR data (above) also contains a NAP-anion, and is therefore also a state with charge-transfer character. The peak at 1909  $\text{cm}^{-1}$  could be attributed to the formation of cumulated C = C = C bond as shown in **Fig.2.7**. In 2004, Cooper et al. reported a  $\mu\text{s}$  TRIR spectra of trans-bis(tributylphosphine)bis(4-ethynyl-1-(2-phenylethynyl)benzene)Pt(II) in DCM following a 355 nm laser pump; the spectra collected in time range 0 – 2.5  $\mu\text{s}$  showed a peak at 1890  $\text{cm}^{-1}$  which they attributed to a  $\nu(\text{Pt} = \text{C} = \text{C} = \text{Ar})$  mode in

a cumulated structure.<sup>12</sup> Similar structure could also be observed in ground state allenylidene Pt(II) complexes which are suggested to have a  $Pt = C = C = C$  structure in the ground state, with  $\nu(C = C = C)$  mode at around  $2095\text{ cm}^{-1}$  detected by FTIR spectroscopy.<sup>13,14</sup> In an organic triazine-based donor-acceptor molecule drastic changes in the TRIR features from  $2060\text{ cm}^{-1}$  to around  $1970\text{ cm}^{-1}$  were attributed to a photoinduced isomerisation from alkyne to allene.<sup>15</sup> Similar extremely intense IR-absorption at around  $1900\text{ cm}^{-1}$  has also been observed in a series of asymmetric  $NAP - C \equiv C - Pt - C \equiv C - Ph - Donor$  complexes,  $NAP - C \equiv C - Pt - C \equiv C - Ph$  (NAP-Pt-Ph),  $NAP - C \equiv C - Pt - C \equiv C - Ph - CH_2 - PTZ$  (NAP-Pt-CH<sub>2</sub>-PTZ), and  $NAP - C \equiv C - Pt - C \equiv C - Ph - PTZ$  (NAP-Pt-PTZ).<sup>2</sup> However, for  $NAP - C \equiv C - Pt - Cl$  (NAP-Pt-Cl) complex, this intense signal was not observed, indicating that two strongly coupled acetylide groups are required.<sup>1</sup> In the donor-bridge-acceptor (D-B-A) complexes, NAP-Pt-CH<sub>2</sub>-PTZ and NAP-Pt-PTZ, the intense signal at around  $1910\text{ cm}^{-1}$  disappear when the MLCT state decayed into a charge separated state (CSS) shifting electron hole away from the -CC-Pt-CC- fragment. Therefore, a peak at around  $1910\text{ cm}^{-1}$  could be used as a characteristic signal of the formation of MLCT/Inter-ligand CT state in Pt complexes with  $Pt - C \equiv C - Ph$  structure where the electron density donated from the opposite side of the NAP anion ligand. For **Pt-1** in DCM, the peak at  $1909\text{ cm}^{-1}$  rise could be attributed to the formation of cumulated  $C = C = C$  structure in MLCT/Inter-ligand CT state, which is formed from the initially populated MMLLCT state. The positive signals at  $1980\text{ cm}^{-1}$  and  $2046\text{ cm}^{-1}$  (show in **Fig.2.4(d)**) maintained at 3000 ps are attributed to <sup>3</sup>NAP state, the  $1980\text{ cm}^{-1}$  is attributed to the  $\nu(CC_{Pt})_{a+s}$  mode and the  $2046\text{ cm}^{-1}$  is attributed to the  $\nu(CC_{NAP})_{a+s}$  mode. The peak arising at  $1993\text{ cm}^{-1}$  could be attributed to  $C \equiv C$  fragment on the opposite side of NAP anion formed in CT state which decay into  $1909\text{ cm}^{-1}$  when the cumulated structure formed. The peaks at  $2056\text{ cm}^{-1}$  and  $2115\text{ cm}^{-1}$  are also associated with the CT state, which may be caused by the  $C \equiv C$  fragment on the NAP anion side.

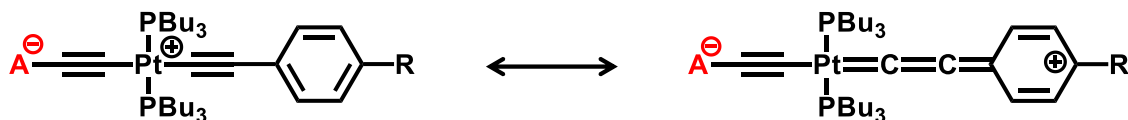
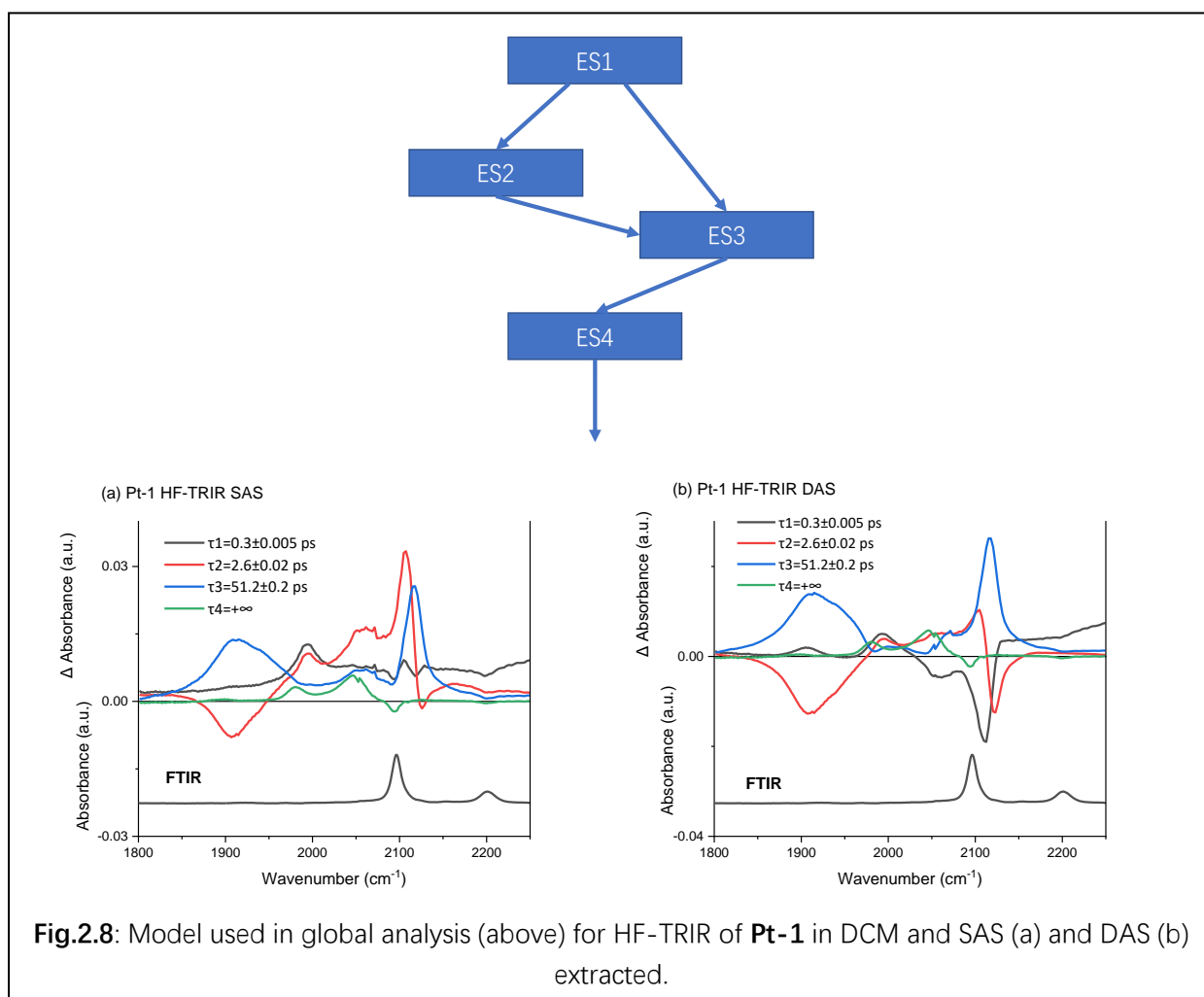


**Fig.2.7:** Isomerisation process in MLCT/Inter-ligand CT state of *Acceptor – Pt – C ≡ C – Ph – R* complex. Here the cumulated CCC structure leads to the intense peak at around 1910  $\text{cm}^{-1}$ .



To test this hypothesis, target analysis based on a model with 4 components was performed for the **Pt-1** HF-TRIR data. The first excited state ES1 populated by the pump pulse decays into the second and third states ES2 and ES3, the ES2 also decays into ES3, the ES3 decays to ES4, and ES4 decays to the ground state (shown in **Fig.2.8**). This scheme yielded components' lifetimes of 0.3 ps, 2.6 ps, 51.2 ps and a long-lived excited state; their SAS and DAS are given in **Fig.2.8**. The SAS of the first and second

components show a peak at  $1993\text{ cm}^{-1}$  which indicates that both states are of an MMLCT character: we propose that the ES1 is Franck-Condon (FC) state which is a mixture of the second and third singlet excited state S2 and S3 based on modelling result done by Heather Carson (show in **Fig.2.S12**), the second excited state, ES2, is a singlet MMLCT state, which in turn decays into ES3. The nature of the ES3 state could be either a triplet MMLCT state or a triplet inter-ligand CT state.

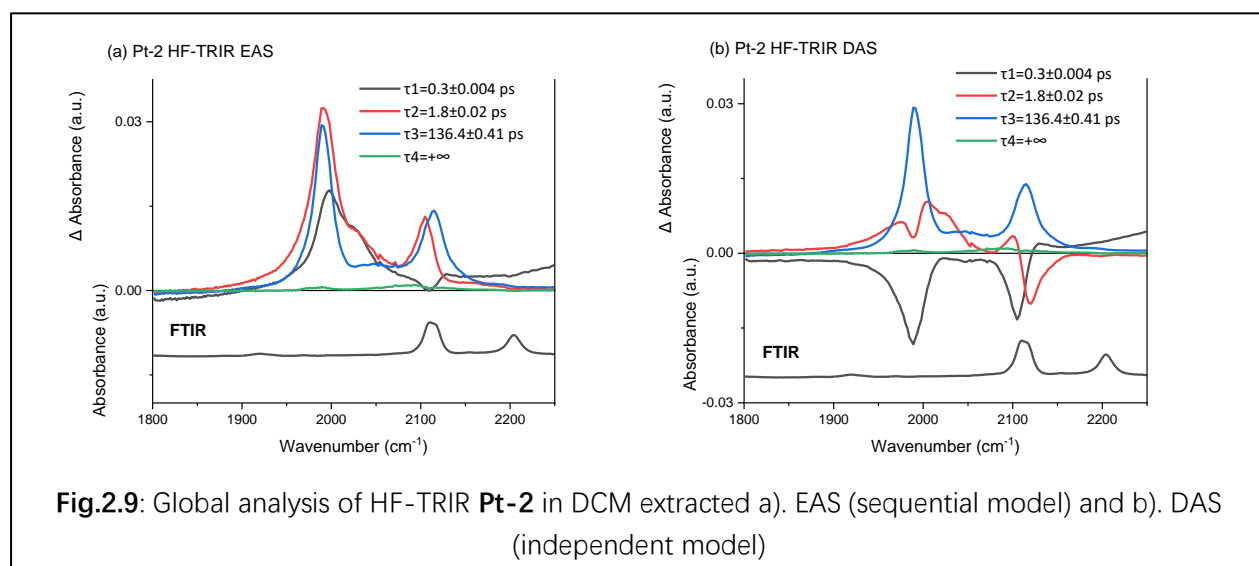
### 2.3.2.3 TRIR of Pt-2

LF-TRIR spectra of **Pt-2** in DCM are shown in **Fig.2.4 (e)**. Immediately after excitation, absorbances at  $1568\text{ cm}^{-1}$  and  $1625\text{ cm}^{-1}$  which correspond to delocalised  $-\text{CC}-\text{Ph}-\text{CC}-$  fragment vibrational mode and  $\nu(\text{CO})$  mode of  $\text{NAP}^-$  are observed, indicating that the first detected excited state is a CT state.

HF-TRIR spectra of **Pt-2** in DCM (shown in **Fig.2.4(f)**) show a band at  $1991\text{ cm}^{-1}$  and  $2105\text{ cm}^{-1}$  which are attributed to  $\nu(\text{CC}_{\text{Pt}})_{a+s}$  and  $\nu(\text{CC}_{\text{NAP}})_{a+s}$  in a  $^1\text{MMLCT}$   $\{\text{Ph}-\text{C}\equiv\text{C}-\text{Ph}-\text{C}\equiv\text{C}\rightarrow\text{NAP}\}$  state. At early times, the whole spectrum appears slightly elevated by a broad-band absorbance feature centred at  $2025\text{ cm}^{-1}$ . At 4.3 ps after the pump, the broad feature disappears, the peak at  $1991\text{ cm}^{-1}$  shifts very slightly to higher energies and becomes narrower, whilst the peak at  $2105\text{ cm}^{-1}$  is also shifted to higher energies, to  $2113\text{ cm}^{-1}$ . These observations can be explained by either  $^1\text{MMLCT}$  intersystem crossing to a intraligand charge transfer (ILCT) state, cooling, or both.

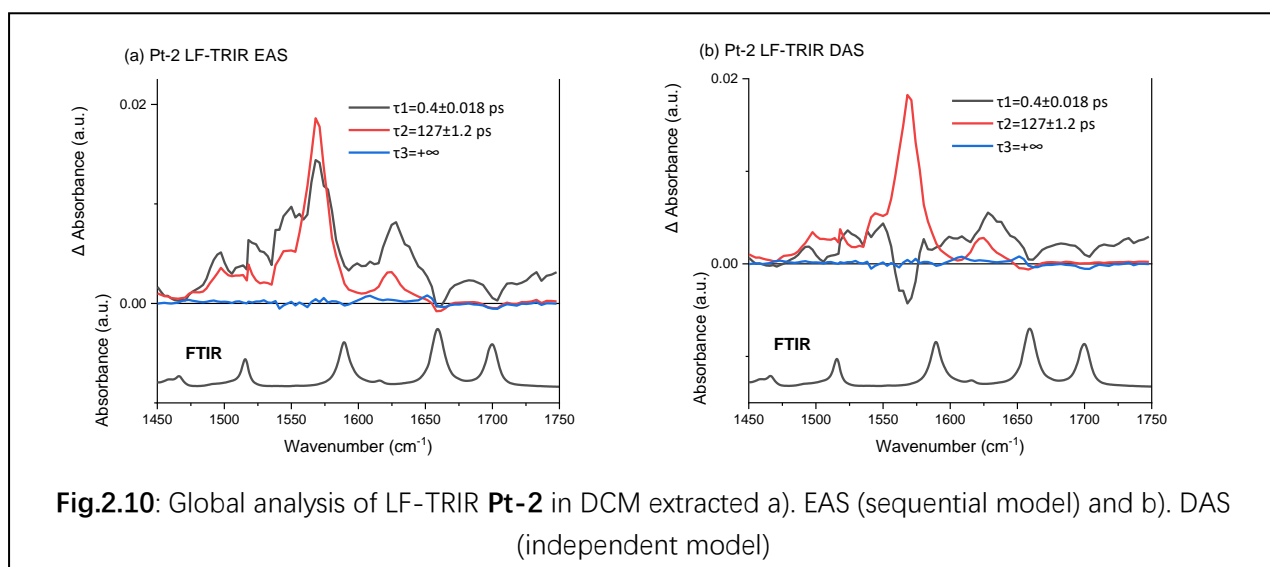
Importantly, in **Pt-2**, the intense signal at around  $1910\text{ cm}^{-1}$  so prominent in **Pt-1**, and other analogs containing Pt-CC-Ph units, is not observed at any time, which indicates that the MLCT/inter-ligand CT state is not populated and the Pt=C=C=C structure is not formed. However, a very short-lived broad feature ( $2024\text{ cm}^{-1}$ ) might be a signature of a more delocalised variant of an MMLCT state – the results of DFT calculations suggest (**Fig.2.S13**) that both S2 and S1 states which will be populated by 400 nm excitation

have major character of the bridge-to-NAP charge transfer, with the entire bridge, CC-Ph-CC-Ph-CC, being involved. Importantly, this charge transfer happens partially across the Pt-center, this supporting the idea of a vastly delocalised excited states at early times. The **Pt-2** spectrum shows the peak at  $1991\text{ cm}^{-1}$  (**Fig.2.4(f)**), at a similar position to that observed at early times in **Pt-1** ( $1996\text{ cm}^{-1}$ ) but this peak does not decay into the  $1910\text{ cm}^{-1}$  band as in case of **Pt-1** (**Fig.2.4(d)**). We suggest that the band at  $1991\text{ cm}^{-1}$  in **Pt-2** might be localised on the “oxidised”  $-\text{C}\equiv\text{C}-\text{Ph}-\text{C}\equiv\text{C}-\text{Ph}-\text{C}\equiv\text{C}-$  bridge, across the Pt-center from the NAP-anion side. The spectrum of **Pt-2** also has a peak at around  $2110\text{ cm}^{-1}$  when CT state is populated; finally, there is residual absorbance around  $2063\text{ cm}^{-1}$  which might indicate a presence of another, delocalised, state.



Global analysis of HF-TRIR of **Pt-2** based on a sequential model with 4 components yielded lifetime 0.3 ps, 1.8 ps, 136.4 ps and a long-lived state. The EAS and DAS are given in **Fig.2.9**; the 0.3 ps component corresponds to the transformation from a delocalised and hot initial singlet manifold. The EAS and DAS give the  $^1\text{MMLLCT}$  state lifetime as 1.8 ps and  $^3\text{ILCT}$  state as 136.4 ps. The low-intensity residual spectrum with a long lifetime has absorbances at  $1989\text{ cm}^{-1}$  and  $2087\text{ cm}^{-1}$ , attributed to  $\nu(\text{CC}_{\text{Pt}})_{a+s}$  and  $\nu(\text{CC}_{\text{NAP}})_{a+s}$  mode of  $^3\text{NAP}$  state.





Global analysis of LF-TRIR of **Pt-2** in DCM yielded satisfactory results with a sequential model with 3 components (cf. 4 components in the HF-TRIR) with the lifetimes of 0.4 ps, 127 ps and a long-lived state. Fitting kinetic traces at selected wavenumbers are shown in **Fig.2.4(i)** and the EAS and DAS are given in **Fig.2.10** in supporting information. For LF-TRIR, the 127 ps component replaces the 1.8 ps and 136 ps components evident in HF-TRIR. Similarly to the hypothesis presented above for **Pt-1**, we argue that the LF-TRIR detects  $\text{NAP}^-$  anion features which are the same for  $^1\text{MMLLCT}$  and  $^3\text{ILCT}$ . The long-lived state SAS/DAS extracted has absorbances at  $1609\text{ cm}^{-1}$  and  $1651\text{ cm}^{-1}$  which are attributed to the  $^3\text{NAP}$  state (shown in **Fig.2.6**). The signals of  $^3\text{NAP}$  and the ground-state bleach at longer times in both the LF and HF regions are extremely weak, indicating that most of excited state decay into ground state directly instead of populating the  $^3\text{NAP}$  state (as was the case in **Pt-0** and **Pt-1**). Need to note is, in the DAS of **Pt-2** LF-TRIR shown in **Fig.2.10**, the component with constant (infinite) lifetime gives a tiny peak at  $1621\text{ cm}^{-1}$  (a characteristic signal of  $\text{NAP}^-$  anion), but in the LF-TRIR of **Pt-2** shown in **Fig.2.4 (e)** does not show this peak 3000 ps but in 590 ps and 660 ps. This indicates there is a hidden charge transfer state with relatively longer lifetime than 127 ps extracted and it is a different charge transfer state with the positive charge hole far more away from the  $\text{NAP}^-$  anion, in other word, a different charge transfer state compared with the one with 127 ps component.

### 2.3.3 Femtosecond Broadband Fluorescence Up-conversion Spectroscopy (FLUPs)

Time resolved fluorescence spectra of **Pt-0**, **Pt-1** and **Pt-2** are collected by using FLUPs. Detailed setup and background of FLUPs were reported by Zhang et al.<sup>16</sup> and Gerecke et al.<sup>17</sup> Briefly, a 400 nm laser pulse with 40 fs FWHM is used to pump the sample, emission of the sample is collected and focused onto a 0.1 mm thick  $\beta$  – *barium borate crystal* (BBO crystal) where the 1300-nm gate pulse is used to up-convert the emission signal by sum-frequency generation. The up-converted signal is directed into a homemade spectrograph and dispersed onto an Andor CCD camera. The original spectra are processed by a homemade software to remove cosmic rays, correct for group velocity dispersion (GVD) based on the wavelength, and the up-converted signal are converted back to original emission wavelength.

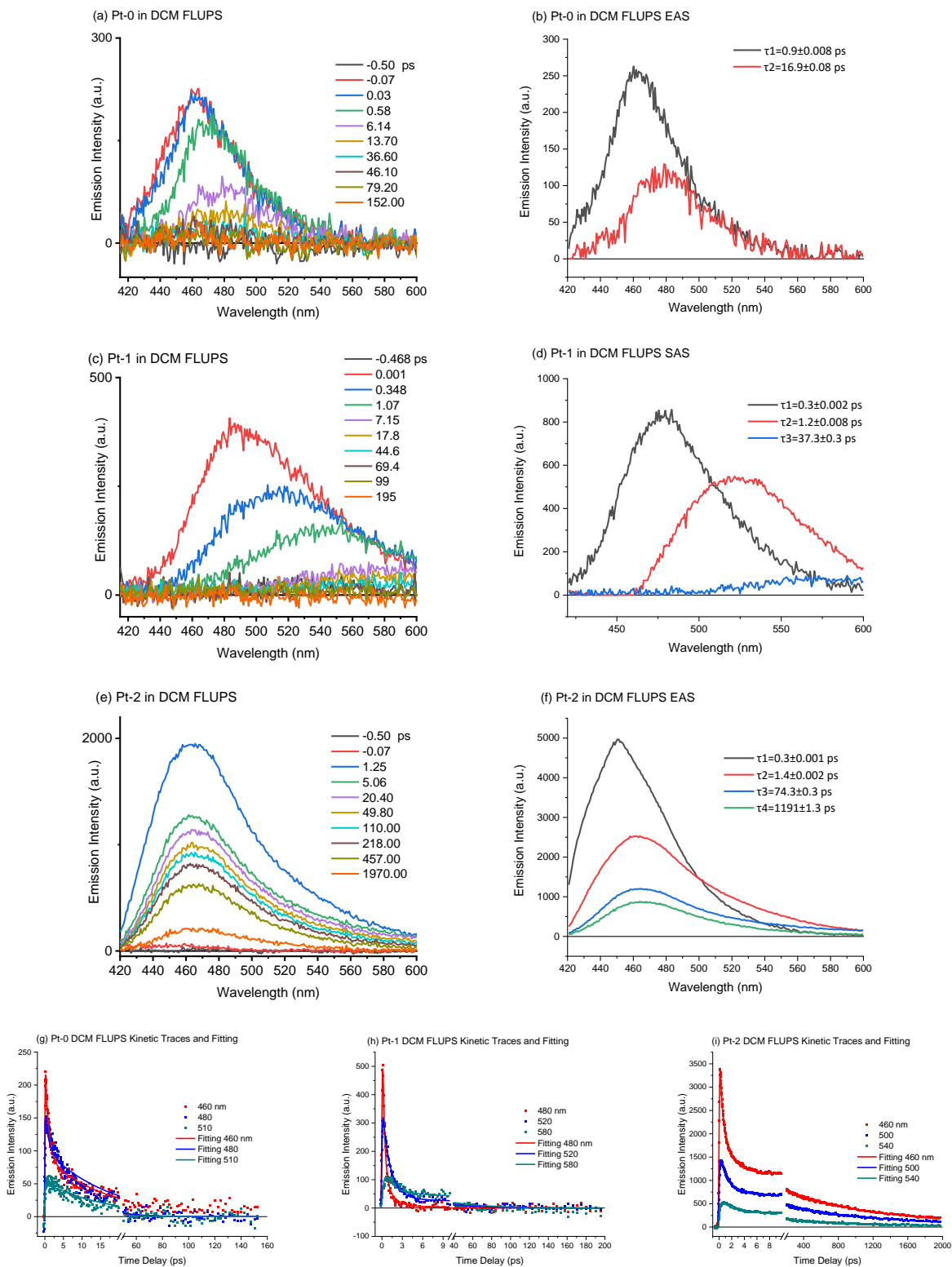


**Fig.2.11:** FLUPS spectra of **Pt-0** (a), **Pt-1** (c) and **Pt-2** (e) in DCM and EAS/SAS extracted by global/target analysis of the FLUPS spectra of **Pt-0** (b), **Pt-1** (d) and **Pt-2** (f). Kinetic traces and fitting of **Pt-0** (g), **Pt-1** (h) and **Pt-2** (i)

### 2.3.3.1 FLUPs of Pt-0 in DCM

The FLUPs spectra of **Pt-0** in DCM are given in **Fig.2.11 (a)**. At early times, the emission peak appears at around 465 nm, shifting with time by about  $700\text{ cm}^{-1}$  to 480 nm. Global analysis based on a sequential model with 2 components extracted lifetimes with 0.9 ps and 16.9 ps, for which the EAS spectra are shown in **Fig.2.11 (b)**. The long-lived  $^3\text{NAP}$  state observed by TRIR is not detected by FLUPs because this state emits at around 660 nm whose up-converted signal is overlapped with third order sum-frequency from 1300 nm gate beam on the BBO crystal. Also, the phosphorescence from  $^3\text{NAP}$  state is extremely long lived, up to  $\sim 190\ \mu\text{s}$  based on previous research,<sup>1</sup> and the pulse duration of gate beam is only about 80 fs FWHM, so there are not enough  $^3\text{NAP}$  phosphorescence photons could be up-converted by the gate beam and detected.

### 2.3.3.2 FLUPs of Pt-1 in DCM

The FLUPs spectra of **Pt-1** in DCM obtained with 400-nm excitation are given in **Fig.2.11 (c)**. At early time, the emission peak is at around 480 nm then it red-shifted to around 580 nm whilst approximately half of emission intensity is retained. Target analysis is done on FLUPs spectra of **Pt-1** in DCM with a model taken from the TRIR data, where the first excited state populates excited states 2 and 3 in parallel, whilst ES2 also populates ES3. The target analysis extracts lifetime: 0.3 ps, 1.2 ps and 37.3 ps. The SAS extracted by target analysis is given in **Fig.2.11(d)** with peaks at 480 nm, 525 nm and 595 nm. The 3 lifetime components do not in themselves have physical meaning: they may represent a continuous evolution of one state(s) into another convolved with vibrational cooling, change of the nature of the state, and its multiplicity. The physical meaning of these three components need to be discussed in conjunction with TRIR and TA data.

The  $^3\text{NAP}$  state of **Pt-1** is too long-lived to be detected on this time-scale with FLUPs.

The component with 580-nm emission maximum has much lower intensity than the

fastest component observed, global analysis gives its lifetime as 37.3 ps which is shorter than the EAS3 extracted from TRIR and TA (around 56 ps). Considering FLUPS is more sensitive in detecting fluorescent excited states, we suggest a hypothesis that the 37.3 ps is corresponding with singlet cumulenenic MLCT state ISC process but TRIR and TA is detecting a mixture of singlet and triplet cumulenenic MLCT state and the cumulenenic MLCT state mixture decays into <sup>3</sup>NAP with lifetime around 56 ps.

#### 2.3.3.3 FLUPs of Pt-2 in DCM

The initial FLUPs spectra of **Pt-2** in DCM show a peak at 450 nm which then red-shifted to 465 nm. Global analysis for FLUPs spectra of **Pt-2** in DCM is based on a sequential model with four components, lifetime extracted are 0.3 ps, 1.4 ps, 74.3 ps and a very small contribution with a 1191 ps lifetime. This 1191 ps component may be attributed to the longer lived tiny amount charge transfer state observed in LF-TRIR but not extracted by global analysis.

On the basis of FLUPs data, we tentatively propose the timescales of intersystem crossing of up to 17 ps (**Pt-0**, similar to previously reported NAP-CC-Pt-CC-Ph), 37.3 ps in **Pt-1** and 74.3 ps and 1191 ps (two different ILCT state) in **Pt-2**.

#### 2.3.4 Femtosecond Transient Absorption Spectroscopy in DCM

Transient absorption (TA) spectra of **Pt-0**, **Pt-1** and **Pt-2** were obtained with a 40 fs FWHM 400 nm pump pulse and the broadband probe beam is generated by a 40 fs FWHM 800 nm laser pulse interact with a 3 mm calcium fluoride crystal to generate UV-Vis probe beam (340-750 nm), then the probe beam is reflected into a fibre bundle and detected by a CMOS detector. All of the original TA spectra are processed by using *Surface Explorer* to do chirp correction and background correction.

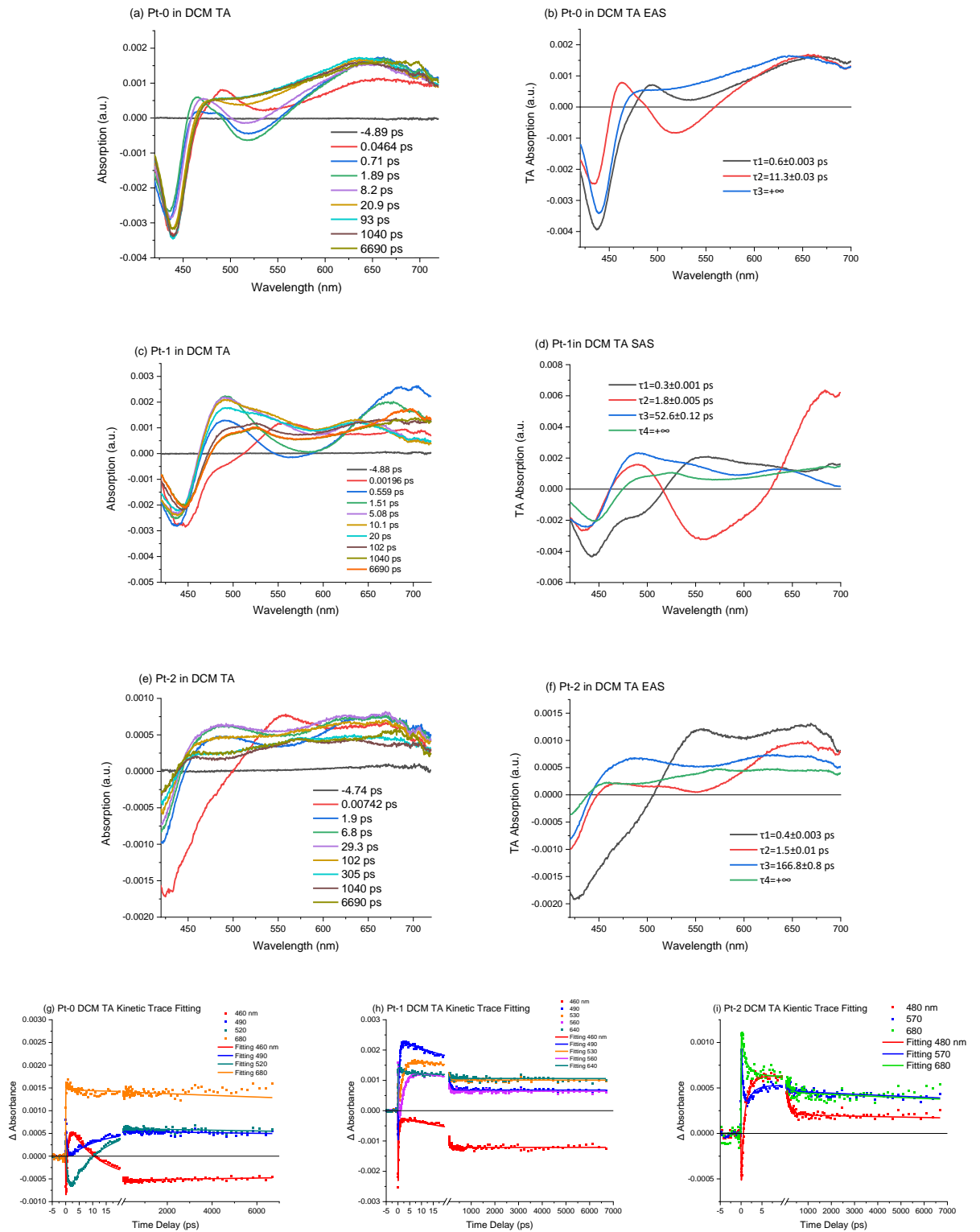


**Fig.2.12:** Femtosecond transient absorption spectra of **Pt-0** (a), **Pt-1** (c) and **Pt-2** (e) in DCM and EAS/SAS extracted by global/target analysis (b, d, f). Kinetic trace at selected wavelength (dots) and global analysis fitting (line) of **Pt-0** (g), **Pt-1** (h) and **Pt-2** (i).

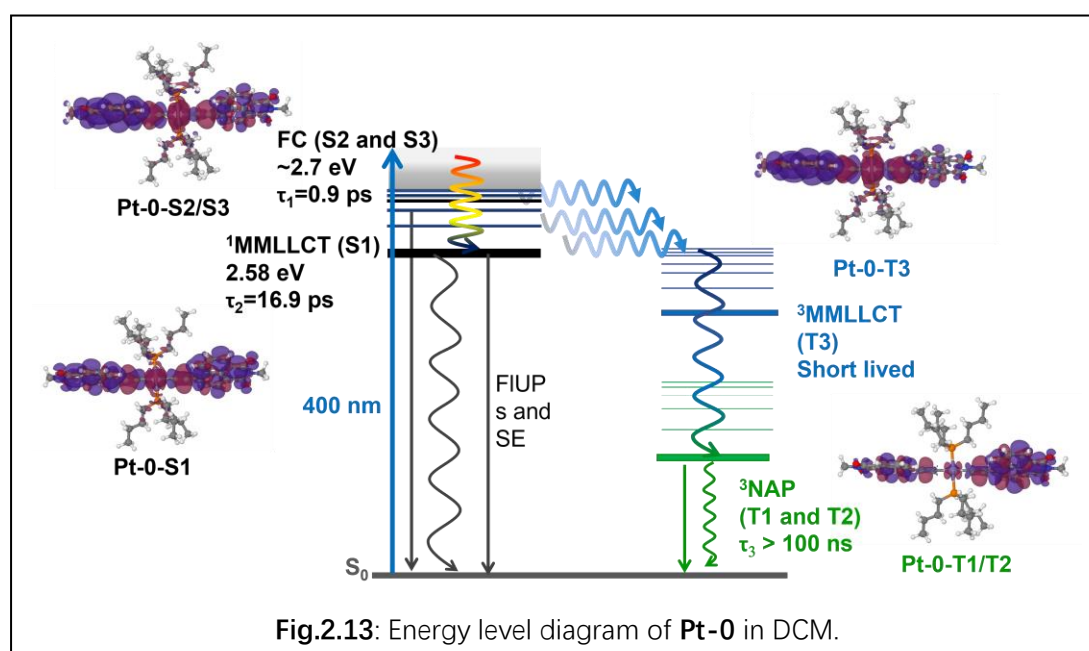
#### 2.3.4.1 Transient Absorption and energy level diagram of Pt-0

For **Pt-0**, the absorption peak (shown in **Fig.2.12(a)**) at early times appears at 490 nm: stimulated emission (SE) at 460 nm overlaps with the expected absorption of  $\text{NAP}^-$  which coincidentally is also 460-470 nm. As the absorption peak at 490 nm shifts to 460 nm (due to SE at 460 nm decaying), another negative signal at 520 nm grows in. As there are no ground state absorbances at >460 nm in the ground state absorption spectrum of **Pt-0**, the negative feature at 520 nm is attributed to stimulated emission from another singlet state. The lifetime of the SE2 coincides with the lifetime of the second component extracted from FLUPs. The decays of SE2 is accompanied by grow-in of the absorption spectrum characteristic of  $^3\text{NAP}$  state. Global analysis done with a 3-component sequential model yields lifetimes of 0.6 ps, 11.3 ps and a long-lived state, the EAS are given in **Fig.2.12(b)**. The first component could be attributed to a Franck-Condon state which may be attributed to a mixture of 2<sup>nd</sup> and 3<sup>rd</sup> singlet state based on modelling result, the 2<sup>nd</sup> component - to a  $^1\text{MMLLCT}$ , and the last component - to the long-lived  $^3\text{NAP}$  state.

Pt-0				
Technique	$\tau_1/\text{ps}$	$\tau_2/\text{ps}$		$\tau_3/\text{ps}$
HF-TRIR	$1.2 \pm 0.06$	$9.5 \pm 0.14$		$+\infty$
LF-TRIR	$0.02 \pm 0.02$	$8.4 \pm 0.16$		$+\infty$
FLUPs	$0.9 \pm 0.008$	$16.9 \pm 0.08$		
TA	$0.6 \pm 0.003$	$11.3 \pm 0.03$		$+\infty$
Pt-1				
	$\tau_1/\text{ps}$	$\tau_2/\text{ps}$	$\tau_3/\text{ps}$	$\tau_4/\text{ps}$
HF-TRIR	$0.3 \pm 0.005$	$2.6 \pm 0.02$	$51.2 \pm 0.2$	$+\infty$
LF-TRIR		$1.4 \pm 0.03$	$56 \pm 0.6$	$+\infty$
FLUPs	$0.3 \pm 0.002$	$1.2 \pm 0.008$	$37.3 \pm 0.3$	
TA	$0.3 \pm 0.001$	$1.8 \pm 0.005$	$52.6 \pm 0.12$	$+\infty$
Pt-2				
	$\tau_1/\text{ps}$	$\tau_2/\text{ps}$	$\tau_3/\text{ps}$	$\tau_4/\text{ps}$
HF-TRIR	$0.3 \pm 0.004$	$1.8 \pm 0.02$	$136 \pm 0.41$	$+\infty$
LF-TRIR	$0.4 \pm 0.018$		$127 \pm 1.2$	$+\infty$
FLUPs	$0.3 \pm 0.001$	$1.4 \pm 0.002$	$74.3 \pm 0.3$	$1191 \pm 1.3$
TA	$0.4 \pm 0.003$	$1.5 \pm 0.01$	$166.8 \pm 0.8$	$+\infty$

**Table.1** Summary of components' lifetime extracted from HF-TRIR, LF-TRIR, FLUPs and TA measurements for **Pt-0**, **Pt-1** and **Pt-2** in DCM. The error show here is given by Glotaran data fitting analysis.

Global analysis of the results obtained by TA, TRIR and FLUPs of **Pt-0** in DCM are summarised in **Table 1 (Top)**, and the energy level diagram is given in **Fig.2.13**. The timescale of ISC is up to 16.9 ps.

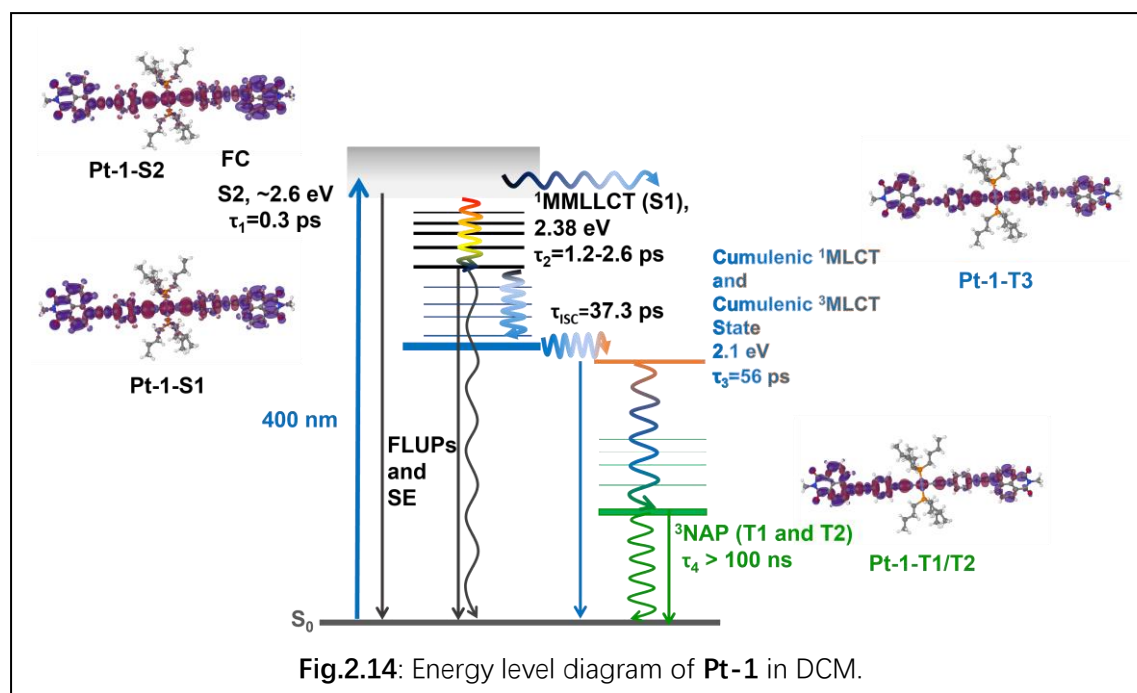




### 2.3.4.2 Transient Absorption and energy level diagram of Pt-1

For TA spectra of **Pt-1** in DCM after excitation with a 400 nm laser pulse (shown in **Fig.2.12(c)**) shows a negative signal at around 490 nm due to stimulated emission from  $^1\text{MMLCT}$  state. Then this trace decays into another negative signal at around 560 nm and a positive peak at around 460 nm, the peak at 460 nm is attributed to  $\text{NAP}^-$  anion which supported the idea this state is a charge transfer state, and the negative signal at 560 nm agrees well with the second component extracted from FLUPs which is stimulated emission caused by singlet cumulated MLCT/Inter-ligand CT state. Then the bleach at 560 nm also decays with the peak at 490 nm, 530 nm, and 640 nm growing in: this indicates that a new state is populated, and as the 530 nm peak corresponds with  $\text{NAP}^-$ , this new state is also a CT state as a mixture of singlet and triplet cumulenic MLCT state. Then this new CT state also decays, and leaves a characteristic  $^3\text{NAP}$  absorption signal at a later time.

Lifetimes of **Pt-1** in DCM extracted from different ultrafast spectroscopy methods by global analysis are given in **Table 1 (Middle)**. The energy level diagram of **Pt-1** in DCM is given in **Fig.2.14**.

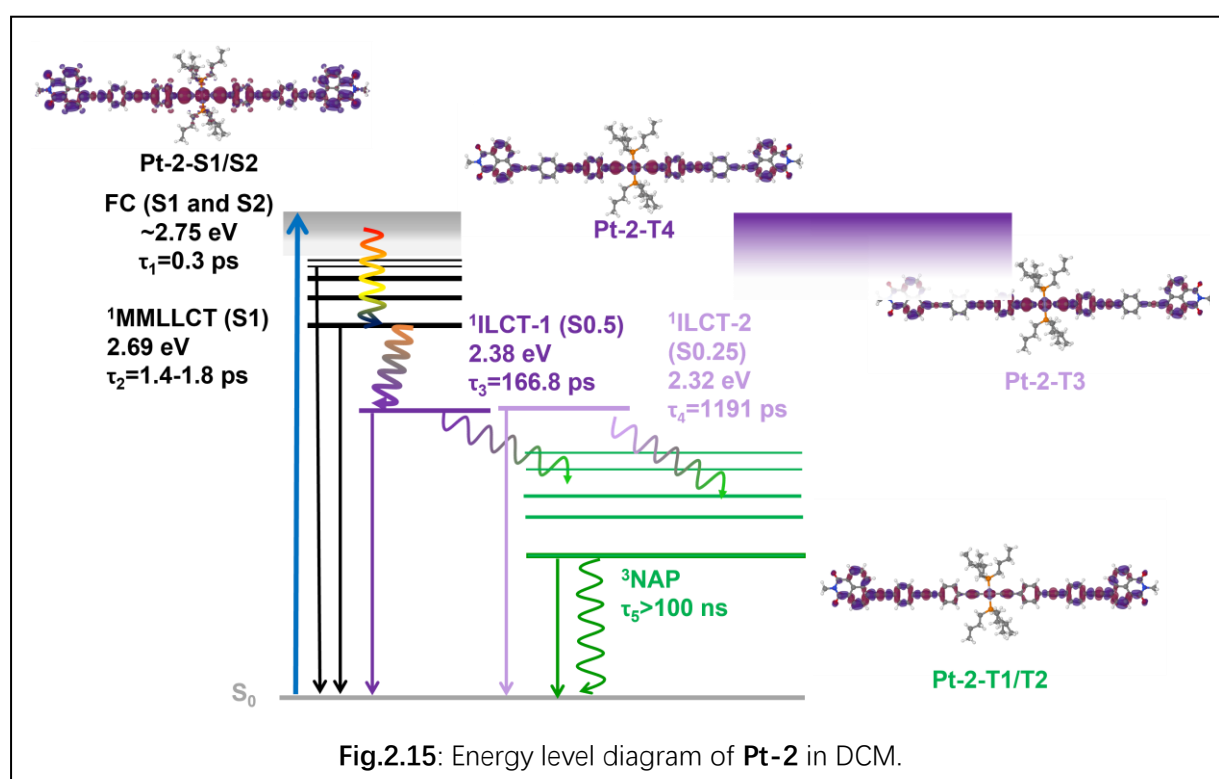


#### 2.3.4.3 Transient Absorption and energy level diagram of Pt-2

In the TA spectra of **Pt-2** in DCM pumped by 400 nm (shown in **Fig.2.12(e)**), the first spectrum that grows in shows negative signal at around 480 nm (there are no ground state absorbencies at 480 nm). This band, which is also observed by FLUPs (shown in **Fig.2.11(e)**), is attributed to the stimulated emission caused by the  $^1\text{MMLLCT}$  state of **Pt-2**. With the decay of the stimulated emission signal, a broad peak at 480 nm grows in which corresponds to  $\text{NAP}^-$ . This feature fits well with the idea suggested from TRIR analysis that another-CT state is formed. The peak at 480 nm decays and leaves an absorption band that looks similar to the  $^3\text{NAP}$  state observed in **Pt-0**, but there is a small peak at around 570 nm which indicates this  $^3\text{NAP}$  state still has a tiny amount of  $\text{NAP}^-$  character: this agrees well with the long-lived component extracted from LF-TRIR of **Pt-2** in DCM shown in **Fig.2.10** and **Fig.2.S6** of supporting information, which shows a tiny peak at  $1621.6\text{ cm}^{-1}$  which corresponds to  $\text{NAP}^-$  (which is more obvious after normalisation as shown in **Fig.2.S6** in SI). The last state populated in **Pt-2** still has a tiny amount of negative charge on the  $\text{NAP}^-$ . This tiny amount of the  $\text{NAP}^-$  anion character could be attributed to a different, relatively long-lived CT state with a lifetime of 1191 ps observed by FLUPs, and supported by the LF-TRIR results: this CT state has a much larger distance between the  $\text{NAP}^-$  anion and the “hole”.

Global analysis of TA of **Pt-2** in DCM (shown in **Fig.2.12(f)**) is based on a sequential model with four components, which gives lifetimes of 0.4 ps, 1.5 ps, 166.8 ps and a long-lived state. The first component is attributed to the decay of Franck-Condon (FC) state and the 1.5 ps state is attributed to the  $^1\text{MMLLCT}$  state, the 166.8 ps state is the  $^1\text{ILCT-1}$  state, the long-lived state is attributed to the  $^3\text{NAP}$  state, which agrees well with the results from HF-TRIR and LF-TRIR. There is another tiny amount populated in a different  $^1\text{ILCT-2}$  state based on TA, LF-TRIR results, it is the 1191 ps component extracted from FLUPs spectra because FLUPs is far more sensitive to the emissive states compared with TA and TRIR.

Lifetime of **Pt-2** in DCM extracted by different ultrafast spectroscopy methods by global analysis are given in **Table 1 (Bottom)**. From this table, the energy level diagram of **Pt-2** in DCM is given in **Fig.2.15** and the excited state evolution could be described as after pumped by 400 nm laser pulse, the FC state is populated, then it decays into  $^1\text{MMLLCT}$  state within 0.3 ps. The  $^1\text{MMLLCT}$  state then populates  $^3\text{ILCT-1}$  state and  $^1\text{ILCT-2}$  within 1.8 ps, the  $^1\text{ILCT-1}$  mostly decays into the ground state with 166.8 ps lifetime, and the  $^1\text{ILCT-2}$  state also mostly decays into the ground state with 1191 ps lifetime, with a small 25% yield population of  $^3\text{NAP}$  state.



### 2.3.5 Density Functional Theory (DFT)

DFT calculations have been performed for **Pt-0**, **Pt-1** and **Pt-2**, the  $-\text{C}_8\text{H}_{17}$  group was replaced by  $-\text{CH}_3$  for computational efficiency and the DFT calculations were done by using the SMP version of the Gaussian09 package, revision D.01 and all of the calculations are performed by Dr. Heather Carson, further details of the DFT calculation setup could be found in Dr. Heather Carson's PhD graduation thesis, 2022.<sup>10</sup>

**Fig.2.S8** in supporting information shows a good match between the DFT modelling results and experimental FTIR spectra of **Pt-0**, **Pt-1** and **Pt-2** which confirms the peak at around  $1580\text{ cm}^{-1}$  is attributed to NAP ring stretching and the  $1653\text{ cm}^{-1}$  and  $1692\text{ cm}^{-1}$  are asymmetric and symmetric carbonyl vibrational mode. The peaks in the range  $2000\text{ cm}^{-1}$  to  $2250\text{ cm}^{-1}$  are attributed to different vibrational mode caused by the alkyne fragment.

**Fig.2.16** shows the DFT modelling of the last populated excited state ( $^3\text{NAP}$ ) TRIR spectra which fits well with the experimental result in **Pt-0** (**Fig.2.16a**), but models only part of the features in **Pt-1** (**Fig.2.16b**) and **Pt-2** (**Fig.2.16c**). There are several experimentally observed but not obtained computationally bands in the spectra of **Pt-1** and **Pt-2** may be caused by the change of complex geometry in the excited state. A comparison of the DFT modelling result of  $^3\text{NAP}$  state for **Pt-1** with different conformations is shown in **Fig.2.S9**, where with the change of conformation of **Pt-1**, the band at  $2050\text{ cm}^{-1}$  can down-shift to  $2000\text{ cm}^{-1}$ .

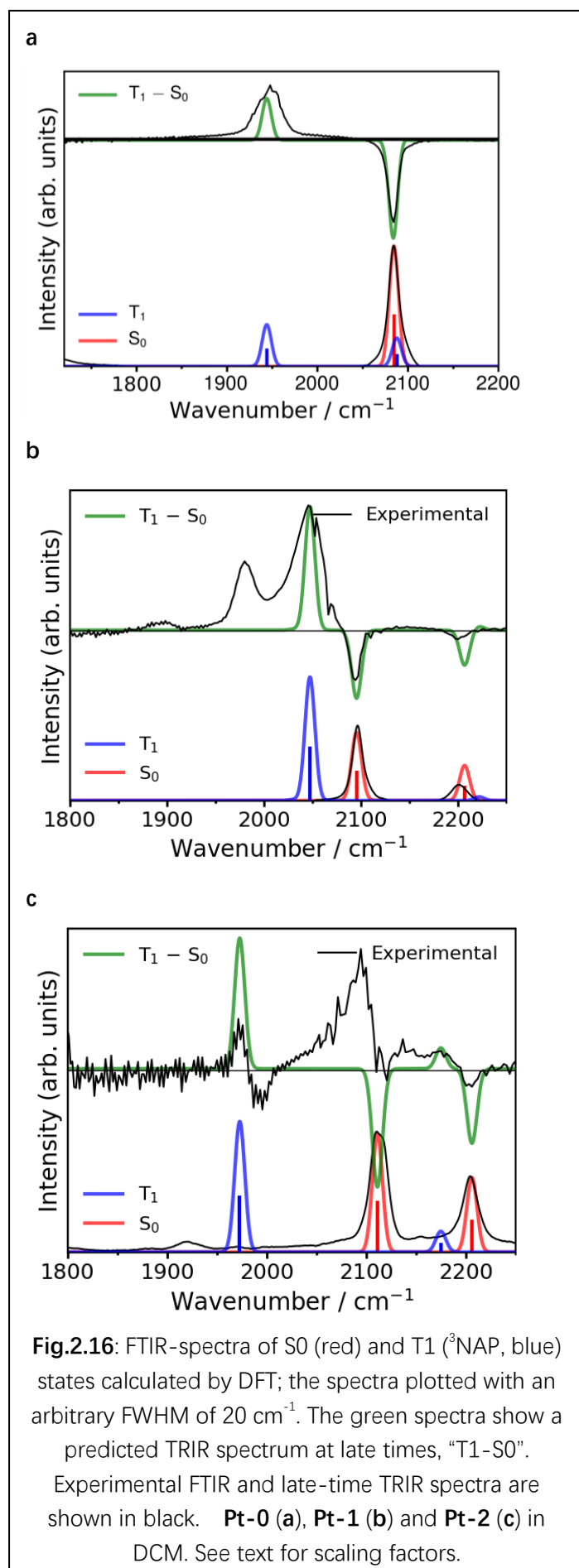


**Fig.2.S10** shows the DFT modelling results of UV-Vis absorption spectra of **Pt-0** (**Fig.2.S10a**), **Pt-1** (**Fig.2.S10b**) and **Pt-2** (**Fig.2.S10c**) that match well the experimental spectra. The electron density map given for **Pt-0** (**Fig.2.S11**), **Pt-1** (**Fig.2.S12**) and **Pt-2** (**Fig.2.S13**), supports the assignments of the electronic states, in all cases largely delocalised.

**Fig.2.S11** shows that excitation of **Pt-0** in DCM by a 400-nm laser pulse populates singlet excited states S3 and S4, in which the electron density shifts from the Pt centre and alkyne group to one of the NAP fragments. These states cannot be treated as pure MLCT states (which are states S7 and S8, with much higher energy). The initially populated Franck-Condon state should be treated as a mixed metal-ligand-to-ligand charge transfer (MMLLCT) state. **Fig.2.S12** and **Fig.2.S13** demonstrate the same MMLLCT assignment for the singlet states populated with a 400-nm pulse.

## 2.4 Conclusion

This research contributes to the understanding of the role of  $-C \equiv C - Ph -$  part plays in the Pt complexes includes *Pt - Bridge - Acceptor* structure. In this research, a series of A-B-A Pt complex where here the A is naphthalene-mono-imide (NAP) and the bridge length increase from **Pt-0**:  $-C \equiv C -$ , to **Pt-1**:  $-C \equiv C - Ph - C \equiv C -$  and **Pt-2**:  $-C \equiv C - Ph - C \equiv C - Ph - C \equiv C -$ . The results show that in all 3 complexes, the initially populated state is a CT state with bridge/Pt-to-NAP, or MMLLCT, character. The degree of delocalisation increases from **Pt-0** to **Pt-2**, whilst the contribution of Pt orbitals decreases. The resulting decay pathways of the initially populated <sup>1</sup>MMLLCT state depends on the length of the bridge. In the complex with the shortest bridge length, **Pt-0**, this <sup>1</sup>MMLLCT state decays into an MLCT and <sup>3</sup>NAP states. In **Pt-1**, the <sup>1</sup>MMLLCT state decays into a delocalised MLCT/Inter-ligand CT state which means the electron is donated from the *Pt - C  $\equiv$  C - Ph - C  $\equiv$  C -* bridge first, then the hole is transferred to the Pt center. In **Pt-1**, an isomerisation process

from Pt-alkyne-phenyl structure to cumulated CCC structure is also observed where the  $\nu(Pt = C = C = Ar)$  mode could be used as characteristic of MLCT/Inter-ligand CT state formation in TRIR. In **Pt-2** which has the longest bridge, the  $^1MMLCT$  state decays primarily into two different  $^3ILCT$  states with positive charge hole at different distance to the  $NAP^-$  anion, bridge-to-NAP state instead, which in turn decay to the ground state, with a small percentage populating the  $^3NAP$  state.

It is noteworthy that the rate of ISC does not change systematically in this series. **Pt-0** displays an ISC time-constant of up to 17 ps, very similar to a NAP-CC-Pt-CC-Ph compound published previously.<sup>1,3</sup> **Pt-1** and **Pt-2** exhibit a much slower ISC, lifetime up to 37.3 ps for **Pt-1** and 166.8 ps and 1191 ps for **Pt-2**, this could be explained as with the increase of the bridge length, the Pt center contributes much less to the ISC process. The 1191 ps is from a different singlet CT state with different nature which could give even slower ISC rate. However, as corresponding stimulated emission is not observed in TA, to further understand its ISC rate, further experiments such as transient electron spin resonance (trEPR) spectroscopy could be done but at the moment its time-resolution is not sufficient for this purpose as its time resolution can only low to 10 ns at 30-50 GHz (Q-band) and 50 ns at 8-12 GHz (X-band).<sup>18</sup>

With the increase of bridge length between Pt centre and NAP acceptor from **Pt-0**, **Pt-1** to **Pt-2**, back electron transfer or the formation of  $^3NAP$  state lifetime increases from 16.9 ps (**Pt-0**), to 56 ps (**Pt-1**) and 166.8 ps (**Pt-2**). However, this increase is not caused by the increase of distance between Pt centre and NAP acceptor but with the bridge length increase, the bridge itself starts to trap positive charge on the bridge so the positive charge 'hole' could be hold by the bridge.

## 2.5 Reference

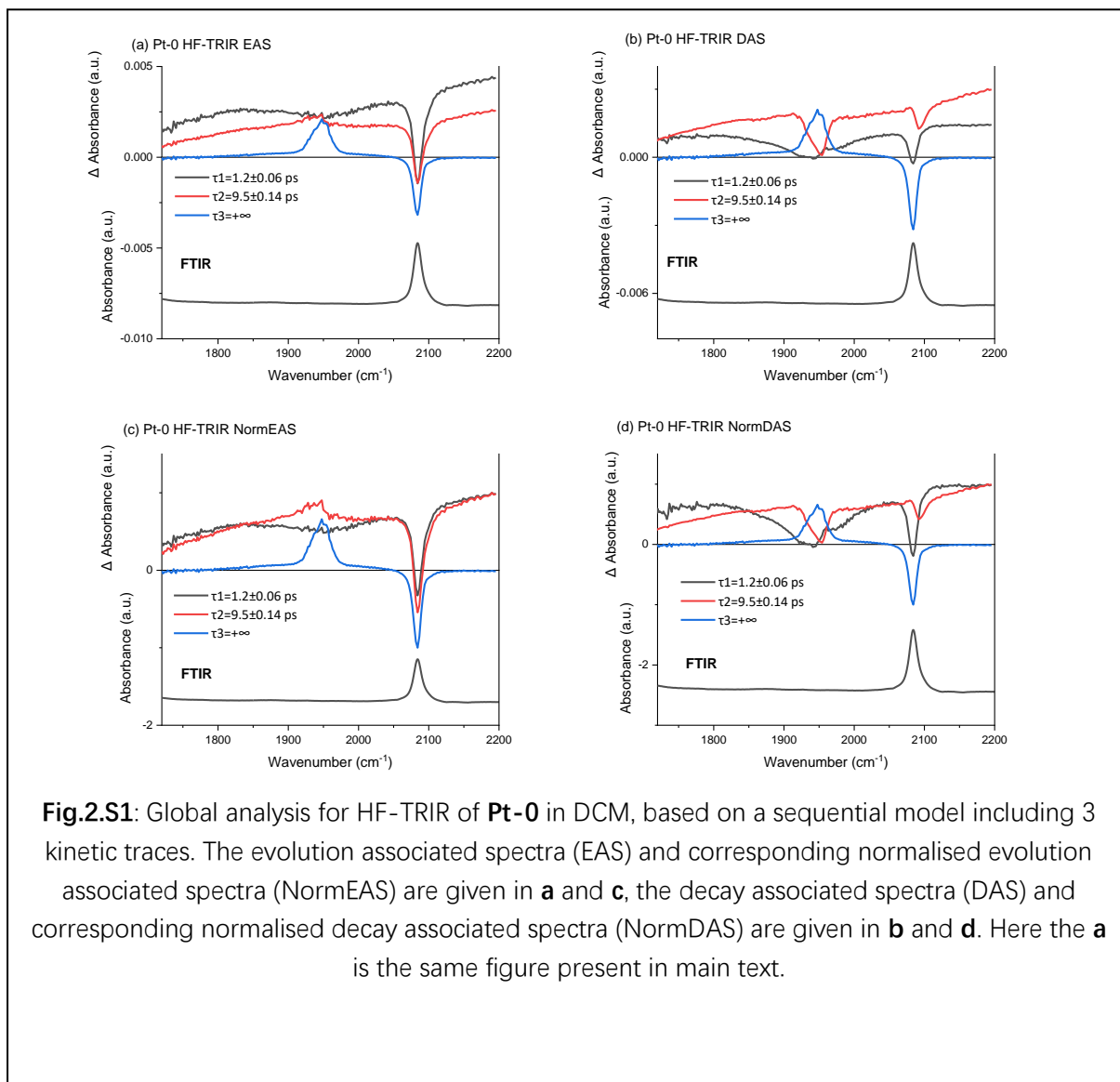
- 1 P. A. Scattergood, M. Delor, I. v. Sazanovich, O. v. Bouganov, S. A. Tikhomirov, A. S. Stasheuski, A. W. Parker, G. M. Greetham, M. Towrie, E. S. Davies, A. J. H. M. Meijer and J. A. Weinstein, *Dalton Transactions*, 2014, **43**, 17677–17693.
- 2 M. Delor, T. Keane, P. A. Scattergood, I. v. Sazanovich, G. M. Greetham, M. Towrie, A.

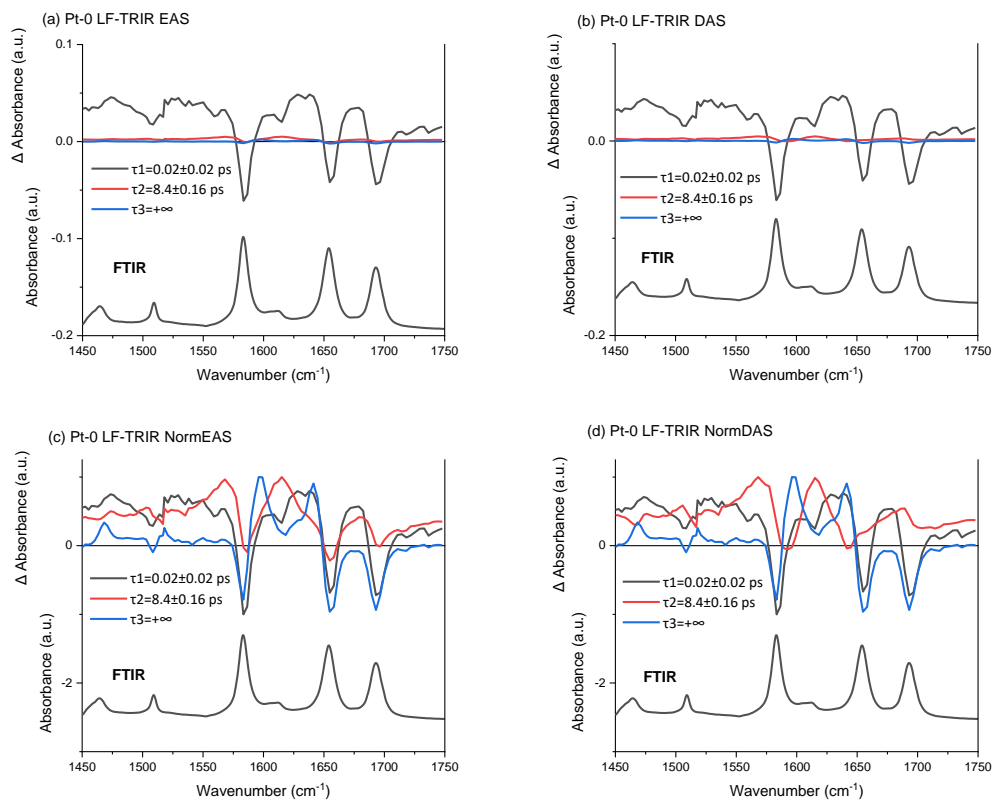
- J. H. M. Meijer and J. A. Weinstein, *Nat Chem*, 2015, **7**, 689–695.
- 3 G. A. Farrow, M. Quick, S. A. Kovalenko, G. Wu, A. Sadler, D. Chekulaev, A. A. P. Chauvet, J. A. Weinstein and N. P. Ernsting, *Physical Chemistry Chemical Physics*, 2021, **23**, 21652–21663.
- 4 J. Wiberg, L. Guo, K. Pettersson, D. Nilsson, T. Ljungdahl, J. Mårtensson and B. Albinsson, *J Am Chem Soc*, 2007, **129**, 155–163.
- 5 K. Pettersson, J. Wiberg, T. Ljungdahl, J. Mårtensson and B. Albinsson, *Journal of Physical Chemistry A*, 2006, **110**, 319–326.
- 6 M. R. Pollard and G. M. Greetham, 2012.
- 7 I. H. M. van Stokkum, D. S. Larsen and R. van Grondelle, *Biochimica et Biophysica Acta (BBA)-Bioenergetics*, 2004, **1657**, 82–104.
- 8 A. A. Rachford, S. Goeb, R. Ziessel and F. N. Castellano, *Inorg Chem*, 2008, **47**, 4348–4355.
- 9 I. v Sazanovich, M. A. H. Alamiry, A. J. H. M. Meijer, M. Towrie, E. S. Davies, R. D. Bennett and J. A. Weinstein, *Pure and Applied Chemistry*, 2013, **85**, 1331–1348.
- 10 Heather Carson, PhD Graduation Thesis, the University of Sheffield, 2022.
- 11 J. D. Cyran, J. M. Nite and A. T. Krummel, *J Phys Chem B*, 2015, **119**, 8917–8925.
- 12 T. M. Cooper, J.-P. Blaudeau, B. C. Hall, J. E. Rogers, D. G. McLean, Y. Liu and J. P. Toscano, *Chem Phys Lett*, 2004, **400**, 239–244.
- 13 F. Kessler, B. Weibert and H. Fischer, *Organometallics*, 2010, **29**, 5154–5161.
- 14 F. Kessler, E. Wuttke, D. Lehr, Y. Wang, B. Weibert and H. Fischer, *Inorganica Chim Acta*, 2011, **374**, 278–287.
- 15 B. Dereka, D. Svehkarev, A. Rosspeintner, M. Tromayer, R. Liska, A. M. Mohs and E. Vauthey, *J Am Chem Soc*, 2017, **139**, 16885–16893.
- 16 X.-X. Zhang, C. Würth, L. Zhao, U. Resch-Genger, N. P. Ernsting and M. Sajadi, *Review of Scientific Instruments*, 2011, **82**, 063108.
- 17 M. Gerecke, G. Bierhance, M. Gutmann, N. P. Ernsting and A. Rosspeintner, *Review of Scientific Instruments*, 2016, **87**, 053115.
- 18 M. D. E. Forbes, L. E. Jarocho, S. Sim and V. F. Tarasov, in *Advances in physical organic chemistry*, Elsevier, 2013, vol. 47, pp. 1–83.

## 2.SI. Supplementary Information for Chapter 2

### SI1. Global Analysis Result of Pt-0

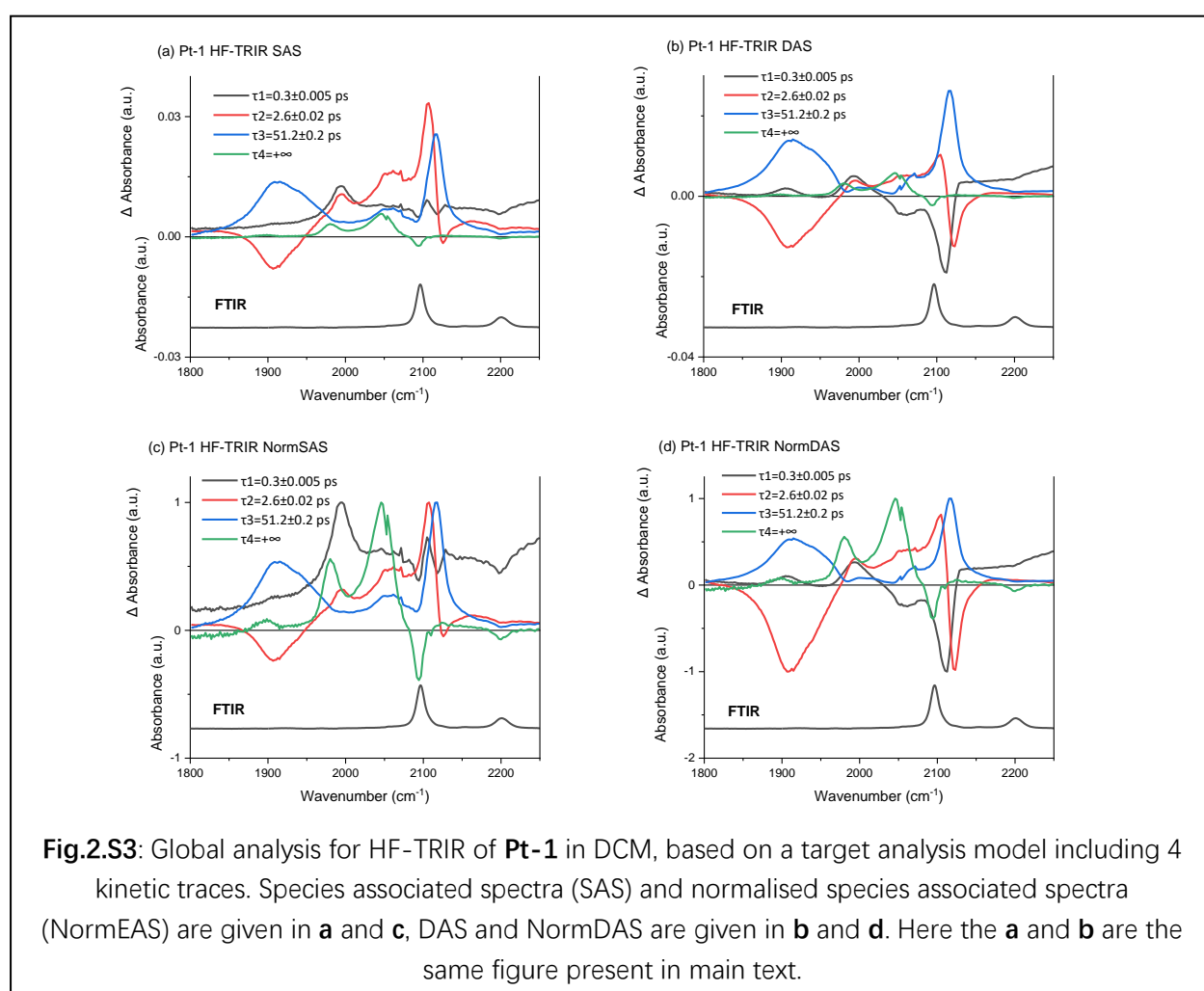


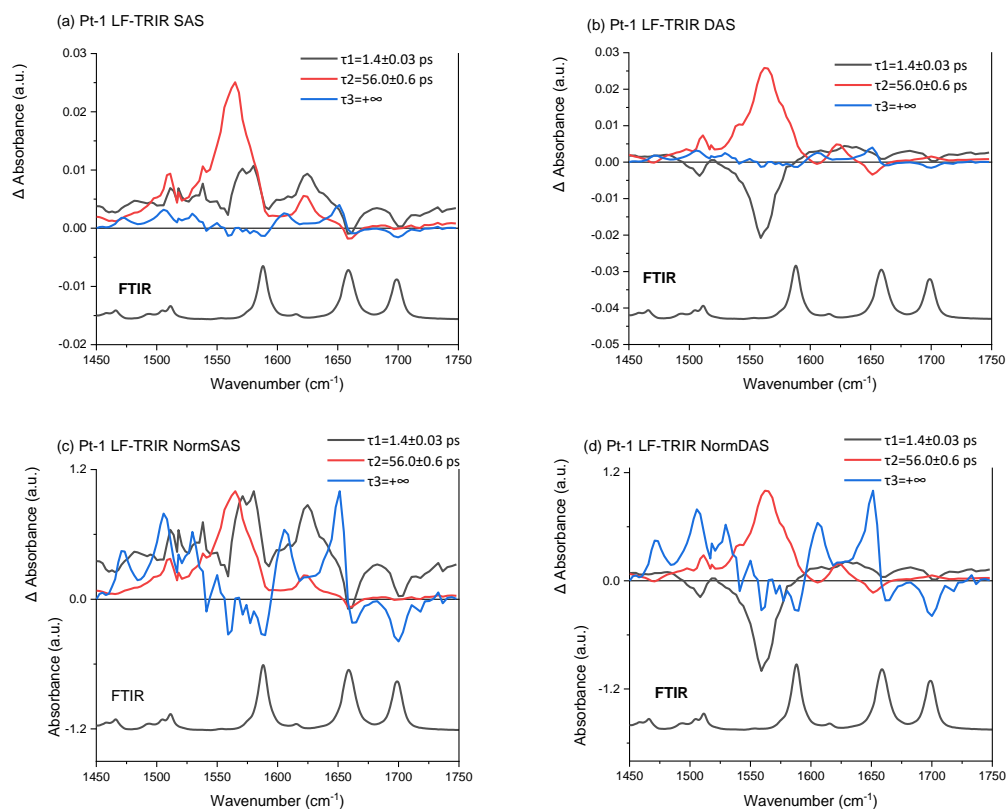




**Fig2.S2:** Global analysis for LF-TRIR of **Pt-0** in DCM, based on a sequential model including 3 kinetic traces. EAS and NormEAS are given in **a** and **c**, DAS and NormDAS are given in **b** and **d**. Here the **a** is the same figure present in main text.

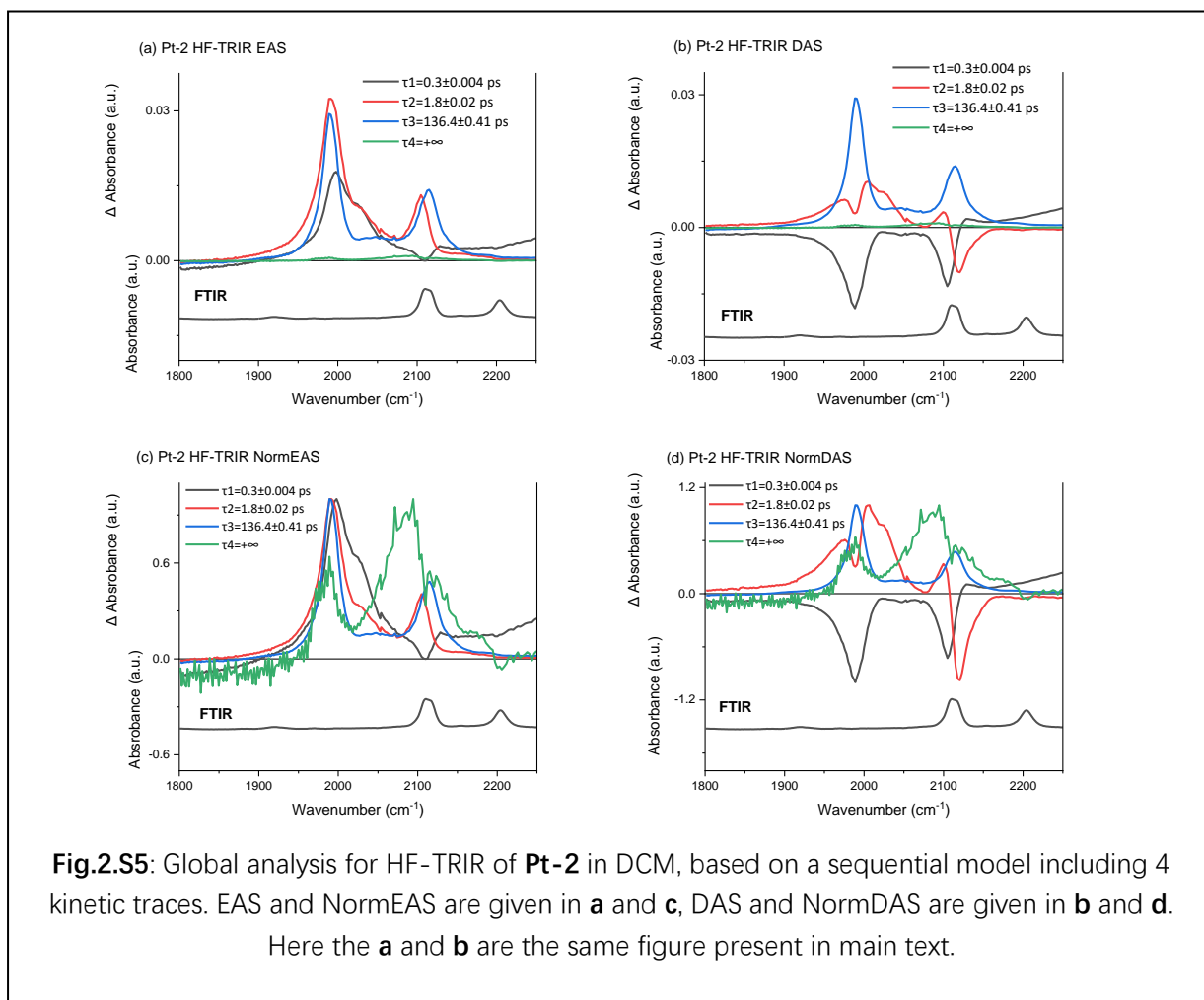
## S12. Global Analysis Result of Pt-1

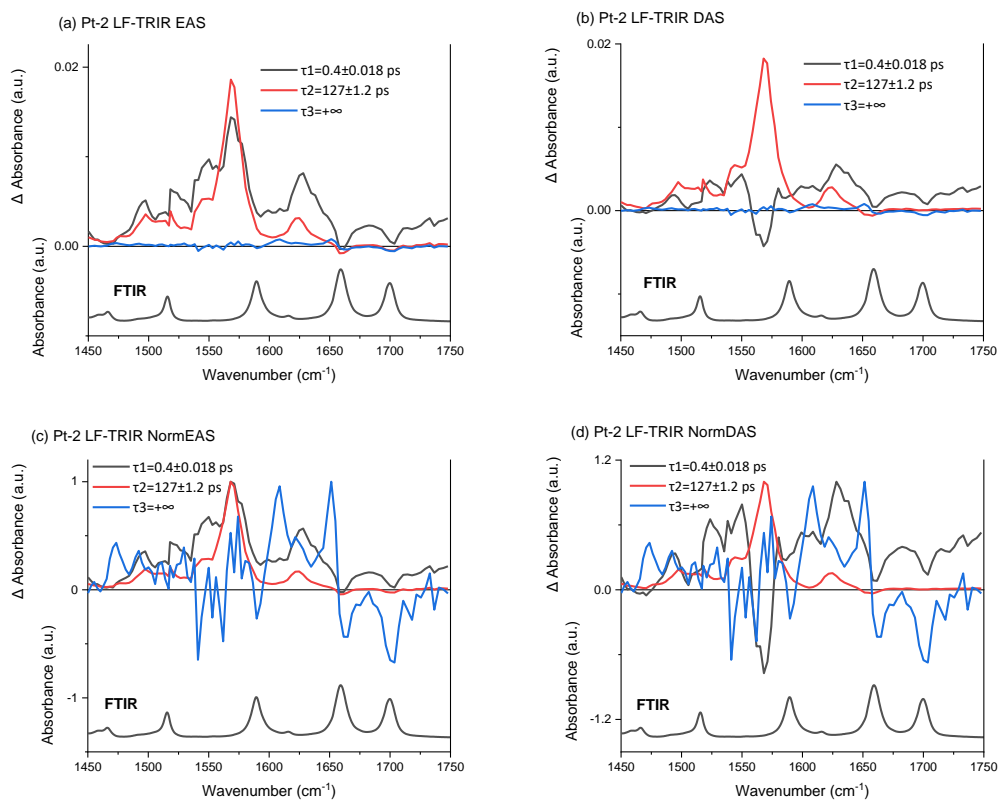




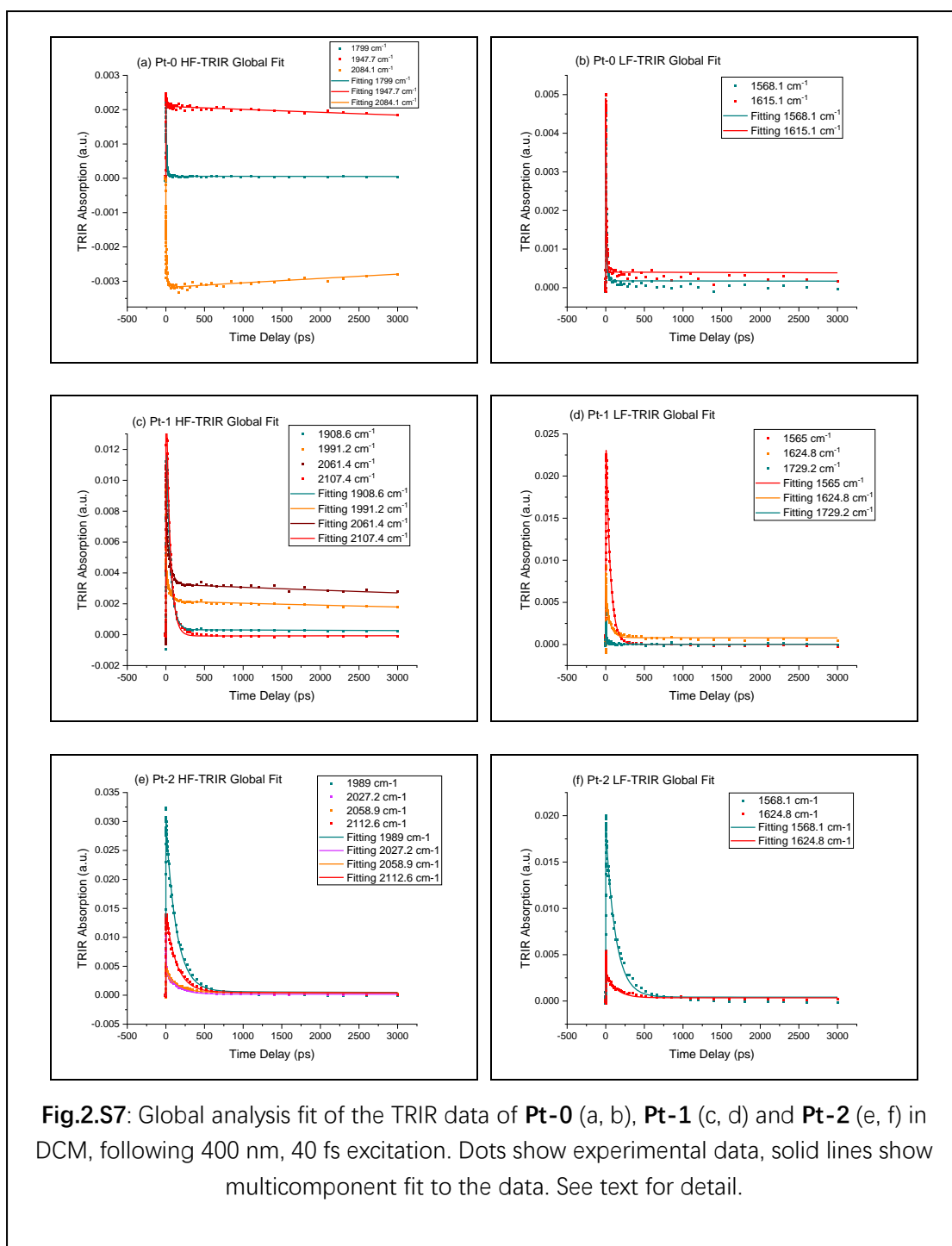
**Fig.2.S4:** Global analysis for LF-TRIR of **Pt-1** in DCM, based on a target analysis model including 3 kinetic traces. Species associated spectra (SAS) and normalised species associated spectra (NormEAS) are given in **a** and **c**, DAS and NormDAS are given in **b** and **d**. Here the **a** and **b** are the same figure present in main text.

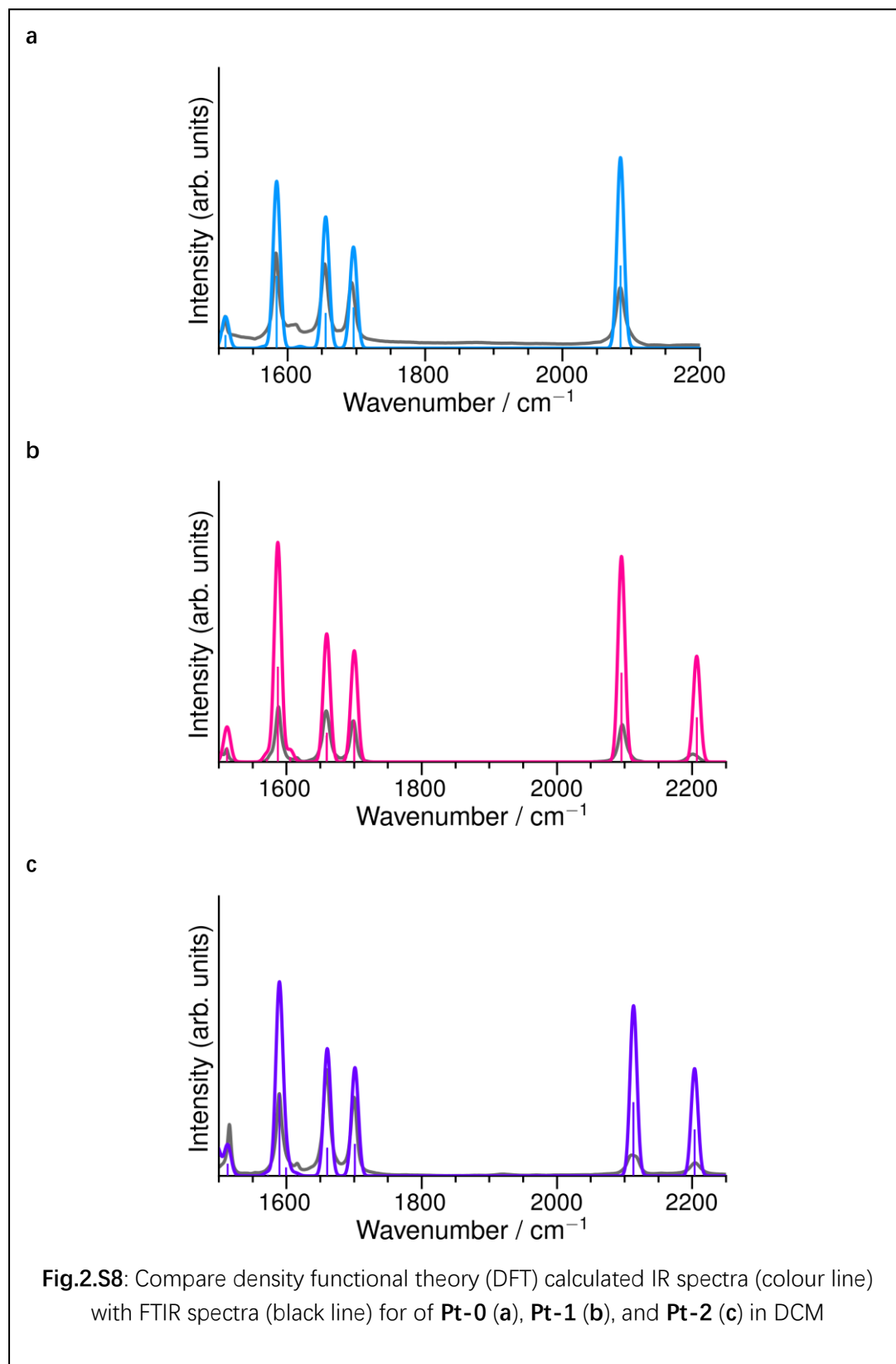
### S13. Global Analysis Result of Pt-2



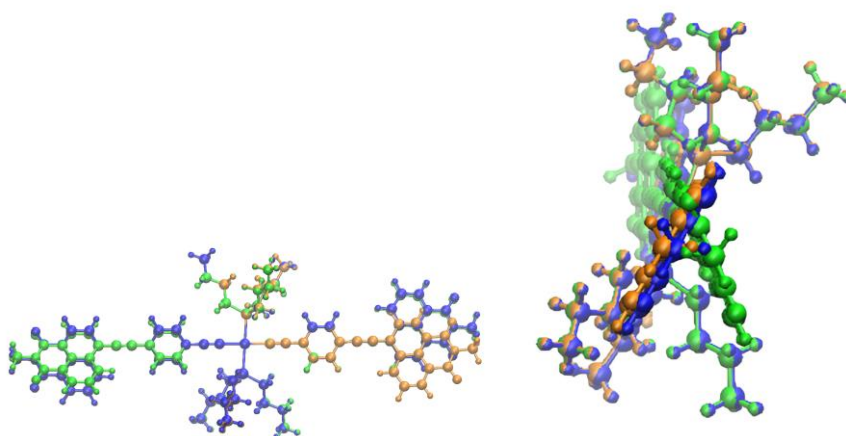
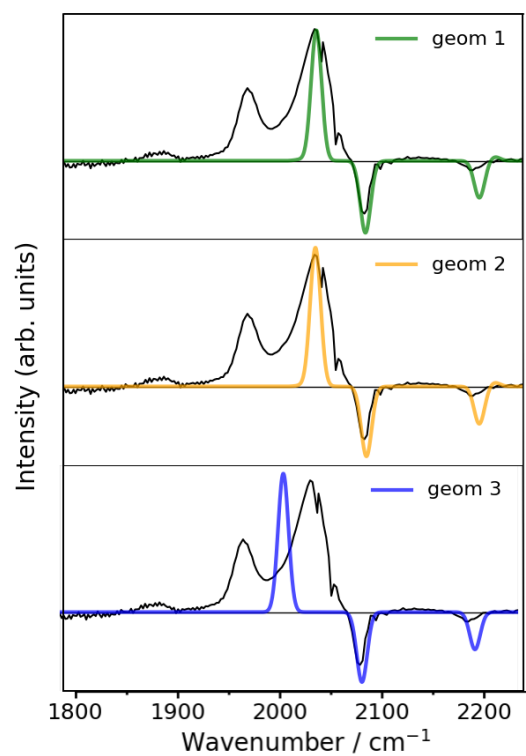


**Fig.2.S6:** Global analysis for LF-TRIR of **Pt-2** in DCM, based on a sequential model including 3 kinetic traces. EAS and NormEAS are given in **a** and **c**, DAS and NormDAS are given in **b** and **d**. Here the **a** and **b** are the same figure present in main text.

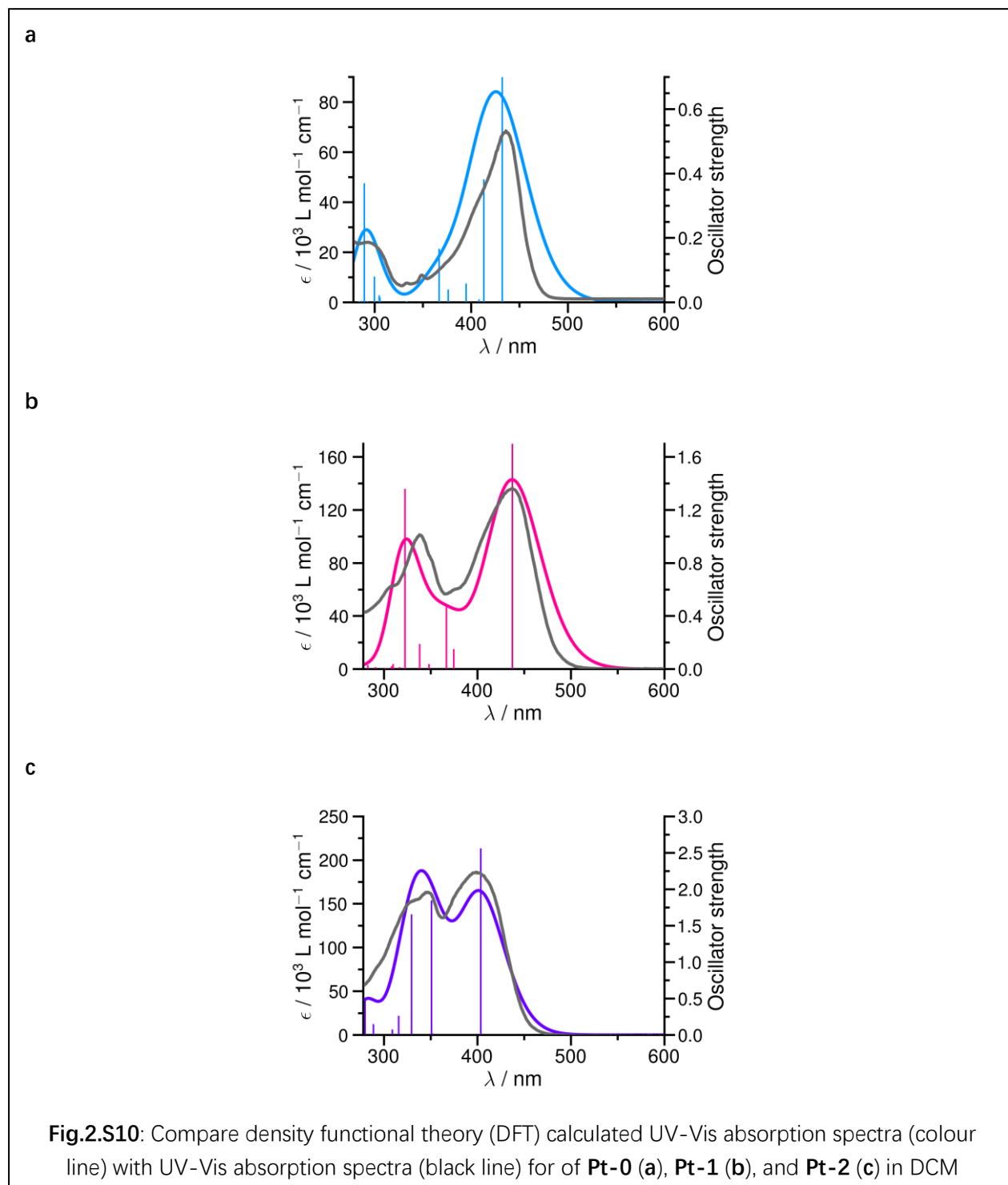








**Fig.2.S9:** Compare the DFT modelling of **Pt-1** with different conformation in  $^3\text{NAP}$  state with experimental TRIR spectra, where the spectra and corresponding geometry is shown with different colour, **geom.1** (green), **geom.2** (yellow) and **geom.3** (blue).



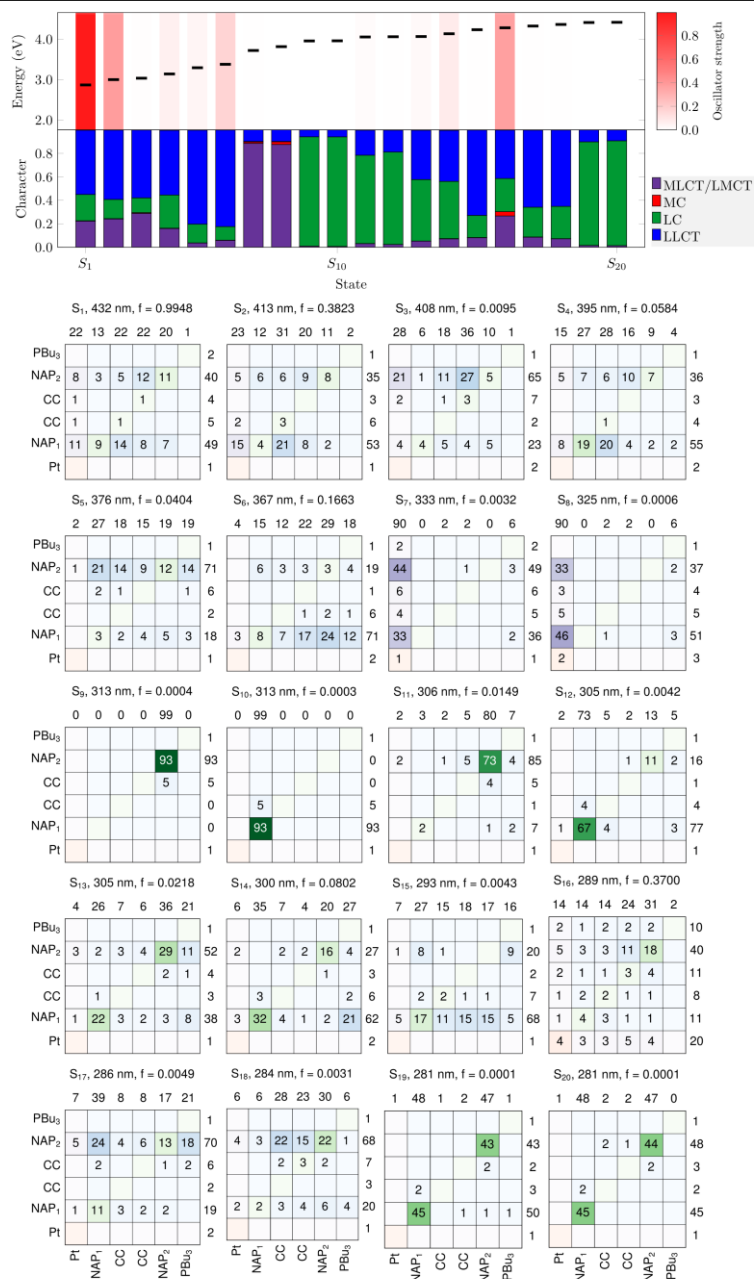


**Fig.2.S11: Pt-0.** (a) Fragment decomposition plot for **Pt-0**. The top half of the diagram shows the excitation energies of the 20 lowest singlet excited states along with their oscillator strengths. The bottom half of the diagram shows the character of excited states which has been automatically assigned using charge transfer numbers. Colours show character of the states: purple = MLCT/LMCT, red = MC, green = LC, blue = LLCT.

(b) Electron-hole correlation grids for **Pt-0**. The fragment labels are shown along the bottom and left-hand side of the grid. The horizontal axis shows the origin of the electron density, i.e the electron hole, whilst the vertical axis shows the final location of the electron density (a transition is from “x to y axis”). The main diagonal of each grid represents localised character, whilst the off-diagonal represents a CT character.



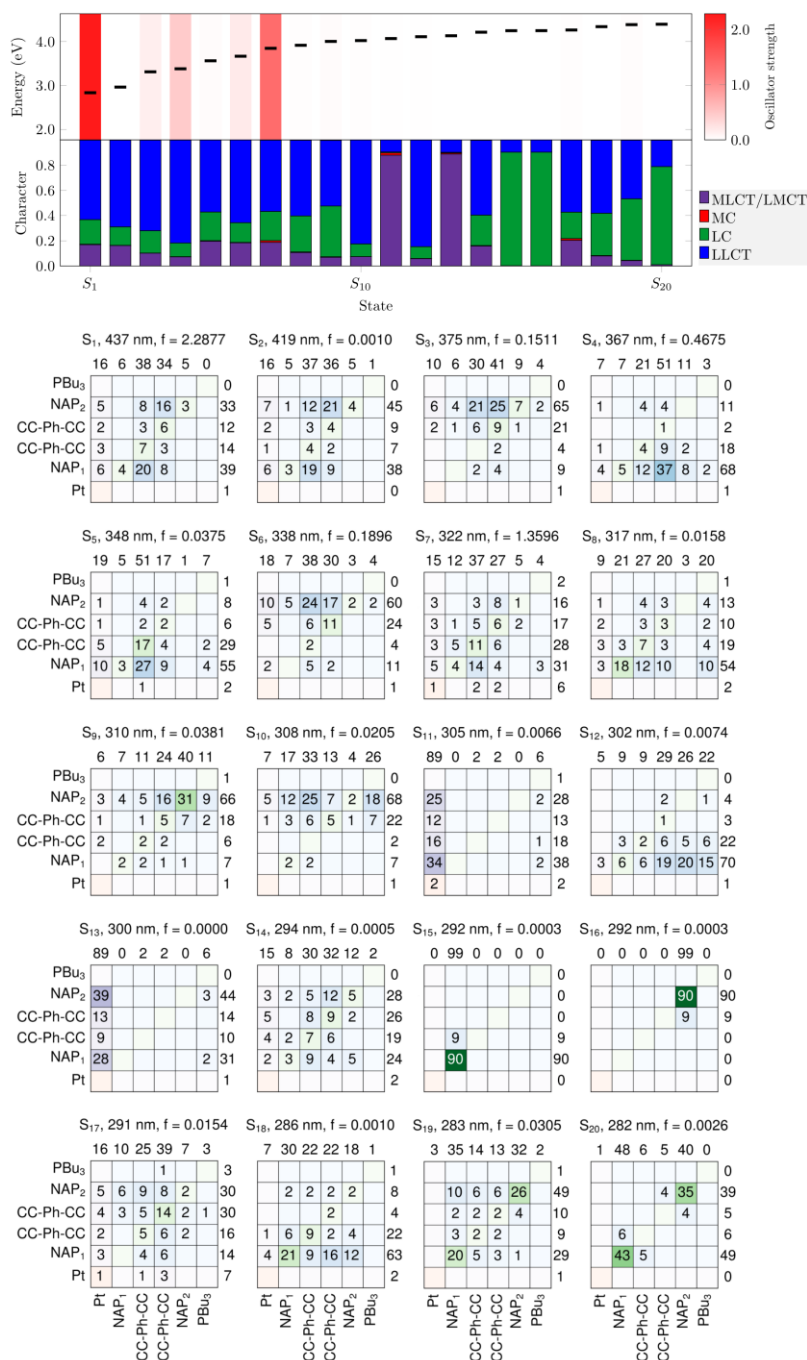


**Fig.2.S12. Pt-1.** (a) Fragment decomposition plot for **Pt-1**. The top half of the diagram shows the excitation energies of the 20 lowest singlet excited states along with their oscillator strengths. The bottom half of the diagram shows the character of excited states which has been automatically assigned using charge transfer numbers. Colours show character of the states: purple = MLCT/LMCT, red = MC, green = LC, blue = LLCT. (b) Electron-hole correlation grids for **Pt-1**. The fragment labels are shown along the bottom and left-hand side of the grid. The horizontal axis shows the origin of the electron density, i.e. the electron hole, whilst the vertical axis shows the final location of the electron density (a transition is from "x to y axis"). The main diagonal of each grid represents localised character, whilst the off-diagonal represents a CT character.

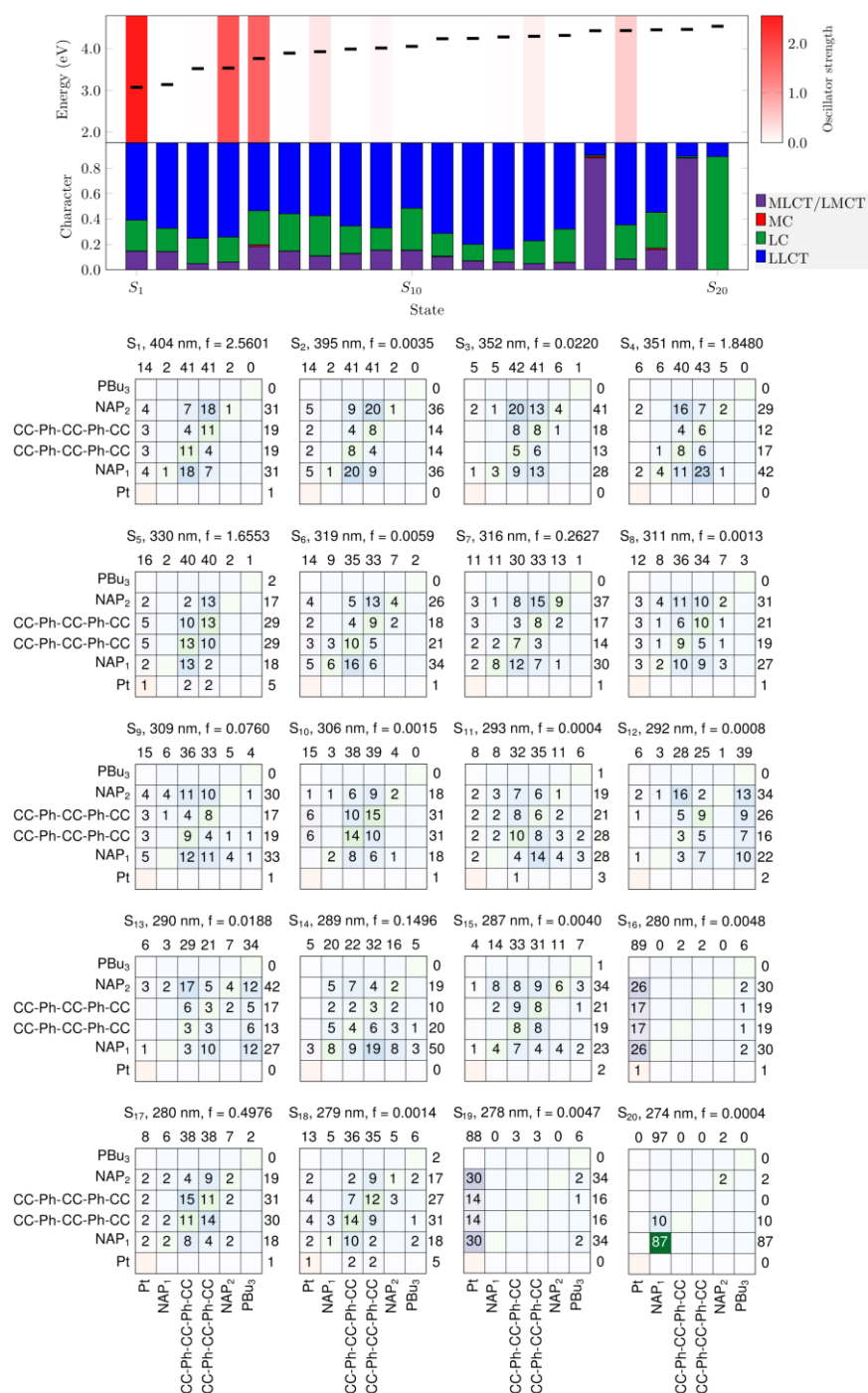


**Fig.2.S13. Pt-2.** (a) Fragment decomposition plot for **Pt-2**. The top half of the diagram shows the excitation energies of the 20 lowest singlet excited states and their oscillator strengths. The bottom half of the diagram shows the character of excited states which has been automatically assigned using charge transfer numbers. Colours show character of the states: purple = MLCT/LMCT, red = MC, green = LC, blue = LLCT. (b) Electron-hole correlation grids for **Pt-2**. The fragment labels are shown along the bottom and left-hand side of the grid. The horizontal axis shows the origin of the electron density, i.e the electron hole, whilst the vertical axis shows the final location of the electron density (a transition is from “x to y axis”). The main diagonal of each grid represents localised character, whilst the off-diagonal represents a CT character.

## 3. Chapter 3-Solvent Effect on Acceptor-Bridge-Acceptor Complexes

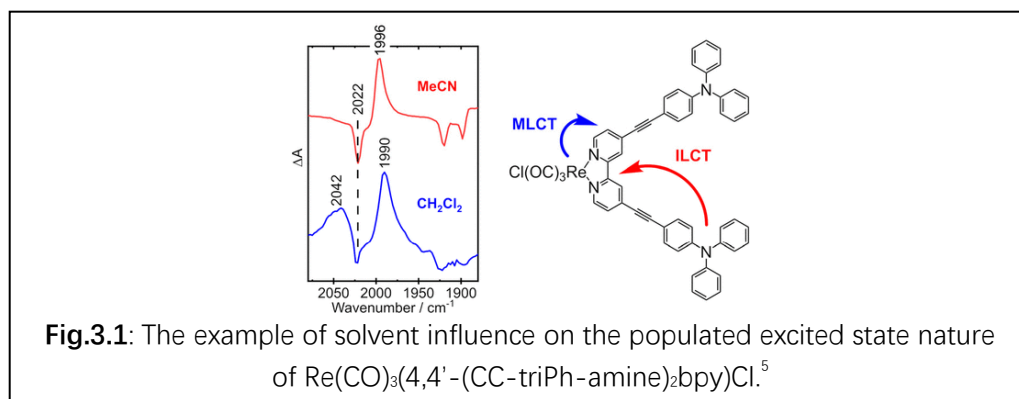
### 3.1. Introduction

In **Chapter 2**, energy levels and excited states dynamics of **Pt-0**, **Pt-1** and **Pt-2** in DCM has been investigated by applying transient absorption spectroscopy (TA), transient infrared absorption spectroscopy (TRIR) and fluorescence up-conversion spectroscopy (FLUPS). The excited state energy can also be influenced by the solvent's polarity and this phenomenon is known as solvatochromic effect which depends on the nature of both ground and excited states.

Solvatochromism is classified into 'negative solvatochromism' and 'positive solvatochromism'. For negative solvatochromism, with the increase of solvent dipole moment, the UV-Vis absorption or emission peak shifts to higher energies ("blue shift") and for the positive solvatochromism, with the increase of solvent dipole moment the UV-Vis absorption spectra and emission spectra will shift to lower energies ("red shift"). Or in other words, if the ground state is stabilized more by the solvent surrounding it than the excited state with the increasing solvent dipole moment, then it exhibits negative solvatochromism. And if the ground state is stabilized less by the solvent surrounding the molecule, then it exhibits positive solvatochromism. Normally, when the excited state dipole moment is larger than ground state ( $\mu_e > \mu_g$ ), the molecule shows positive solvatochromism in both absorption and emission spectra, and when the excited state dipole moment is smaller than ground state ( $\mu_e < \mu_g$ ), negative solvatochromism resulted.<sup>1</sup> However, as the solvatochromic effect in the absorption transition relates to the difference of  $\vec{\mu}_g$  vs.  $|\vec{\mu}_e - \vec{\mu}_g|$  the dipole moment vectors, it is in fact possible to observe a negative solvatochromism in

the absorption band, when  $\mu_e > \mu_g$ , but the direction of the dipole moment in the excited state is opposite to that of the ground state. Solvatochromic effect on Pt(II) complexes has been widely researched,<sup>2-4</sup> and a series of empirical parameters to reflect solvent polarity influence on Pt complexes were proposed. For example, Eisenberg et al established parameters for DMF (0.901), DCM (0.765), THF (0.494) and toluene (0.172).<sup>2</sup> These parameters were derived specifically for platinum(II) diimine complexes, and take into account not just the solvent polarity, but also potential specific interactions and/or coordination.

Also, as the ability of the solvent to stabilize excited states depends on the polarity of both the solvent and the excited state, one can also change the relative population of the excited states by changing the solvent: the energy of a charge transfer (CT) state would be much more affected by the solvent polarity than the energy of a  $\pi-\pi^*$  or  $n\pi^*$  states. For example, when the  $\text{Re}(\text{CO})_3(4,4'-(\text{CC-triPh-amine})_2\text{bpy})\text{Cl}$  shown in **Fig.3.1**: is dissolved in DCM, the photon induced excitation leads to the population of an MLCT state, but when MeCN is used, the lowest excited state populated changes into an ILCT state.<sup>5</sup>



### 3.2. Chapter Aims

1. Investigate solvent effect on the energy of excited states of Acceptor-Bridge-Acceptor complexes discussed in **Chapter 2**.
2. Investigate solvent effect on the rate of intersystem crossing process, and on the overall ultrafast dynamics of excited states of Acceptor-Bridge-Acceptor Pt(II)



complexes.

3. Construct the energy level diagrams of the Acceptor-Bridge-Acceptor Pt(II) complexes in different solvents used, and make conclusions about the nature of the manifold of close-lying excited states, and how they can potentially be switched around.

### 3.3. Results and Discussion

The structures together with simplified energy level diagrams based on spectra collected in dichloromethane (DCM) of the Acceptor-Bridge-Acceptor Pt complexes investigated are given in **Fig.3.3**, as a starting point for this investigation. Solvents chosen are varying in dipole moment from high to low: N,N-dimethylformamide (DMF), 3.82; tetrahydrofuran (THF), 1.75; dichloromethane (DCM), 1.60 and toluene, 0.36.<sup>6</sup> These number is based on solvatochromic property of charge transfer (CT) state of Pt(dbbpy)(tdt) (structure shown in **Fig.3.2**) and used as mimic of solvatochromic influence on other Pt complexes.

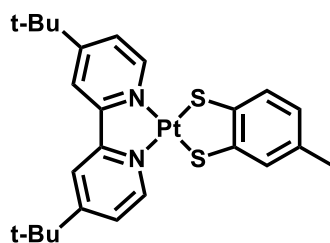


**Fig.3.2:** Structure of Pt(dbbpy)(tdt), here dppby is 4,4'-di-*tert*-butyl-2,2'-bipyridine and tdt is 3,4-toluenedithiolate.

The dielectric constants of the solvents are 40 (DMF), 9 (DCM), 6 (THF), and 2.2 (toluene). Another scale of solvents that will be considered is that by Eisenberg which is also shown below.<sup>2</sup>

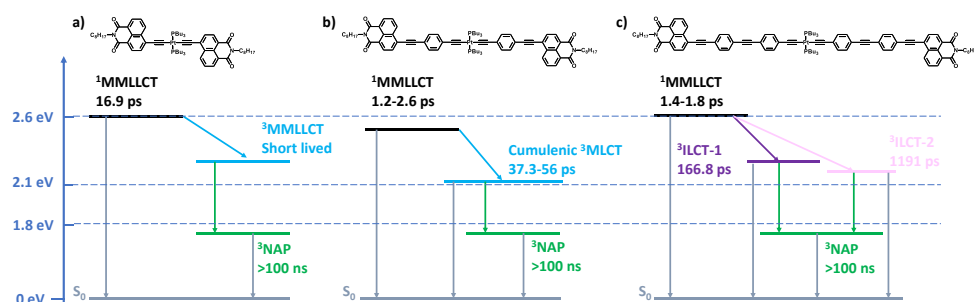


**Fig.3.3:** Simplified energy level diagrams of Acceptor-Bridge-Acceptor Pt complexes in DCM with bridge length increasing from **Pt-0** (left), **Pt-1** (middle) and **Pt-2** (right) based on energy level diagrams presented in **Chapter 1**. The compounds were provided by Prof. Kirk Schanze, the University of Texas at San Antonio.

	DMF	DCM	THF	Toluene
Dipole Moment	3.82	1.60	1.75	0.36
Solvatochromic parameter <sup>2</sup>	0.901	0.765	0.494	0.172
Dielectric Constant	40	9	6	2.2

**Table.3.1:** Dipole moment, solvatochromic parameter, and dielectric constants of the solvents used in this research.

### 3.3.1. UV-Vis Absorption Spectra, Steady-state emission Spectra and Time-Resolved fluorescence Spectra

#### 3.3.1.1. Pt-0

##### 3.3.1.1.1. UV-Vis Absorption Spectra and Emission Spectra

The absorption spectra and emission spectra of **Pt-0** in various solvents are shown in **Fig.3.4** and corresponding absorption and emission maxima are summarized in **Table.3.2**. Based on the results discussed in **Chapter 2**, when **Pt-0** in DCM is excited at 400 nm, the first populated state is a singlet mixed metal-ligand to ligand charge transfer (<sup>1</sup>MMLLCT) state.

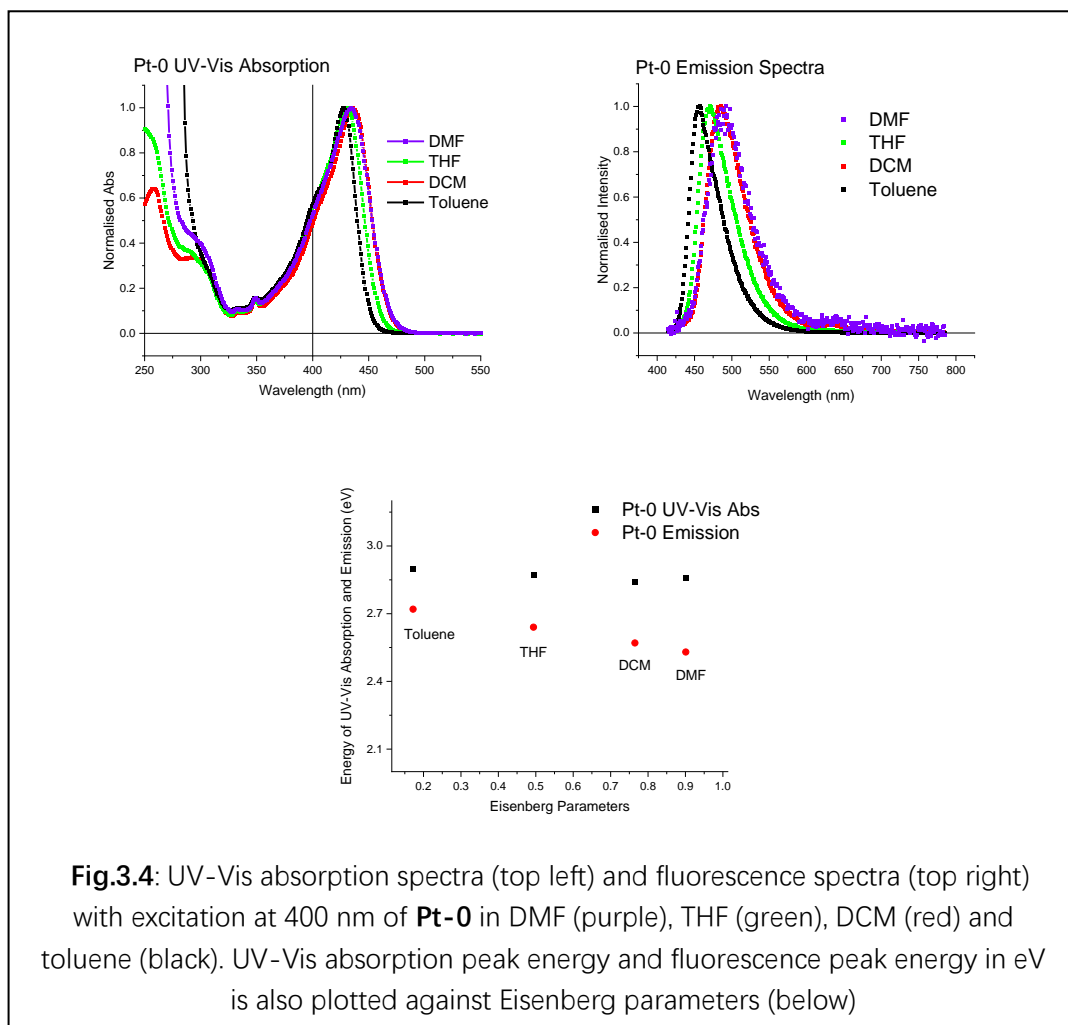


**Fig.3.4:** UV-Vis absorption spectra (top left) and fluorescence spectra (top right) with excitation at 400 nm of **Pt-0** in DMF (purple), THF (green), DCM (red) and toluene (black). UV-Vis absorption peak energy and fluorescence peak energy in eV is also plotted against Eisenberg parameters (below)

Solvent (Eisenberg Parameters) <sup>2</sup>	$\lambda_{abs}/nm$	$\lambda_{fl}/nm$	Stokes Shift/ $cm^{-1}$
DMF (0.901)	434	485	2675
DCM (0.765)	436	483	2232
THF (0.494)	431	469	1880
Toluene (0.172)	427	456	1489

**Table.3.2:** UV-Vis absorption and fluorescence maxima and Stokes Shift of **Pt-0**. Here  $\lambda_{abs}$  indicates UV-Vis absorption maxima and  $\lambda_{fl}$  is emission (fluorescence) maxima.

The lowest absorption maximum in the UV-Vis absorption spectrum and the emission maximum for **Pt-0** do not change considerably when DCM is replaced with DMF. Based on the shift of the fluorescence maximum with the change of solvent (summarised in **Table.3.2**), the energy of the <sup>1</sup>MMLCT state in **Pt-0** decreases by only 0.04 eV in DMF compared to DCM. This

indicates that in DMF, the  $^1\text{MMLLCT}$  state is only slightly more stabilised than in DCM, i.e. the stabilization caused by dipole moment difference between DMF and DCM is negligible. However, when THF which has similar dipole moment to DCM is used as a solvent, the fluorescence blue-shifts to 469 nm, an increase in energy of about 0.07 eV. This indicates that when **Pt-0** is dissolved in THF, the energy gap between ground state and  $^1\text{MMLLCT}$  state is increased, which may be caused by the oxygen atom in THF which can donate its electron lone pair to Pt center to stabilize the ground state **Pt-0** more than DCM, but  $^1\text{MMLLCT}$  being less stabilised (higher energy) by THF which has lesser polarity than DCM.

When **Pt-0** is dissolved in toluene, both UV-Vis absorption spectra and fluorescence spectra shift to higher energy compared with the solution in DCM. The fluorescence spectrum shifts to 456 nm, because the low dipole moment of toluene cannot stabilise  $^1\text{MMLLCT}$  excited state

The UV-Vis absorption maximum (black dots) and emission maximum (red dots) are also plotted against Eisenberg's parameters as shown in **Fig.3.4** (low panel). The UV-Vis absorption peak remains almost unchanged with the increase of polarity which indicates the initially populated FC state has a similar dipole moment to the ground state. But the emission signal of **Pt-0** demonstrates positive solvatochromism which indicates the fluorescent state's dipole moment is much larger than that of the ground state and so this emissive state could be attributed to an asymmetric charge transfer (CT) state. Here, the fluorescence energy reflects the energy of CT state, the more polar the state is, the state could more stabilised by more polar solvent. As the ground state of **Pt-0** is highly symmetric and its dipole moment could be assumed as 0 so would not be affected by solvent polarity. If the excited CT state is symmetric (partial CT to both acceptors), this CT state would be more

stabilised in nonpolar solvent and under this condition, both ground and excited CT state are destabilised in more polar solvent so the energy gap between CT state and ground state would remain unchanged. If the excited CT state is asymmetric (CT to only one acceptor), it would be more stabilised (lower in energy) in polar solvent but the symmetric ground state would be more destabilised (higher in energy), so with the increase of solvent dipole moment, the energy gap between ground state and excited state would decrease and give us a positive solvatochromism. In other words, the fluorescence energy is low in DMF (polar solvent) and high in toluene (nonpolar solvent) which is what observed in **Pt-0** – thus, it appears that the CT state is asymmetric, with preferential localisation of electron density on one of the two acceptors.

### *3.3.1.1.2. Transient Absorption (TA) and Fluorescence Up-Conversion Spectra (FLUPS) of Pt-0*

#### **DMF**

TA spectra of **Pt-0** in DMF are given in **Fig.3.5**. After excitation at 400 nm, a peak at 470 nm arises which is attributed to NAP<sup>-</sup> anion formed in MMLLCT state (based on previous research of **NAP-Pt** complexes reported by Weinstein et al.)<sup>7,8</sup> This result supports the idea that the first populated state remains a charge transfer (CT) state when the solvent is changed to DMF. Together with the peak at 470 nm, there is a bleach at 510 nm which is due to stimulated emission from a singlet state, supporting the assignment of the first detected state as an <sup>1</sup>MMLLCT state. Then the bleach together with the peak at 470 nm decay into a broadband absorption that covers from 468 to 700 nm, which persists until the 7 ns limit of the delay stage. Its shape is similar to the absorption of the <sup>3</sup>NAP state observed in DCM (as well as hexane and acetonitrile, see our work on previous NAP systems),<sup>7,8</sup> therefore

the long-lived state is assigned to the  $^3\text{NAP}$  excited state. This indicates that the lowest excited state in **Pt-0** in DMF is similar to that in DCM, and overall for **Pt-0**, the change in the solvent does not alter the order of the excited states.

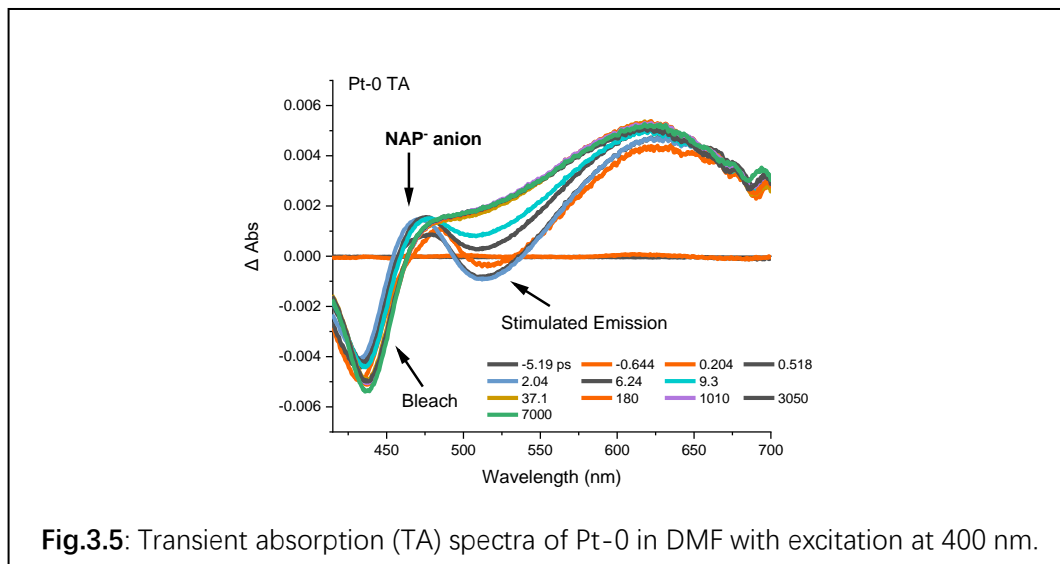
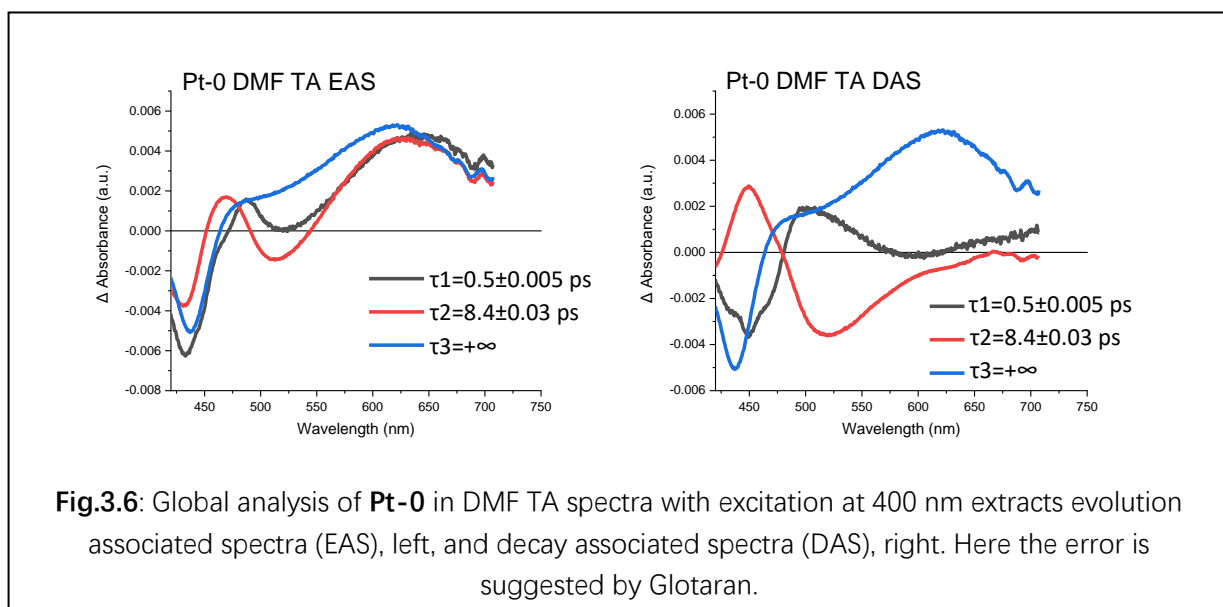
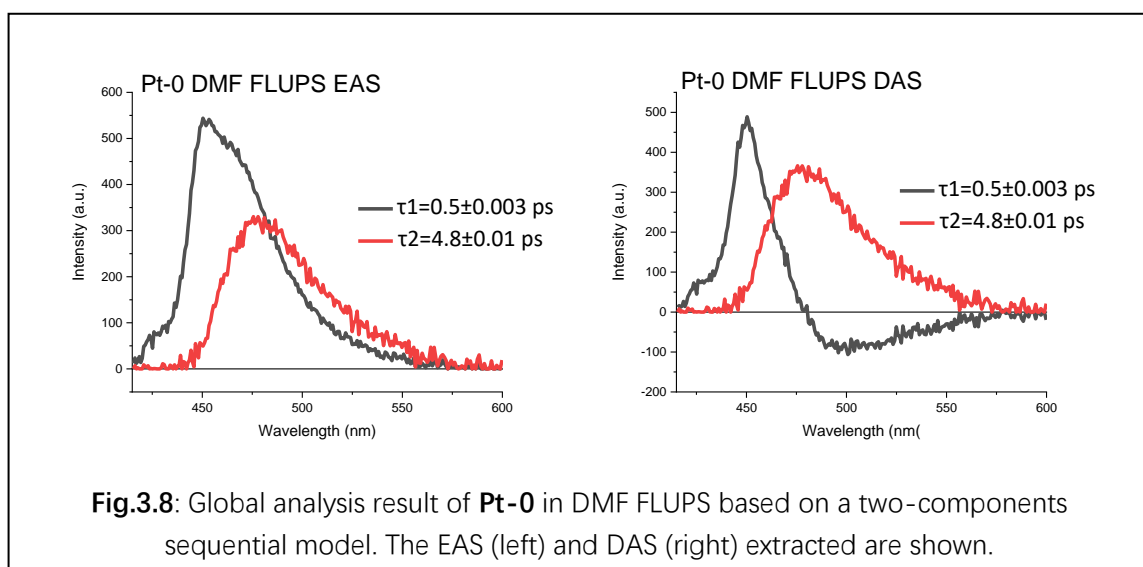
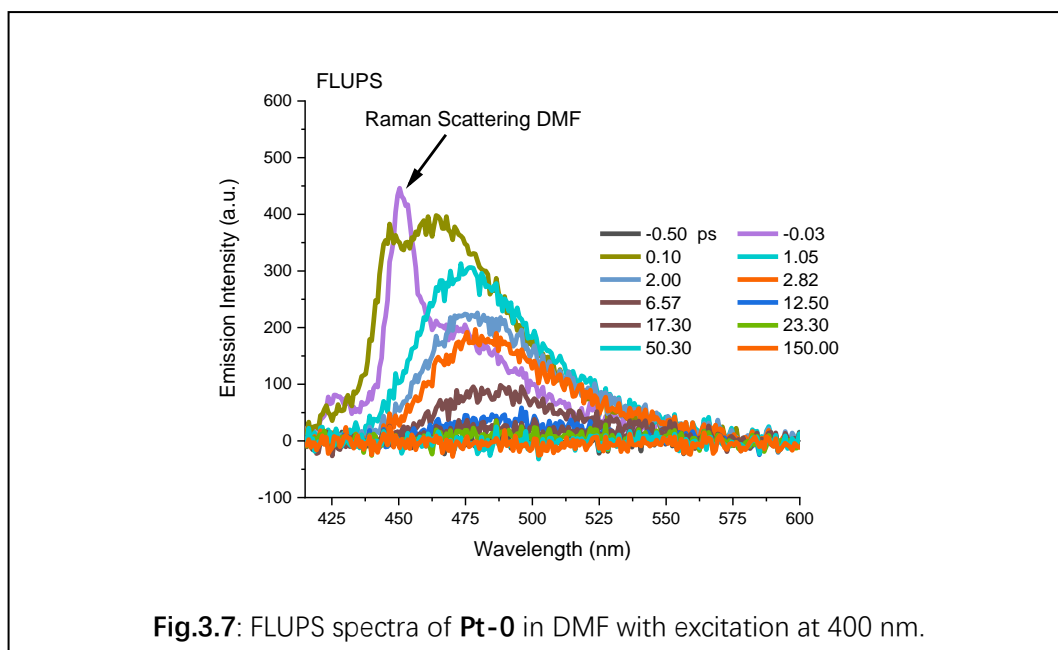


**Fig.3.5:** Transient absorption (TA) spectra of Pt-0 in DMF with excitation at 400 nm.

To extract lifetimes of these states mentioned above, global analysis of TA spectra of **Pt-0** in DMF was done based on a sequential model that includes three components. Global analysis resulted in the decay-associated spectra, given in **Fig.3.6**, with lifetimes of 0.5 ps, 8.4 ps and a long-lived state. The first short-lived state could be attributed to the Franck-Condon (FC) state and the 8.4 ps lifetime is attributed to the  $^1\text{MMLLCT}$  state considering that stimulated emission, which is an attribute of a singlet state decay to the ground singlet state, is evident in the raw spectra and in evolution associated spectra (EAS). The last long-lived excited state is the  $^3\text{NAP}$  state. A faster decay process from  $^1\text{MMLLCT}$  state to  $^3\text{NAP}$  is observed in DMF (8.4 ps) compared with the 11.3 ps extracted from the TA data of **Pt-0** in DCM. The bleach at 440 nm is due to the loss of the ground state absorption.



To confirm that the 8.4 ps component is a decay of a singlet state, and extract ISC rate of **Pt-0** in DMF, FLUPS spectra are collected as shown in **Fig.3.7**. After excitation, an emission band at 460 nm rises together with a peak at 450 nm. The peak at 450 nm is caused by solvent Raman scattering of 400 nm pump pulse, and the 460 nm peak decay and shift to a peak centred at 480 nm. This indicates at early time the emission is from a hot state, which cools down into vibrational ground state of the excited state with the energy of 2.53 eV. This state decays fully by around 20 ps. To extract ISC rate from FLUPS spectra global analysis is done. Because FLUPS is only sensitive to fluorescent states (or, more precisely, to a short-lived emission), fewer excited states could be observed by FLUPS and only two components are used in the sequential model as shown in **Fig.3.8**, as the <sup>3</sup>NAP state can not be detected.

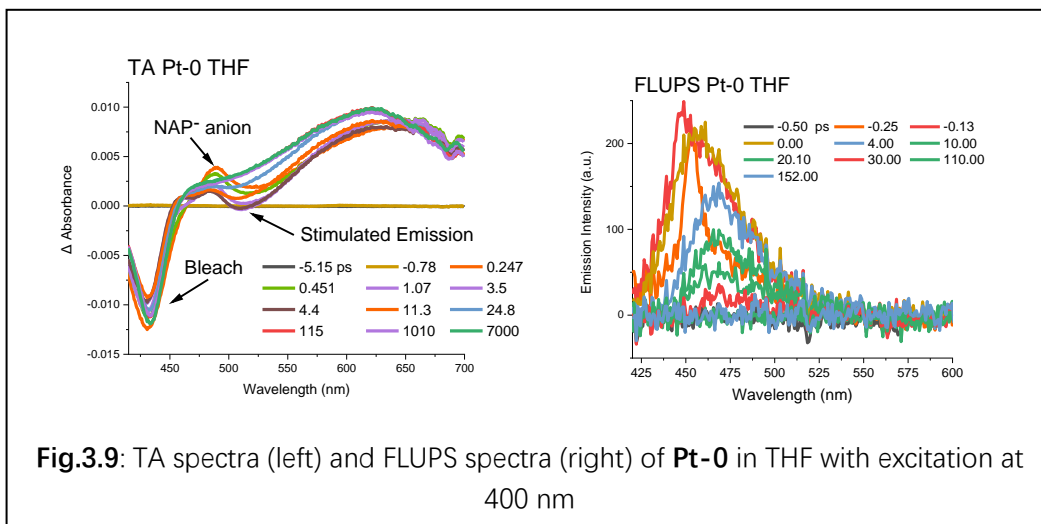


Global analysis based on a sequential model extracted two kinetic components with the lifetimes of 0.5 ps and 4.8 ps (show in **Fig.3.8**). The first component with the emission peak at 460 nm, which is assigned to emission from a vibrationally hot excited state that cools down to the ground vibration state within 0.5 ps. The second emission band, with the maximum at 480 nm, is assigned to an <sup>1</sup>MMLLCT state and decays with the 4.8 ps lifetime, no longer-lived components were detected in FLUPS (although in degassed solution, in a steady-state spectra, <sup>3</sup>NAP phosphorescence could be detected).



We therefore assign the ISC process to the lifetime of 4.8 ps. This indicates that the ISC process of **Pt-0** <sup>1</sup>MMLLCT state is accelerated in DMF compared to that in DCM (ISC, 16.9 ps).

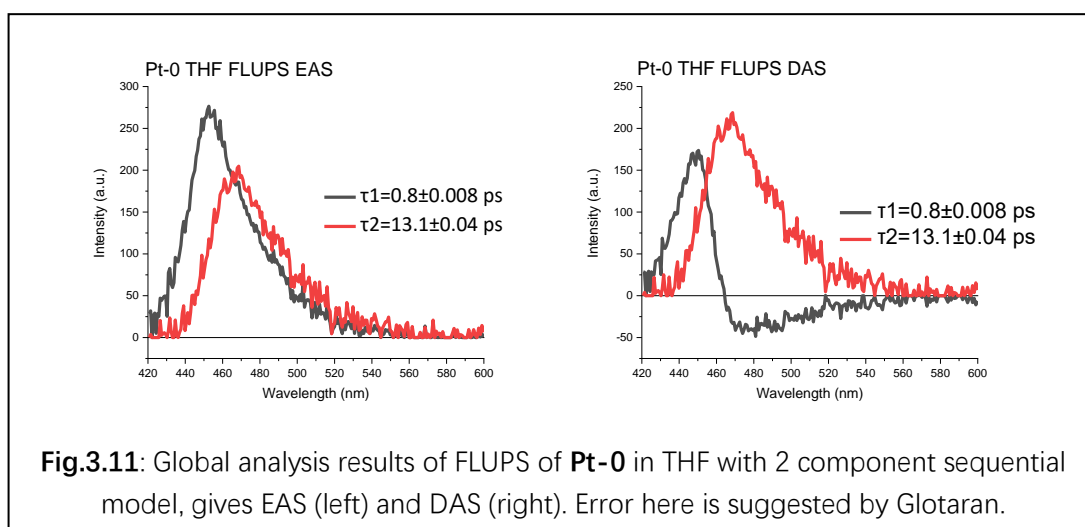
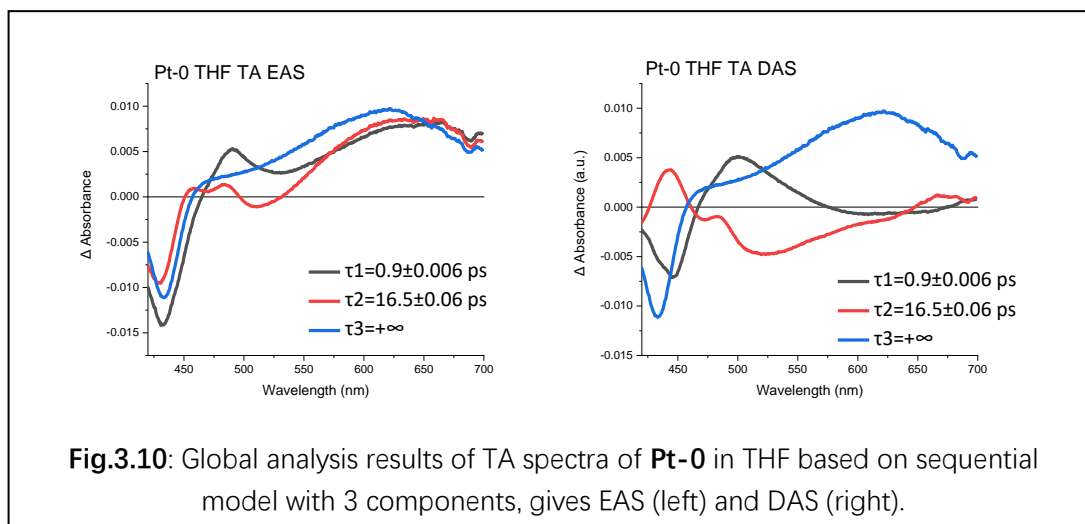
### THF



TA and FLUPS spectra of **Pt-0** in THF with excitation at 400 nm are given in **Fig.3.9**. In TA, after excitation a peak at around 490 nm rises, which is attributed to  $\text{NAP}^-$  absorption formed in MMLLCT state as discussed before. Corresponding with the peak at 490 nm there is a negative peak at around 510 nm which is caused by stimulated emission of the MMLLCT state and indicates the MMLLCT state detected by TA is a singlet state. This <sup>1</sup>MMLLCT state further decays into the long lived <sup>3</sup>NAP state at around 46 ps.

The peak at 453 nm that rises in FLUPS spectra of Pt-0 (show in **Fig.3.9**) immediately after excitation is caused by solvent Raman scattering of 400 nm excitation pulse. At early time after excitation, the emission band centred at 457 nm appears, and decays into the emission band centred at 470 nm which is similar to 469 nm fluorescence detected by steady-state spectroscopy. This process is still attributed to the cooling down from Franck-Condon state to <sup>1</sup>MMLLCT state and its energy (2.64 eV) in THF is slightly higher than the energy observed in <sup>1</sup>MMLLCT state of **Pt-0** in DCM and DMF (2.58 eV). This

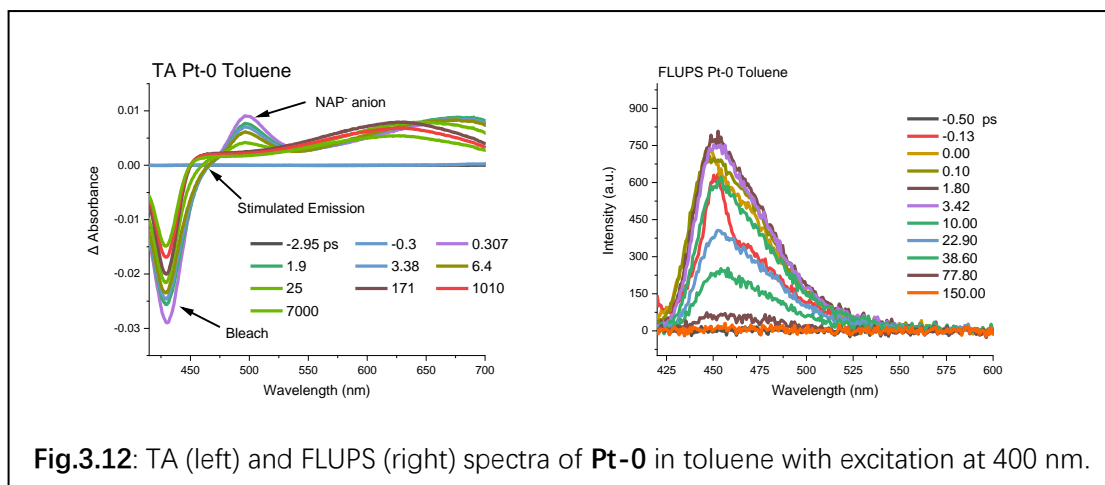
result meets well with trends observed in the steady-state fluorescence spectra.



Global analysis (GLA) results of TA and FLUPS spectra of **Pt-0** in THF are given in **Fig.3.10** and **Fig.3.11**. Three traces obtained by GLA from the TA data are shown in **Fig.3.10**, their lifetimes are 0.9 ps, 16.5 ps and a long-lived state (“infinity”, or “a constant”, component). The long-lived state is attributed to the <sup>3</sup>NAP state. The 16.5 ps trace is corresponding with the <sup>1</sup>MMLLCT state as the peak at 485 nm indicates this state includes a NAP<sup>-</sup> fragment; the bleach at 510 nm is caused by stimulated emission which is characteristic of a singlet state. The 0.9 ps trace extracted from TA corresponds well with the 0.8 ps

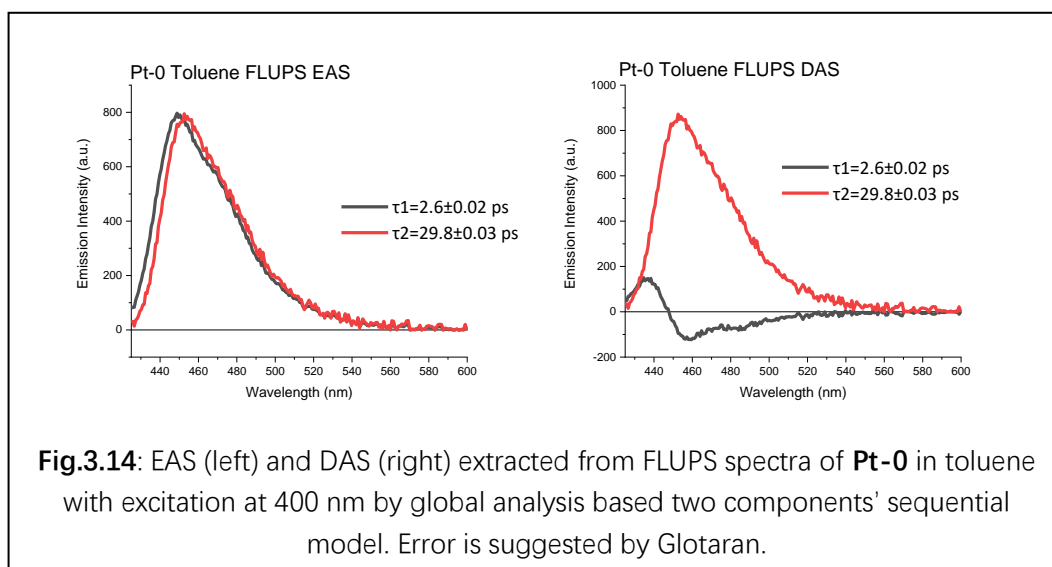
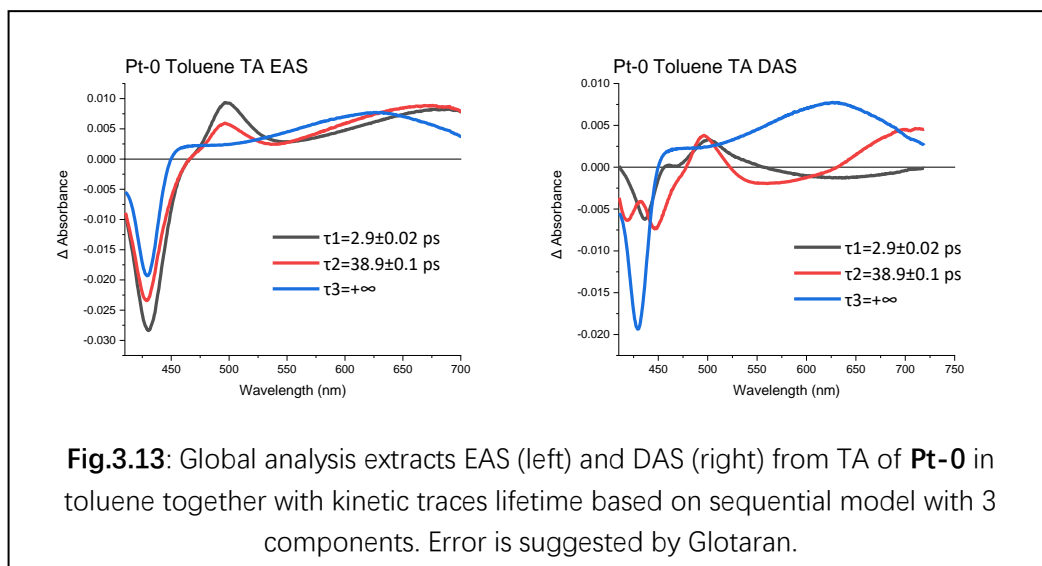
trace extracted from FLUPS global analysis results which is attributed to the FC state. As the second trace from FLUPS is attributed to  $^1\text{MMLLCT}$  state, we conclude that the ISC lifetime is 13.1 ps, which is slower than in DMF but faster than in DCM. From EAS of FLUPS global analysis result, the second trace is centred at 470 nm which corresponds well with fluorescence spectra shown in **Fig.3.4** and **Table.3.2**.

### Toluene



TA and FLUPS spectra of **Pt-0** in toluene collected under 400 nm excitation are given in **Fig.3.12**. In TA spectra, the peak corresponding with  $\text{NAP}^-$  at 495 nm rises first after the excitation, which indicates that the first populated excited state is still the  $^1\text{MMLLCT}$  state. With the decay of 495 nm peak, the signal corresponding with  $^3\text{NAP}$  is developing, which indicates that an  $\text{MMLLCT}$  state decays into  $^3\text{NAP}$  state; considerable bleach recovery also indicates that part of the  $\text{MMLLCT}$  state decays to the ground state (directly or via another transient state). Unlike what was observed in TA of **Pt-0** in polar solvents such as DCM and DMF, there is no stimulated emission signal at 510 nm, which may be because in toluene,  $^1\text{MMLLCT}$  state's energy is much higher and stimulated emission is shifted to around 460 nm and overlapped with the bleach caused by the loss of the ground state. From FLUPS spectra, the emission from **Pt-0** in toluene lives much longer than in polar solvents with

emission signal still visible at 77.8 ps as shown in **Fig.3.12**. The peak at 450 is attributed to the Raman scattering of 400 nm laser pulse of solvent toluene.



To extract lifetimes of corresponding excited states populated after excitation at 400 nm, global analysis is done to TA and FLUPS spectra, associated spectra and lifetimes are extracted and shown in **Fig.3.13** (TA) and **Fig.3.14** (FLUPS). The first component extracted from TA and FLUPS share similar lifetimes: 2.8 ps from TA and 2.6 ps from FLUPS. The second component's lifetime extracted from TA is 38.9 ps which is longer than FLUPS result 29.8 ps. This may be because  $^1\text{MMLLCT}$  state and  $^3\text{MMLLCT}$  state share similar transient absorption spectra and TA technique cannot tell the difference between these two states, so it

gives an average lifetime which is longer than ISC process observed in FLUPS with lifetime 29.8 ps. The energy difference between two emissive components (peak at 448.8 nm and 452.6 nm) extracted from FLUPS is only  $187.1 \text{ cm}^{-1}$  which indicates the decay from component 1 to 2 is not caused by vibrational relaxation and may be caused by reorganization of surrounding solvents. The second component lifetime, 29.8 ps could be treated as ISC process which is much slower than in polar solvents discussed before. Lifetimes extracted from **Pt-0** in different solvents and ultrafast techniques are summarized in **Table.3.3**.

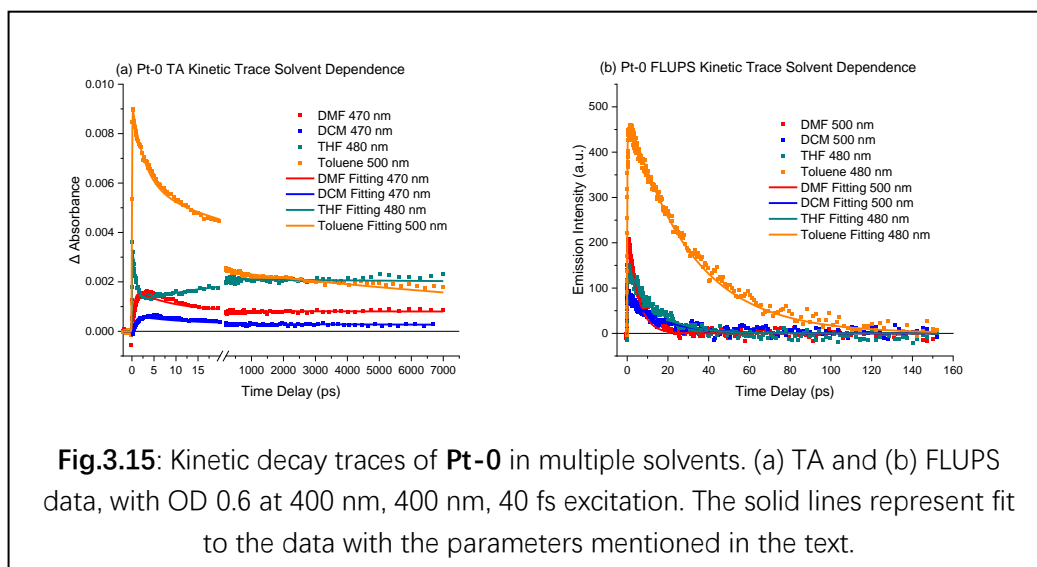
### Summary of Pt-0 in Multiple Solvents

Pt-0 TA	$\tau_1/\text{ps}$	$\tau_2/\text{ps}$	$\tau_3/\text{ps}$
DMF (0.901)	$0.5 \pm 0.005$	$8.4 \pm 0.03$	$+\infty$
DCM (0.765)	$0.6 \pm 0.003$	$11.3 \pm 0.03$	$+\infty$
THF (0.494)	$0.9 \pm 0.006$	$16.5 \pm 0.06$	$+\infty$
Toluene (0.172)	$2.9 \pm 0.02$	$38.9 \pm 0.1$	$+\infty$

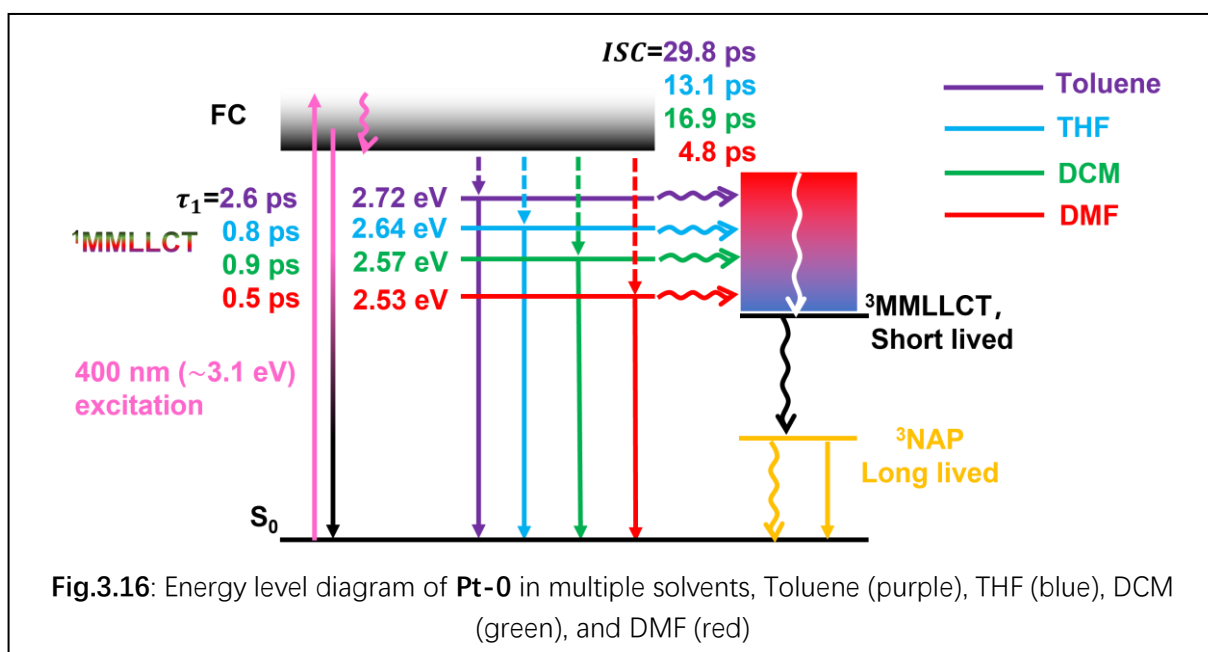
Pt-0 FLUPS	$\tau_1/\text{ps}$	$\tau_2/\text{ps}$
DMF (0.901)	$0.5 \pm 0.003$	$4.8 \pm 0.01$
DCM (0.765)	$0.9 \pm 0.008$	$16.9 \pm 0.08$
THF (0.494)	$0.8 \pm 0.008$	$13.1 \pm 0.04$
Toluene (0.172)	$2.6 \pm 0.02$	$29.8 \pm 0.03$

**Table.3.3:** Lifetimes of different excited states of **Pt-0** in multiple solvents (DMF, THF, DCM and toluene) extracted from TA and FLUPS spectra, Eisenberg parameters of the solvent are also given in brackets. The error shown here is given by Glotaran (and is unrealistically small).



The lifetimes of **Pt-0** in different solvents are summarised in **Table.3.3**. The kinetic traces together with fitting result of TA and FLUPS at selected wavelengths are shown in **Fig.3.15**. It is clear that the solvent dependent ISC process is observed. For **Pt-0**, with the increase of solvent dipole moment, ISC rate of **Pt-0** <sup>1</sup>MMLLCT state increases. Such solvent dependent ISC rate was observed in PtPOP complexes,<sup>9</sup> and explained as follows: the stabilisation energy of ligand-to-Pt CT state is dependent on solvent or ISC is induced by symmetry breaking and different solvent can stabilise lower symmetry conformation to a different extent. This mechanism may also explain the solvent dependent ISC rate observed in **Pt-0**. For **Pt-0**, ISC lifetime in different solvents could be ranked as DMF<DCM~THF<Toluene and solvent dipole moment rank is DMF>THF~DCM>Toluene as shown in **Table.3.1**. This indicates that a lower symmetry conformation of **Pt-0** MMLLCT state could be more stabilised by a more polar solvent. Another possible mechanism to explain solvent-dependent ISC rate in **Pt-0** could be that the <sup>1</sup>MMLLCT state and <sup>3</sup>MMLLCT state of **Pt-0** undergo ultrafast ISC and reverse ISC (rISC) process and reach an equilibrium between <sup>1</sup>MMLLCT and <sup>3</sup>MMLLCT state, so the decay of <sup>1</sup>MMLLCT state (lifetimes detected by FLUPS) depends on the decay rate of <sup>3</sup>MMLLCT to <sup>3</sup>NAP state. The MMLLCT state is CT state which could be

stabilised by a polar solvent and  $^3\text{NAP}$  is a ligand-localised excited state which cannot be stabilised by polar solvent. The MMLLCT state energy decreases with an increase in solvent polarity, and the energy of  $^3\text{NAP}$  state remains constant so the energy gap between MMLLCT state and  $^3\text{NAP}$  state decreases with the increase of solvent polarity and ISC rate increases (lifetime decreases). We suggest this explanation for solvent-dependent ISC rate but to confirm it we need to do more modelling.



Energy level diagrams of **Pt-0** in multiple solvents are given in **Fig.3.16**. The energy level diagram is similar to **Pt-0** in DCM suggested in **Chapter 2** and **Cl-Pt-NAP** complex published before.<sup>8</sup> With excitation at 400 nm, the first populated FC state decays into vibrationally relaxed  $^1\text{MMLLCT}$  state which then ISC to  $^3\text{MMLLCT}$  state; the  $^3\text{MMLLCT}$  state is very short lived, it undergoes a fast decay process to  $^3\text{NAP}$  state. The rate of the ISC process from  $^1\text{MMLLCT}$  to  $^3\text{MMLLCT}$  state is solvent dipole moment dependent. The sub-

picosecond decay from FC state to  $^1\text{MMLCT}$  state of **Pt-0** in DMF, THF and DCM could be attributed to vibrational decay process as the energy gap between two emission band extracted from FLUPS is ranging from  $700\text{ cm}^{-1}$  to  $900\text{ cm}^{-1}$ , but this energy gap of **Pt-0** in toluene is only  $187\text{ cm}^{-1}$ . Also, for **Pt-0** in toluene this decay is  $2.6\text{ ps}$  which is much slower than in other solvents and this decay process is attributed to rearrangement of surrounding solvent molecules.

### 3.3.1.2. Pt-1

#### 3.3.1.2.1. UV-Vis Absorption Spectra and Fluorescence Spectra

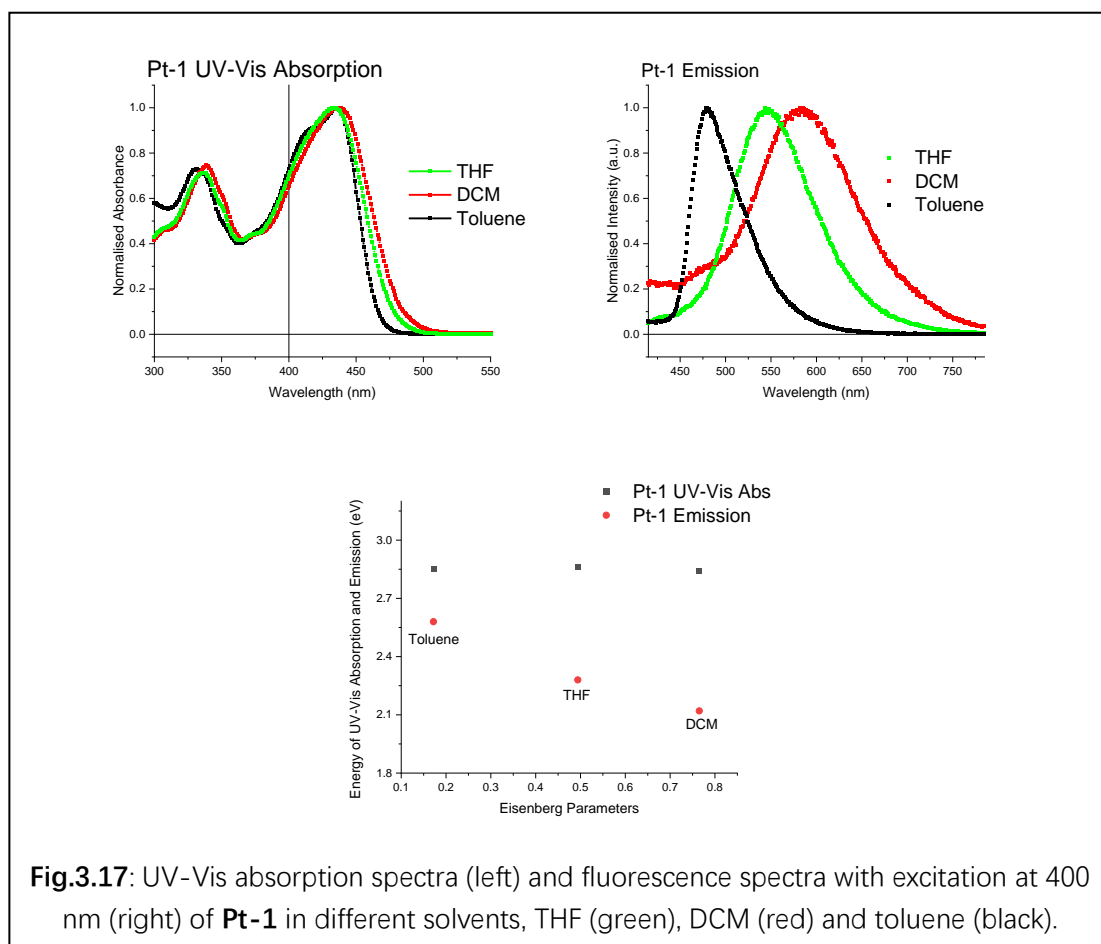


**Fig.3.17:** UV-Vis absorption spectra (left) and fluorescence spectra with excitation at 400 nm (right) of **Pt-1** in different solvents, THF (green), DCM (red) and toluene (black).



Solvent (Eisenberg Parameter)	$\lambda_{abs}/nm$	$\lambda_{fl}/nm$	Stokes Shift/ $cm^{-1}$
DCM (0.765)	437	585	5789
THF (0.494)	433	543	4678
Toluene (0.172)	435	480	2115

**Table.3.4:** Summary of UV-Vis absorption band peak and Emission band peak collected in fluorescence spectra of **Pt-1** in multiple solvents.

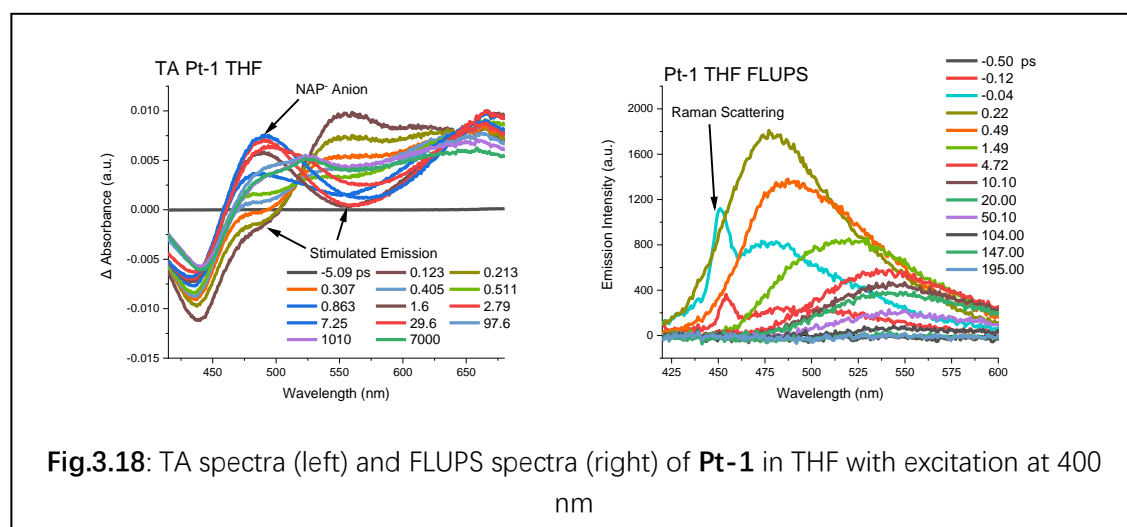
As show in **Fig.3.17**, UV-Vis absorption spectra of **Pt-1** in THF, DCM and toluene are similar (difference in hundreds  $cm^{-1}$  which is small) which indicates that the energy of the first populated  $^1MMLLCT$  state is not influenced a lot by the solvent dipole moment – this is different from the condition discussed in **Pt-0**. Also, in fluorescence spectra shown in **Fig.3.17** (top right) and summarised in **Table.3.4**, the emission bands' position of **Pt-1** in different solvents are very different from each other. The different extent of solvent influence in UV-Vis spectra and fluorescence spectra is because UV-Vis spectra is detecting ground state ( $S_0$ )- $^1MMLLCT$  state transition but fluorescence signal is corresponding with cumulenic MLCT state (emission peaked at 580 nm in DCM extracted from FLUPS) and  $^1MMLLCT$  state (emission peaked at 480 nm in DCM extracted from FLUPS) as discussed in **Chapter 2** for **Pt-1** in DCM, the cumulenic MLCT state is populated after isomerisation of initial populated  $^1MMLLCT$  state so the fluorescence spectra peaks is dependent on the ratio of  $^1MMLLCT$  state and cumulenic MLCT state formed after isomerisation and this ratio could be influenced by solvent. Also, the Stokes shift observed in **Pt-1** in toluene is  $2115\text{ cm}^{-1}$  which indicates that the absorption signal and emission signal correspond to the same excited state. However, the Stokes shift observed in **Pt-1** in DCM and THF are around  $5000\text{ cm}^{-1}$  which is much larger than in toluene, and indicate that emission and absorption may correspond to different excited states.

Similar to **Pt-0**, the UV-Vis absorption maximum of the lowest (in energy) absorption transition of **Pt-1** is barely influenced by the change of solvent dipole moment (as shown in **Fig.3.17**) but the emission spectrum shows positive solvatochromism. This indicates that the FC state of **Pt-1** is nearly nonpolar as the ground state is highly symmetric and with small dipole moment, but the fluorescent state has much higher dipole moment and could be assigned as a CT state.

### 3.3.1.2.2. Transient Absorption (TA) and Fluorescence Up-Conversion Spectra of Pt-1

To investigate what excited states are populated and their ultrafast dynamics of **Pt-1** in THF and toluene, TA and FLUPS techniques are used together with global analysis to extract information from ultrafast time-resolved spectra.

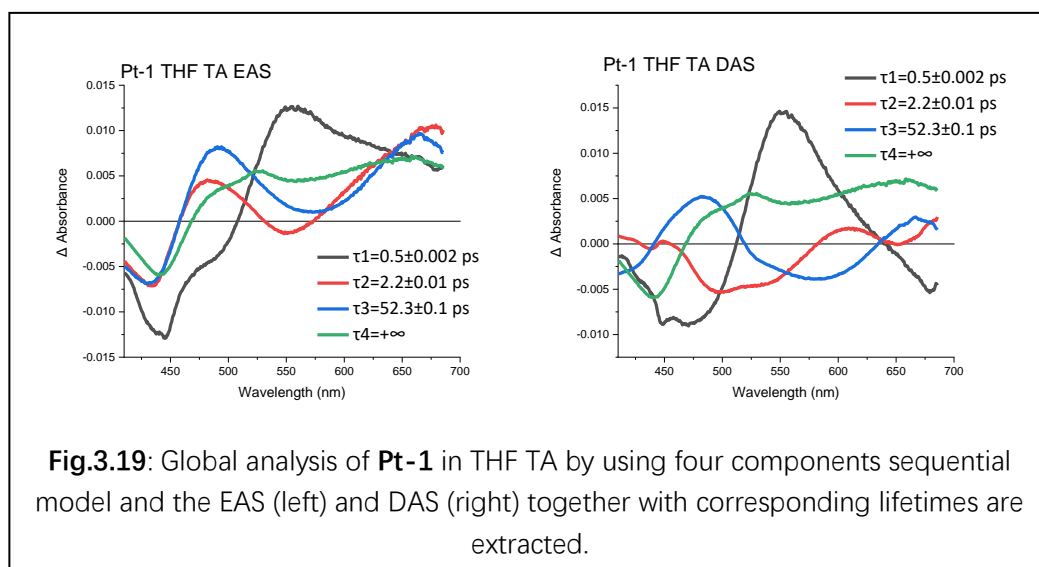
#### THF



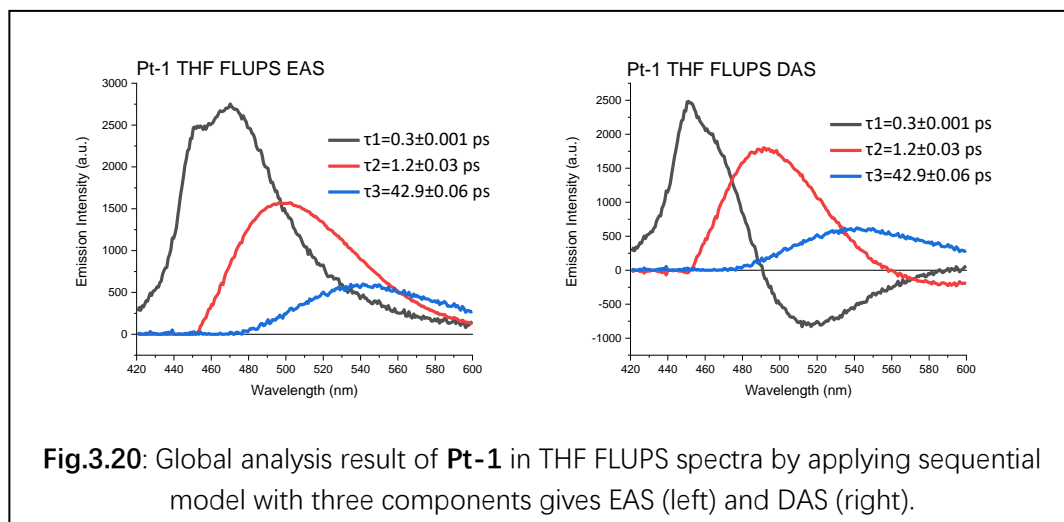
The TA spectra of **Pt-1** in THF after 400 nm excitation are shown in **Fig.3.18**. After excitation, a stimulated emission band at around 485 nm is observed which is overlapped with the broad bleach at 440 nm. The stimulated emission at 485 nm band is caused by the first populated FC state, then with the decay of the stimulated emission, another stimulated emission band at 550 nm rises which is attributed to the <sup>1</sup>MMLCT state population. The peak at around 490 nm then rises which is attributed to NAP<sup>-</sup> anion absorption of

CT. Then with the decay of 550 nm peak corresponding to the CT state, a broadband absorption from 460 to 700 nm rises and stays, which is attributed to the long lived  $^3\text{NAP}$  state. This  $^3\text{NAP}$  state is not the same as in **Pt-0**, as the spectrum includes a tiny peak at around 520 nm which indicates this  $^3\text{NAP}$  state has tiny amount anion component.

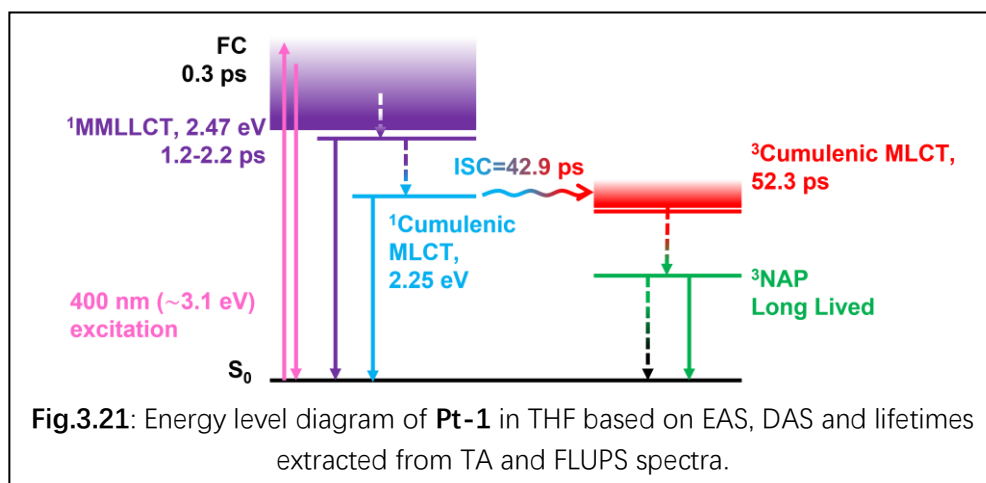
To investigate further the formation and decay of the excited states suggested based on TA spectra, and to investigate the ISC process, FLUPS spectra with excitation at 400 nm were recorded, the result is given in **Fig.3.18** (right). At early times after the excitation, an emission peak at around 475 nm is observed which corresponds well with the stimulated emission band at around 485 nm observed in TA and it is assigned to a FC state. Then this emission decays into a band with the maximum at around 525 nm at 1.5 ps which corresponds well with the stimulated emission at 550 nm observed in TA at the same time delay. Then this emission band further decays into an emission band centred at 540 nm which decays to zero 115 ps later, this indicates there are three excited states emissive on the timescale of FLUPS (under 1 ns) that could be populated after 400 nm excitation of **Pt-1** in THF.



To extract more details about excited state dynamics of **Pt-1** in THF after excitation at 400 nm, global analysis is done to TA spectra and four components with lifetimes 0.5, 2.2, 52.3 ps and a long-lived excited state are extracted (show in **Fig.3.19**). The long-lived excited state is attributed to  $^3\text{NAP}$  state and the first kinetic component with 0.5 ps lifetime could be attributed to FC state. The second and third trace lifetime for **Pt-1** in THF are very close to those for **Pt-1** in DCM. But the shape of the EAS extracted with 52.3 ps from TA of **Pt-1** in THF is very different to the 52.6 ps EAS component extracted from TA of **Pt-1** in DCM. This third EAS trace of **Pt-1** in THF shows an 'eat in' caused by stimulated emission centred at 575 nm which indicates this spectrum corresponds to a singlet state which is similar condition for **Pt-1** in DCM.

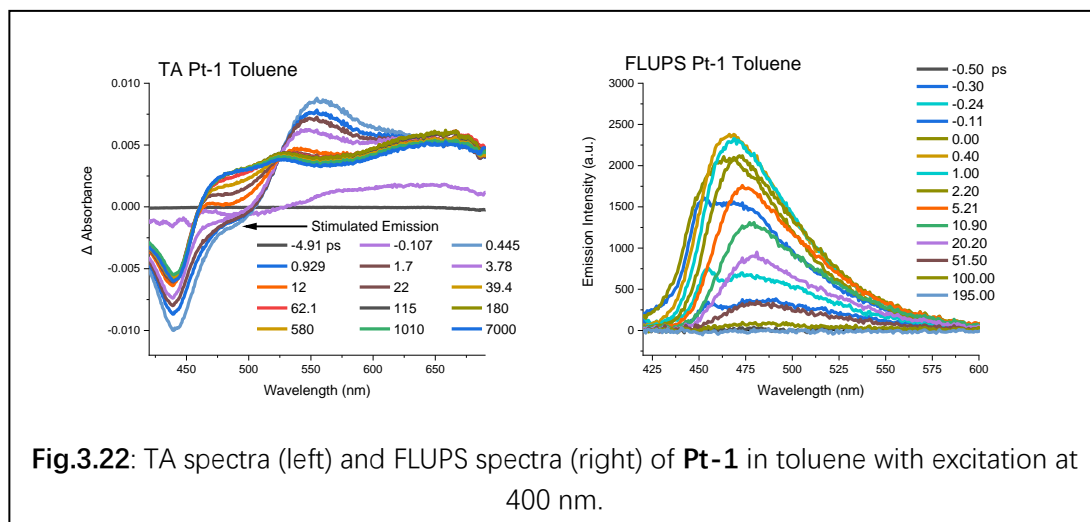


Global analysis of FLUPS of **Pt-1** in THF is shown in **Fig.3.20**. The first component with 0.3 ps is attributed to emission from FC state and the second trace is attributed to the <sup>1</sup>MMLCT state suggested from TA, with 1.2 ps lifetime. The third fluorescent trace with 42.9 ps lifetime is centred at around 550 nm which is very different from the condition in DCM, and this emission band corresponds well with the stimulated emission observed in TA. Also, the third trace extracted from TA in THF shows the stimulated emission trace and with lifetime 52.3 ps which is longer than the third trace 42.9 ps extracted from FLUPS spectra. This could be explained as TA is probing mixture of singlet and triplet cumulenic MLCT state which decays into <sup>3</sup>NAP state with lifetime 52.3 ps as extracted by TA but ISC rate is around 42.9 ps extracted by FLUPS considering FLUPS is more sensitive to fluorescent state compared with TA as discussed in this thesis' introduction. However, stimulated emission is not shown in the third trace extracted from TA of **Pt-1** in DCM which may be because in DCM TA is probing a mixture of singlet and triplet cumulenic MLCT state and triplet state is dominant which makes the stimulated emission not so obvious for **Pt-1** in DCM. Considering the difference between **Pt-1** in THF and DCM observed by TA and FLUPS, the third excited state populated in **Pt-1** in THF after 400 nm excitation could be attributed to a singlet state instead.



Energy level diagram of **Pt-1** in THF is given in **Fig.3.21**, after excitation to FC state by 400 nm pulse. The FC state decay into <sup>1</sup>MMLLCT state within 0.3 ps. Then the isomerisation of <sup>1</sup>MMLLCT state generates the cumulenic structure shown in **Fig.2.7** in **Chapter 2** and gives <sup>1</sup>Cumulenic MLCT state which ISC into <sup>3</sup>Cumulenic MLCT state. Then ISC process occurs with the lifetime of 42.9 ps according to FLUPS spectra and lifetime of <sup>3</sup>Cumulenic MLCT generated is at least 52.3 ps according to TA spectra as this 52.3 ps could be from the mixture of <sup>1</sup>Cumulenic MLCT state and <sup>3</sup>Cumulenic MLCT state. The change in the multiplicity of the cumulenic MLCT state may arise because in THF the energies of both singlet and triplet cumulenic MLCT states decreased further than in DCM which makes the energy of the singlet cumulenic MLCT state energy lower than <sup>1</sup>MMLLCT in THF, and it could be populated from <sup>1</sup>MMLLCT state.

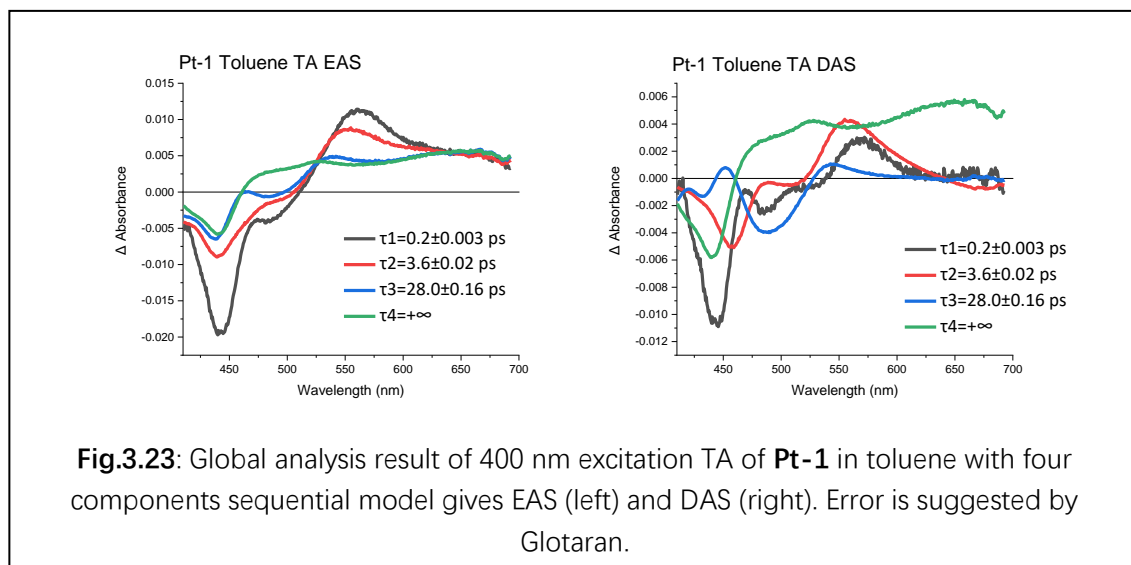
## Toluene



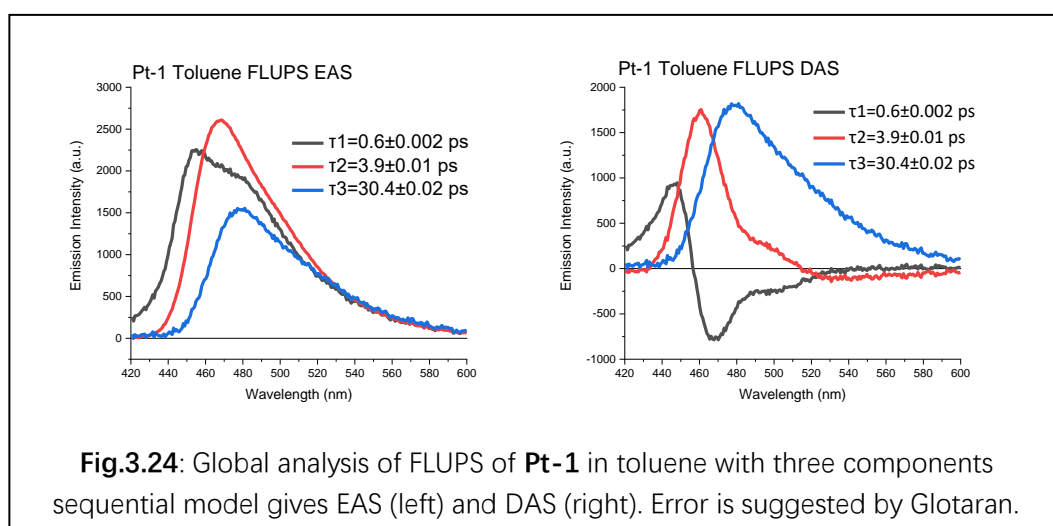
As discussed before, the Stokes shift of **Pt-1** in toluene is very different from that in DCM or THF and indicates a potentially different decay mechanism for **Pt-1** in toluene. To investigate the excited state dynamics of **Pt-1** in toluene, TA and FLUPS with excitation at 400 nm is processed and the results are given in **Fig.3.22**.

The TA spectra of **Pt-1** in toluene are very different from those recorded in DCM and THF. The stimulated emission at 560 nm is not observed; instead, a stimulated emission at around 480 nm which is attributed to  $^1\text{MMLLCT}$  state rises and persists.

From the FLUPS spectra of **Pt-1** in toluene, FC state with maxima at 465 nm decays into a state with emission maxima at 475 nm which is attributed to  $^1\text{MMLLCT}$  state, then this state decays slowly into zero and does not shift to lower wavelength. This result indicates the **Pt-1**  $^1\text{MMLLCT}$  state emission dominates in toluene but the cumulenic structure emission dominates in DCM and THF. The emission band detected after 5 ps is relatively broadband, tailing as far as 600 nm, this indicates there might be a tiny amount singlet cumulenic MLCT state populated, perhaps in equilibrium with  $^1\text{MMLLCT}$  state.



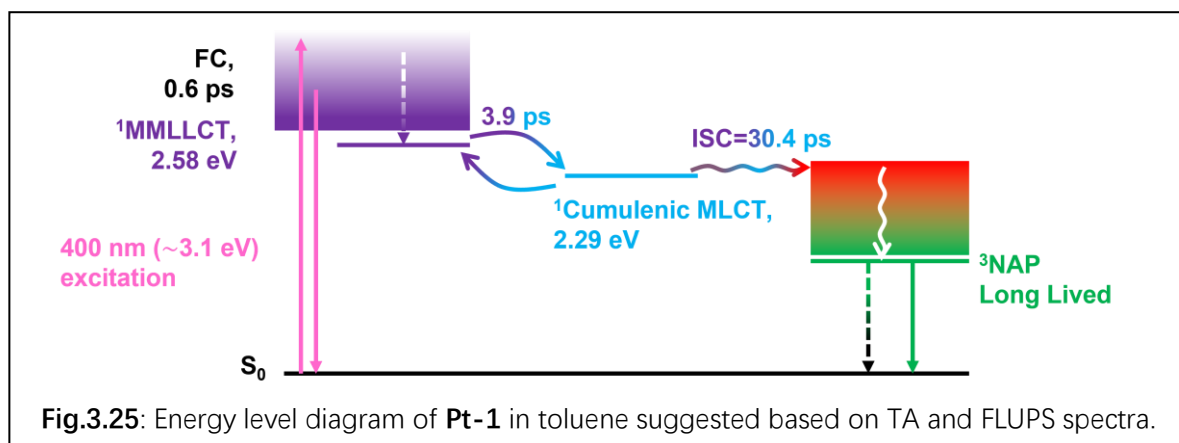
Global analysis extracted four components from TA by using a sequential model (show in **Fig.3.23**). Unlike the results for **Pt-1** in THF and DCM, there is no stimulated emission band at around 560 nm in any EAS traces, but the stimulated emission at around 485 nm is present in the three short lived components which is corresponding with <sup>1</sup>MMLLCT state. The first 0.2 ps lifetime component could be attributed to FC state and the other two traces are both attributed to <sup>1</sup>MMLLCT state.



To get more details about the excited state dynamics of **Pt-1** in toluene, FLUPS spectra is also globally analysed by using three components sequential model. The first trace extracted is the short-lived FC state and the



lifetimes extracted for the second and third components meet well with the second and third components extracted from TA. From the analysis of TA, the second and third trace are both attributed to  $^1\text{MMLLCT}$  state but why there are two decay process with different lifetimes for the same excited state? If we focus on the third EAS trace extracted from FLUPS, it includes a major peak at around 480 nm, and a tail from 520 to 600 nm. For this phenomenon, a hypothesis is there are two emissive excited states in equilibrium with each other, so it gives broadband emission and decay together within 30.4 ps and this process is ISC process. Also, from DAS (shown in **Fig.3.24** right) that were extracted based on a parallel model, the second trace with lifetime 3.9 ps includes a negative band from 520 to 600 nm which indicates grows-in in the next component; so the 3.9 ps could be treated as a fast process from  $^1\text{MMLLCT}$  state to the equilibrium between  $^1\text{MMLLCT}$  state and  $^1\text{cumulenic MLCT}$  state.



An energy level diagram is shown in **Fig.3.25** for **Pt-1** in toluene. With the excitation at 400 nm, the first populated FC state decays into  $^1\text{MMLLCT}$  state within 0.6 ps, then this  $^1\text{MMLLCT}$  state decay into  $^1\text{Cumulenic MLCT}$  state and form an equilibrium between these two states within 3.9 ps. These two singlet states in equilibrium intersystem cross together with the average lifetime of 30.4 ps to form the  $^3\text{NAP}$  state which is long-lived.

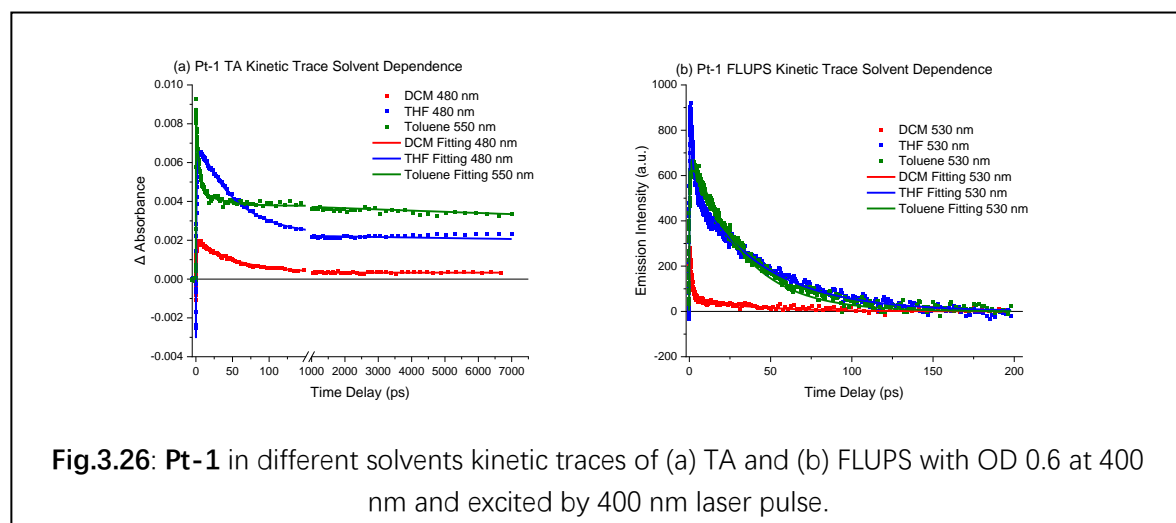
### Summary of Pt-1 in Multiple Solvents

Pt-1 TA	$\tau_1/\text{ps}$	$\tau_2/\text{ps}$	$\tau_3/\text{ps}$	$\tau_4/\text{ps}$
DCM (0.765)	$0.3 \pm 0.001$	$1.8 \pm 0.005$	$52.6 \pm 0.12$	$+\infty$
THF (0.494)	$0.5 \pm 0.002$	$2.2 \pm 0.01$	$52.3 \pm 0.1$	$+\infty$
Toluene (0.172)	$0.2 \pm 0.003$	$3.6 \pm 0.02$	$28 \pm 0.16$	$+\infty$

Pt-1 FLUPS	$\tau_1/\text{ps}$	$\tau_2/\text{ps}$	$\tau_3/\text{ps}$
DCM (0.765)	$0.3 \pm 0.002$	$1.2 \pm 0.008$	$37.3 \pm 0.3$
THF (0.494)	$0.3 \pm 0.001$	$1.2 \pm 0.03$	$42.9 \pm 0.06$
Toluene (0.172)	$0.6 \pm 0.002$	$3.9 \pm 0.01$	$30.4 \pm 0.02$

**Table.3.5:** Lifetimes of **Pt-1** in THF, DCM and Toluene extracted from TA spectra (above) and FLUPS spectra (down). Eisenberg Parameters of the solvents are also given in brackets. The error show here is given by Glotaran.

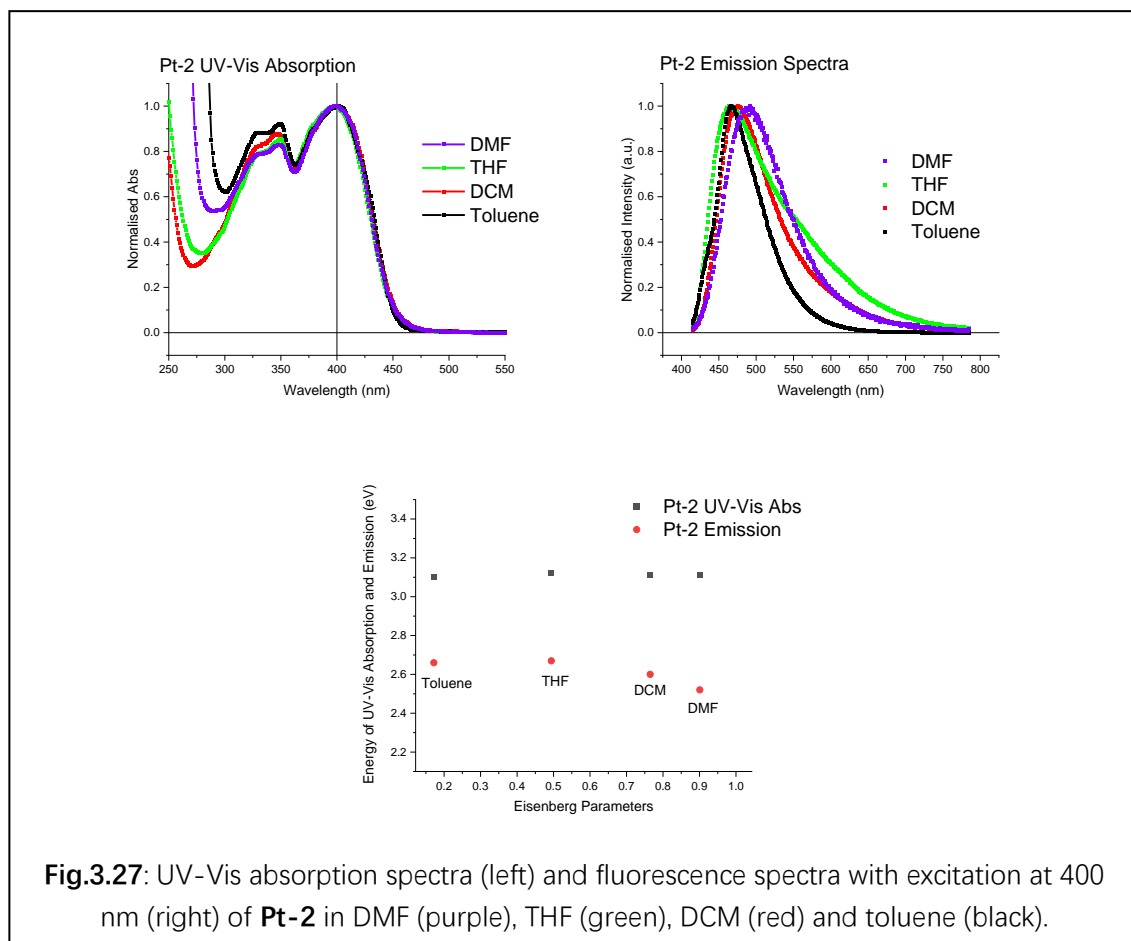


**Fig.3.26:** **Pt-1** in different solvents kinetic traces of (a) TA and (b) FLUPS with OD 0.6 at 400 nm and excited by 400 nm laser pulse.

For **Pt-1**, the change of solvent dipole moment does not change the energy of the first populated state a lot but changes the extent of the isomerization process from the -CC-triple bonds in the MMLLCT state to an MLCT state with cumulenlic structure. With the decrease of the dipole moment of the solvent used, the energy of the cumulenlic MLCT state increases, which further influences the energy levels and the lifetimes of corresponding states. The energy level diagrams of **Pt-1** deduced from TA and FLUPS spectra are given in **Fig.2.14** (in DCM) in **Chapter 2**, **Fig.3.21** (in THF) and **Fig.3.25** (in toluene), to further understand the isomerisation process in **Pt-1** in THF and toluene, 400 nm excitation TRIR is required.

### 3.3.1.3. Pt-2

#### 3.3.1.3.1. UV-Vis Absorption Spectra and Fluorescence Spectra



Solvent (Eisenberg Parameter)	$\lambda_{abs}/nm$	$\lambda_{fl}/nm$	Stokes Shift/ $cm^{-1}$
DMF (0.901)	399	492	4737
DCM (0.765)	399	476	4054
THF (0.494)	398	465	3620
Toluene (0.172)	401	466	3478

**Table.3.6:** Summary of UV-Vis absorption band peak and Emission band peak collected in fluorescence spectra of **Pt-2** in multiple solvents. Eisenberg Parameters of the solvents are also given in the bracket.

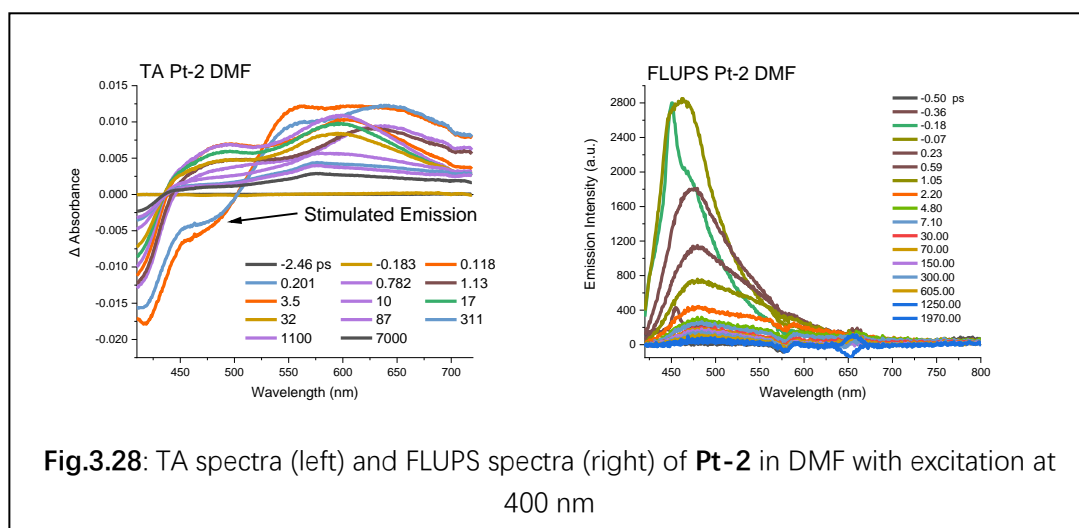
As the UV-Vis absorption spectra show in **Fig.3.27**, the absorption band maxima of **Pt-2** in different solvents are at around 400 nm which is much higher in energy than **Pt-0** and **Pt-1**. Which indicates that with the increase of bridge length between Pt centre and NAP acceptor, the energy required

to induce metal to ligand charge transfer increases. Also, with the increase of the size of the complex, the solvent dipole moment influence on the energy gap between ground and excited state is weaker. The Stokes shift for **Pt-2** in different solvents are all relatively large, which indicates the dominant emission band may correspond to a different excited state than that populated by 400 nm excitation.

As show in **Fig.3.27**, the energy of the lowest UV-Vis absorption band of **Pt-2** does not show obvious solvatochromism, this indicates with change of solvent dipole moment, energy of the excited state corresponding with absorption at around 400 nm does not change. This indicates this excited state has a similar dipole moment to the ground state or the dipole moments of the ground state and excited state is pointing in opposite directions but are equal to each other in number which is unlikely. However, the maximum of fluorescence spectra shift from 466 nm to 492 nm with change solvent from nonpolar toluene to polar DMF. This indicates the fluorescent state majorly populated undergoes solvatochromism and is polar as **Pt-2** is symmetric in structure and behaves nonpolar based on modelling result discussed in **Chapter 2** and Dr. Heather Carson's graduation thesis.<sup>10</sup> Also, with the increase of solvent dipole moment from toluene to DCM and THF, there is a shoulder emission rises at around 550 nm, and in DMF the emission peak shifts to 492 nm compared with 466 nm observed in toluene. This indicates there maybe two different fluorescent state be populated and with the change of solvent dipole moment, the ratio of these two states change. Further details about the nature of these fluorescent states will be investigated by using FLUPS and TA which will be discussed later.

### 3.3.1.3.2. *Transient Absorption (TA) and Fluorescence Up-Conversion Spectra of Pt-2*

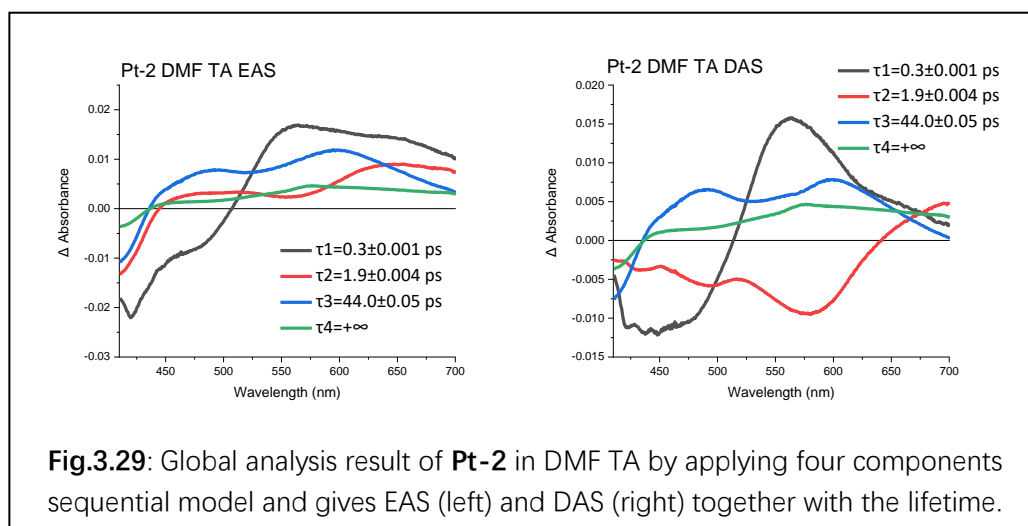
## DMF



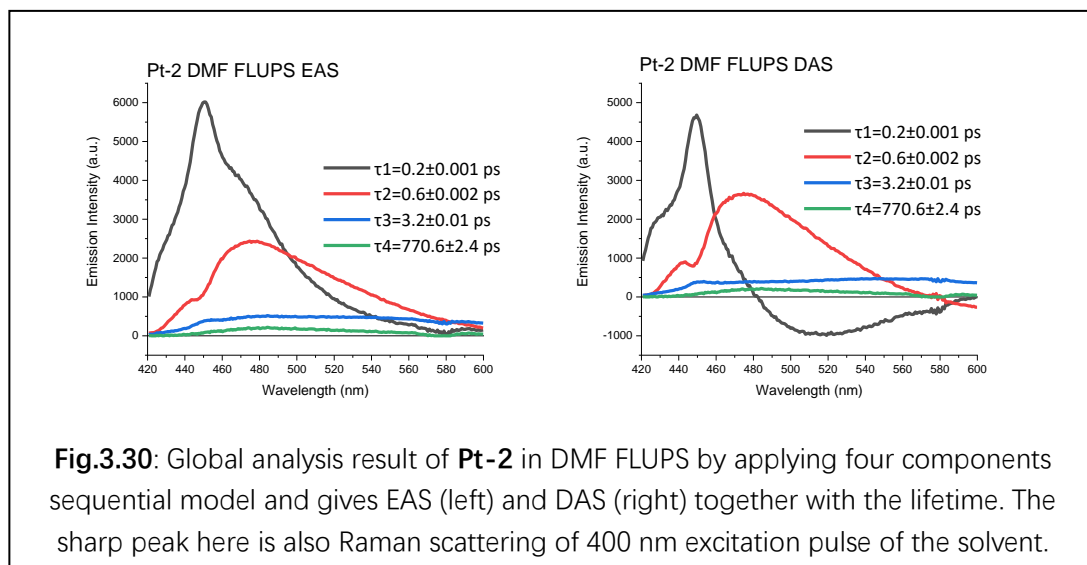
The stimulated emission band at around 460 nm in TA rises with the excitation pulse, then decays quickly, with positive features arising, which indicates a fast ISC process of **Pt-2** in DMF as shown in **Fig.3.28** (left). The broadband absorption rises with the decay of stimulated emission, the peak at around 480 nm (490 nm would be a  $\text{NAP}^-$  anion absorption) becomes relatively broader and weaker than in **Pt-0** in DMF and **Pt-1** in DCM. Thus for **Pt-2** in DMF, the negative charge on NAP ligand in CT state is probably smaller than in **Pt-0** and **Pt-1**, and perhaps the delocalisation is taking place even in the course of the excitation. After about 60 ps, this absorption band decays into a long-lived broad band which is similar to  $^3\text{NAP}$  state absorption observed in **Pt-1** in DCM; this absorption band is attributed to  $^3\text{NAP}$  state absorption in **Pt-2** in DMF. A peak at around 575 nm in **Pt-2** in DMF, similar to a peak at 570 nm also observed in **Pt-2** in DCM, could possibly be explained by a tiny amount negative charge component in  $^3\text{NAP}$  state of **Pt-2**. Alternatively, there is a charge-transfer state, with  $\text{NAP}^-$  anion, which lies slightly higher in energy than  $^3\text{NAP}$ , and therefore there are two distinct states, perhaps in equilibrium.

To further investigate the photo physics of **Pt-2** in DMF, and establish if it undergoes ultrafast ISC process proposed on the basis of TA data, FLUPS

spectra of **Pt-2** in DMF are also collected and shown in **Fig.3.28** (right). There, a picosecond decay of the emission peak at 465 nm is observed and the rest of the emission is broadband and covers the whole detection range of FLUPS from 420 to 800 nm. This emission is much weaker than the emission at 465 nm which is still assigned to singlet state but only tiny amount is populated because phosphorescence is much longer lived so low intensity in small time scale (time resolution for FLUPS is 200 fs) which cannot be detected by FLUPS.



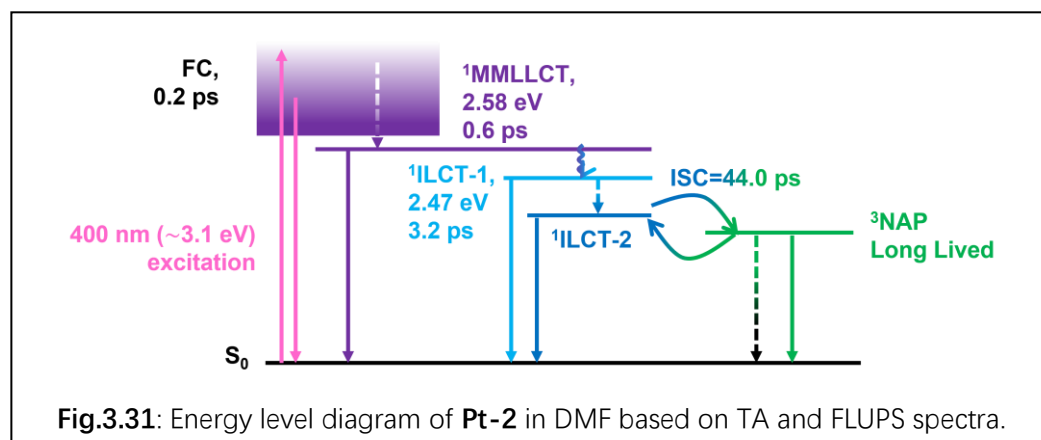
Global analysis based on a four-component sequential model is applied to TA of **Pt-2** in DMF (shown in **Fig.3.29**). The first EAS trace with a 0.3 ps lifetime shows a stimulated emission band at around 470 nm which indicates this is a singlet state. The second and third EAS traces both show absorption at around 470 nm which correspond with  $\text{NAP}^-$  anion absorption, so these two traces correspond to CT states, which are attributed to two different intra-ligand charge transfer states (ILCT) in **Pt-2** in DCM as discussed in **Chapter 2**. The last long-lived state is then attributed to  $^3\text{NAP}$  state and the tiny peak at 573 nm indicates this  $^3\text{NAP}$  state has a weak negative charge contribution on NAP ligand (or there are two distinct states, as proposed above).



To investigate ISC rate of **Pt-2** in DMF with excitation at 400 nm, global analysis is applied to its FLUPS spectra with a four-component sequential model (the results are shown in **Fig.3.30**). The first and second EAS extracted, with strong emission signals, are attributed to fluorescence signal from a singlet state; the two remaining EAS with weak emission signal are attributed to the two different ILCT state discussed previously and they are assigned to a singlet state, as FLUPS detects relatively strong emission signal with intensity around 500 nm, similar to with the emission of <sup>1</sup>MMLLCT state of **Pt-0** under similar condition.

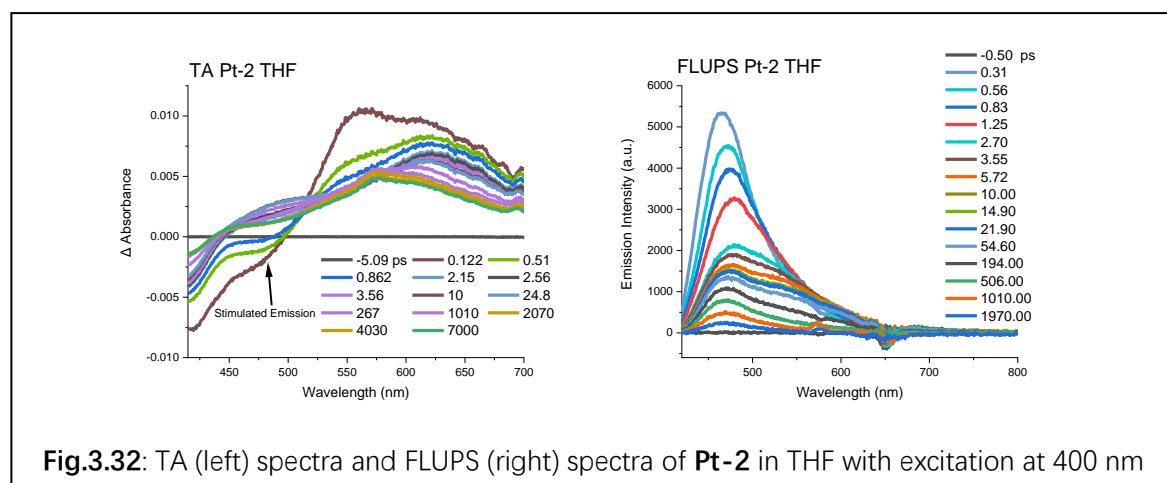
The first two sub-picosecond EAS extracted from FLUPS of **Pt-2** corresponds well with the first 0.3 ps EAS trace extracted from TA which indicates the FC state fast decay into <sup>1</sup>MMLLCT state. The third EAS with 3.2 ps lifetime could be matched to the second EAS trace from TA with 1.9 ps lifetime <sup>1</sup>ILCT-1 state. The 44 ps component extracted from TA and the 770.6 ps component extracted from FLUPS do not meet well with each other, and the current hypothesis is the 770.6 ps is from another ILCT state (<sup>1</sup>ILCT-2) which forms equilibrium with <sup>3</sup>NAP via ISC and rISC process and this equilibrium is reached with lifetime 44 ps and <sup>3</sup>NAP is dominant here according to GLA result of TA (show in **Fig.3.29**) where the EAS3 (CT state) decays into EAS4

(<sup>3</sup>NAP state).



Energy level diagram of **Pt-2** in DMF is suggested in **Fig.3.31**, in which after excitation at 400 nm, the FC state populated decays into <sup>1</sup>MMLCT state within 0.2 ps and the <sup>1</sup>MMLCT state undergoes ultrafast ISC process with 0.6 ps lifetime to a <sup>1</sup>ILCT-1 state which further decays into another <sup>1</sup>ILCT-2 state within 3.2 ps, these two ILCT state are different in the distance between positive charge centre and the NAP anion. Then the <sup>1</sup>ILCT-2 state reaches an equilibrium with <sup>3</sup>NAP state within 44.0 ps.

## THF

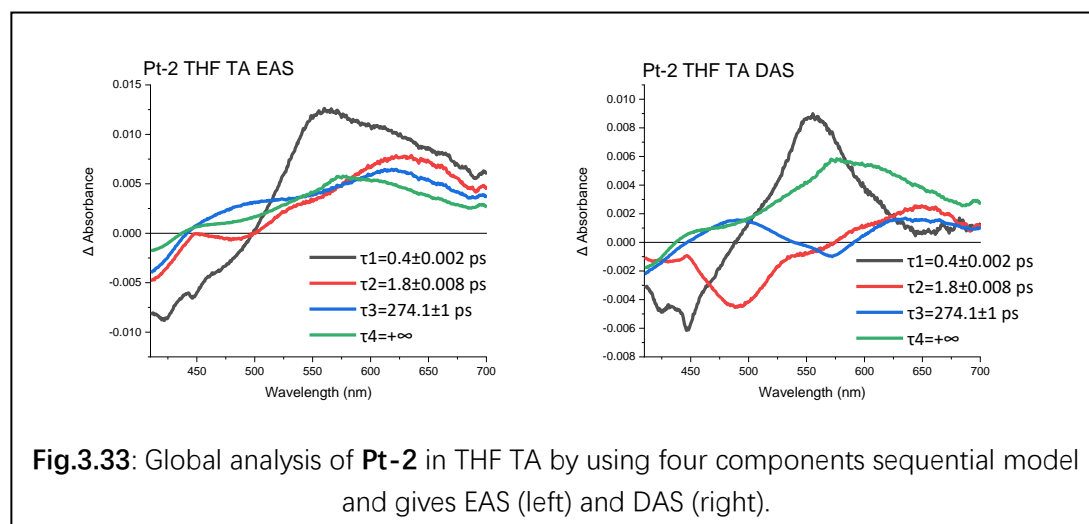


The TA spectra show in **Fig.3.32** show similar phenomenon as **Pt-2** in THF and DMF. The stimulated emission signal at around 480 nm rises first and then undergoes an ultrafast decay into a state with absorption at 500 nm

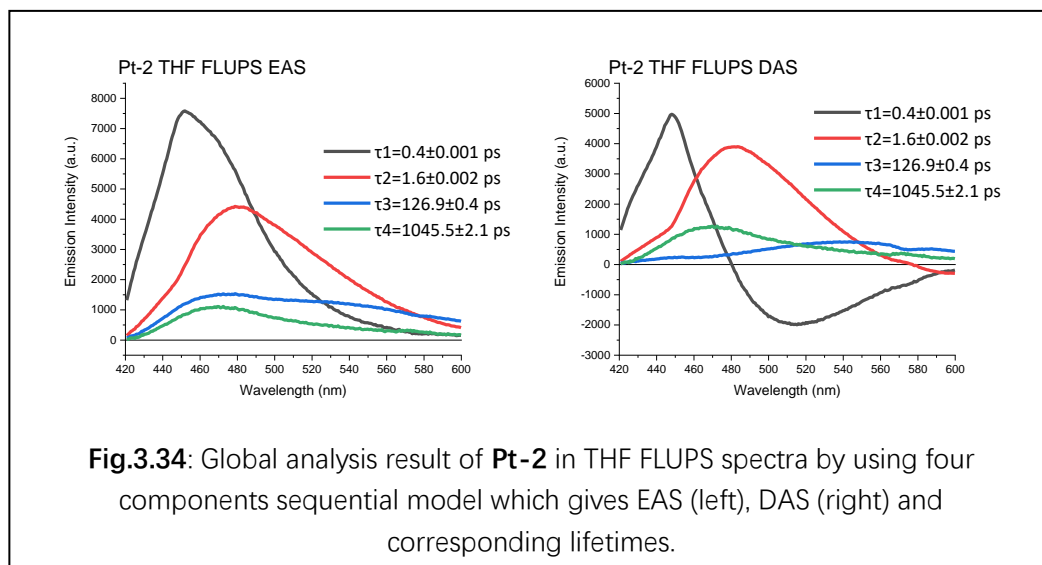


which could be attributed to the  $^1\text{ILCT}$  state then this state decays into a long lived  $^3\text{NAP}$  excited state at around 400 ps and the long-lived state also absorbs at 575 nm which is hypothesised to be partly due to a negative charge on the NAP ligand in  $^3\text{NAP}$  state/ a CT state equilibrium.

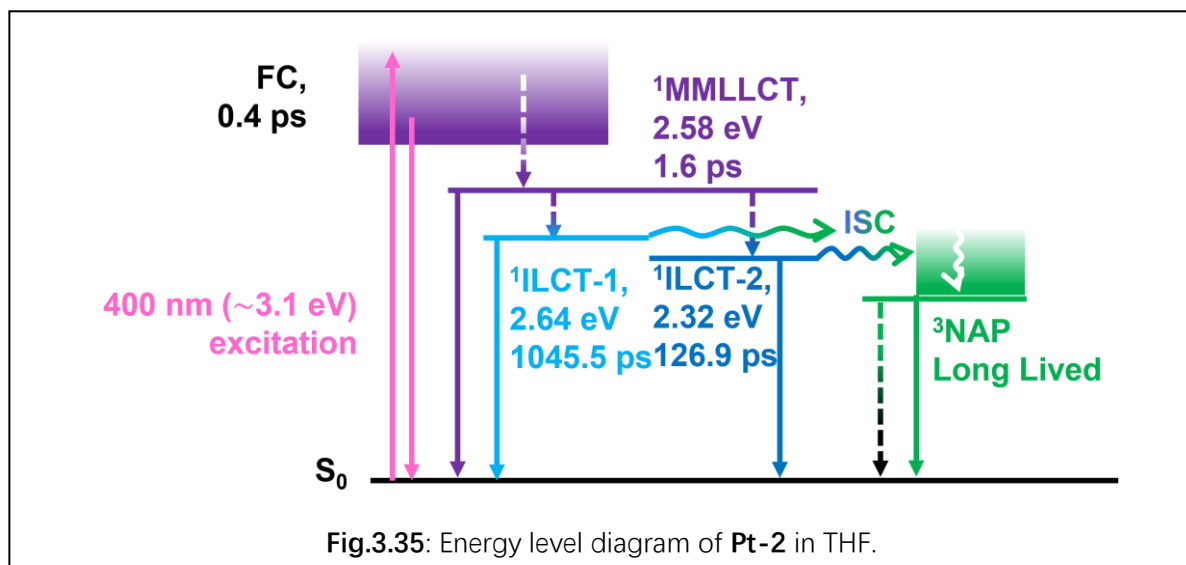
From the FLUPS spectra collected, a fast decay at 465 nm at early time is also observed. The emission spectra formed from the decay of the 465 nm spectrum has a peak at 470 nm and a shoulder at around 530 nm which decay together with a very long lifetime, there are still emission observed at 1970 ps. This result indicates that there could be a long-lived fluorescent state.



Global analysis results of **Pt-2** in THF TA are given in **Fig.3.33**, in which the first two EAS traces show stimulated emission band at around 460 nm and the other at around 480 nm, this indicates decay process from one singlet state to another with lifetime 0.4 ps. In the third EAS with the lifetime 274.1 ps there is no stimulated emission band. The 274.1 ps EAS shows a broadband absorption at 500 nm which corresponding with a somewhat broadened  $\text{NAP}^-$  anion absorption which indicates this state is a CT state and could be attributed to ILCT state based on the condition discussed in **Chapter 2**.

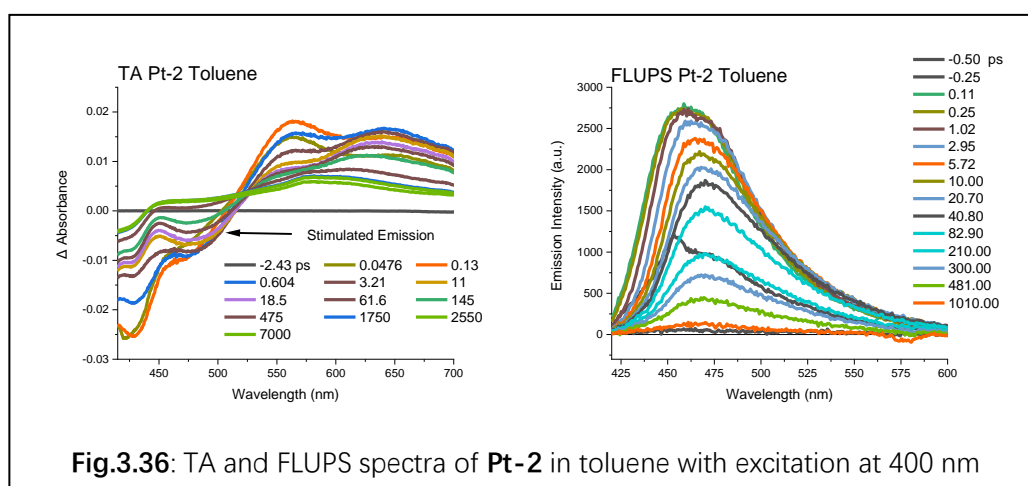


Global analysis of FLUPS of **Pt-2** in THF is given in **Fig.3.34**. The first two excited states extracted with lifetime 0.4 ps (460 nm) and 1.6 ps (480 nm) meet well with the first two components extracted from TA, which could be attributed to FC state and <sup>1</sup>MMLLCT state. However, the two slower components extracted from FLUPS do not meet well with the TA result. The third EAS extracted in FLUPS, contains two peaks, one at 470 nm, the other at 535 nm which indicates that there are two different excited states decaying together. The third and fourth DAS extracted show peaks at 470 nm and 535 nm, respectively. But the third DAS does not show a negative band which indicated it does not decay into the fourth DAS which indicates there are two independently decaying states, one with a 470 nm band and the other with a 535 nm band. These two states are different singlet ILCT states as FLUPS can detect strong emission from these two states. Both populated by the decay of a higher-lying excited state, to whom the second EAS corresponds. This hypothesis explains why global analysis extracted only one trace with 271.1 ps lifetime because it is a mixture of two ILCT state with similar absorption bands in TA, with the lifetimes 126.9 ps and 1045.5 ps.



The energy level diagram of **Pt-2** in THF is given in **Fig.3.35**. With 400 nm excitation, the FC state is populated and decay into the  $^1\text{MMLCT}$  state with 0.4 ps lifetime, then the  $^1\text{MMLCT}$  state intersystem crosses with lifetime of 1.6 ps to generate two independent  $^1\text{ILCT}$  state, one of the  $^1\text{ILCT}$  state ( $^3\text{ILCT-1}$ ) lifetime is 126.9 ps, the other ( $^3\text{ILCT-2}$ ) is 1045.5 ps. Then these two ILCT state decay into  $^3\text{NAP}$  which is long lived.

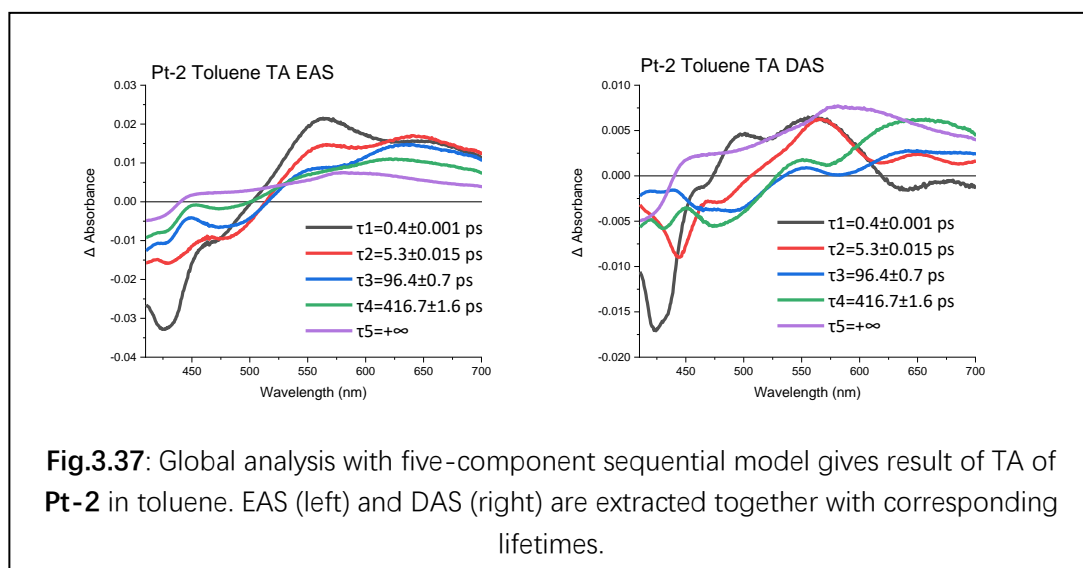
## Toluene



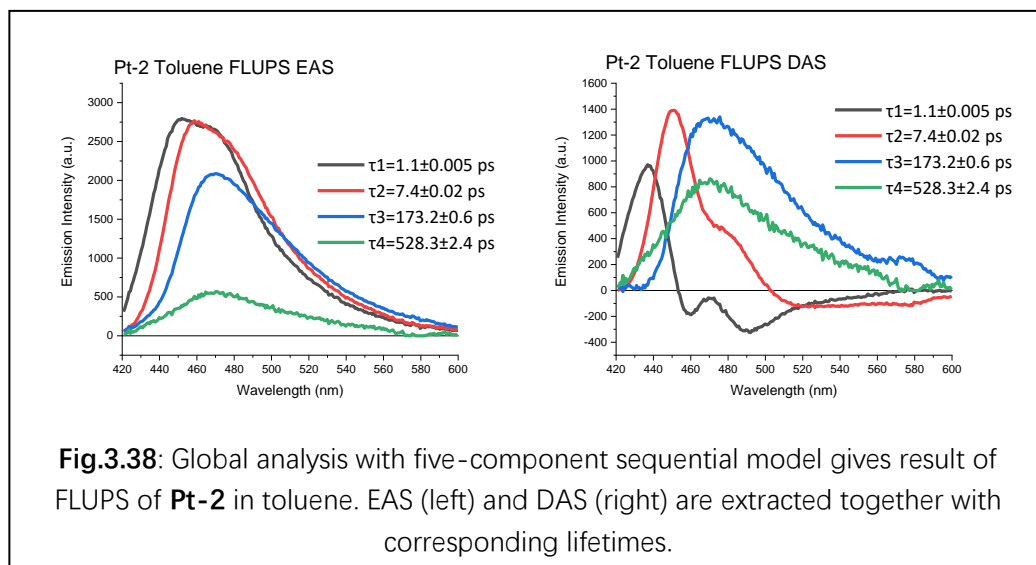
TA spectra of **Pt-2** in toluene with excitation at 400 nm is shown in **Fig.3.36**, a stimulated emission signal is observed at 460 nm which corresponds to a singlet state. This stimulated emission signal decays slowly until 475 ps, then the last  $^3\text{NAP}$  state is populated with low yield, and this  $^3\text{NAP}$  state also has

a tiny peak at 575 nm which indicates it contains a tiny amount negative charge on the NAP ligand like **Pt-2** in polar solvents discussed before.

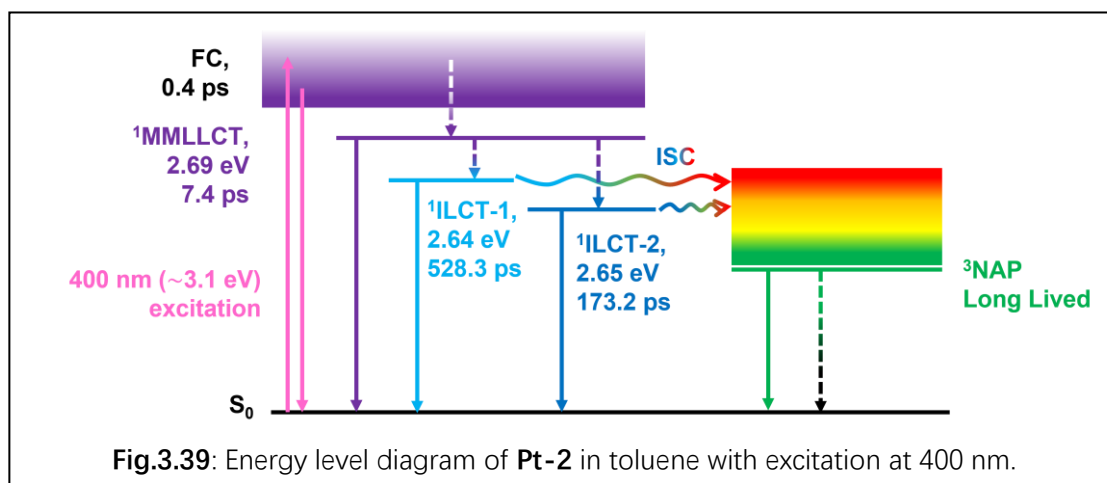
A strong and slowly decaying emission band is also observed in FLUPS spectra shown in **Fig.3.36** which indicates the ISC process of **Pt-2** in toluene is also slow and the rate need to be extracted by GLA.



By applying global analysis to TA spectra of **Pt-2** in toluene (result show in **Fig.3.37**), five components are needed to fit the data. The first four EAS show stimulated emission signal at 480 nm; and the last state is long-lived and attributed to  $^3$ NAP state. Lifetimes extracted for the first four states are 0.4 ps, 5.3 ps, 96.4 ps and 416.7 ps. The first state populated is attributed to FC state and the 5.3 ps component is attributed to  $^1$ MMLLCT state. The other two components could be attributed to  $^1$ ILCT states which is similar to the process observed in **Pt-2** in DMF, DCM and THF.



Global analysis extracts four components from FLUPS spectra of **Pt-2** in Toluene and corresponding lifetimes (show in **Fig.3.38**). The first trace with lifetime of 1.1 ps could be attributed to FC state and the 7.4 ps trace is attributed to <sup>1</sup>MMLCT state. The other two emissive states could be attributed to two different singlet ILCT state as the stimulated emission signal at the same wavelength is extracted from TA spectra with similar lifetimes. Also, from DAS extracted, there are negative signal of the second DAS which indicates there is a decay into a successor state, whilst the third EAS does not show such negative signal. This indicates the third and fourth populated excited states are populated by decay from the second EAS corresponding excited state and then decay independently which is similar to the situation in THF.



Energy level diagram of **Pt-2** in toluene is given in **Fig.3.39**. In which the first populated FC state decays into  $^1\text{MMLCT}$  state with lifetime 0.4 ps. Then this singlet state decays into two different singlet ILCT state, the  $^1\text{ILCT-1}$  and  $^1\text{ILCT-2}$ , which is different in lifetime. Then these two states ISC to  $^3\text{NAP}$  state but the rate cannot be obtained as there are two singlet state ISC at the same time and grows in rate of  $^3\text{NAP}$  cannot be extracted from TA spectra as the absorption band of  $^3\text{NAP}$  state and the CT states overlapped with each other.

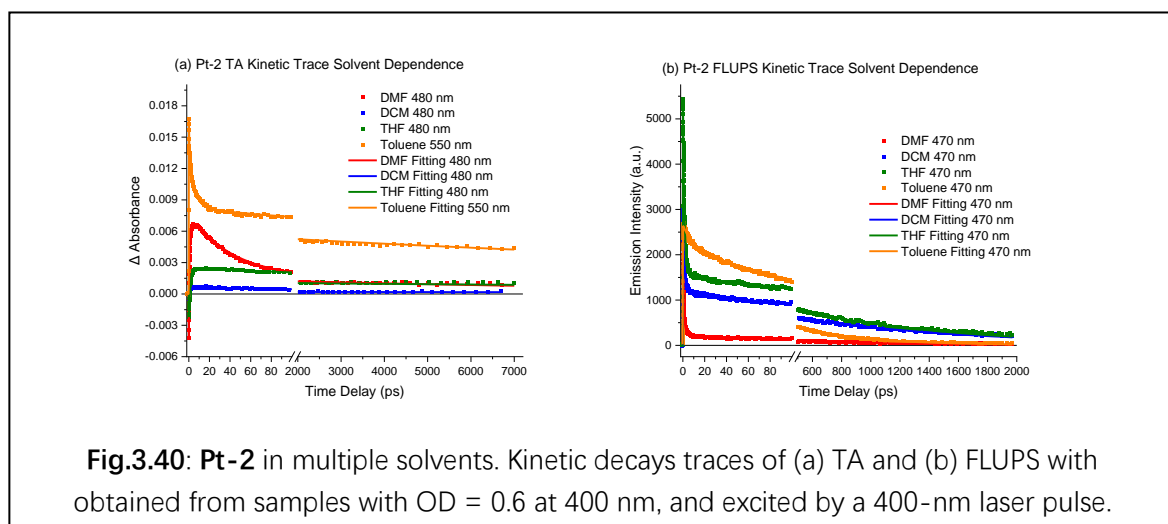
### Summary of excited state dynamics of Pt-2 in Multiple Solvents

Pt-2 TA	$\tau_1/\text{ps}$	$\tau_2/\text{ps}$	$\tau_3/\text{ps}$	$\tau_4/\text{ps}$	$\tau_5/\text{ps}$
DMF (0.901)	$0.3 \pm 0.001$	$1.9 \pm 0.004$	$44 \pm 0.05$	-	$+\infty$
DCM (0.765)	$0.4 \pm 0.003$	$1.5 \pm 0.01$	$166.8 \pm 0.8$	-	$+\infty$
THF (0.494)	$0.4 \pm 0.002$	$1.8 \pm 0.008$	$274 \pm 1$	-	$+\infty$
Toluene (0.172)	$0.4 \pm 0.001$	$5.3 \pm 0.015$	$96.4 \pm 0.7$	$416.7 \pm 1.6$	$+\infty$

Pt-2 FLUPS	$\tau_1/\text{ps}$	$\tau_2/\text{ps}$	$\tau_3/\text{ps}$	$\tau_4/\text{ps}$
DMF (0.901)	$0.2 \pm 0.001$	$0.6 \pm 0.002$	$3.2 \pm 0.01$	$770.6 \pm 2.4$
DCM (0.765)	$0.3 \pm 0.001$	$1.4 \pm 0.002$	$74.3 \pm 0.3$	$1191 \pm 1.3$
THF (0.494)	$0.4 \pm 0.001$	$1.6 \pm 0.002$	$126.9 \pm 0.4$	$1045.5 \pm 2.1$
Toluene (0.172)	$1.1 \pm 0.005$	$7.4 \pm 0.02$	$173.2 \pm 0.6$	$528.3 \pm 2.4$

**Table.3.7:** Conclusion of lifetimes of **Pt-2** in multiple different solvents (DMF, THF, DCM and toluene) extracted from TA (up) and FLUPS (down) spectra. Eisenberg's solvent Parameters are given in the brackets. The error shown here is given by Glotaran.



**Fig.3.40:** Pt-2 in multiple solvents. Kinetic decays traces of (a) TA and (b) FLUPS with obtained from samples with OD = 0.6 at 400 nm, and excited by a 400-nm laser pulse.

Lifetimes extracted from TA and FLUPS data of **Pt-2** are given in **Table.3.7**, the first short lived state corresponds with the FC state, the second state is an  $^1\text{MMLLCT}$  state, and the last populated long-lived state is attributed to  $^3\text{NAP}$  state. For **Pt-2**, the solvent does not influence energy levels of the excited states a lot but changes the energy level diagram and excited states dynamics by influencing ISC rate and equilibrium formed between excited states. **Pt-2** in different solvents undergoes similar decay pathways but may change the ratio of  $^1\text{ILCT-1}$  and  $^1\text{ILCT-2}$ . The corresponding energy level diagrams based on FLUPS and TA has been given in **Fig.2.15** in **Chapter 2** (DCM), **Fig.3.31** (DMF), **Fig.3.35** (THF) and **Fig.3.39** (Toluene).

### 3.4. Conclusion

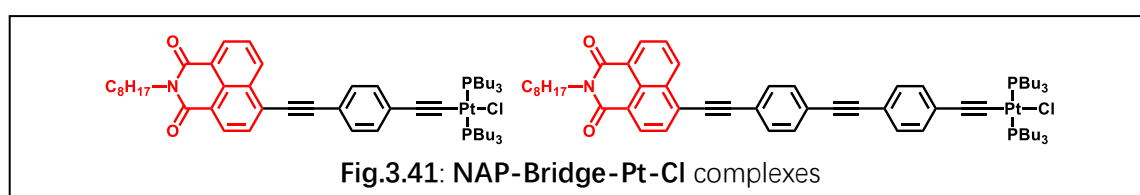
Solvent effect on the excited state dynamics of A-B-A Pt complexes occurs via different mechanisms, depending on the length of the bridge. For **Pt-0**, solvents with different dipole moments influence the energy of the  $^1\text{MMLLCT}$  state to a different extent, and the difference in the excited state energy further influences the dynamics of the excited states, which makes the ISC rate rank from high to low as  $\text{DMF} > \text{THF} \sim \text{DCM} > \text{toluene}$ . This effect could be explained as with the decrease of solvent dipole moment, energy gap difference between singlet and targeted triplet states is increasing which makes it hard for the starting singlet

state to reach a suitable geometry to make it have the same energy before and after ISC, so the ISC rate is decreased.

For **Pt-1**, the solvent effect also changes the energy of different excited states and leads to an equilibrium between excited states. The change of states energy and their decay pathways makes the solvent effect on ISC rate of **Pt-1** very different to that for **Pt-0**, with the ISC rate rank from high to low as toluene>DCM >THF. This may be because the nature of <sup>1</sup>MMLLCT state in **Pt-0** and <sup>1</sup>Cumulenic MLCT state in **Pt-1** are different, or the ISC process observed in **Pt-0** is actually decay process from <sup>1</sup>MMLLCT and <sup>3</sup>MMLLCT state mixture to <sup>3</sup>NAP which is dominated by decay rate of <sup>3</sup>MMLLCT to <sup>3</sup>NAP but ISC rate detected in **Pt-1** is from <sup>1</sup>Cumulenic MLCT to <sup>3</sup>Cumulenic MLCT. So in **Pt-0**, the ISC observed could be treated as a decay process from a CT state to a ligand-localised state. More polar the solvent, lower the CT state energy, lower the energy gap between CT state and <sup>3</sup>NAP, and higher the rate of the ISC. In **Pt-1**, the observed ISC is between two states with similar electronic structure which makes solvent polarity much less important, as it offers similar stabilisation to the singlet and triplet states.

For **Pt-2**, the solvent effect on ISC process can happen in two different <sup>1</sup>ILCT states. For <sup>1</sup>ILCT-1, the ISC rate rank is DMF>DCM>THF>toluene. For <sup>1</sup>ILCT-2, the ISC rate rank is toluene>DMF>THF>DCM. However, for **Pt-2** there could be equilibrium between <sup>1</sup>ILCT-1 and <sup>1</sup>ILCT-2 or even between ILCT state and <sup>3</sup>NAP state. The nature of excited states of **Pt-2** need to be further investigated.

### 3.5. Future Work





To further investigate the nature of excited states generated when solvent polarity is changed from toluene to DMF, TRIR of **Pt-0**, **Pt-1** and **Pt-2** in toluene, THF and DMF could be done, for example cumulenenic structure generation process of **Pt-1** in toluene. Also, the ligand opposite to NAP ligand may also influence excited nature and lifetime which will be discussed in **Chapter 5** later, excited state dynamics of **NAP-Bridge-Pt-Cl** (structure show in **Fig.3.41**) should be investigated.

### 3.6. Reference

- 1 C. Reichardt, *Chem Rev*, 1994, **94**, 2319–2358.
- 2 S. D. Cummings and R. Eisenberg, *J Am Chem Soc*, 1996, **118**, 1949–1960.
- 3 W. Paw, S. D. Cummings, M. A. Mansour, W. B. Cennick, D. K. Geiger and R. Eisenberg ~', *Luminescent platinum complexes: tuning and using the excited state*, 1998, vol. 171.
- 4 J. A. Zuleta, J. M. Bevilacqua and R. Eisenberg, *Coord Chem Rev*, 1991, **111**, 237–248.
- 5 J. J. Sutton, D. Preston, P. Traber, J. Steinmetzer, X. Wu, S. Kayal, X. Z. Sun, J. D. Crowley, M. W. George, S. Kupfer and K. C. Gordon, *J Am Chem Soc*, 2021, **143**, 9082–9093.
- 6 J. Clayden, *Organic chemistry*, Oxford : Oxford University Press, 2001, Oxford, 2001.
- 7 P. A. Scattergood, M. Delor, I. V. Sazanovich, O. V. Bouganov, S. A. Tikhomirov, A. S. Stasheuski, A. W. Parker, G. M. Greetham, M. Towrie, E. S. Davies, A. J. H. M. Meijer and J. A. Weinstein, *Dalton Transactions*, 2014, **43**, 17677–17693.
- 8 G. A. Farrow, M. Quick, S. A. Kovalenko, G. Wu, A. Sadler, D. Chekulaev, A. A. P. Chauvet, J. A. Weinstein and N. P. Ernsting, *Physical Chemistry Chemical Physics*, 2021, **23**, 21652–21663.
- 9 R. M. Van Der Veen, A. Cannizzo, F. Van Mourik, A. Vlček and M. Chergui, *J Am Chem Soc*, 2011, **133**, 305–315.
- 10 Heather Carson, PhD *Graduation Thesis, the University of Sheffield, 2022.*

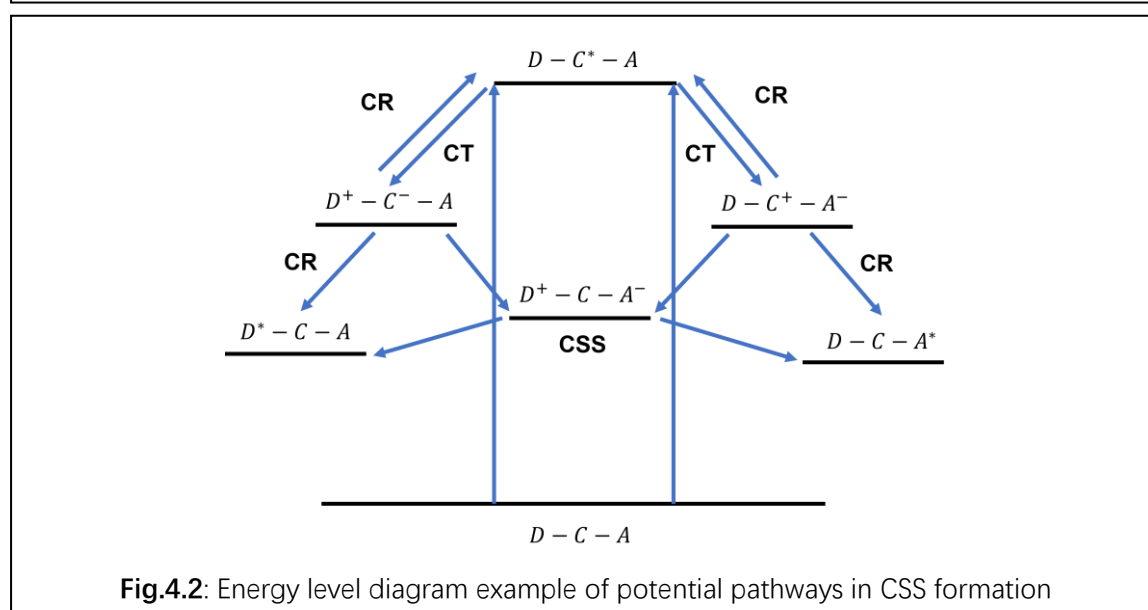
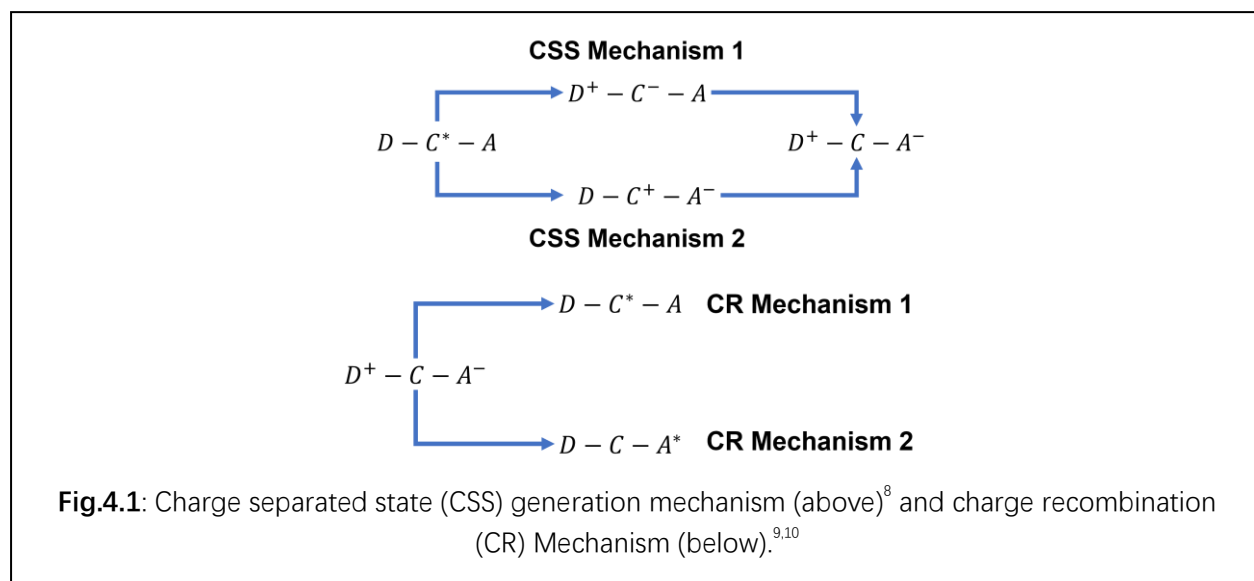
## 4. Chapter 4- Pt A-B-A Complex IR Control

### 4.1 Introduction

Photoinduced charge transfer and charge separation process are key steps in harvesting solar energy and converting the harvested energy into chemical energy, as a potential path for photocatalysis of water splitting or carbon dioxide reduction. To perform a photoinduced charge separation process, donor-bridge-acceptor ( $D - B - A$ ) systems are used. However, the quantum yield of the formation of photoinduced charge separation state (CSS), and the lifetime of the CSS are limited. This is mainly because charge recombination (CR) process plays a major role in the loss of the populated charge separated state<sup>1</sup> or the population of CSS is inhibited/outcompeted by other reactions.<sup>2</sup>

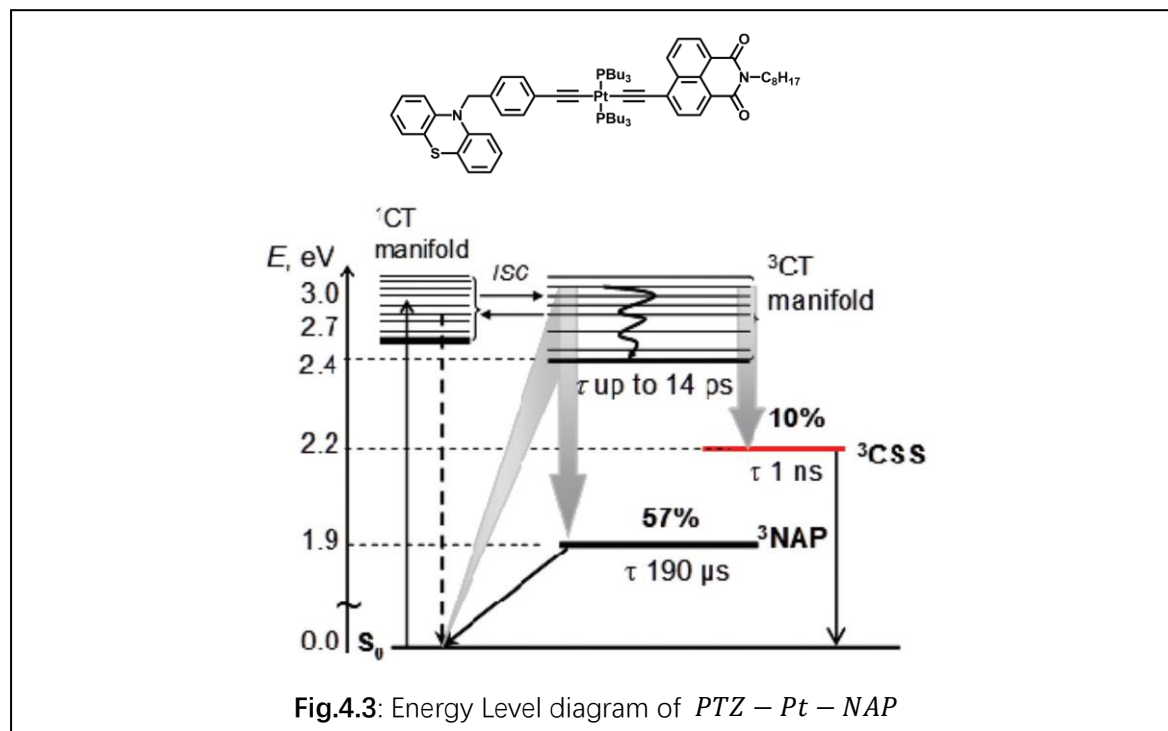
In a typical  $D - B - A$  photocatalysis system, after photoexcitation, the electron transfer from the donor side to the acceptor side and produce  $D^+ - B - A^-$  product directly,<sup>3</sup> via through-space<sup>4</sup> or through-bond (super-exchange) mechanism.<sup>5-7</sup> Instead of  $D - B - A$  system, a Donor-Chromophore-Acceptor ( $D - C - A$ ) system is developed to increase light harvesting ability by using a chromophore to replace the 'bridge' in  $D - B - A$  system. Then the chromophore (C) absorbs light or excite an antenna array and then the antenna array transport energy to C to get excited  $C^*$ . Then there are two mechanisms to achieve charge-separated state (CSS) which are shown in **Fig.4.1**. The two mechanisms differ in the intermediate state before the CSS:  $D^+ - C^- - A$  is formed for **CSS Mechanism 1** and  $D - C^+ - A^-$  is formed for **CSS Mechanism 2**.<sup>8</sup> However, the CSS formed can also be quenched by charge recombination (CR) process (show in **Fig.4.1**) and generate  $D - C^* - A$  (**CR Mechanism 1**), or  $D - C - A^*$  (**CR Mechanism 2**).<sup>9,10</sup> CR process can also inhibit CSS formation process by quenching the charge transfer (CT) state formed: 1).  $D - C^+ - A^- \rightarrow D^* - C - A$ ,<sup>11</sup> or 2).  $D - C^+ - A^- \rightarrow D - C - A^*$ .<sup>12</sup> For  $D - B - A$  complexes, the charge separated state formed can also be quenched via: 1).  $D^+ -$

$B - A^- \rightarrow D - B - A^*$  or 2).  $D^+ - B - A^- \rightarrow D^* - B - A$ .<sup>13</sup> An example energy level diagram for potential pathways is shown in **Fig.4.2**.



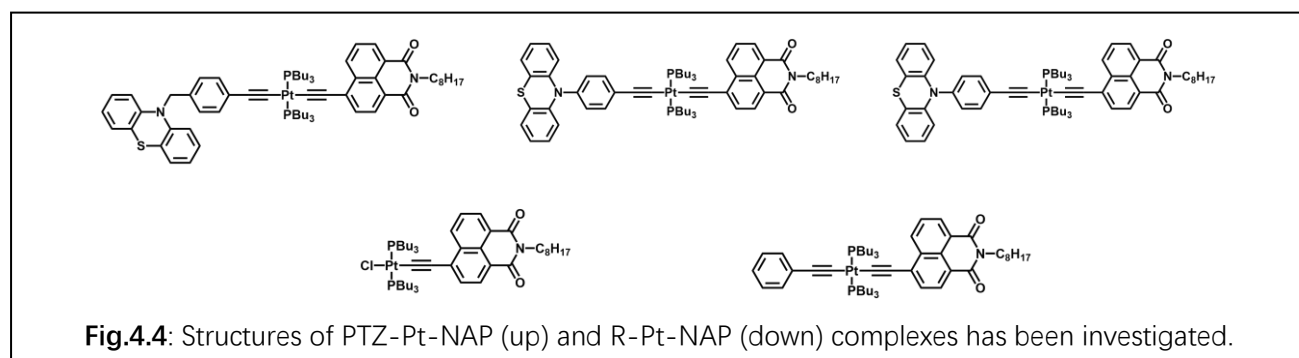
To construct a  $D - C - A$  system that can populate a CSS state, Pt(II) could be used as the chromophore with naphthalimide (NAP) as electron acceptor and phenothiazine (PTZ) as electron donor, the NAP and PTZ are linked with Pt centre by acetylide to give  $PTZ - Pt - NAP$  complexes (structure show in **Fig.4.3**).<sup>12,14</sup> These complexes, after photo-excitation, form a metal to ligand charge transfer (MLCT) state:  $PTZ - Pt - NAP \rightarrow PTZ - Pt^+ - NAP^-$ , followed by an electron donation from the PTZ ligand to Pt centre:  $PTZ - Pt^+ - NAP^- \rightarrow PTZ^+ - Pt - NAP^-$  to give charge

separated state (CSS); or charge recombination can take place:  $PTZ - Pt^+ - NAP^- \rightarrow PTZ - Pt - NAP^*$  to give triplet NAP state ( $^3NAP$ ), in other words, the MLCT state branches into CSS state and  $^3NAP$  state as shown in **Fig.4.3**.<sup>12,14,15</sup>



These  $PTZ - Pt - NAP$  and corresponding  $R - Pt - NAP$  complexes (Structures shown in **Fig.4.4**) all undergo ultrafast (tens of picoseconds) internal conversion (IC) and intersystem crossing (ISC) process<sup>14,15</sup> compared with hundreds picosecond to nanoseconds lifetime of these processes in full organic  $R - NAP$  molecules,<sup>16</sup> which indicates for these complexes, their potential energy surfaces (PES) of  $^1MLCT$ ,  $^3MLCT$ ,  $^3CSS$ , and  $^3NAP$  states are strongly coupled with each other. Strong coupling of PESs or in other words small energy gap between excited electronic states is one of the conditions that the Born-Oppenheimer (BO) approximation (or adiabatic approximation) breaks down.<sup>17,18</sup> When the Born-Oppenheimer approximation breaks down, non-adiabatic coupling between excited states means that the vibrational modes can influence the electronic states populated.<sup>19,20</sup> Furthermore, under such a non-BO regime, one can introduce an infrared (IR) laser pulse to pump specific

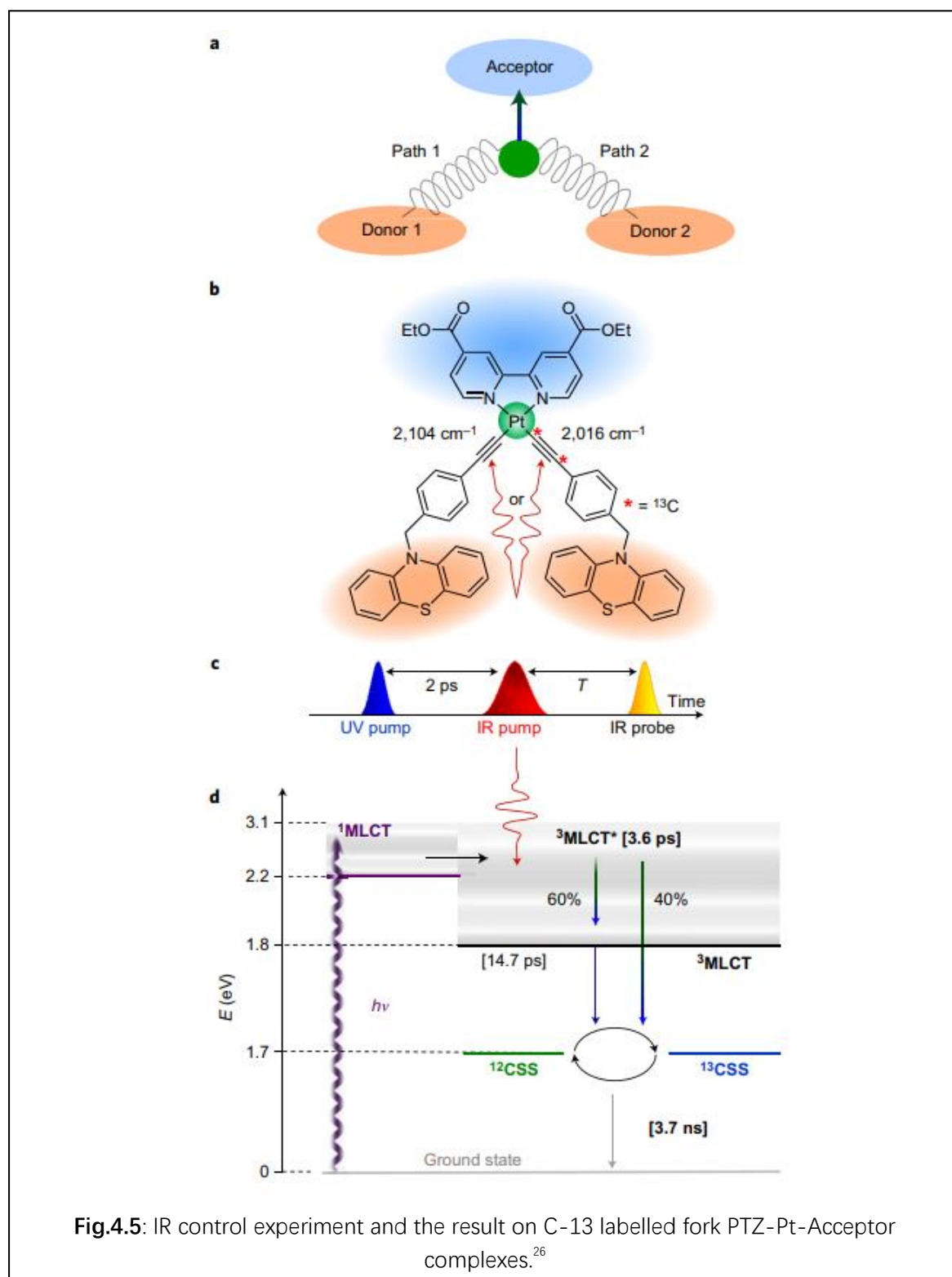
vibrational modes in the excited state, and selectively increase the yield of a specific product excited state, the  $^3\text{NAP}$  state in  $\text{PTZ} - \text{Pt} - \text{NAP}$ .<sup>15,21,22</sup> Also, similar IR control phenomenon is also reported in organic D...A dyads linked by hydrogen bonds.<sup>23</sup>



IR control phenomenon in  $\text{PTZ} - \text{Pt} - \text{NAP}$  was explained as the IR pulse pump the  $\text{C} \equiv \text{C}$  bond into its higher vibrational states which increase the  $\text{C} \equiv \text{C}$  bond length, the change in bond length makes the potential energy of  $^3\text{CSS}$  state being higher than  $^3\text{MLCT}$  state, so the population of  $^3\text{CSS}$  path is blocked,  $^3\text{NAP}$  state is populated instead.<sup>15,21,24,25</sup>

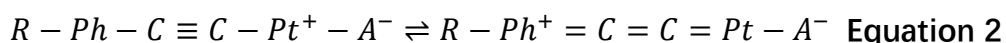
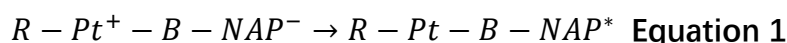
To develop these systems towards control of channelling charges in a particular direction, a  $^{13}\text{C}$  labelled Pt complex  $\text{PTZ}-(^{12}\text{C} \equiv ^{12}\text{C})-\text{Pt}(\text{Bpy})-(^{13}\text{C} \equiv ^{13}\text{C})-\text{PTZ}$  complex is synthesized (**Figure 4.4**).<sup>26</sup> In this complex, two PTZ groups are linked with the acceptor via  $\text{C} \equiv \text{C}$  bonds, but as one of them is  $^{13}\text{C}$ -labelled, the two bonds will have different vibrational frequency (by about  $80 \text{ cm}^{-1}$ ), so either of these two  $\text{C} \equiv \text{C}$  bond could be selectively pumped by using an appropriate frequency IR-pump. After UV-Vis pump, this complex can form two CSS state one with positive charge hole donated from the PTZ linked with  $^{12}\text{C} \equiv ^{12}\text{C}$  ( $^{12}\text{CSS}$ ) and one with positive charge hole donated from the PTZ linked with  $^{13}\text{C} \equiv ^{13}\text{C}$  ( $^{13}\text{CSS}$ ). The IR control experiment result suggests that when pump at  $^{12}\text{C} \equiv ^{12}\text{C}$ , the formation of  $^{12}\text{CSS}$  is blocked and vice versa. This result indicates that IR pump of  $\text{C} \equiv \text{C}$  bond will block the charge transfer process

from donor to the Pt center, so the decay path from MLCT to  $^3\text{CSS}$  is hindered.<sup>26</sup>



Also, result of IR control on  $Ph - Pt - NAP$  indicates when IR pump  $C \equiv C$  bond of this complex in MLCT state, the population rate of  $^3\text{NAP}$  state is increased. To further

understand how bridge length between Pt center and NAP ligand influence back electron transfer kinetics (shown in **Equation 1**), an isomerisation process (shown in **Equation 2**) is recognized, which indicates the absorption at around 1900  $\text{cm}^{-1}$  in MLCT state for  $PTZ - Pt - NAP$  complexes is not oriented from  $C \equiv C$  bond but cumulenenic  $C = C = Pt$  structure instead.



## 4.2 Chapter Aims

1. Explore IR-control in a series of symmetric A-B-A Pt complexes introduced in **Chapter 2**. Transient two-dimensional infrared spectroscopy (T-2DIR) is used in this investigation which has a UV excitation followed by IR excitation and then broadband IR probe pulse (Shown in **Fig.4.6**). By comparing the IR probe transmission change with and without IR excitation, the influence caused by IR excitation is recognized.
2. Use the results to compare with the previous molecules showing IR-control, and deduce any correlations with the structure, coupling, and energetics of different steps.

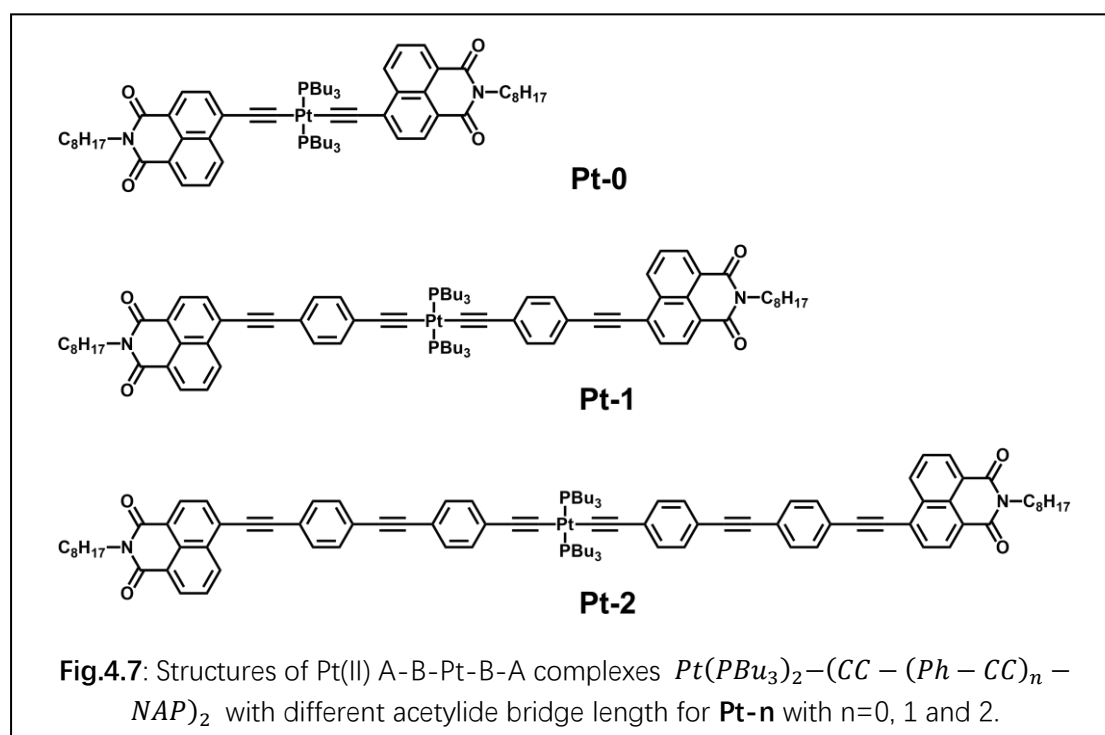


**Fig.4.6:** Pulse sequence example of T-2DIR experiment setup, here the time delay between UV pump and IR pump ( $T$ ) is fixed for certain experiment and the time delay between IR pump and IR probe are scanned to get full spectra.

## 4.3 Results and Discussion

The complexes **Pt-0**, **Pt-1** and **Pt-2** (Shown in **Fig.4.7**) are chosen as models to investigate IR excitation influence on back electron transfer dynamics from an excited charge transfer (CT) state. These complexes,  $Pt - ((C \equiv C - Ph)_n - C \equiv C - NAP)_2$  with  $n = 0, 1, 2$ , are characterised by transient absorption spectroscopy (TA),

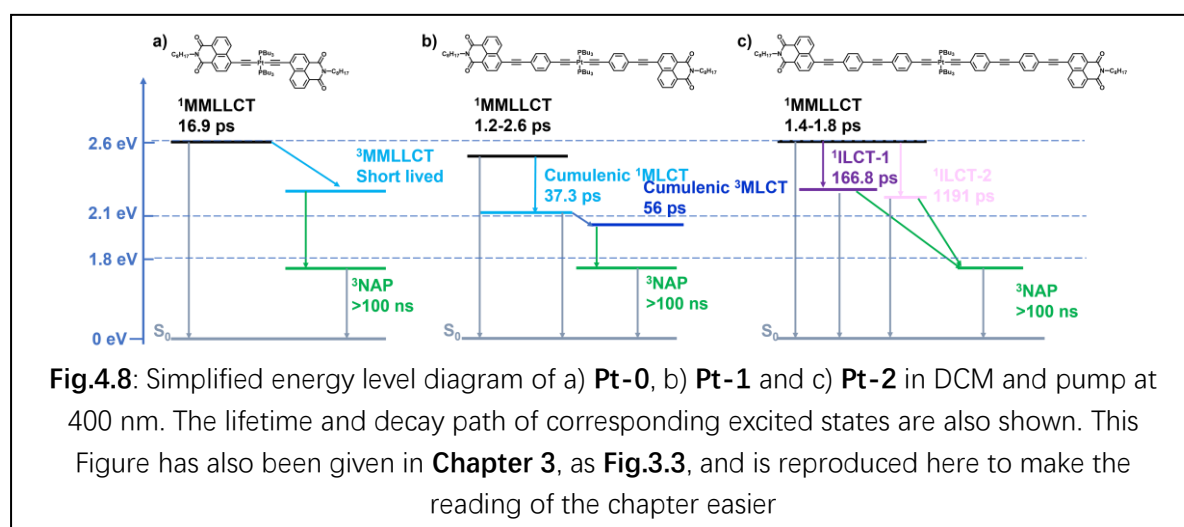
femtosecond fluorescence up-conversion spectroscopy (FLUPs) and transient infrared absorption spectroscopy (TRIR). The results discussed in **Chapter 2** indicate that with the increase of bridge length, the positive charge hole could be trapped on the bridge so back electron transfer rates decreased with the increase of bridge length, the energy level diagrams of these complexes in DCM are also reported in **Chapter 2**. In  $A - B - Pt - B - A$  complexes, only metal centre and electron acceptor groups are present. Without electron donors, the only excited states possible in A-B-Pt-B-A complexes are a {Pt/B}-to-NAP CT state, and a NAP-localised state ( $^3\text{NAP}$ ). Therefore, these  $A - B - Pt - B - A$  complexes are a good model for investigating how IR pump pulse influence back charge transfer dynamics and the contribution of different vibrational mode to IR control efficiency.



The setup of IR control experiment is by introducing IR pump pulse between ultraviolet-visible (UV-Vis) pump pulse and broadband IR probe beam, the introduced IR pump pulse is narrowband (with spectral width  $\sim 12 \text{ cm}^{-1}$ , 1.5 ps) with wavenumber which could be absorbed by excited state compound and excite the electronic excited state compound in ground vibrational state into its excited



vibrational state. The perturbation to the excited state induced by the IR pump can change the decay path of the excited state and the absorption and decay kinetics (IR range under this setup) change is observed, this change is caused by the ratio change of different excited states. However, with this setup, transient two-dimension infrared (T-2DIR) signal is also collected, so when processing IR control experiment data, IR control and T-2DIR signal should be distinguished from each other.



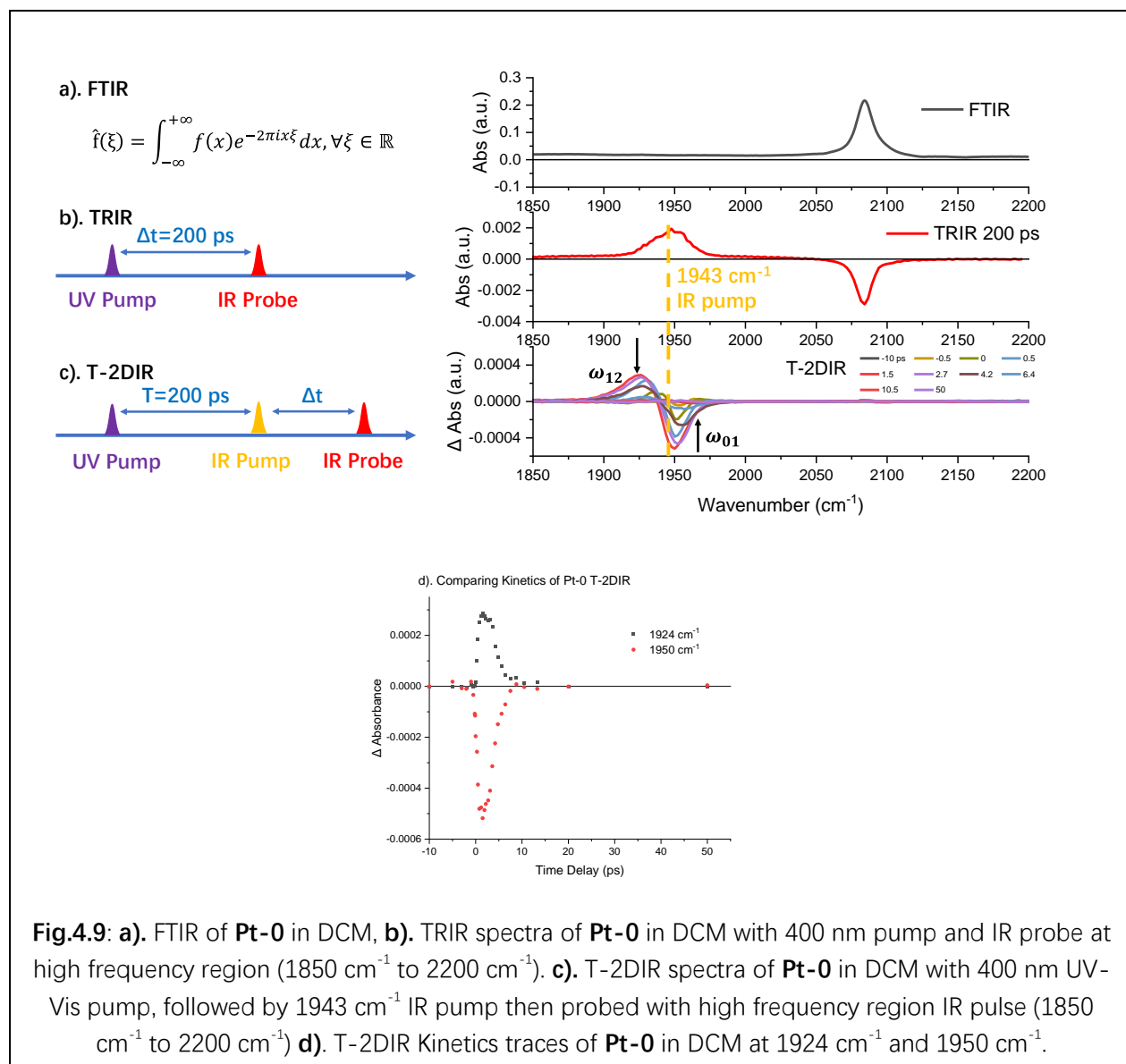
Simplified energy level diagrams of **Pt-0**, **1** and **2** are given in **Fig.4.8**. All of these complexes are investigated in DCM. An excitation with a 400 nm laser pulse populates a singlet metal-ligand-to-ligand charge transfer state ( $^1\text{MMLLCT}$ ), which is a charge transfer with charge donated from Pt metal centre/-CC- bonds to one of the NAP acceptors. The kinetic behaviour of the populated  $^1\text{MMLLCT}$  state in these complexes are different from one another as in **Pt-1** and **Pt-2**  $^1\text{MMLLCT}$  state decays into other CT state with different nature. For **Pt-0**, the  $^1\text{MMLLCT}$  state intersystem crosses (16.9 ps lifetime) to a short lived  $^3\text{MMLLCT}$  state, which then decays into a localised excited  $^3\text{NAP}$  state via back electron transfer process. (Note that we were not able to detect the  $^3\text{MMLLCT}$  state, but its presence is necessary to explain the dynamics) An alternative mechanism for this process could be for **Pt-0**,  $^1\text{MMLLCT}$  reaches equilibrium with  $^3\text{MMLLCT}$  state via ISC and reverse ISC (rISC) process within sub-picosecond time scale and  $^3\text{MMLLCT}$  decay into  $^3\text{NAP}$  state with 16.9 ps lifetime. For **Pt-1**, the  $^1\text{MMLLCT}$  state undergoes isomerisation process with lifetime 1.2 ps and

decays into cumulenenic  $^1\text{MLCT}$  state. This cumulenenic  $^1\text{MLCT}$  state contains a cumulenenic  $Pt = C = C = Ph$  fragment which is isomerised from  $Pt - C \equiv C - Ph$ , that gives an absorption band at  $1900\text{ cm}^{-1}$  in TRIR spectra, but this cumulenenic  $^1\text{MLCT}$  state undergoes ISC process to cumulenenic  $^3\text{MLCT}$  state with lifetime 37.3 ps and the cumulenenic  $^3\text{MLCT}$  state decays into  $^3\text{NAP}$  state with lifetime 56 ps. For **Pt-2**, the  $^1\text{MMLLCT}$  state with lifetimes 1.4 to 1.8 ps branches into two different intra ligand charge transfer (ILCT) state, these two ILCT states differ in the distance between positive charge and negative charge centres. These two ILCT states both decay into  $^3\text{NAP}$  state but with different lifetimes. Further details about kinetics of **Pt-0**, **Pt-1** and **Pt-2** in DCM have been discussed in **Chapter 2**.

#### 4.3.1 Transient 2DIR of Pt-0

**Pt-0** complex is used as a model to investigate kinetics of T-2DIR signal and helps extracting IR control signal from the mixture of T-2DIR and IR control signals which is what is observed experimentally. The three-pulse experiment spectra are given in **Fig.4.9**. In these spectra, IR pump pulse at  $1943\text{ cm}^{-1}$  which targets at  $C \equiv C$  vibration modes of  $^3\text{NAP}$  state is introduced after 200 ps of 400 nm pump pulse. Broadband IR pulse with wavenumber  $1850\text{ cm}^{-1}$  to  $2250\text{ cm}^{-1}$  is used as probe beam which covers the stretching vibrational mode corresponding with  $C \equiv C$  in the ground and excited state. For **Pt-0**, at 200 ps after UV pump, the only populated excited state is  $^3\text{NAP}$  which, as the lowest state, cannot branch into other states, but can only decay into the ground state. Under these conditions, the introduced IR-pump pulse leads to three potential outcomes: 1). Pump the excited electronic state from its vibrational ground state to vibrational excited state, 2). Accelerate or decelerate decay kinetics of  $^3\text{NAP}$  state to ground state. 3). No influence. In **Fig.4.9(c)**, there is a negative peak at  $\omega_{01} = 1950\text{ cm}^{-1}$  together with a neighbouring positive peak at lower frequency, with  $\omega_{12} = 1925\text{ cm}^{-1}$ , these two peaks decay synchronously and return to the baseline after 10 ps. Then the positive peak at  $1925\text{ cm}^{-1}$  corresponds to the  $1 \rightarrow 2$  absorption from the first excited vibrational state to the second excited vibrational

state and the negative peak at  $1950\text{ cm}^{-1}$  is attributed to the loss of the ground vibrational state population (depletion of  $0 \rightarrow 1$  transition).

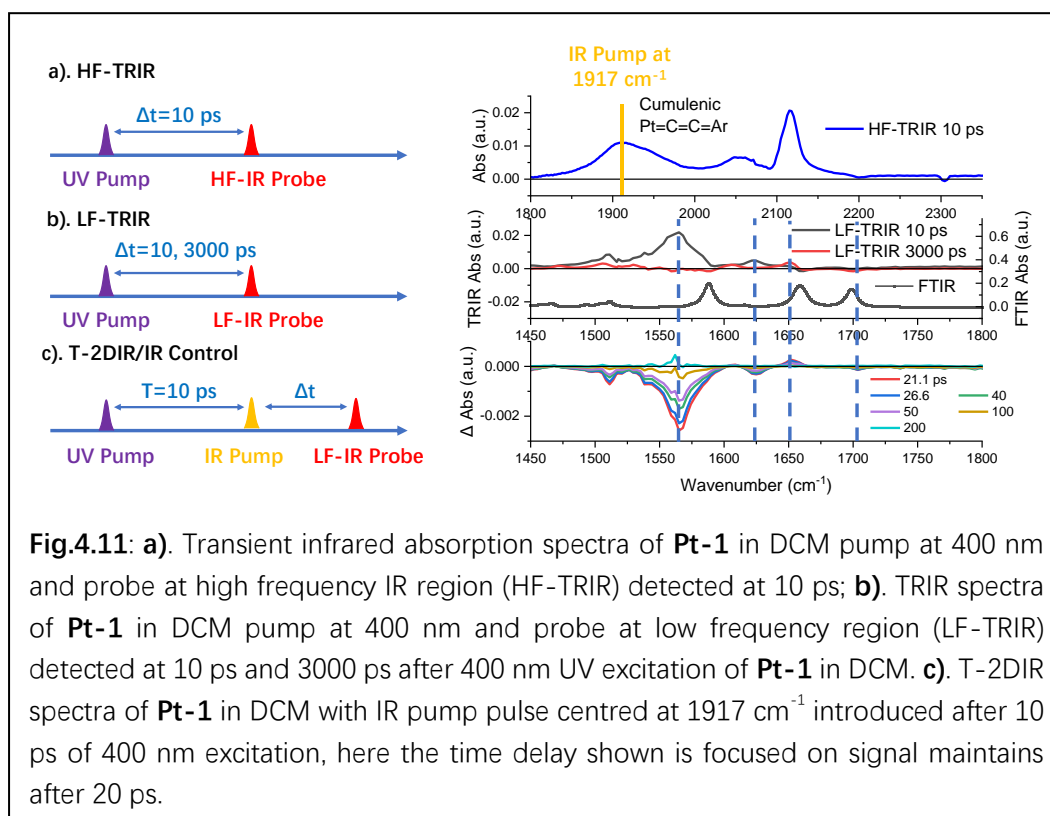
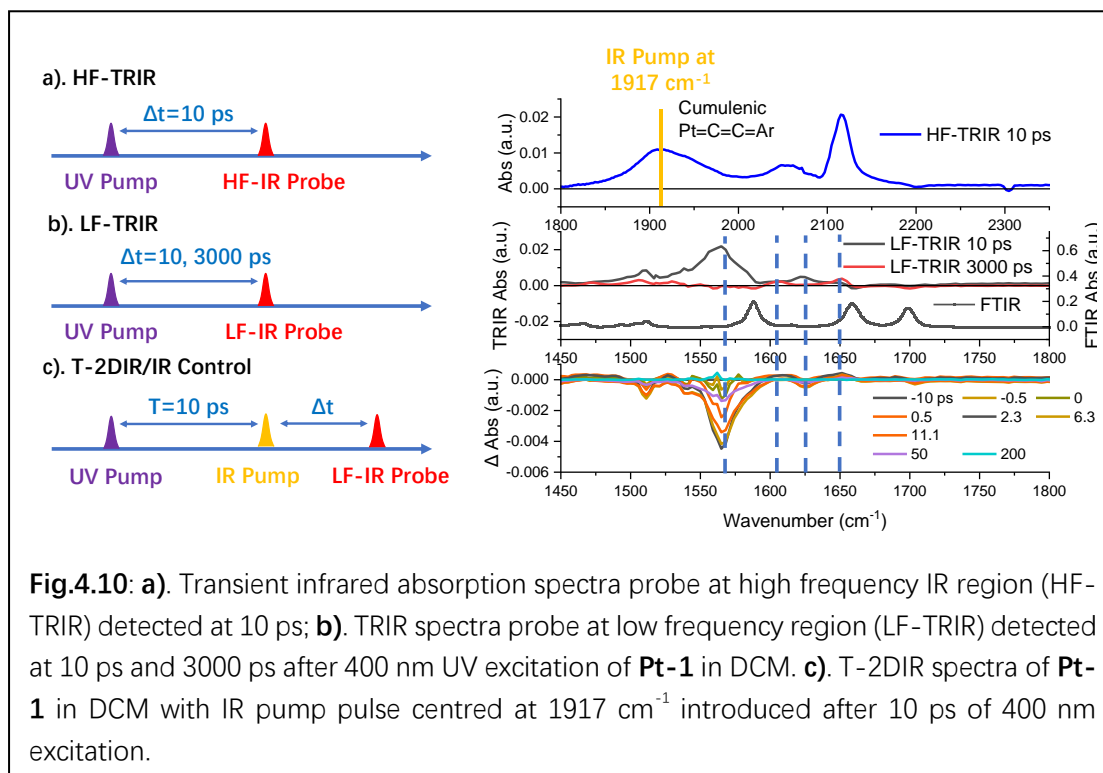


The T-2DIR spectra of **Pt-0** in DCM with UV-Vis excitation at 400 nm followed by IR excitation at  $1943\text{ cm}^{-1}$  is shown in **Fig.4.9(c)**. The  $1943\text{ cm}^{-1}$  IR excitation is delayed to 200 ps after UV-Vis excitation and is targeting at  $C \equiv C$  symmetric and asymmetric vibration mode of  $^3\text{NAP}$  state of **Pt-0**. After IR excitation, no grow-in is observed at  $2084\text{ cm}^{-1}$  which corresponds to the  $C \equiv C$  symmetric and asymmetric vibrational mode of **Pt-0** in DCM in the ground state; this result indicates that IR-excitation does not induce acceleration of  $^3\text{NAP}$  decay into ground state. The bleach and peak rise at

around  $1940\text{ cm}^{-1}$  are attributed to 2DIR signal of  $^3\text{NAP}$  excited state of **Pt-0** in DCM so there is no IR-control signal. This result is not surprising given that there is no excited state branching. Furthermore, both bleach and peak decays completely by 10 ps which is used as a reference for distinguishing a 2DIR signal of the excited states and IR controlled signal, any signal maintained after 20 ps could be treated as an IR control result and we apply this conclusion in discussing the following results.

#### 4.3.2 Transient 2DIR of Pt-1

After excitation at 400 nm, the first populated state of **Pt-1** is  $^1\text{MMLLCT}$ , which undergoes an isomerisation reaction together with ISC within 1.2-2.6 ps, forming a  $^3\text{MLCT}$  state with cumulenic  $Pt = C = C = Ph$  structure and a characteristic transient IR absorption at around  $1900\text{ cm}^{-1}$  as discussed in **Chapter 2**. This peak at  $1900\text{ cm}^{-1}$  was attributed to  $C \equiv C$  vibration in Donor-Pt-Acceptor complexes and it was used to be excited by the IR-pump in the IR-control experiments reported previously. In Donor-Pt-Acceptor systems, once this  $1900\text{ cm}^{-1}$  peak is pumped by an IR-pulse, the decay path from MLCT state to CSS state is blocked and the MLCT state only decays into  $^3\text{NAP}$  under this condition.<sup>15,21</sup> Based on our previous research, this process is caused by IR pump inhibit charge transfer process from PTZ donor to Pt positive charge centre formed in MLCT state.<sup>26</sup>



In **Pt-1**, there is no strong donor fragment but only two acceptors, which makes it a model to focus on the influence of introduced IR-pulse on the decay path from MLCT state to  $^3\text{NAP}$  state. In **Fig.4.10**, T-2DIR spectra of **Pt-1** in DCM with IR pump at 1917

$\text{cm}^{-1}$  after 10 ps of UV excitation pulse and then probe with low frequency (1450-1800  $\text{cm}^{-1}$ ) IR (LF-IR) pulse is given in **Fig.4.10(c)** comparing with TRIR spectra probe at high frequency IR (HF-IR) range in **Fig.4.10(a)** and probe at low frequency range in **Fig.4.10(b)**. However, unlike IR control experiments reported previously, there is no signal remaining at very late times with  $\Delta t \geq 200$  ps, which indicates that in this system, the introduced IR pulse does not change the population ratio of electronic excited states after 200 ps. However, based on T-2DIR signal of **Pt-0**, the T-2DIR signal vanishes after 10 ps of IR pump introduced, so all of the signal maintained after 10 ps could be treated as signal caused by electronic state population. There is still a bleach observed at 1563  $\text{cm}^{-1}$  after 50 ps which corresponds to vibration mode on the conjugated bridge of the cumulenenic form of the MLCT state of **Pt-1** in DCM. This result suggests that the IR pulse (centred at 1917  $\text{cm}^{-1}$ ) induced the loss of the cumulenenic MLCT state (detailed signal at later time, after 20 ps, is given in **Fig.4.11**). Also, from 11.1 ps to 50 ps in the three-pulse experiment, a bleach at 1625  $\text{cm}^{-1}$  is observed, which matches with the peak at the same position of LF-TRIR shown in **Fig.4.10 (b)**: this peak at 1625  $\text{cm}^{-1}$  corresponds with NAP anion ( $\text{NAP}^-$ ) absorption in LF-IR range, and thus this feature indicates the loss of MLCT state population when IR pump pulse is introduced.

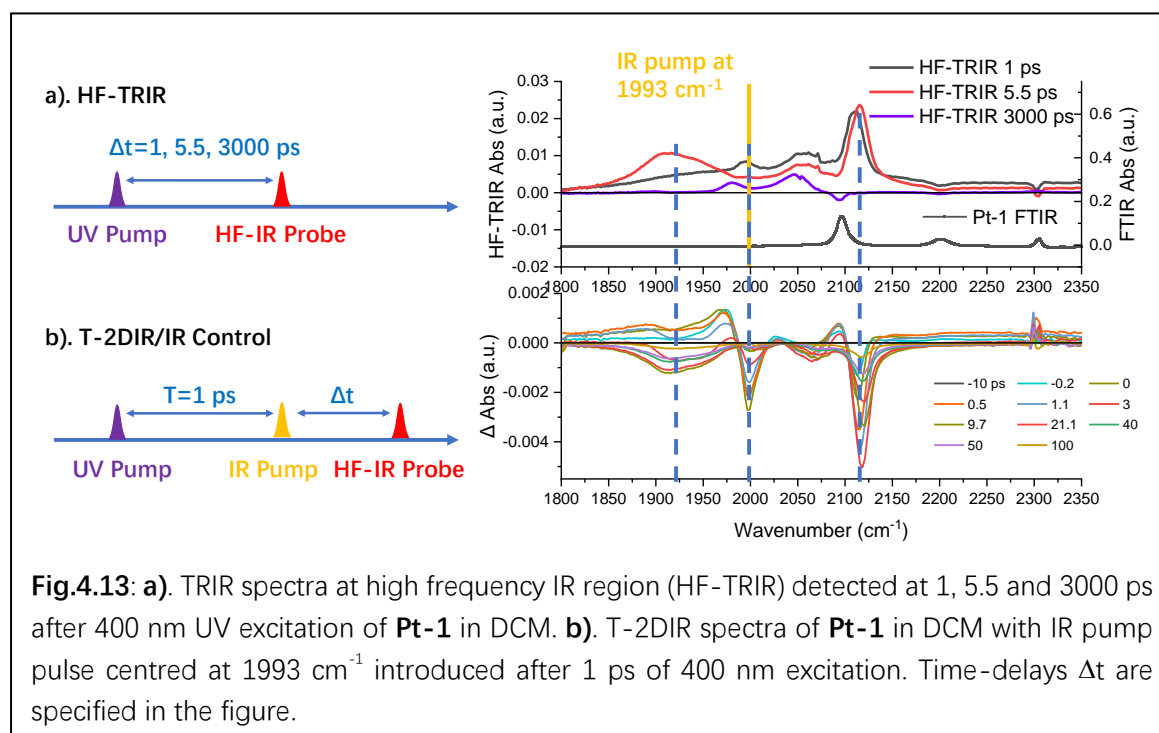
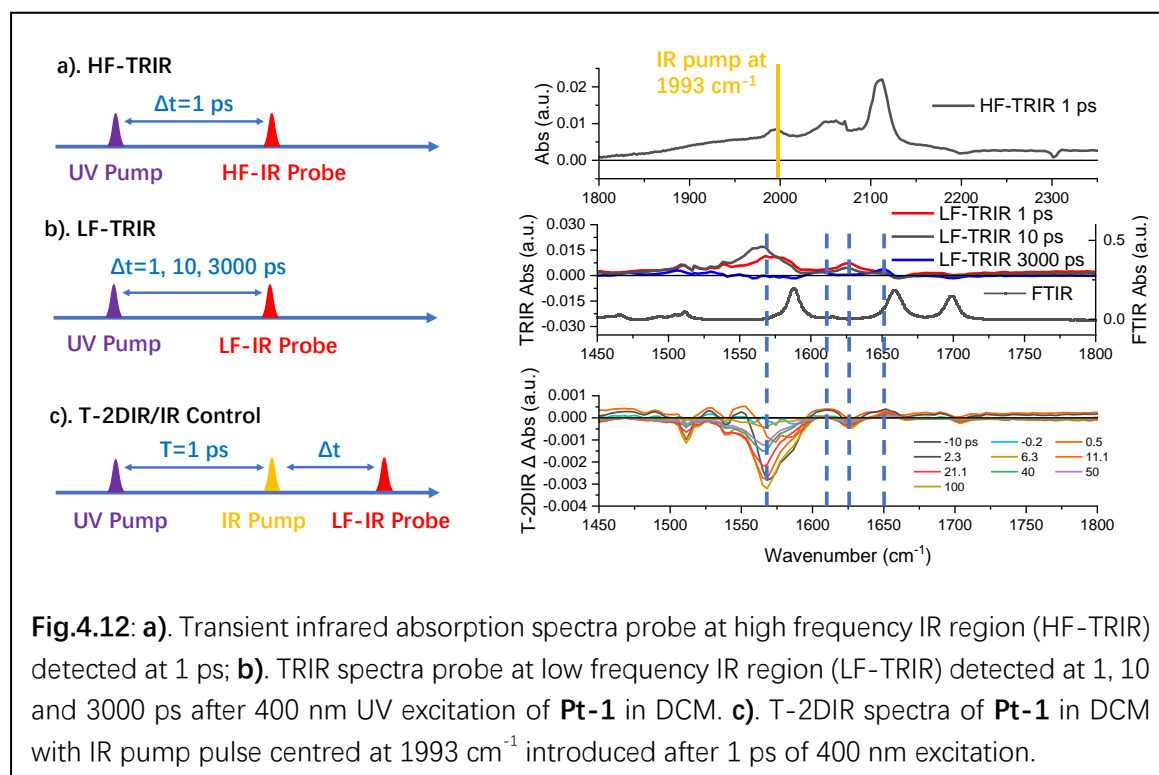
Furthermore, together with the bleach at 1625  $\text{cm}^{-1}$ , two neighboring peaks at 1608  $\text{cm}^{-1}$  and 1651  $\text{cm}^{-1}$  appear, which correspond to the formation of  $^3\text{NAP}$  state when the IR-pump pulse is introduced. This indicates that with the introduction of IR excitation on the  $Pt = C = C = Ph$  cumulenenic structure formed in the MLCT state, the decay from MLCT state to  $^3\text{NAP}$  state is accelerated. However, as **Fig.4.11** shows, after 200 ps of IR pump pulse introduction, there is no more signal. This indicates at 200 ps time delay, the introduction of IR pump pulse at 10 ps does not induce any population change in excited states. This result could be explained by all MLCT states populated with or without IR pump decaying fully to  $^3\text{NAP}$  state. This is a reasonable assumption as the lifetime of MLCT state is 37.3-56 ps without IR pump introduction and with IR pump introduction, the decay process from MLCT to  $^3\text{NAP}$  is accelerated which leads

to much shorter lifetime of MLCT state, and therefore after 200 ps no MLCT state can be populated with or without IR-pump, and the bleach corresponding with  $\text{NAP}^-$  anion vanished. Also, the lifetime of  $^3\text{NAP}$  is much longer compared with that of the MLCT state, so the difference in the amount of the decay of the  $^3\text{NAP}$  state by 200 ps is negligible whether there is between early populated caused by IR pump and without IR pump is negligible so there is also no signal corresponding with  $^3\text{NAP}$  maintains at 200 ps. For **Pt-1**, there is also no other state that could be branched into from MLCT state so the change of population ratio is also not observed.

In conclusion, when the vibrational mode of the cumulenenic structure formed in **Pt-1** MLCT state is excited, the decay from MLCT state to  $^3\text{NAP}$  state is accelerated 30.6% comparing OD at  $1563\text{ cm}^{-1}$  with the condition that no IR pump pulse is introduced to excite the vibrational mode of the cumulenenic structure formed in **Pt-1** MLCT state.

To further investigate the influence of the IR pump on the bridge vibrational mode on the excited state dynamics, the IR control experiments were conducted with the IR-pump at  $1993\text{ cm}^{-1}$  introduced at 1 ps after UV excitation, which corresponds to  $C \equiv C$  vibration mode of  $^1\text{MMLLCT}$  state before isomerisation into the cumulenenic structure; the resulting spectra with IR probe at low frequency region ( $1450\text{-}1800\text{ cm}^{-1}$ ) and high frequency region ( $1800\text{-}2350\text{ cm}^{-1}$ ) are shown in **Fig.4.12** and **Fig.4.13**. As **Fig.4.12 (c)** shows, the IR pump at  $1993\text{ cm}^{-1}$  at 1 ps causes similar changes to those introduced by the IR-pump at  $1917\text{ cm}^{-1}$  (the  $1917\text{ cm}^{-1}$  vibrations correspond to a bridge vibration in the cumulenenic structure in the “cumulenenic MLCT” state, this pump was introduced at 10 ps after the UV pump to allow for the population of this cumulenenic state to take place). The bleach at  $1563\text{ cm}^{-1}$  which corresponds to the vibration mode of the Ph bridge, together with the bleach of the peak at  $1625\text{ cm}^{-1}$  which corresponds to  $\text{NAP}^-$  anion loss, are observed. The rise of peaks at  $1604\text{ cm}^{-1}$  and  $1650\text{ cm}^{-1}$  which are attributed to gain in  $^3\text{NAP}$  state population were observed just after the IR excitation is introduced. This result indicates with the pump at  $C \equiv C$  vibration instead of  $C =$

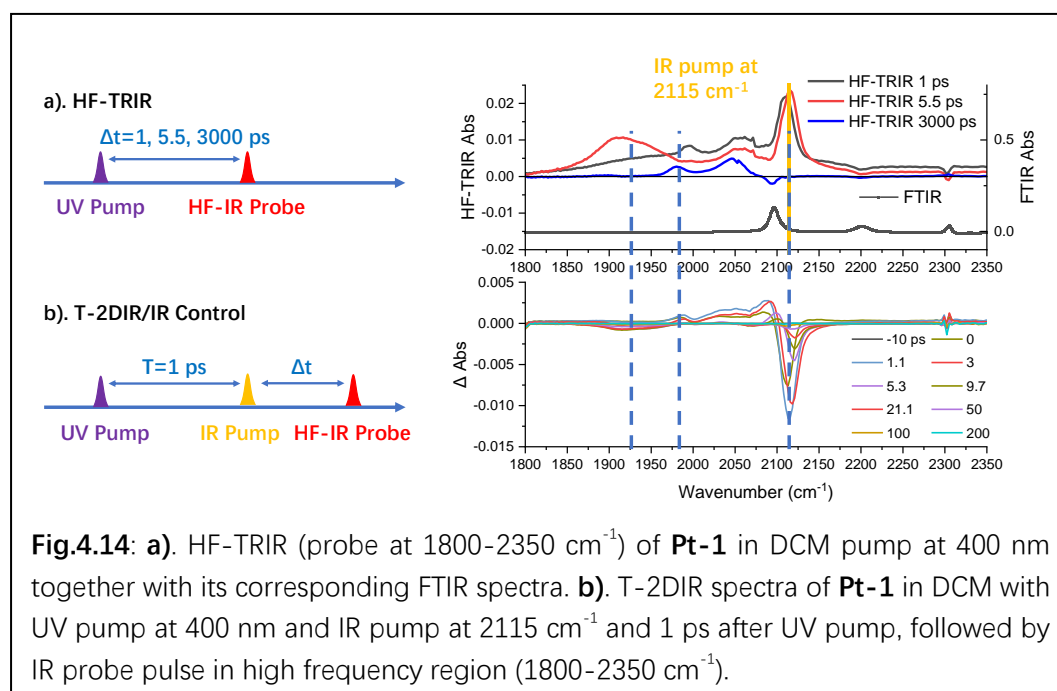
$C = C$  can also accelerate the back electron transfer process, and accelerate the decay from  $^1\text{MMLLCT}$  state to  $^3\text{NAP}$  state.



With the IR excitation of  $^1\text{MMLLCT}$  state of **Pt-1** at  $1993 \text{ cm}^{-1}$ , followed by IR probe pulse in high frequency region ( $1800\text{-}2350 \text{ cm}^{-1}$ ), two bleaches at  $1993 \text{ cm}^{-1}$  and  $2115$



$\text{cm}^{-1}$  appear together with the neighboring peak at lower wavenumber. At early time ( $< 10$  ps) after IR excitation, the signal is a combination of T-2DIR and IR control. This indicates with the pump at  $C \equiv C$  opposite to  $\text{NAP}^-$ , the vibration excitation is transported along the whole bridge so the vibration mode corresponding with  $C \equiv C$  bond with Pt center and the  $C \equiv C$  bond with  $\text{NAP}^-$  anion are also excited. In the similar experiment but with the probe with IR-beam in the low-frequency region ( $1450\text{-}1800\text{ cm}^{-1}$ ), at early times after IR excitation, the peak at  $1545\text{ cm}^{-1}$  with a neighboring bleach at  $1571\text{ cm}^{-1}$  appear, that correspond with vibration mode of delocalized bridge structure in **Pt-1**  $^1\text{MMLLCT}$  state. This indicates for  $^1\text{MMLLCT}$  state of **Pt-1**, all vibration modes in the bridge are coupled with each other and the pump at the bridge can change the distance between Pt center and NAP anion which supports the method that with the pump at vibration mode corresponding with bridge can accelerate back electron transfer of CT state to generate  $^3\text{NAP}$  state. The appearance of the bleach at  $1917\text{ cm}^{-1}$  later could be explained as follows, with the back electron transfer acceleration of  $^1\text{MMLLCT}$  state into  $^3\text{NAP}$  state, the cumulenenic  $^3\text{MLCT}$  state is 'bypassed', its population is lower in comparison to the experiment without IR-pump, the signal corresponding to this cumulenenic structure also diminishes, hence the overall "negative absorption" signal is detected.



Similar phenomenon is also observed when the introduced IR excitation pulse is targeting the vibration of  $C \equiv C$  directly linked to NAP anion in  $^1\text{MMLLCT}$  state at  $2115\text{ cm}^{-1}$ . As show in **Fig.4.S1 (c)**, when IR pump centred at  $2115\text{ cm}^{-1}$  is introduced after 1 ps of 400 nm excitation, the peaks at  $1615\text{ cm}^{-1}$  and  $1648\text{ cm}^{-1}$  rise with the bleach at  $1625\text{ cm}^{-1}$  rise. The two peaks at  $1615\text{ cm}^{-1}$  and  $1648\text{ cm}^{-1}$  are attributed to the gain of  $^3\text{NAP}$  state, as TRIR of **Pt-1** in DCM at 3000 ps is shown in **Fig.4.S1(b)** in SI at the same position there are two absorption peak which is attributed to the last excited state populated. The bleach at  $1625\text{ cm}^{-1}$  is a symbol of NAP anion loss because the NAP anion absorbs at  $1625\text{ cm}^{-1}$  as **Fig.4.S1(b)** in SI show the LF-TRIR spectra at 5.5 ps which is at the time delay when cumuleninc MLCT state is populated, there is an absorption peak at  $1625\text{ cm}^{-1}$  which is corresponding with MLCT state. This result indicates, with the IR pump at  $C \equiv C$  bond bind with NAP anion in  $^1\text{MMLLCT}$  state can also accelerate the back electron transfer process to form  $^3\text{NAP}$  state from CT state. The two bleaches at  $1915\text{ cm}^{-1}$  and  $2123\text{ cm}^{-1}$  which are corresponding with the loss of CT state also rise and still exist until 50 ps as the T-2DIR spectra probe at high frequency region show in **Fig.4.14(b)** which supports the signal is caused by IR pump induced loss of CT state instead of loss of ground vibration state in CT state.

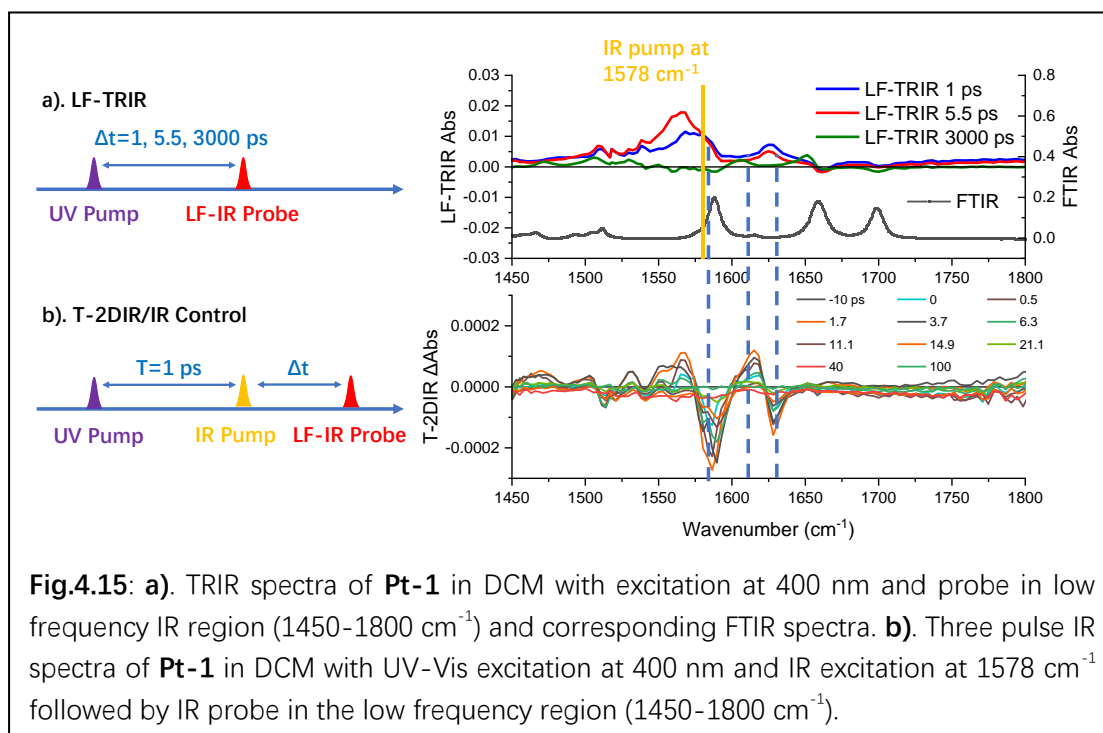
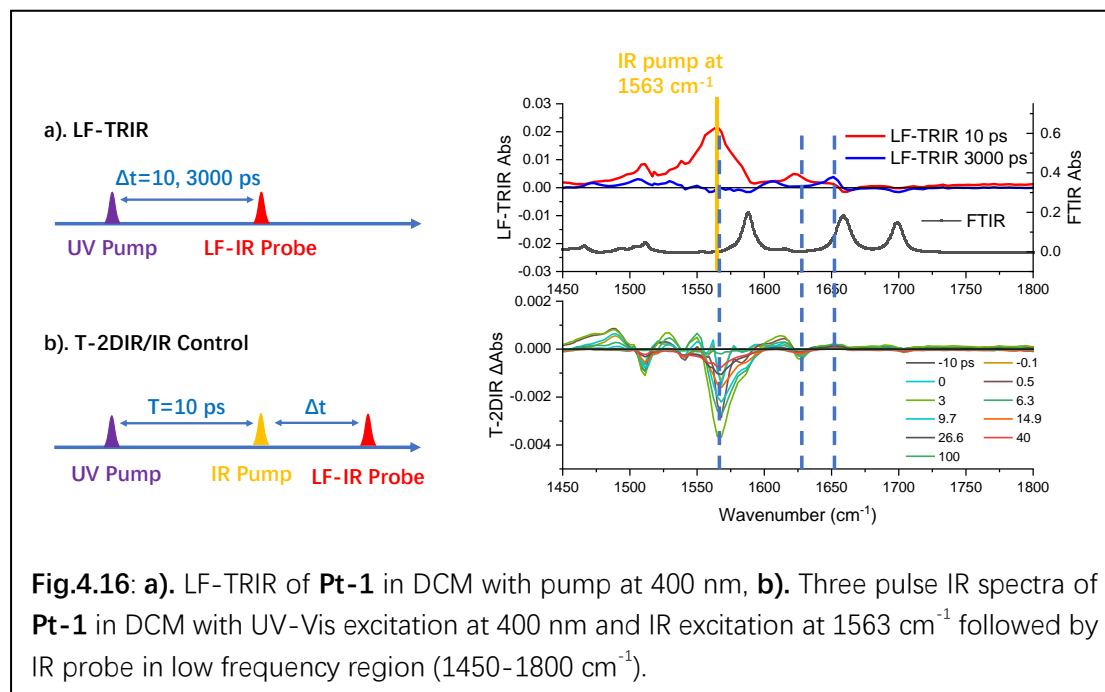


**Fig.4.15:** a). TRIR spectra of **Pt-1** in DCM with excitation at 400 nm and probe in low frequency IR region (1450-1800  $\text{cm}^{-1}$ ) and corresponding FTIR spectra. b). Three pulse IR spectra of **Pt-1** in DCM with UV-Vis excitation at 400 nm and IR excitation at 1578  $\text{cm}^{-1}$  followed by IR probe in the low frequency region (1450-1800  $\text{cm}^{-1}$ ).

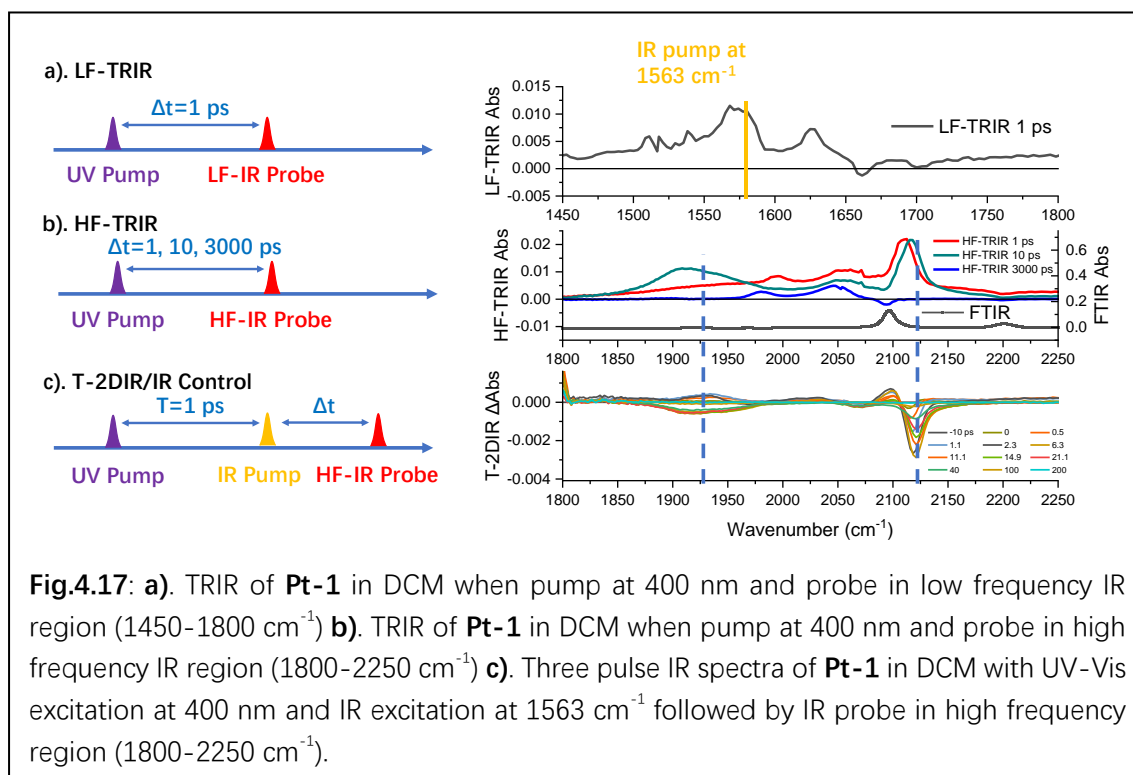
The  $^1\text{MMLCT}$  state of **Pt-1** in DCM populated when pump at 400 nm also has other vibration modes which is not observed in the published PTZ-Pt-NAP and Ph-Pt-NAP complexes. After 1 ps of 400 nm excitation, a peak at 1578  $\text{cm}^{-1}$  rises as shown in **Fig.4.15(a)**, this signal is attributed to vibration of the phenyl group included in the bridge of **Pt-1**, as discussed in **Chapter 2**. The peak at 1578  $\text{cm}^{-1}$  is not observed in **Pt-0** but becomes more intense (comparing with NAP $^-$  absorption at 1624  $\text{cm}^{-1}$ ) in **Pt-2** compared with in **Pt-1** which indicates that the absorption at 1578  $\text{cm}^{-1}$  is related to the bridge. Considering that 1578  $\text{cm}^{-1}$  is much lower in wavenumber than that of the stretching vibration of the  $\text{C} \equiv \text{C}$  bond, it is attributed to phenyl group vibrations in the MLCT state. The rise of the bleach at 1624  $\text{cm}^{-1}$  is caused by a loss of the MLCT state population after IR pump at 1578  $\text{cm}^{-1}$  indicates pumping this vibration mode may also be able to induce acceleration of back electron transfer.

The IR pump at 1578  $\text{cm}^{-1}$  is introduced after 1 ps of 400 nm UV-Vis excitation, then the IR probe pulse in low frequency region (1450-1800  $\text{cm}^{-1}$ ) is introduced and gives the T-2DIR spectra in **Fig.4.15 (b)**. At 14.9 ps the bleaches at 1631  $\text{cm}^{-1}$  and 1589  $\text{cm}^{-1}$  maintain, and decay to zero by 40 ps, which indicates the IR pump at 1578  $\text{cm}^{-1}$  induced

acceleration of back electron transfer which leads to the loss of a CT state because the absorption at  $1631\text{ cm}^{-1}$  corresponds to  $\text{NAP}^-$  anion fragment formed in the CT state.



After 10 ps of 400 nm laser pulse excitation of **Pt-1** in DCM, the bridge structure isomerizes from  $C \equiv C - Ph$  to generate  $C = C = C$  structure and the phenyl fragment also isomerize to generate quinone like conjugated fragment based on previous research and **Chapter 2**. This quinone-like fragment gives the vibrational mode with absorption at  $1563\text{ cm}^{-1}$  which is also a vibrational mode corresponding with the bridge between the Pt center and NAP acceptor. When this vibrational mode is pumped by the IR pulse centered at  $1563\text{ cm}^{-1}$  as show in **Fig.4.16(b)**, the bleach at  $1628\text{ cm}^{-1}$  which corresponds to the loss of  $\text{NAP}^-$  anion of CT state also appears, and persists until 40 ps, as does a positive peak at  $1654\text{ cm}^{-1}$  ( $^3\text{NAP}$ ), indicating that pumping this quinone-like fragment in bridge can also accelerate the back electron transfer process of the CT state to generate  $^3\text{NAP}$  state.



To further understand how IR excitation at Ph fragment in **Pt-1** bridge in CT state induce the acceleration of back electron transfer, another three pulse IR spectroscopy experiment was performed, 400 nm UV-Vis pump was followed by IR excitation centered at 1563  $\text{cm}^{-1}$  1 ps after the 400-nm pump. The resulting data obtained with IR-probe in high frequency region (1800-2250  $\text{cm}^{-1}$ ) are shown in **Fig.4.17(c)**. After IR pump was introduced, the peaks at 1933  $\text{cm}^{-1}$  and 2097  $\text{cm}^{-1}$  appear, which could be attributed to  $1 \rightarrow 2$  absorption from excited vibrational energy level of CT state, the 1933  $\text{cm}^{-1}$  peak is due to  $C = C = C$  cumulenlic structure fragment and the 2097  $\text{cm}^{-1}$  is due to  $C \equiv C$  bond bind with  $\text{NAP}^-$  anion in CT state. This result indicates that when the *Ph* fragment in the bridge is pumped, the whole bridge is influenced and pumped into its higher vibration energy level. After 20 ps, only two bleaches at 1919  $\text{cm}^{-1}$  and 2120  $\text{cm}^{-1}$  that are left, which indicate the loss of the CT state.

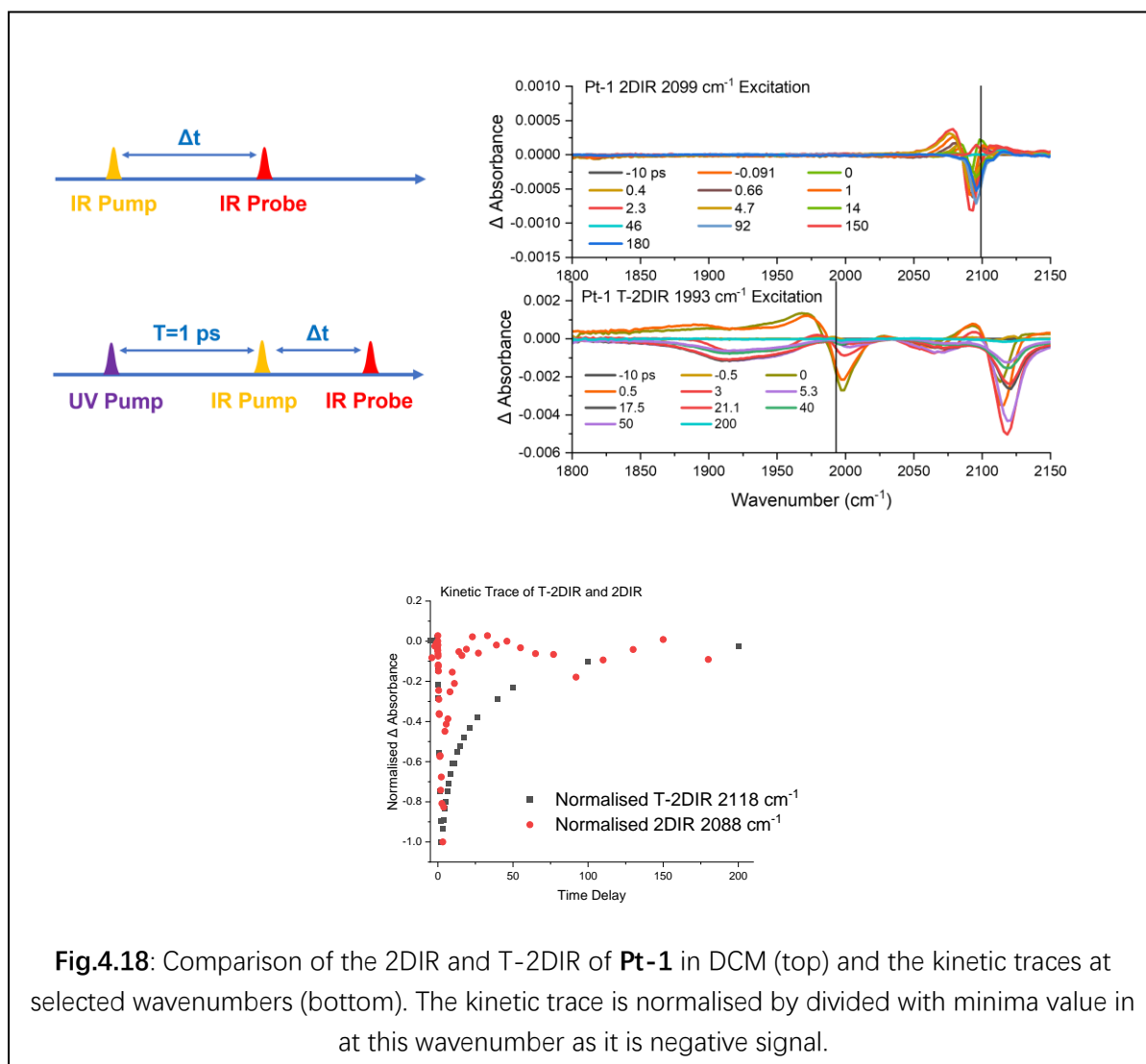
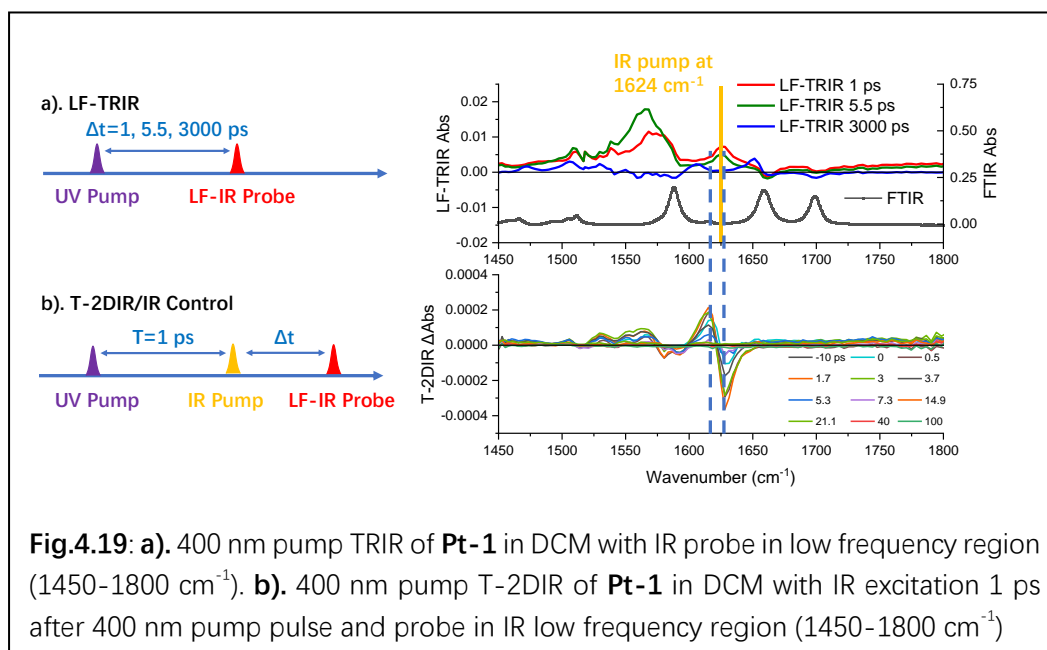


**Fig.4.18** shows a comparison between the kinetic trace of 2DIR and T-2DIR. The lifetime is much longer for T-2DIR (black dots) than for 2DIR (red dots) that relate to vibrational lifetime of state  $v=1$ . This indicates the signal observed in T-2DIR spectra at later time (after 10 ps of IR excitation) is caused by IR control mechanism as at later time delay, all of the vibrational excited state has decayed and the signal observed is caused by the change of excited state population.

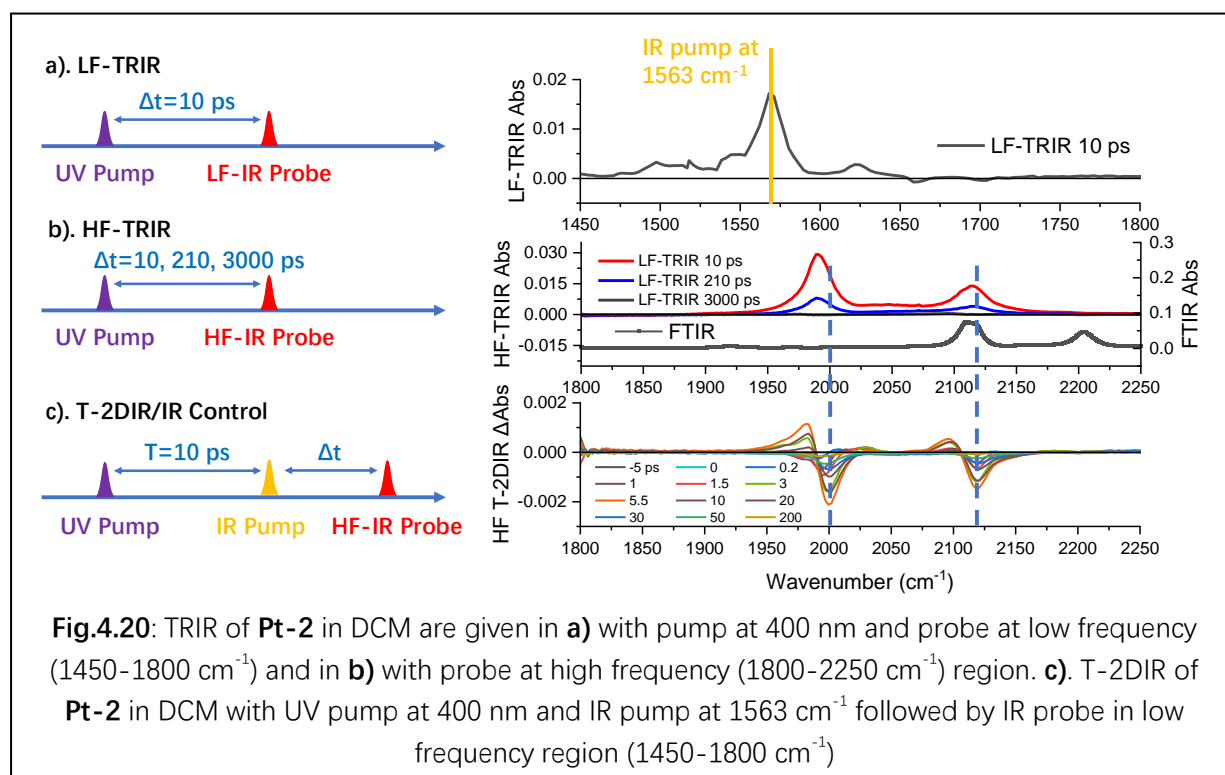


However, if the IR pump is tuned to excite the carbonyl group vibration ( $1624 \text{ cm}^{-1}$ ) of  $\text{NAP}^-$  anion in the charge transfer state, no acceleration of changes to back electron transfer process is observed as shown in **Fig.4.19 (b)**. In **Fig.4.19 (b)**, after IR pump centered at  $1624 \text{ cm}^{-1}$  is introduced 1 ps after UV-Vis pump, a peak at  $1615 \text{ cm}^{-1}$  rise together with a bleach at  $1628 \text{ cm}^{-1}$ , these are caused by  $1 \rightarrow 2$  absorption of excited vibrational state in CT state and the partial loss of  $0 \rightarrow 1$  IR absorption caused by loss of the population of ground vibrational state. These neighboring peak and bleach decay fully after 10 ps which indicates they correspond to vibrationally excited  $\text{NAP}^-$  anion and not to a change in the ratio of excited electronic state. Thus, excitation of vibrational mode on the  $\text{NAP}^-$  anion does not induce acceleration of back electron transfer or any other IR control phenomenon.

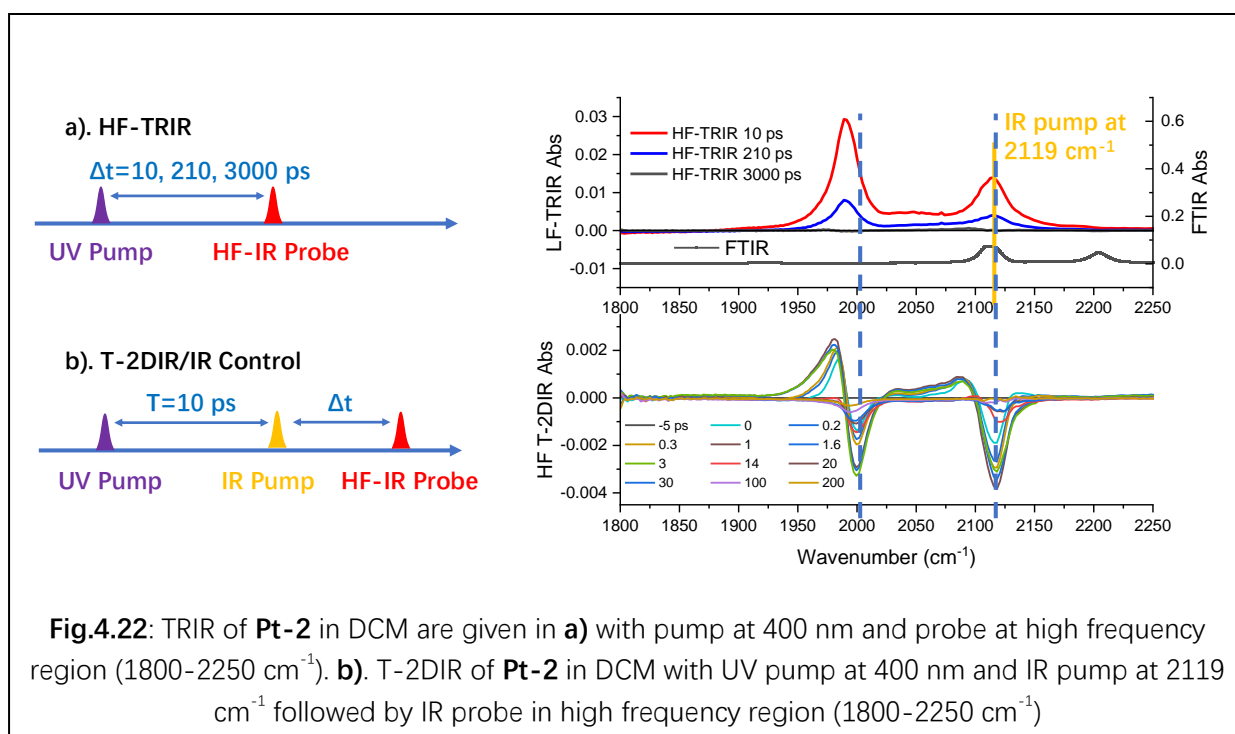
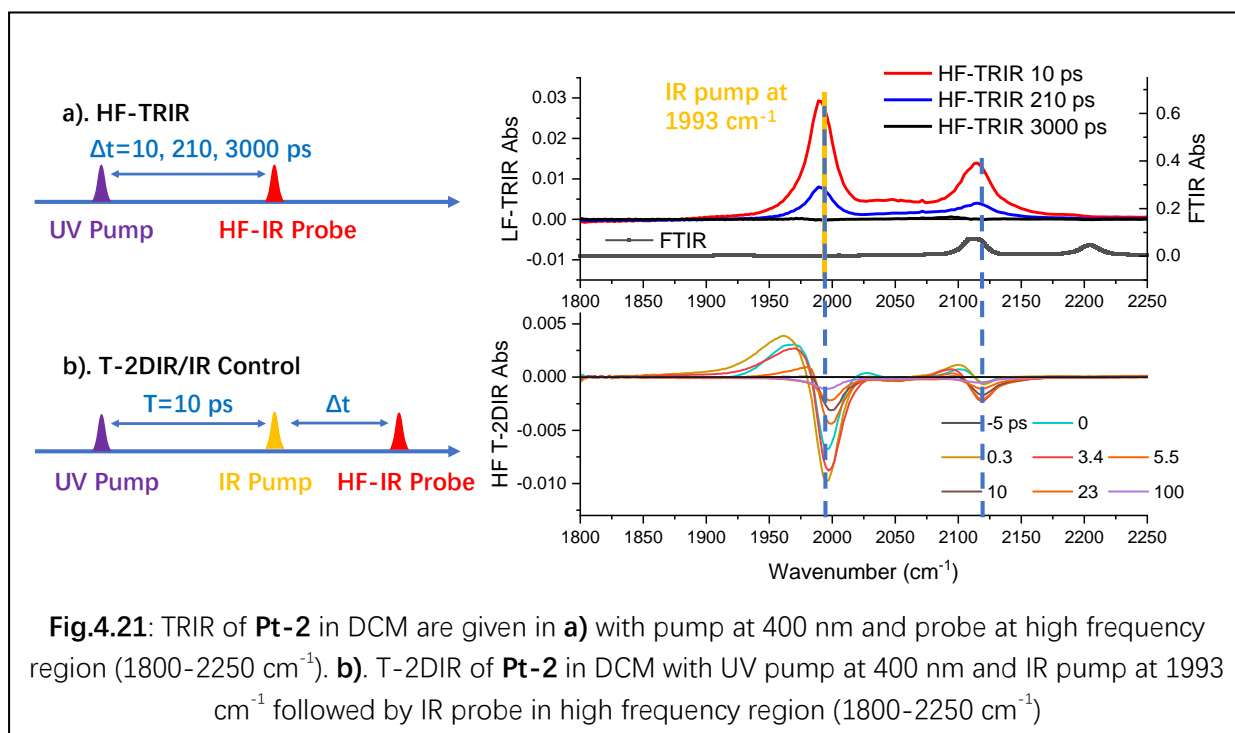
In conclusion, for **Pt-1** in its CT excited state including  $^1\text{MMLLCT}$  state and the cumulenic  $^3\text{MLCT}$  state, IR-control has been observed. Once the vibration mode of the bridge, such as  $\text{Pt} = \text{C} = \text{C} = \text{C}$  ( $1917 \text{ cm}^{-1}$ ), phenyl group ( $1578 \text{ cm}^{-1}$ ), and quinoidal phenyl group ( $1563 \text{ cm}^{-1}$ ) are excited by an IR laser pulse after the UV-Vis excitation pulse, back electron transfer from CT to  $^3\text{NAP}$  state is accelerated as the loss of vibrations corresponding to the CT state, and grow-in of vibrations due to  $^3\text{NAP}$  state are observed.

### 4.3.3 Transient 2DIR of Pt-2

Based on previous research discussed in **Chapter 2**, it was concluded that a mixture of two different ILCT states with different lifetimes are formed after 400 nm excitation of **Pt-2** in DCM. These two ILCT states give undistinguishable IR absorptions when probed in the high frequency region. The TRIR spectra in the low frequency region suggest that these two ILCT states are different in the distance between positive charge (“hole”) and negative charge centers, and in their lifetimes. However, these states give similar vibrational modes on the bridge with absorption at 1563, 1993 and 2119  $\text{cm}^{-1}$ , and thus offer a possibility for IR-control.







As shown in **Fig.4.20 (c), 21 (b)** and **22 (b)**, by comparing with corresponding TRIR absorption spectra and FTIR spectra show in **Fig.4.20(a,b), 21(a)** and **22(a)**, when these three vibrations are excited, the population loss of CT states is induced and gives

bleaches at  $2000\text{ cm}^{-1}$  which corresponds with vibration of  $C \equiv C$  opposite to NAP anion side in ILCT states formed, and at  $2119\text{ cm}^{-1}$  which corresponds with vibration of  $C \equiv C$  linked with  $\text{NAP}^-$  anion in ILCT states. However, the peaks corresponding with  $^3\text{NAP}$  state or with the increase of the ground state recovery were not observed, the only phenomenon observed is the loss of CT state.

Also, no matter which vibrational mode is excited, the  $1 \rightarrow 2$  peak is observed at  $1979\text{ cm}^{-1}$  and  $2084\text{ cm}^{-1}$  which correspond with the  $C \equiv C$  vibration of the bridge. This result indicates that the  $C \equiv C$  vibration modes included in the bridge are coupled together in CT state.

#### 4.4 Conclusion

In this research, we characterized three Acceptor-Bridge-Pt-Bridge-Acceptor complexes with variable bridge length,  $-C \equiv C -$  (**Pt-0**),  $-C \equiv C - Ph - C \equiv C -$  (**Pt-1**), and  $-C \equiv C - Ph - C \equiv C - Ph - C \equiv C -$  (**Pt-2**) with T-2DIR method, by exciting different vibrational modes in the excited states by an IR pulse after UV excitation at 400 nm. Once the vibrational mode corresponding to the bridge vibration in the CT states are excited, the back electron transfer process is accelerated. In **Pt-1**, the CT state decays into  $^3\text{NAP}$  state and in **Pt-2** it decays into the ground state. However, in **Pt-0** no vibration mode corresponding with the bridge is observed in TRIR so no target vibration is available. In **Pt-1** and **Pt-2**, the vibrational mode can be excited and induce such acceleration could be the vibration from  $Pt = C = C = C -$  cumulenenic structure,  $-C \equiv C -$  on the bridge which are in high frequency region and  $Ph$  fragment vibration in low frequency region.

This research also suggest that one possible mechanism of IR-control observed in our previous research, for a D-B-A system  $PTZ - Pt - NAP$ . There, the vibrational mode excited to induce IR-control could be due to  $Pt = C = C = C -$  cumulenenic structure that is formed by isomerization of the  $Pt - C \equiv C - Ph$  structure. This might explain

why only  $PTZ - Pt - NAP$  and  $Ph - Pt - NAP$  complexes can undergo IR control  $Cl - Pt - NAP$  in which the isomerization to form  $Pt = C = C = C$  structure is impossible.

In the broader picture of IR-control research, this result could help us explain the previous results on the DBA molecules. We suggest that when the Acceptor-Pt-Acceptor systems undergoes IR control,<sup>15,21</sup> the IR-pump causes two effects. First, IR pump pulse blocks the electron transfer from donor to the oxidised Pt centre;<sup>26</sup> second, it accelerates the back electron transfer from  $NAP^-$  anion to the oxidised Pt centre. We conclude so because the introduction of IR excitation pulse targeting vibrations of the bridge in the CT state, bleaches corresponding with vibrations of  $NAP^-$  formed in CT state deepen and the peaks corresponding with  $^3NAP$  state rise which indicates the loss or partial loss of CT state population and gain of  $^3NAP$  state population. Taken together, these 2 effects cause the MLCT state of A-B-A system to decay into  $^3NAP$  state more efficiently.

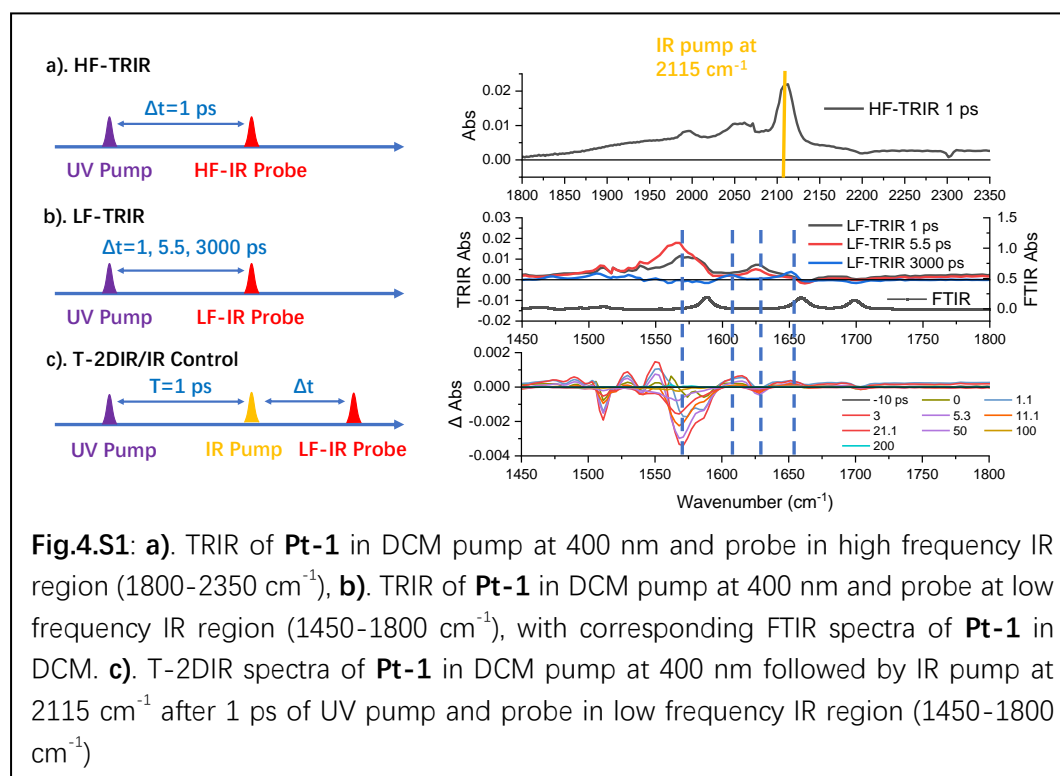
Also, the fact that IR pump pulse accelerates the population of  $^3NAP$  state in **Pt-1** indicates that the IR control phenomenon in Donor-Pt-Acceptor systems reported before,<sup>15,21</sup> can be due to two effects: first, the excitation of the bridge vibration blocks the charge transfer from the donor to the positively charged in the CT-state Pt/bridge;<sup>26</sup> second, back electron transfer from  $NAP^-$  anion to Pt/bridge positive charge is accelerated to generate  $^3NAP$  state. Together, the IR control result observed is that the decay path from MLCT state to  $^3CSS$  state is inhibited and only  $^3NAP$  state is populated when IR excitation is introduced.

## 4.5 Reference

- 1 Y. Tachibana, L. Vayssieres and J. R. Durrant, *Nat Photonics*, 2012, 6, 511–518.
- 2 P. A. Scattergood, M. Delor, I. v. Sazanovich, M. Towrie and J. A. Weinstein, *Faraday Discuss*, 2015, **185**, 69–86.
- 3 Y. A. Berlin, F. C. Grozema, L. D. A. Siebbeles and M. A. Ratner, *Journal of Physical*

- Chemistry C*, 2008, **112**, 10988–11000.
- 4 N. S. Hush, *Coord Chem Rev*, 1985, **64**, 135–157.
- 5 K. Kilså, J. Kajanus, A. N. Macpherson, J. Mårtensson and B. Albinsson, *J Am Chem Soc*, 2001, **123**, 3069–3080.
- 6 H. M. McConnell, *J Chem Phys*, 1961, **35**, 508–515.
- 7 A. H. A. Clayton, G. D. Scholes, K. P. Ghiggino and M. N. Paddon-Row, *J Phys Chem*, 1996, **100**, 10912–10918.
- 8 J. H. Alstrum-Acevedo, M. K. Brennaman and T. J. Meyer, *Inorg Chem*, 2005, **44**, 6802–6827.
- 9 Q. Mi, E. T. Chernick, D. W. McCamant, E. A. Weiss, M. A. Ratner and M. R. Wasielewski, *Journal of Physical Chemistry A*, 2006, **110**, 7323–7333.
- 10 Y. Huang, M. D. Krzyaniak, R. M. Young and M. R. Wasielewski, *Appl Magn Reson*, , DOI:10.1007/s00723-021-01402-6.
- 11 Y. Hou, X. Zhang, K. Chen, D. Liu, Z. Wang, Q. Liu, J. Zhao and A. Barbon, *J Mater Chem C Mater*, 2019, **7**, 12048–12074.
- 12 P. A. Scattergood, M. Delor, I. V. Sazanovich, O. V. Bouganov, S. A. Tikhomirov, A. S. Stasheuski, A. W. Parker, G. M. Greetham, M. Towrie, E. S. Davies, A. J. H. M. Meijer and J. A. Weinstein, *Dalton Transactions*, 2014, **43**, 17677–17693.
- 13 M. T. Colvin, A. B. Ricks and M. R. Wasielewski, *Journal of Physical Chemistry A*, 2012, **116**, 2184–2191.
- 14 G. A. Farrow, M. Quick, S. A. Kovalenko, G. Wu, A. Sadler, D. Chekulaev, A. A. P. Chauvet, J. A. Weinstein and N. P. Ernsting, *Physical Chemistry Chemical Physics*, 2021, **23**, 21652–21663.
- 15 M. Delor, T. Keane, P. A. Scattergood, I. v. Sazanovich, G. M. Greetham, M. Towrie, A. J. H. M. Meijer and J. A. Weinstein, *Nat Chem*, 2015, **7**, 689–695.
- 16 X. Li, J. Valdiviezo, S. D. Banziger, P. Zhang, T. Ren, D. N. Beratan and I. V. Rubtsov, *Physical Chemistry Chemical Physics*, 2020, **22**, 9664–9676.
- 17 G. A. Worth and L. S. Cederbaum, *Annu Rev Phys Chem*, 2004, **55**, 127–158.
- 18 M. Baer, *Phys Rep*, 2002, **358**, 75–142.
- 19 M. P. Bircher, E. Liberatore, N. J. Browning, S. Brickel, C. Hofmann, A. Patoz, O. T. Unke, T. Zimmermann, M. Chergui, P. Hamm, U. Keller, M. Meuwly, H. J. Woerner, J. Vaníček and U. Rothlisberger, *Structural Dynamics*, , DOI:10.1063/1.4996816.
- 20 J. W. Kim, C. H. Kim, C. Burger, M. Park, M. F. Kling, D. E. Kim and T. Joo, *Journal of Physical Chemistry Letters*, 2020, **11**, 755–761.
- 21 M. Delor, P. A. Scattergood, I. v. Sazanovich, A. W. Parker, G. M. Greetham, A. J. H. M. Meijer, M. Towrie and J. A. Weinstein, *Science (1979)*, 2014, **346**, 1492–1495.
- 22 M. Delor, P. A. Scattergood, I. v. Sazanovich, T. Keane, G. M. Greetham, A. J. H. M. Meijer, M. Towrie, A. W. Parker and J. A. Weinstein, in *Physical Chemistry of Interfaces and Nanomaterials XIV*, SPIE, 2015, vol. 9549, p. 95490U.
- 23 Z. Lin, C. M. Lawrence, D. Xiao, V. v. Kireev, S. S. Skourtis, J. L. Sessler, D. N. Beratan and I. v. Rubtsov, *J Am Chem Soc*, 2009, **131**, 18060–18062.
- 24 X. Yang, A. Pereverzev and E. R. Bittner, *Advances in Chemical Physics, Volume 163*, 2018, **163**, 167.
- 25 X. Yang, T. Keane, M. Delor, A. J. H. M. Meijer, J. Weinstein and E. R. Bittner, *Nat*

## 4.SI. Supplementary Information for Chapter 4



Another phenomenon worth to note is with the IR pump introduced, the peak at 1550  $\text{cm}^{-1}$  rise (shown in **Fig.4.S1(c)**) and decay into baseline within 10 ps, so this peak is corresponding with 2DIR signal of MLCT state formed after excitation at 400 nm with  $1 \rightarrow 2$  absorption of bridge vibration in state of Pt-1 when introduced IR pump is at 2115  $\text{cm}^{-1}$ . This indicates the vibration mode at 1565  $\text{cm}^{-1}$  is also coupled with the vibration of  $C \equiv C$  bond linked with NAP anion in  $^1\text{MMLLCT}$  state and support the idea that once the vibration mode on the bridge is excited, the vibration excitation distributes among the whole bridge and causes the prolong of bridges which leads to the acceleration of back electron transfer from CT state.

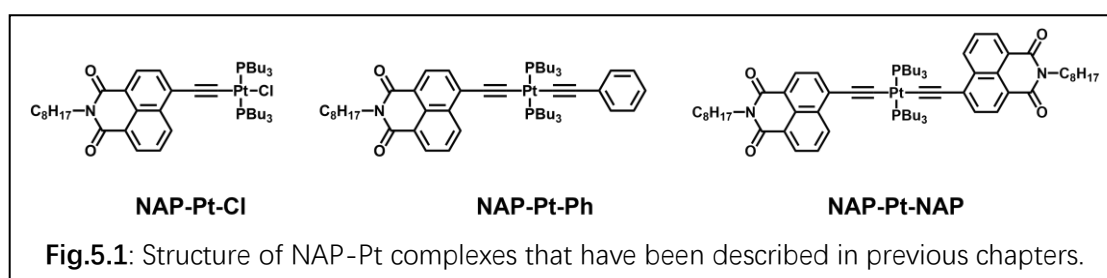
To compare the influence of back electron transfer dynamics on CT states by exciting vibration mode, magnitude of the IR control effect is calculated and the result is given in **Table.1**. These IR control experiments are focused on IR excitation influence on back electron transfer of CT state generated after the compounds are excited by 400 nm laser pulse. All of the yield of IR control is calculated based on the spectra collected after 10 ps of IR excitation pulse incidence to get ride of the influence from T-2DIR signal. These results indicates, for the complexes interested, when IR pump are introduced to excite vibration modes corresponding with bridge including from  $C \equiv C$ ,  $Pt = C = C = C$  and  $Ph$  most of these give similar IR control yield around 30%. This result supports the method that the change of distance between Pt centre and acceptor domines the acceleration of back electron transfer process from CT state.

Sample	Probe Range	UV-IR Time Delay	IR pump Point	Calculated Yield
Pt-1	LF	10 ps	1513	15.29%
Pt-1	LF	10 ps	1563.5	34.86%
Pt-1	LF	1 ps	1578	29.03%
Pt-1	HF	1 ps	2115	34.60%
Pt-1	HF	1 ps	2115	32.74%
Pt-2	HF	10 ps	1993	35.23%
Pt-2	HF	10 ps	2119	28.82%
Pt-2	HF	1 ps	1993	31.54%

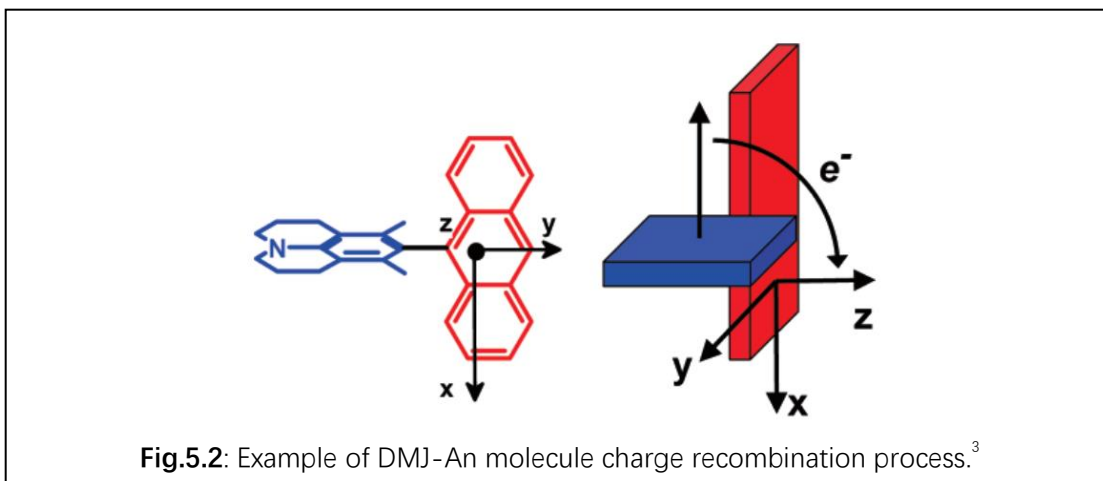
**Table.1:** Magnitude of the IR control effect of Pt-1 and Pt-2 in DCM, with 400 nm pulse excitation followed by IR excitation pulse.

## 5. Chapter 5- The Influence of the *Trans*-Ligand L (the “opposite” ligand) on The Photophysics of L-Pt-C≡C-NAP Complexes

### 5.1. Introduction



In the previous research in our group (done by Scattergood and Farrow et al.), the excited states dynamics of a series NAP-Pt complexes (structures shown in **Fig.5.1**) has been investigated by using TA, TRIR and FLUPS spectroscopies.<sup>1,2</sup> In **Chapter 2**, excited state dynamics of **NAP-Pt-NAP** complex in DCM are investigated by using the same spectroscopic methods has been presented. A comparison of the rate of intersystem crossing (ISC) in these three complexes revealed an interesting observation: that even though these three NAP-Pt complexes have similar energy of the <sup>1</sup>MMLCT state, the ISC rate of **NAP-Pt-Ph** ( $\tau_{ISC} = 21.5 \text{ ps}$ ) and **NAP-Pt-NAP** ( $\tau_{ISC} = 16.9 \text{ ps}$ ) is about ten-fold higher than that of **NAP-Pt-Cl** ( $\tau_{ISC} = 198 \text{ ps}$ ). These complexes differ by the ligand in a trans-position (opposite) to the NAP acceptor across the Pt-center. For **NAP-Pt-Ph** and **NAP-Pt-NAP**, the opposite ligand has a two-dimensional (2D) structure, whilst in **NAP-Pt-Cl** the “opposite” ligand is Cl which could be treated as a “mathematical point”.



The influence of ISC rate caused by the opposite 2D ligand of the NAP acceptor could be explained by spin-orbit, charge transfer intersystem crossing (SOCT-ISC) mechanism.<sup>3</sup> This mechanism suggested that in a Donor-Acceptor (D-A) system, when the relative orientation of the donor and acceptor planes is perpendicular to each other, significant change in orbital angular momentum could be induced via back electron transfer process, then the charge recombination process can happen together with the multiplicity change:  ${}^1D^+ - A^- \rightarrow D - {}^3A^*$ .<sup>3</sup> In this mechanism, the ISC process  ${}^1D^+ - A^- \rightarrow {}^3D^+ - A^-$  is inefficient,<sup>4</sup> if there is no spin-orbit coupling, no break of orthogonality of the D/A orbital arrangement, and no vibrations involved. This mechanism gives another possible explanation why in previous research of **NAP-Pt-Cl**, **NAP-Pt-Ph** and **NAP-Pt-NAP**, the  ${}^3$ MMLLCT state population was not observed. Previously, we hypothesised that  ${}^1$ MMLLCT state must populate the  ${}^3$ MMLLCT, which undergoes an ultrafast charge recombination process to decay into  ${}^3$ NAP state. We did not detect a spectral feature due to  ${}^3$ MMLLCT, and its absence was explained by the ultrafast nature of charge recombination<sup>1</sup> the SOCT-ISC mechanism is another possible explanation. Also, the rate of ISC via SOCT-ISC mechanism is highly dependent on the relevant orientation of electron donor and electron acceptor in CT state: when the donor and acceptor are perpendicular to each other, SOCT-ISC is highly efficient as in the example of dimethyl julolidine-anthracene (DMJ-An) molecule shown in **Fig.5.2**. There, when back electron transfer happens from the electron donor (DMJ) to electron acceptor



(anthracene) in the charge transfer state, the difference in the orientation between donor and acceptor leads to angular momentum change, which makes the ISC possible. Similar phenomenon is also observed in Bodipy molecules,<sup>5</sup> and 9,10-dicyanoanthracene (DCA) or 2,6,9,10-tetracyanoanthracene (TCA) molecules.<sup>6</sup>

In this chapter, three new NAP-Pt Donor-Acceptor complexes are characterised by TA and FLUPS to obtain the ISC rate, and to compare them with the ISC rates in the previously reported NAP-Pt complexes, to investigate the influence of the “opposite” ligand on the ISC rate.

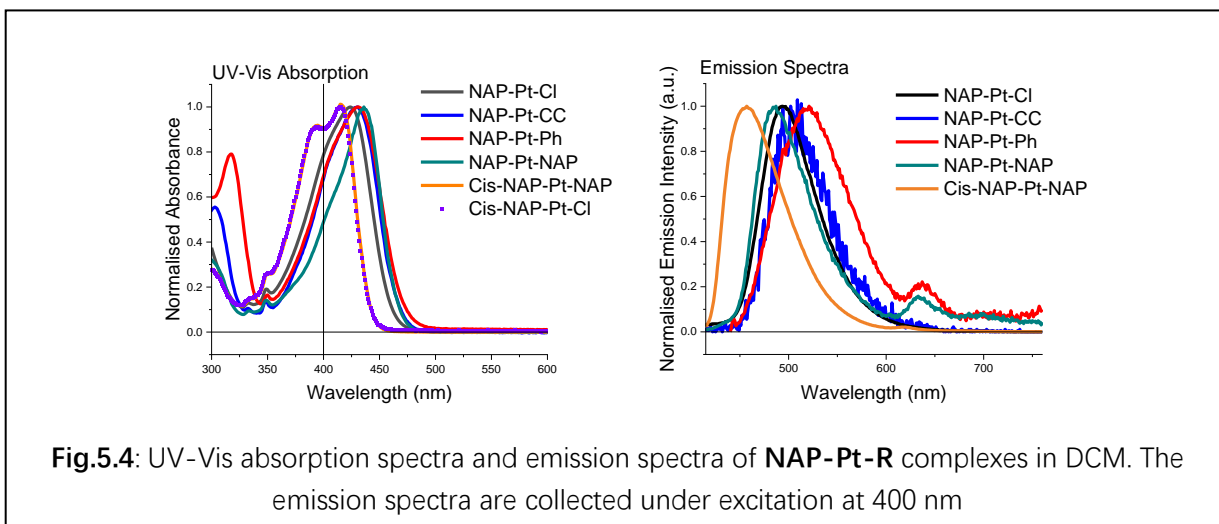
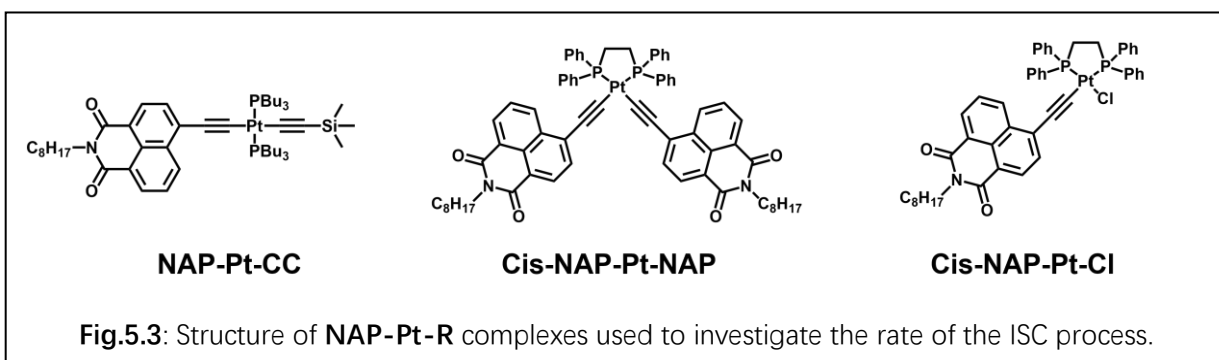
## 5.2. Chapter Aims

To further our understanding on the mechanism of intersystem crossing (ISC), several NAP-Pt complexes with different opposite ligand are investigated by using transient absorption (TA) and fluorescence up-conversion (FLUPS) spectroscopy. ISC rate of these complexes are extracted based on TA and FLUPS and compared with those of the large family of NAP-Pt complexes.

## 5.3. Results and Discussion

### 5.3.1. UV-Vis Absorption and Emission Spectra

To investigate the influence of the ligand opposite to the acceptor on the rate of intersystem crossing (ISC) in Pt complexes, three more complexes (structure shown in **Fig.5.3**) are characterised by TA and FLUPS spectroscopy. Here, three NAP-Pt complexes are investigated: one with only a trans  $C \equiv C - Si(Me)_3$  group as the opposite ligand (i.e., no aromatic group attached as in, e.g.  $-C \equiv C - Ph$ ), and the other two complexes bearing NAP ligand and the R group cis to each other.



Compound	$\lambda_{abs}/\text{nm}$	$\lambda_{fl}/\text{nm}$	Stokes Shift/ $\text{cm}^{-1}$
<b>NAP-Pt-Cl</b>	424	495	3383
<b>NAP-Pt-CC</b>	430	509	3609
<b>NAP-Pt-Ph</b>	431	521	4008
<b>NAP-Pt-NAP</b>	436	487	2402
<b>Cis-NAP-Pt-NAP</b>	415	457	2215
<b>Cis-NAP-Pt-Cl</b>	415	-	-

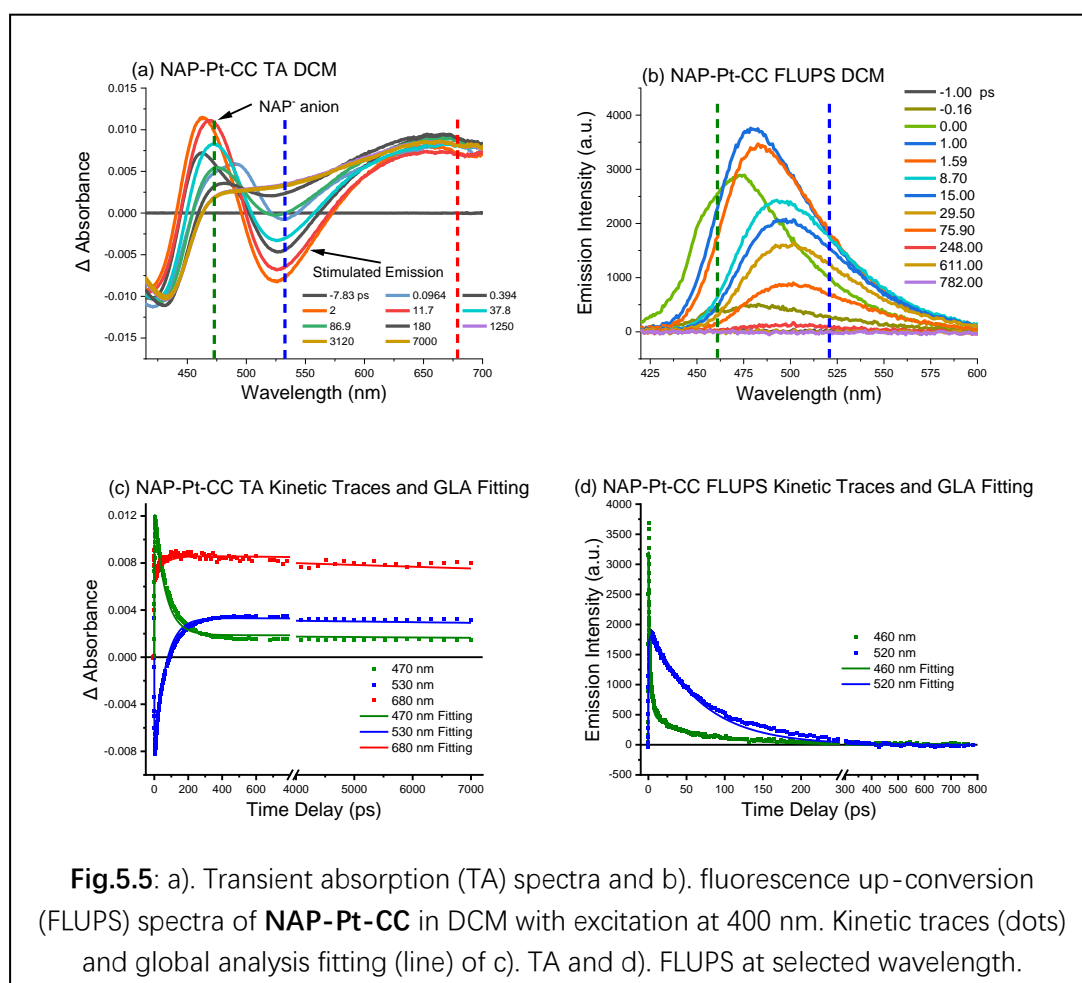
**Table.5.1:** Summary of UV-Vis absorption and *fluorescence* emission spectra.

UV-Vis spectra and emission spectra of three new NAP-Pt complexes in DCM are given in **Fig.5.4** and **Table.5.1** together with the NAP-Pt discussed in previous chapters or in our previous research<sup>1,2</sup>. The **NAP-Pt-CC** compound has an absorption peak due to <sup>1</sup>MMLCT transition at 430 nm, whilst its fluorescence maximum is at 509 nm: both the absorption and the fluorescence maxima lie in between those for **NAP-Pt-Cl** and **NAP-Pt-Ph**, which indicates the energy of the <sup>1</sup>MMLCT state in **NAP-Pt-CC** lies in between those of **NAP-Pt-Cl** and **NAP-Pt-Ph**. This may be caused by the electron donating ability of -CC-SiMe<sub>3</sub> group being

higher than that of -Cl, but lower than that of -CC-Ph group. For **Cis-NAP-Pt-NAP** (orange line) and **Cis-NAP-Pt-Cl** (purple scatter dots), the UV-Vis absorption spectra are nearly overlapped with each other. This indicates the  $^1\text{MMLLCT}$  state of these two complexes has identical energy which is very different from **NAP-Pt-Cl** and **NAP-Pt-NAP**.

### 5.3.2. Transient Absorption Spectra and Fluorescence Up-Conversion Spectra

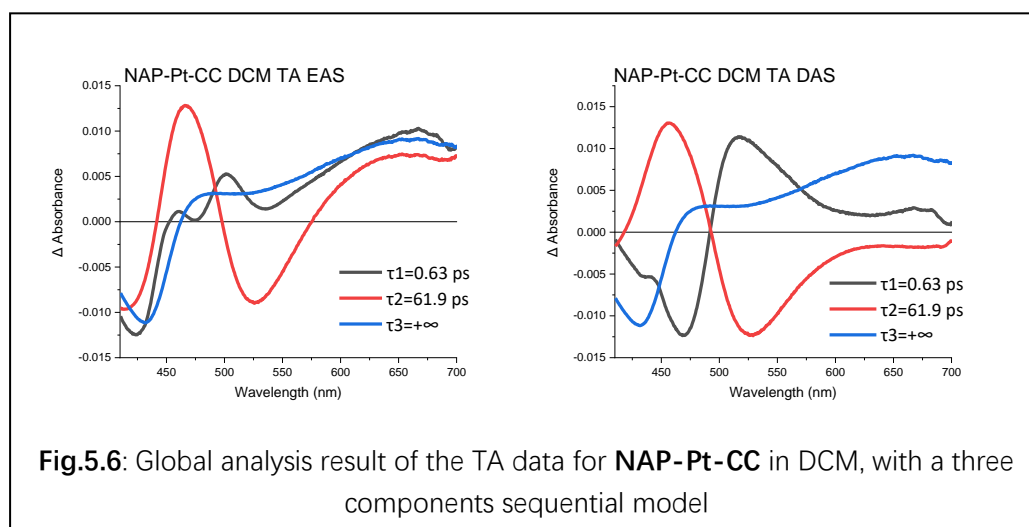
#### 5.3.2.1. NAP-Pt-CC



TA and FLUPS spectra of **NAP-Pt-CC** in DCM with excitation at 400 nm are shown in **Fig.5.5**. After excitation, the TA spectra of **NAP-Pt-CC** shows a peak at 470 nm which corresponds with the  $\text{NAP}^-$  anion absorption (based on **NAP-Pt-NAP** in DCM TA data and UV/Vis spectroelectrochemical data discussed in **Chapter 2**). Together with the positive peak at 470 nm, the bleach at around

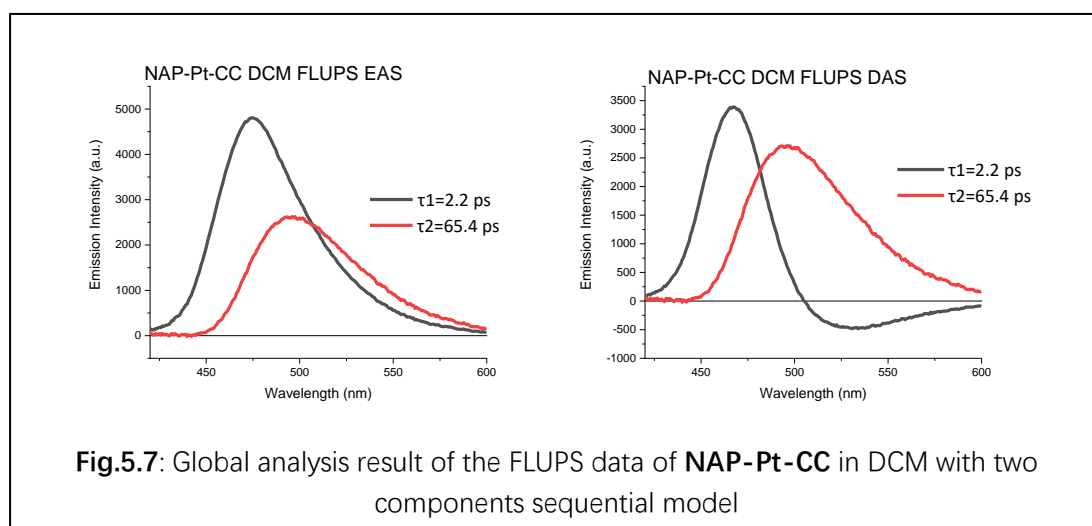
525 nm also arises, the latter is caused by stimulated emission from a singlet excited state: so the first populated excited state of **NAP-Pt-CC** (2.88 eV) could be attributed to an  $^1\text{MMLCT}$  state similar to that in **NAP-Pt-NAP** (2.84 eV), but with different energy. Then the peak at 470 nm and the bleach at 525 nm decay together into a broadband absorption that covers 460 nm to 700 nm; this new absorption band has the spectral shape previously reported for  $^3\text{NAP}$  absorption, and does not show significant decay until 7 ns, so it is attributed to the long-lived  $^3\text{NAP}$  state. Therefore, the outcome of the intersystem crossing (ISC) process leads to the decay from  $^1\text{MMLCT}$  state to  $^3\text{NAP}$  state in this complex. If there is any intermediate state in this process, it was not detected.

To investigate the dynamics by a complimentary method, FLUPS spectra with excitation at 400 nm of **NAP-Pt-CC** have been recorded, as shown in **Fig.5.5** (right). At early time after the excitation, an emission band at 480 nm rises and then decays within several picosecond into the emission with the peak at 500 nm; this process could be treated as the decay from FC state to  $^1\text{MMLCT}$  state. The emission band centred at 500 nm decays into zero after around 350 ps which indicates a relatively slow ISC process ( $\tau_{ISC} = 65.4 \text{ ps}$ ) compared with **NAP-Pt-NAP** ( $\tau_{ISC} = 16.9 \text{ ps}$ ) and **NAP-Pt-Ph** ( $\tau_{ISC} = 21.5 \text{ ps}$ ).



To extract lifetimes of the excited state together with evolution associated

spectra (EAS) and decay associated spectra (DAS), global analysis (GLA) was performed on the TA spectra of **NAP-Pt-CC** in DCM, by using three components sequential model, the results are given in **Fig.5.6**. The first sub-picosecond component could be treated as Franck-Condon (FC) state. The 61.9 ps component is attributed to <sup>1</sup>MMLLCT in which it shows a peak at 457 nm, which is attributed to NAP<sup>-</sup> anion absorption; the bleach at 526 nm due to stimulated emission. Taken together, these observations support the assignment of the 61.9 ps component to a singlet state, and this lifetime corresponds with the ISC process. The last long-lived state is attributed to <sup>3</sup>NAP state whose absorption spectra has a characteristic <sup>3</sup>NAP absorption shape observed in **NAP-Pt-Cl**, **NAP-Pt-Ph** and **NAP-Pt-NAP**, as already noted above.



Global analysis of the FLUPS data for **NAP-Pt-CC** in DCM with a sequential model gives two kinetic components with the lifetimes of 2.2 ps and 65.4 ps. The first component could be attributed to FC state and the 65.4 ps component with emission peaked at around 500 nm is attributed to the <sup>1</sup>MMLLCT state, so the ISC lifetime is 65.4 ps which matches well with the <sup>1</sup>MMLLCT component extracted from the TA. The final <sup>3</sup>NAP state is undetectable for FLUPS as its emission is very long-lived, microseconds, and therefore the number of photons per unit time in the FLUPS experiment is below detection limit. This ISC lifetime of **NAP-Pt-CC** is in between of **NAP-Pt-Cl** ( $\tau_{ISC} = 193$  ps) and **NAP-**

**Pt-Ph** ( $\tau_{ISC} = 21.5 \text{ ps}$ ).<sup>1,7</sup>

### 5.3.2.2. *Cis-NAP-Pt-NAP*

The opposite ligand influence on ISC in NAP-Pt complexes has been discussed above. To further investigate the influence of the other ligands, *Cis-NAP-Pt* complexes are synthesized and characterised by ultrafast spectroscopy to extract their ISC lifetime.

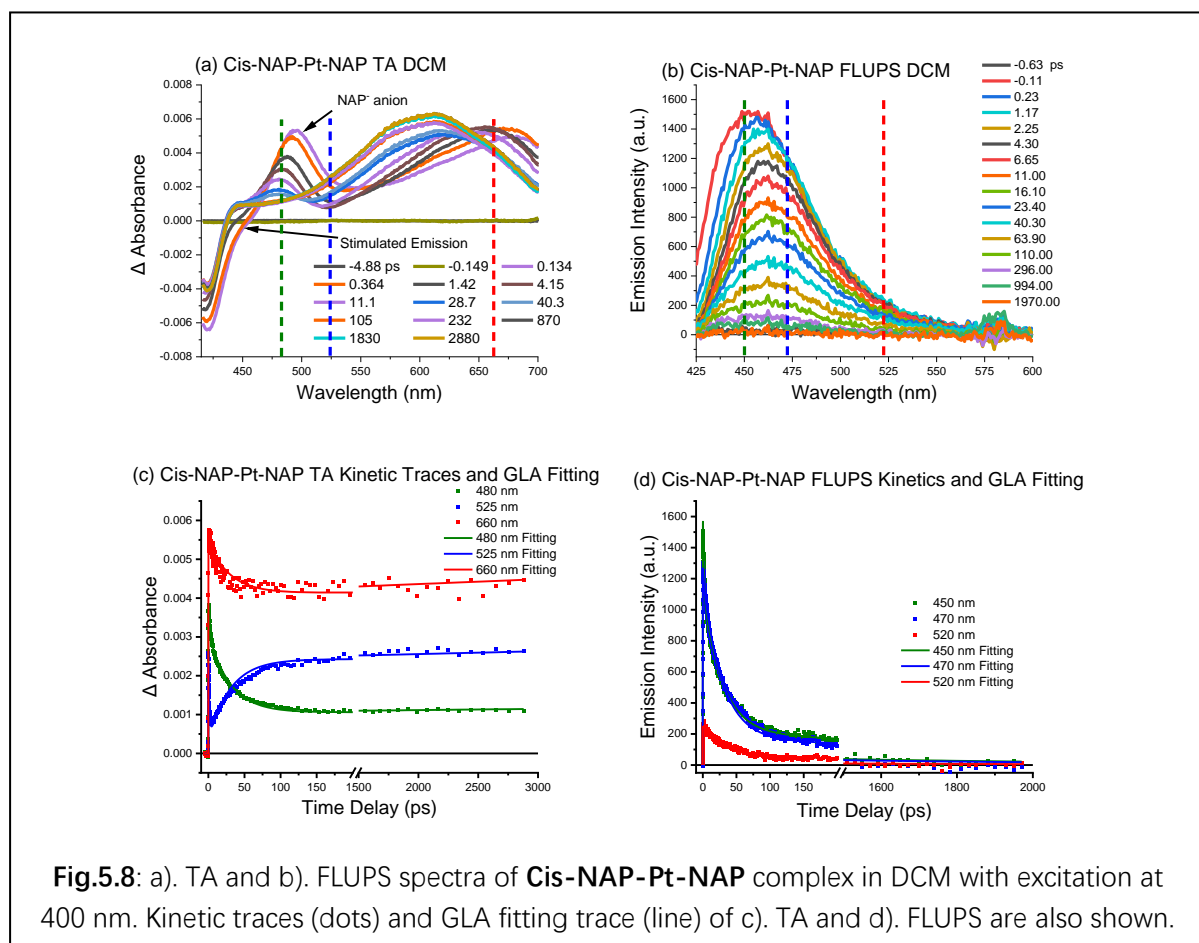
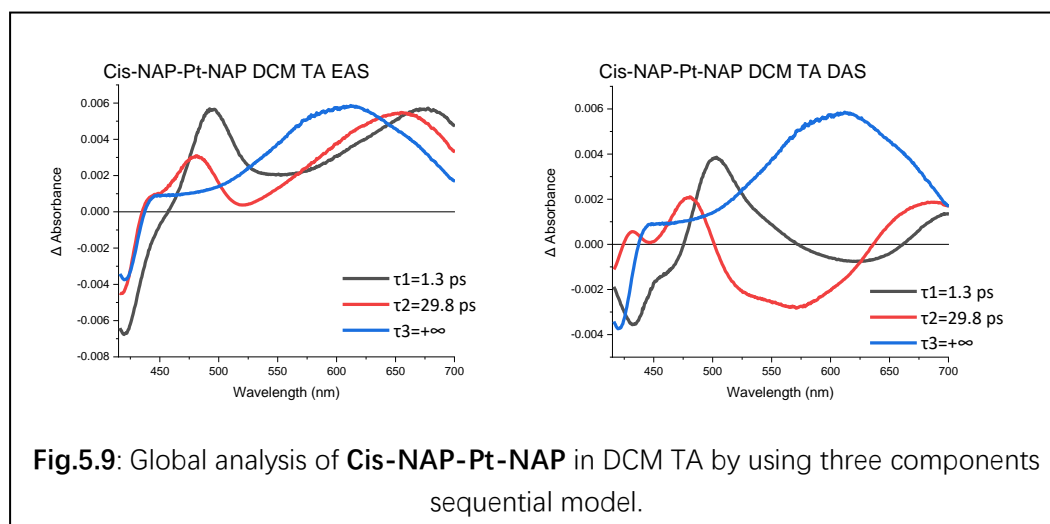


**Fig.5.8:** a). TA and b). FLUPS spectra of *Cis-NAP-Pt-NAP* complex in DCM with excitation at 400 nm. Kinetic traces (dots) and GLA fitting trace (line) of c). TA and d). FLUPS are also shown.

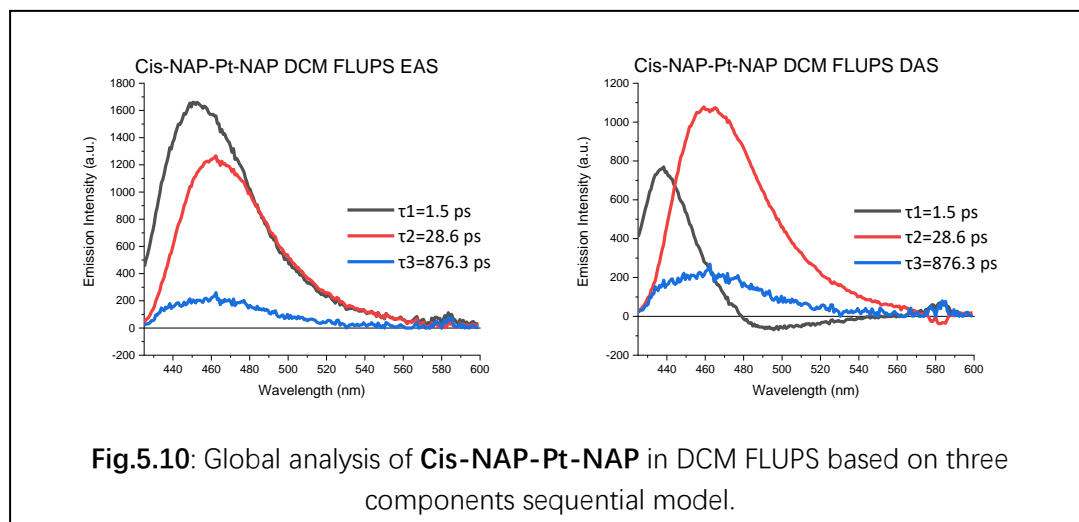
TA spectra of *Cis-NAP-Pt-NAP* show in Fig.5.8 also shows a peak at 490 nm which is attributed to the absorption caused by NAP<sup>-</sup> anion formed after excitation. This indicates that the first populated state in this complex is also a charge transfer (CT) state. However, the stimulated emission band is not obvious in TA spectra because it is overlapped with the bleach caused by the loss of the ground state as its energy is higher than trans-NAP-Pt complexes; there is a tiny amount of stimulated emission signal observed at 450 nm. This

result indicates the first populated excited state after excitation is  $^1\text{MMLLCT}$  state. Then this  $^1\text{MMLLCT}$  state decays into the long-lived  $^3\text{NAP}$  state.

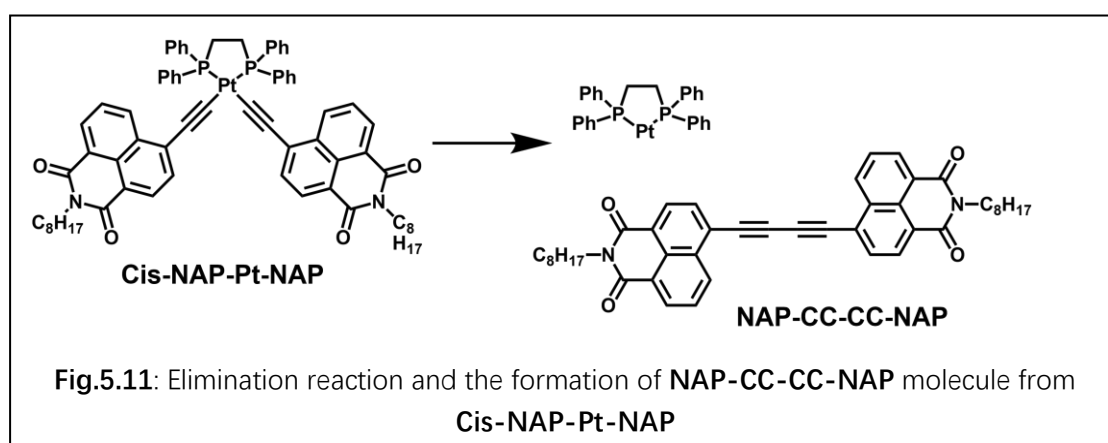
To support or disprove the direct  $^1\text{MMLLCT} \rightarrow ^3\text{NAP}$  process suggested on the basis of the TA data, FLUPS spectra were also collected (shown in **Fig.5.8**, right). The FLUPS spectra show strong emission peaked at 450 nm after excitation, which quickly decays into the emission peaked at 460 nm, so the first emission could be treated as emanating from FC state and the second - as  $^1\text{MMLLCT}$  state suggested by TA. This emission band undergoes fast decay followed by a longer-lived signal which vanishes around 1000 ps.



Lifetimes of excited states are extracted from TA spectra by using sequential model, the first 1.3 ps component is attributed to FC state, the second 29.8 ps component is attributed to  $^1\text{MMLLCT}$  state, and the last long-lived state is the  $^3\text{NAP}$  state. The kinetic decay process is similar to **NAP-Pt-Cl** complex published before with excitation to FC state and then decay into  $^1\text{MMLLCT}$  state, then the  $^1\text{MMLLCT}$  state intersystem crosses to a short lived  $^3\text{MMLLCT}$  state which quickly decays into  $^3\text{NAP}$  state. However, the ISC process can also happen together with back electron transfer process by SOCT-ISC mechanism which means  $^1\text{MMLLCT} \rightarrow ^3\text{NAP}$  happening directly.



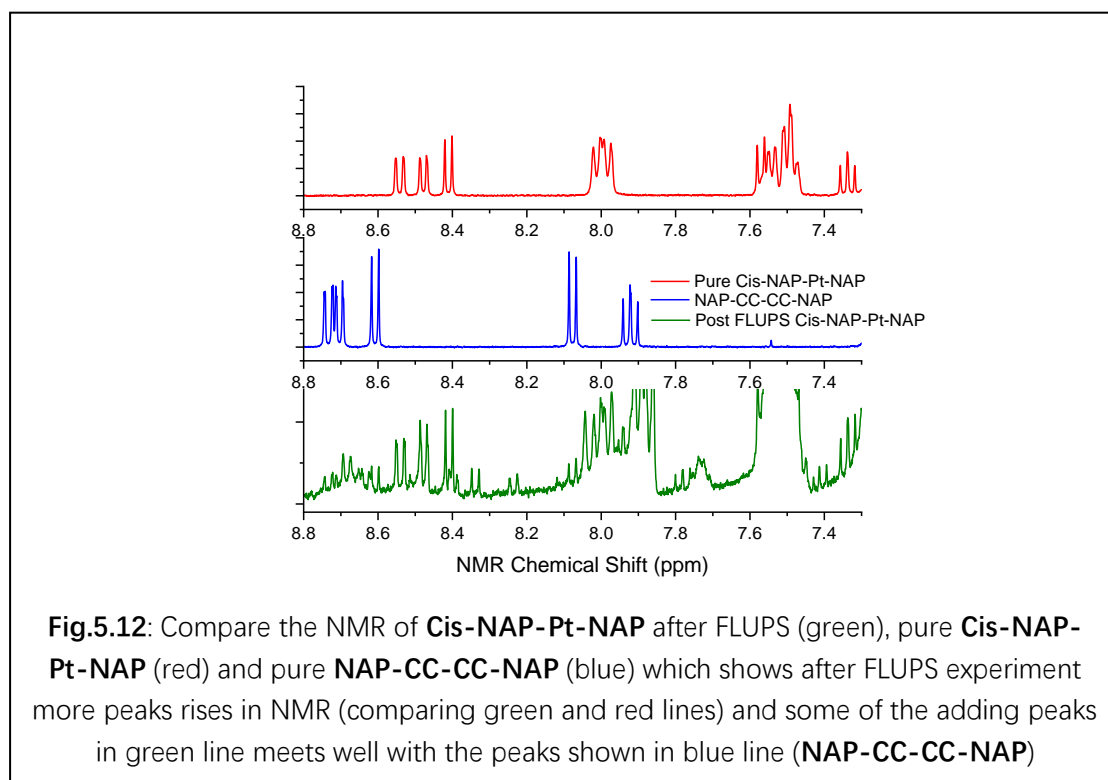
Global analysis of FLUPS spectra of **Cis-NAP-Pt-NAP** extracted three components with sequential model, the first two components agree well with the lifetimes extracted from TA spectra ( $\tau_1 = 1.3 \text{ ps}$ ,  $\tau_2 = 29.8 \text{ ps}$  and  $\tau_3 = +\infty$ ). The ISC process of  $^1\text{MMLCT}$  could be attributed to the lifetime of 28.6 ps which is similar to **NAP-Pt-NAP** and **NAP-Pt-Ph** complex. However, the last 876.3 ps trace is not matching with any components observed from the TA spectra and considering its emission peaked at around 460 nm which cannot be  $^3\text{NAP}$  state and this component is also not observed in NAP-Pt complexes mentioned before.



After considering potential deactivation and decomposition pathways, we observed that the intensity of this long-lived component increases as the experiment progresses, which indicates that the fluorescent component

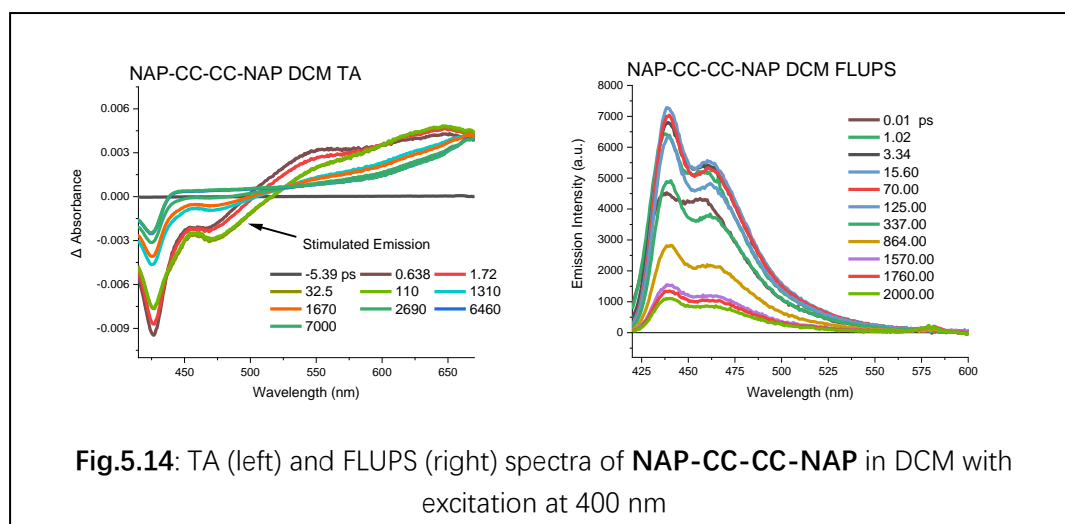
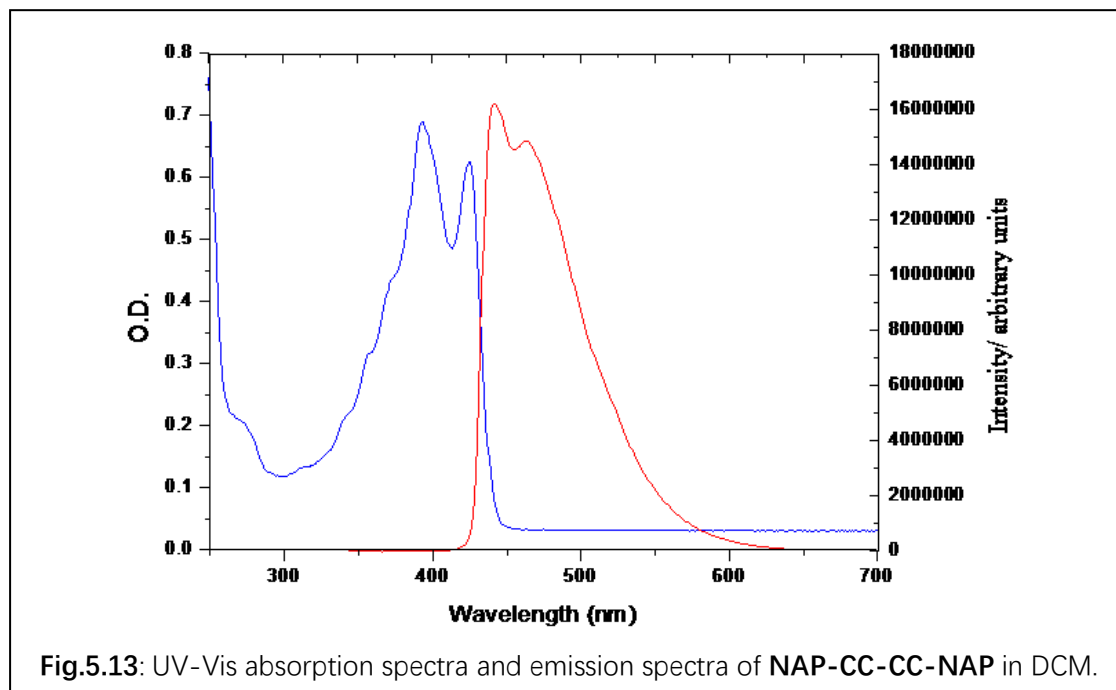


producing this emission is generated during the experiment. We hypothesize that this 876.3 ps component is from a fully organic molecule **NAP-CC-CC-NAP** that is formed via reductive elimination reaction in the excited state of **Cis-NAP-Pt-NAP**, as show in **Fig.5.11**. This reaction can happen only when the two groups are cis to each other, so it is not observed in trans NAP-Pt complexes. To support this hypothesis, **NAP-CC-CC-NAP** was synthesized, and its NMR is compared with pure **Cis-NAP-Pt-NAP** and **Cis-NAP-Pt-NAP** sample after FLUPS experiment, and the NMR result is given in **Fig.5.12**.



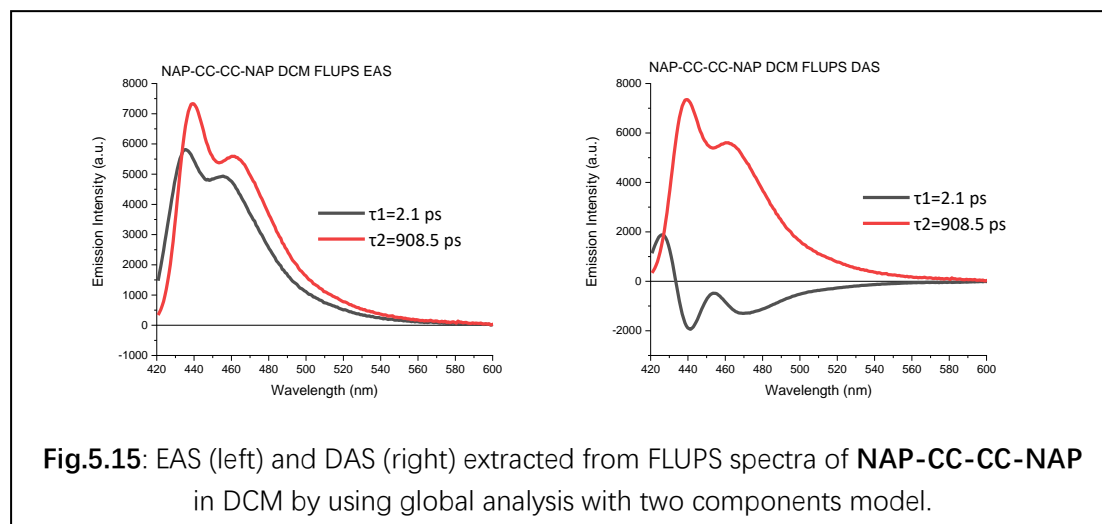
The NMR of **Cis-NAP-Pt-NAP** show in **Fig.5.12** has an extra quartet signal at 8.72 ppm and a doublet signal at 8.6 ppm and another doublet signal at 8.07 ppm which are not present in the fresh solution of **Cis-NAP-Pt-NAP** (red line); these extra signals correspond with the NMR signals of **NAP-CC-CC-NAP** molecule (blue line). This supports the hypothesis that **NAP-CC-CC-NAP** generation is caused by photoexcitation during FLUPS experiment. The **NAP-CC-CC-NAP** molecule's UV-Vis absorption spectra and emission spectra have been published in Lara James' graduation thesis in 2009. Here, we reproduce these spectra (**Fig.5.13.**) which show absorption at 400 nm and emission

peaked at 465 nm; as an organic molecule, it is expected to undergo a slow ISC process which suggests it may be the 876.3 ps component observed in FLUPS of Cis-**NAP-Pt-NAP**. This is further investigated by FLUPS experiments on the NAP-CC-CC-NAP (shown in Fig.5.14).



From the FLUPS spectra of **NAP-CC-CC-NAP**, a long-lived singlet state is observed, which corresponds to a stimulated emission signal at 470 nm observed in TA. This result indicates that if even a tiny amount (<5%) of **NAP-CC-CC-NAP** molecule is generated, it could be excited by 400 nm laser pulse and produce strong emission (fluorescence yield is ~90%). Global analysis

result of **NAP-CC-CC-NAP** FLUPS is given in **Fig.5.15** with a 2.1 ps component and 908.5 ps component, so the 908.5 ps component meets well with the last emissive component observed by FLUPS.



As the last component extracted from FLUPS of **Cis-NAP-Pt-NAP** is attributed to **NAP-CC-CC-NAP**, the ISC lifetime of **Cis-NAP-Pt-NAP** is attributed to 28.6 ps. This rate is slightly slower than **NAP-Pt-NAP** and **NAP-Pt-Ph**.

### 5.3.2.3. *Cis-NAP-Pt-Cl*

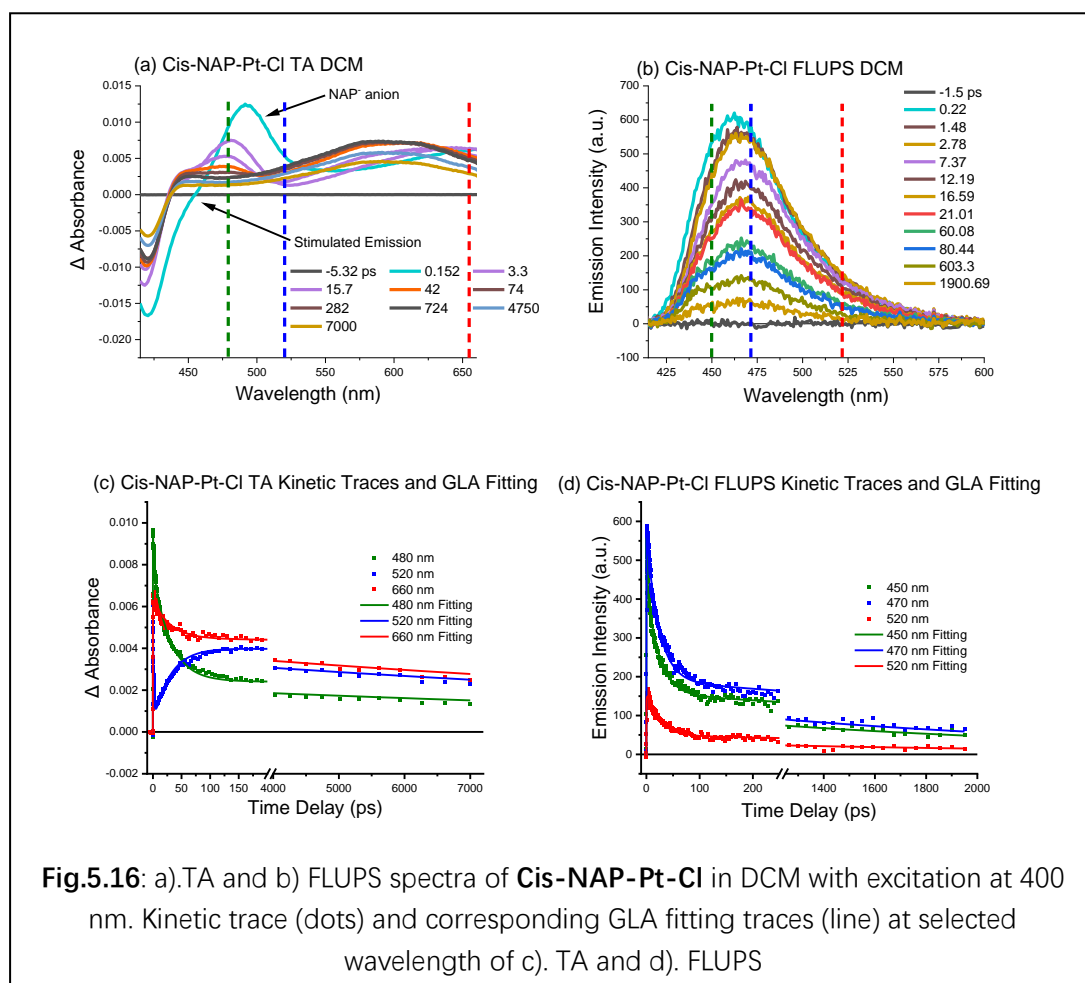
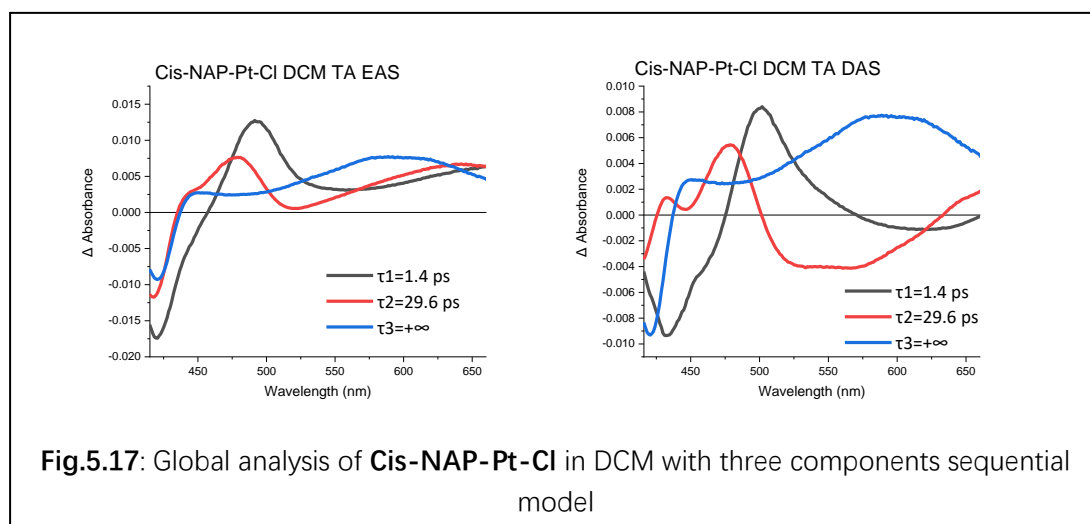
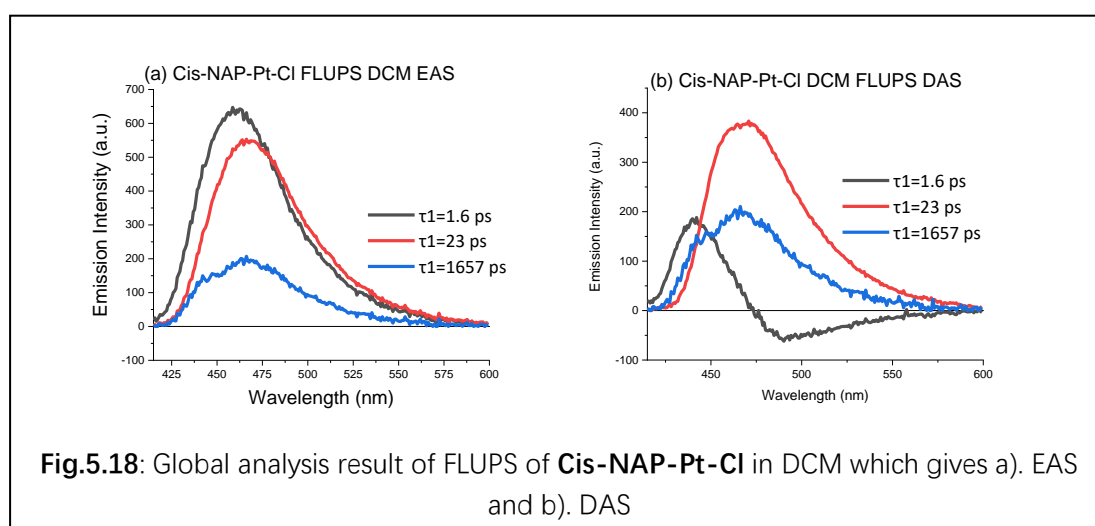


**Fig.5.16:** a).TA and b) FLUPS spectra of **Cis-NAP-Pt-Cl** in DCM with excitation at 400 nm. Kinetic trace (dots) and corresponding GLA fitting traces (line) at selected wavelength of c). TA and d). FLUPS

The structure of **Cis-NAP-Pt-Cl** is shown in **Fig.5.3**. TA spectra of this complex with excitation at 400 nm are given in **Fig.5.16**. After excitation, the peak at 490 nm corresponding to the NAP<sup>-</sup> anion arises which indicates that the first populated state is the <sup>1</sup>MMLCT state. Similar to the **Cis-NAP-Pt-NAP**, its stimulated emission signal is overlapping with the bleach corresponding to the ground state absorption, but a tiny signal at 450 nm is discernible, and supports the assignment of the first CT state as a singlet state. With the decay of <sup>1</sup>MMLCT state, the last long-lived state grows in which is attributed to <sup>3</sup>NAP state.



Global analysis with sequential model is also applied to the TA spectra (shown in **Fig.5.17**) of **Cis-NAP-Pt-Cl** which extracts three components with the lifetimes of 1.4 ps, 29.6 ps and a long-lived state. The long-lived state is attributed to <sup>3</sup>NAP state and the 1.4 ps component is attributed to the FC state. The 29.6 ps component with a peak at 480 nm corresponds to <sup>1</sup>MMLCT state which decays into <sup>3</sup>NAP state and could be treated as the ISC lifetime. This value – 29.6 ps - is very close to the rate of ISC in **Cis-NAP-Pt-NAP** but very different from the rate of ISC in **trans-NAP-Pt-Cl** ( $\tau_{ISC} = 198$  ps).



FLUPS spectra of **Cis-NAP-Pt-Cl** is given in **Fig.5.16(b)** and its kinetic traces and corresponding GLA fitting results in **Fig.5.16(d)**. Global analysis extracts three components with lifetimes 1.6 ps, 23 ps and 1657 ps as shown in **Fig.5.18**. Here

the 1657 ps trace could also be attributed to long lived organic molecule generated during experiment as it is also rise with the progress of FLUPS experiment and as a cis Pt complex it is also easy to undergo reductive elimination reaction to produce organic molecule as discussed in **Cis-NAP-Pt-NAP**. Here we assign the 23 ps component as ISC rate corresponding lifetime which supports the ISC rate ( $\tau_{ISC} = 29.6 \text{ ps}$ ) extracted from TA spectra of **Cis-NAP-Pt-Cl**.

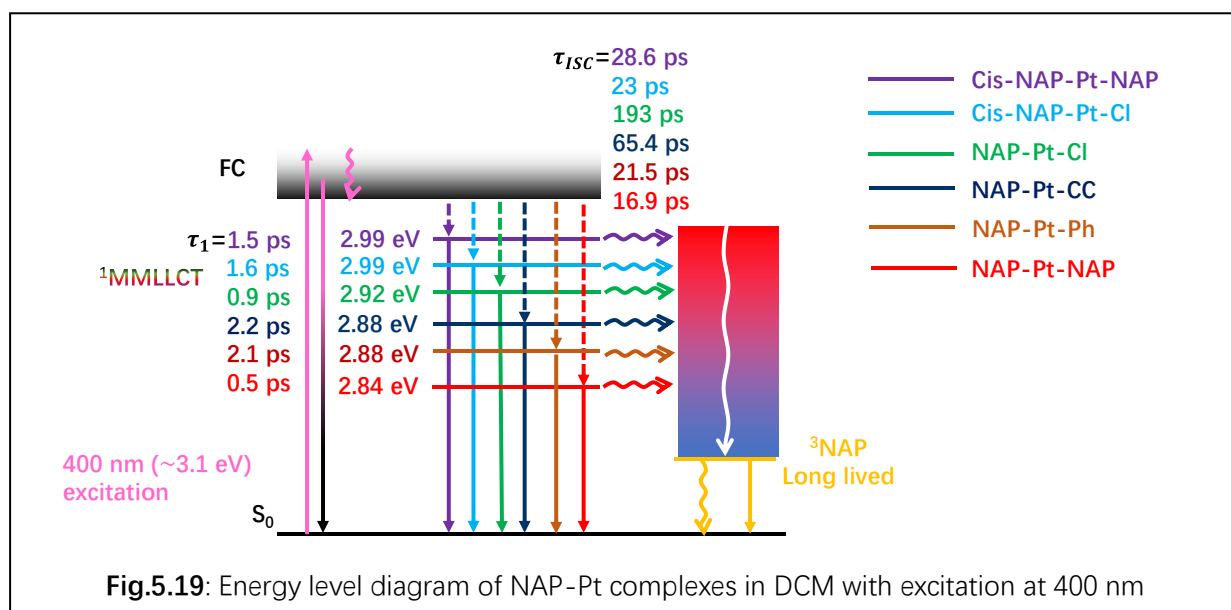
### 5.3.3. Summary and Conclusion

a). TA				
Compound	$\tau_1/\text{ps}$	$\tau_2/\text{ps}$	$\tau_3/\text{ps}$	$\tau_4/\text{ps}$
<b>NAP-Pt-Cl</b> <sup>1,2</sup>	0.9	-	212	$+\infty$
<b>NAP-Pt-CC</b>	$0.6 \pm 0.003$	-	$61.9 \pm 0.1$	$+\infty$
<b>NAP-Pt-Ph</b> <sup>1,2</sup>	0.6	2.2	19	$+\infty$
<b>NAP-Pt-NAP</b>	$0.6 \pm 0.003$	-	$11.3 \pm 0.03$	$+\infty$
<b>Cis-NAP-Pt-NAP</b>	$1.3 \pm 0.004$	-	$29.8 \pm 0.1$	$+\infty$
<b>Cis-NAP-Pt-Cl</b>	$1.4 \pm 0.005$	-	$29.6 \pm 0.1$	$+\infty$

b). FLUPS			
FLUPS-Compound	$\tau_1/\text{ps}$	$\tau_2/\text{ps}$	$\tau_3/\text{ps}$
<b>NAP-Pt-Cl</b> <sup>1,2</sup>	0.7	6.4	198
<b>NAP-Pt-CC</b>	$2.2 \pm 0.006$		$65.4 \pm 0.1$
<b>NAP-Pt-Ph</b> <sup>1,2</sup>	0.7	2.1	21.5
<b>NAP-Pt-NAP</b>	$0.9 \pm 0.008$		$16.9 \pm 0.08$
<b>Cis-NAP-Pt-NAP</b>	$1.5 \pm 0.006$	$28.6 \pm 0.05$	$876.3 \pm 4.6$
<b>Cis-NAP-Pt-Cl</b>	$1.6 \pm 0.01$	$23 \pm 0.04$	$1657 \pm 4.5$

**Table.5.2:** Summary of lifetimes extracted from TA (up) and FLUPS (down) of NAP-Pt complexes. Please note that we do not state errors on the values extracted from global fit as they are unrealistically small. Here the error is suggested by Glotaran



Lifetimes extracted from TA and FLUPS of NAP-Pt complexes are given in **Table.5.2** and the energy level diagram suggested together with excited states lifetimes are shown in **Fig.5.19**. The energy level diagrams suggested here is based on SOCT-ISC mechanism, in which the  $^1\text{MMLCT}$  state directly ISC to  $^3\text{NAP}$  state.

The ISC rate of these NAP-Pt complexes does not follow the energy gap law as the highest energy and lowest energy  $^1\text{MMLCT}$  states both undergo ISC within 30 ps, whilst the energy of the long-lived  $^1\text{MMLCT}$  state in **NAP-Pt-Cl** complex energy is in between of them. This trend in the ISC rate could be explained by spin-orbit, charge transfer intersystem crossing (SOCT-ISC) mechanism: in this mechanism, when donor and acceptor  $\pi$  systems in the CT state are perpendicular to each other, the ISC process will be enhanced by charge transfer. In this research, **NAP-Pt-Cl** undergoes slowest ISC because in its  $^1\text{MMLCT}$  state, only Pt centre works as electron donor and does not have 2D structure, so the ISC process cannot be enhanced. And in **NAP-Pt-Ph** and **NAP-Pt-NAP**, in  $^1\text{MMLCT}$  state, the opposite group (Ph or NAP) of  $\text{NAP}^-$  anion works as part of the electron donor and the 2D donor ligand enhance the ISC process when it is perpendicular to the acceptor ligand. In **Cis-NAP-Pt-NAP** and **Cis-**

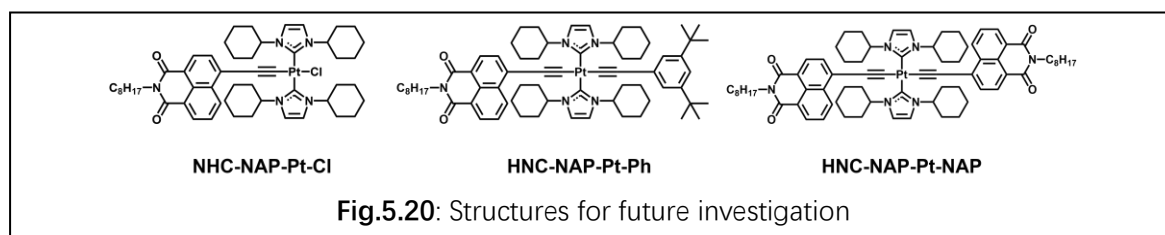
**NAP-Pt-Cl**'s  $^1\text{MMLLCT}$  state, the bidentate ligand forms a five-membered 2D ring including the Pt metal centre, which works as the 2D electron donor and ISC rate is enhanced to a similar extent, so both of these two complexes show similar ISC rate which are much higher than in **NAP-Pt-Cl**. Also, the SOCT-ISC mechanism also explains well why  $^3\text{MMLLCT}$  state is not observed in all of the NAP-Pt complexes discussed here. Also, the isomerization process of **NAP-Pt-Ph** and the formation of cumulenenic structure which changes the delocalisation is not dominant in ISC rate as **NAP-Pt-NAP** and **Cis-NAP-Pt-Cl** which cannot form cumulenenic structure both show similar ISC rate as **NAP-Pt-Ph**.

#### 5.4. Future Work

The SOCT-ISC mechanism meets well with the trend of NAP-Pt complexes discussed in this chapter and also explains the absence of the  $^3\text{MMLLCT}$  state in these complexes. However, in these complexes, both NAP and the opposite ligand are free to rotate, which indicates that the SOCT-ISC mechanism cannot always happen with perfect configuration and so the enhancement of the ISC process caused by SOCT-ISC mechanism is still questionable. To further investigate the contribution of SOCT-ISC mechanism in ISC process of **NAP-Pt** complexes, the following compounds' (shown in **Fig.5.20**) are suggested to be investigated and compared with the current **NAP-Pt** complexes in the future. In these three NAP-Pt complexes shown in **Fig.5.20**, the N-heterocyclic carbene (NHC) ligand is used to limit the rotation of NAP and Phenyl ligand linked with Pt centre. If SOCT-ISC mechanism dominates the ISC of **NAP-Pt** complexes, then these three complexes should undergo similar ISC rate and much slower than the **NAP-Pt** complexes investigated in this chapter so these three compounds suggested in **Fig.5.20** may help tell if SOCT-ISC mechanism dominates the ISC process. If these three compounds shown in **Fig.5.20** maintains similar ISC rate of their corresponding NAP-Pt complexes with  $\text{PBU}_3$  ligand (**NAP-Pt-Cl**, **NAP-Pt-NAP**, and **NAP-Pt-Ph**) instead of NHC ligand, then other properties such as electron donation ability may



domines in ISC process of **NAP-Pt** complexes excited state.



## 5.5. Reference

- 1 G. A. Farrow, M. Quick, S. A. Kovalenko, G. Wu, A. Sadler, D. Chekulaev, A. A. P. Chauvet, J. A. Weinstein and N. P. Ernsting, *Physical Chemistry Chemical Physics*, 2021, **23**, 21652–21663.
- 2 P. A. Scattergood, M. Delor, I. v. Sazanovich, O. v. Bouganov, S. A. Tikhomirov, A. S. Stasheuski, A. W. Parker, G. M. Greetham, M. Towrie, E. S. Davies, A. J. H. M. Meijer and J. A. Weinstein, *Dalton Transactions*, 2014, **43**, 17677–17693.
- 3 Z. E. X. Dance, S. M. Mickley, T. M. Wilson, A. B. Ricks, A. M. Scott, M. A. Ratner and M. R. Wasielewski, *Journal of Physical Chemistry A*, 2008, **112**, 4194–4201.
- 4 B. T. Lim, S. Okajima, A. K. Chandra and E. C. Lim, *Chem Phys Lett*, 1981, **79**, 22–27.
- 5 Z. Wang, M. Ivanov, Y. Gao, L. Bussotti, P. Foggi, H. Zhang, N. Russo, B. Dick, J. Zhao, M. di Donato, G. Mazzone, L. Luo and M. Fedin, *Chemistry - A European Journal*, 2020, **26**, 1091–1102.
- 6 I. R. Gould, J. A. Boiani, E. B. Gaillard, J. L. Goodman and S. Farid, *Journal of Physical Chemistry A*, 2003, **107**, 3515–3524.
- 7 G. Farrow, *PhD Graduation Thesis, the University of Sheffield, 2019.*

## 6. Conclusion

In this work, a series of Pt based organometallic compounds are investigated by combining the results given by different ultrafast spectroscopy techniques. Their photophysical properties including the intersystem crossing (ISC) rate and excited state energy levels and dynamics are concluded in previous several chapters.

In **Chapter 1**, a series of symmetric trans Pt acetylide NAP complexes with different bridge length (**Pt-0**, **Pt-1** and **Pt-2**) in DCM are investigated by transient absorption (TA), transient infrared absorption (TRIR) and fluorescence up-conversion spectroscopy (FLUPS) techniques. The result indicate that with the increase in the bridge length from **Pt-0** to **Pt-1** and **Pt-2**, the nature of the excited states populated, and their ultrafast dynamics change because the conjugated structure between Pt metal centre and the NAP acceptor does not simply work as bridge to change the distance between electron donor and acceptor, but the conjugated structure itself also works as an electron donor, which can trap the positive charge on the bridge with the increase of bridge length.

In **Chapter 2**, the symmetric Pt organometallic compounds investigated in **Chapter 1** are further researched on their solvatochromism together with solvent influence on ISC rate. It is found that the absorption into the FC state exhibits almost no solvatochromism but the fluorescent spectra show positive solvatochromism which indicates the FC state has a small dipole moment and the dominant fluorescent state has a large dipole moment and therefore could be attributed to a charge transfer state. The ISC rate of **Pt-0** show strong solvent polarity dependence, but **Pt-1** and **Pt-2**'s ISC rate show no dependence on solvent polarity. This difference can be explained by the nature of the excited state in **Pt-0** being independent of the solvent, whilst in **Pt-1** and **Pt-2**, the excited state that is populated changes with the change of solvent dipole moment. The energy level diagrams of these compounds in different solvents are also suggested.

In **Chapter 3**, transient two-dimensional infrared (T-2DIR) spectroscopy is used to characterise the influence of excitation of vibrational modes on excited state dynamics of **Pt-0**, **Pt-1** and **Pt-2**. It is found that for **Pt-1** and **Pt-2** in CT state, when the vibrational modes localised on the bridge are excited by IR excitation pulse, the back electron transfer process is accelerated. The vibrational modes which can induce IR control is not only the vibration on  $-C \equiv C-$  but also the vibrational mode on the phenyl groups on the bridge.

In **Chapter 4**, six different **NAP-Pt-L** complexes' ISC rate (extracted from FLUPS data) are compared, and the result indicates that a two-dimensional structure on the opposite side of NAP acceptor can strongly accelerate ISC process to  $^3\text{NAP}$  state. This phenomenon is explained as spin-orbital charge transfer ISC (SOCT-ISC) in which back electron transfer process happens at the same time as the ISC when the NAP acceptor is perpendicular to its 2D opposite ligand. This conclusion is still questionable and a series of N-heterocyclic carbene NAP-Pt complexes are suggested to be investigated and compared with current NAP-Pt complexes in future.

The complexes investigated in this thesis show interesting excited state nature and dynamics which furthers our understanding in light harvesting, CT state generation, back electron transfer process and ISC processes. The combination use of ultrafast spectroscopy methods including TA, TRIR, FLUPS and T-2DIR provides a wider field of vision on excited states' nature and dynamics than only use one ultrafast spectroscopy method. Even though there are still processes and mechanisms unclear in this research, with more systems investigated and other more ultrafast spectroscopy methods used in future, the questions unanswered in this thesis may be answered in future.

## 7. Experimental

### 7.1 Ultrafast Time-Resolved Spectroscopies

All of the samples are prepared in solution when collecting spectra. A flow system including a Harrick cell with path length  $350\ \mu\text{m}$  is used during transient absorption (TA), transient infrared absorption (TRIR) and transient two-dimensional infrared (T-2DIR) experiments are used to minimise the influence of photoinduced decomposition. A similar flow system with a specially designed 1 mm path length cuvette is used for collecting fluorescence up-conversion spectra (FLUPS). Ground state UV-vis absorption and/or infrared absorption spectra are collected before and after every ultrafast experiment to monitor the potential decomposition of the samples.

#### 7.1.1 Femtosecond Fluorescence Up-Conversion Spectroscopy (FLUPS)

Femtosecond fluorescence up-conversion spectroscopy experiments are performed at the Lord Porter Ultrafast Laser Spectroscopy Laboratory in the University of Sheffield. This experimental technique was developed by prof. Niko Ernsting and supplied by LIOP-TEC GmbH. Experimental details of this technique are published<sup>1</sup> and also introduced in our previous research.<sup>2</sup>

##### 7.1.1.1 Sample Excitation

The 400 nm excitation pulse is generated by the following process. A Ti:Sapphire regenerative amplifier (Spitfire ACE PA-40, Spectra-Physics) produces 800 nm pulses (40 fs FWHM, 10 kHz, 1.2 mJ) with the 800 nm seed pulses (25 fs FWHM, 84 MHz) provided by a Ti:Sapphire oscillator (Mai Tai, Spectra-Physics). The pump pulses for the two amplification stages of the Spitfire ACE PA-40 were provided by two Nd:YLF lasers (Empower, Spectra-Physics). The 400 nm excitation pulses (40 fs FWHM, 10 kHz,  $0.3\ \mu\text{J}$ ) were generated by second harmonic generation (SHG) of the 800 nm output of the

amplifier by a  $\beta - BaB_2O_4$  crystal in doubler (TimePlate, Photop Technologies). The excitation pulses were passed through a computer controlled optical delay stage (M-IMS400LM, Newport), providing 2.6 ns of pump-gate time-delay and a resolution of 1.67 fs. A variable attenuation neutral-density filter wheel was used to control the pump pulse power. The pump pulse was compressed by a double-pass, two-prism compressor (AFS-FS Fused Silica Prism Pair, Thorlabs). The prism positions were set by minimising the FWHM of the pump-gate cross-correlation. Polarization of the pump pulse was set to magic angle with respect to the vertical axis by using a  $\lambda/2$  plate. The pump beam was focused onto the sample cell by a lens (f=200 mm, fused silica) with a spot diameter  $\leq 0.1$ mm. The sample was prepared in a flow cuvette with a path length of 1 mm.

#### 7.1.1.2 Signal Collection

A concave and convex mirror pair was used to collect emission from the sample. The transmitted pump pulse was blocked by a beam-stopper, while the emission was focused onto a 0.1 mm thick  $\beta - BaB_2O_4$  crystal (BBO crystal, EKSPA OPTICS). A type II phase matching interaction of the 1320 nm gate pulse with the emission results in sum-frequency generation (SFG), yielding an up-converted emission signal. The angle between the emission signal and gate beam was set to  $21^\circ$  at the crystal, with a 0.6 mm diameter spot.

#### 7.1.1.3 Gate Pulses

The 1320 nm gate pulse (80 fs FWHM, 10 kHz, 60  $\mu$ J) was produced by a traveling-wave optical parametric amplifier of superfluorescence (TOPAS prime, Light Conversion) pumped by the 800 nm (40 fs FWHM, 10 kHz, 0.5 mJ) amplifier fundamental. The gate pulse polarization was set to horizontal using a  $\lambda/2$  plate followed by wire-grid polariser.

#### 7.1.1.4 Up-Converted Emission Signal Detection

The up-converted signal was focused into a fibre bundle (Ceram Optek) by a concave mirror. The signal was dispersed onto a CCD detector (iDus 420 DU440A-BU2, Andor) by a homemade spectrograph. The detection range was set to 286 to 500 nm, which corresponds with an original signal range of 360-780 nm.

#### 7.1.2 Time-Resolved Transient UV-vis Absorption Spectroscopy (TA)

Transient absorption (TA) spectra were collected using a commercially available Helios spectrometer (HE-VIS-NIR-3200), provided by Ultrafast Systems in the Lord Porter Ultrafast Laser Spectroscopy Laboratory in the University of Sheffield.

##### 7.1.2.1 Sample Excitation

The 400 nm excitation pulse was generated in the same way as in the FLUPS setup. A Ti:Sapphire regenerative amplifier (Spitfire ACE PA-40, Spectra-Physics) produces 800 nm pulses (40 fs FWHM, 10 kHz, 1.2 mJ) with the 800 nm seed pulses (25 fs FWHM, 84 MHz) provided by a Ti:Sapphire oscillator (Mai Tai, Spectra-Physics). The pump pulses for the two amplification stages of the Spitfire ACE PA-40 were provided by two Nd:YLF lasers (Empower, Spectra-Physics). The 400 nm excitation pulses (40 fs FWHM, 10 kHz, 0.3  $\mu\text{J}$ ) were generated by second harmonic generation (SHG) of the 800 nm output of the amplifier by a  $\beta - \text{BaB}_2\text{O}_4$  crystal in doubler (TimePlate, Photop Technologies). The repetition rate of the 400 nm excitation signal was reduced for 10 KHz to 2.5 kHz by a mechanical chopper, to allow for both ground state and excited state probing. The excitation pulses were focused onto the Harrick cell (350  $\mu\text{m}$  path length) to a spot diameter of  $\leq 0.3 \text{ mm}$ .

##### 7.1.2.2 Sample Probe

A portion of the 800 nm output of the Spitfire ACE was directed into a computer-controlled delay stage (DDS300, Thorlabs), providing 8 ns of pump-probe time-delay, with a time resolution of 1.67 fs. The broadband probe pulse (340-750 nm) were generated by focusing the 800 nm pulses onto a 3 mm calcium fluoride crystal. The white light was then focused onto the sample cell by a concave mirror ( $f=50$  mm). The polarization of probe pulse was set to magic angle with respect to the pump pulse polarization. The transmitted white light intensity of the pumped and unpumped sample was detected by an aberration-corrected concave grating and a CMOS detector, with a resolution of 1.5 nm.

### **7.1.3 Time-Resolved Infrared Spectroscopy (TRIR)**

Time-resolved infrared spectroscopy (TRIR) was performed using the ULTRA instrument at the STFC Rutherford Appleton Laboratory. Experimental details have been previously published.<sup>3</sup> Briefly, a portion of the 800 nm pulses (40 fs FWHM, 10 kHz, 1 mJ) provided by a Ti:Sapphire regenerative amplifier (Thales) were used to generate tuneable  $400\text{ cm}^{-1}$  broad mid-IR probe pulses. The probe and pump pulses were focused onto a Harrick cell ( $\text{CaF}_2$  windows,  $630\ \mu\text{m}$  path length), with spot sizes of  $70\ \mu\text{m}$   $120\ \mu\text{m}$ , respectively. In addition to the sample being flowed by a peristaltic pump, the Harrick cell was simultaneously raster-scanned to avoid decomposition. The pump pulse polarization was set to magic angle with respect to probe pulse polarization. The IR probe light transmitted through the sample was detected by two linear 128 array HgCdTe detectors (Infrared Associates).

### **7.1.4 Frequency Domain Two-Dimensional Infrared (2DIR) and Transient Two-Dimensional Infrared Spectroscopy (T-2DIR)**

Frequency domain 2DIR and T-2DIR experiments were also performed using the ULTRA instrument at the STFC Rutherford Appleton Laboratory. The IR

probe beam used in 2DIR and T-2DIR was the same probe beam discussed in TRIR setup. The narrowband IR excitation beam was generated from a ps-OPA pumped by part of the output from the ps-amplifier. The UV pump and IR pump pulse sequences required in T-2DIR experiments were generated using mechanical choppers set to 5 kHz for the UV pump and 2.5 kHz for IR pump.

## 7.2 Density Functional Theory (DFT) Calculation

Calculations were performed using the SMP version of the Gaussian09 package, revision D.01.<sup>4</sup> Gaussian was compiled using the Gaussian supplied version of BLAS and ATLAS on the EMT64 architecture.<sup>5,6</sup> The solvent, dichloromethane, was simulated using the integral equation formalism polarisable continuum model (IEFPCM), using the parameters as implemented in Gaussian09.<sup>7-9</sup> All calculations utilized the PBE0 functional.<sup>10</sup> The Karlsruhe basis set, def2-SVP,<sup>11,12</sup> was employed for all atoms except Pt. For these, the Dirac-Hartree-Fock basis set, dhf-SVP,<sup>13</sup> was used instead. Frequencies within the harmonic approximation were calculated for all optimized structures. The absence of imaginary frequencies confirmed that the energy minima had been found. For all calculations, ultrafine integrals were used and no symmetry constraints were applied. Calculated vibrational frequencies were scaled to account for the anharmonicity of the vibrational modes.<sup>14-18</sup>

## 7.3 Steady State Absorption Spectra

### 7.3.1 UV-vis Absorption Spectroscopy

UV-vis absorption spectra of the compounds were collected in quartz cuvettes with a path length 1 cm, using a Cary 60 UV-Vis spectrometer (Agilent). Samples were prepared in solution with solvents: N,N-dimethylformamide (DMF), dichloromethane (DCM), tetrahydrofuran (THF), and toluene. The optical density in the region of interest is kept below 1 by using suitable concentration of analyte.



### 7.3.2 Steady State Fourier-transform Infrared Spectroscopy (FTIR)

Steady state FTIR spectra of the compounds were collected in Harrick cells with CaF<sub>2</sub> windows using a Nicolet iS20 FTIR spectrometer (Thermo Scientific). Samples were prepared in solution with selected solvents.

### 7.3.3 Steady State Emission Spectroscopy

Steady state emission spectra were recorded in a 1 cm path length quartz cuvette using a Fluoromax-4 spectrofluorometer (Horiba). Samples were prepared in solution with selected solvents, with optical densities of ~0.6 at 400 nm.

### 7.3.4 Data Analysis

Several software packages were used for different purposes. Basic analysis and graph plotting was achieved using OriginPro 2020. Raw data processing of FLUPS spectra was carried out using a homemade programme written in Matlab 2019b. Global analysis was performed by glotaran 1.5.1 – a GUI for the R-package TIMP.

## 7.4 Reference

- 1 X.-X. Zhang, C. Würth, L. Zhao, U. Resch-Genger, N. P. Ernsting and M. Sajadi, *Review of Scientific Instruments*, 2011, **82**, 063108.
- 2 G. A. Farrow, M. Quick, S. A. Kovalenko, G. Wu, A. Sadler, D. Chekulaev, A. A. P. Chauvet, J. A. Weinstein and N. P. Ernsting, *Physical Chemistry Chemical Physics*, 2021, **23**, 21652–21663.
- 3 G. M. Greetham, P. Burgos, Q. Cao, I. P. Clark, P. S. Codd, R. C. Farrow, M. W. George, M. Kogimtzis, P. Matousek and A. W. Parker, *Appl Spectrosc*, 2010, **64**, 1311–1319.
- 4 M. J. Frisch, G. W. Trucks, H. B. Schlegel, G. E. Scuseria, M. A. Robb, J. R. Cheeseman, G. Scalmani, V. Barone, G. A. Petersson, H. Nakatsuji, X. Li, M.

- Caricato, A. v Marenich, J. Bloino, B. G. Janesko, R. Gomperts, B. Mennucci, H. P. Hratchian, J. v Ortiz, A. F. Izmaylov, J. L. Sonnenberg, Williams, F. Ding, F. Lipparini, F. Egidi, J. Goings, B. Peng, A. Petrone, T. Henderson, D. Ranasinghe, V. G. Zakrzewski, J. Gao, N. Rega, G. Zheng, W. Liang, M. Hada, M. Ehara, K. Toyota, R. Fukuda, J. Hasegawa, M. Ishida, T. Nakajima, Y. Honda, O. Kitao, H. Nakai, T. Vreven, K. Throssell, J. A. Montgomery Jr., J. E. Peralta, F. Ogliaro, M. J. Bearpark, J. J. Heyd, E. N. Brothers, K. N. Kudin, V. N. Staroverov, T. A. Keith, R. Kobayashi, J. Normand, K. Raghavachari, A. P. Rendell, J. C. Burant, S. S. Iyengar, J. Tomasi, M. Cossi, J. M. Millam, M. Klene, C. Adamo, R. Cammi, J. W. Ochterski, R. L. Martin, K. Morokuma, O. Farkas, J. B. Foresman and D. J. Fox, 2016.
- 5 R. C. Whaley and A. Petitet, *Software - Practice and Experience*, 2005, **35**, 101–121.
- 6 R. Clint Whaley, A. Petitet and J. J. Dongarra, *Parallel Computing*, 2001, **27**, 3–35.
- 7 J. L. Pascual-ahuir, E. Silla and I. Tuñon, *Journal of Computational Chemistry*, 1994, **15**, 1127–1138.
- 8 S. Miertus, E. Scrocco and J. Tomasi, *ELECTROSTATIC INTERACTION OF A SOLUTE WITH A CONTINUUM. I. A DIRECT UTILIZATION OF A6 INITIO MOLECULAR POTENTIALS FOR THE PREVISION OF SOLVENT EFFECTS*, North-Holland PublishingCompany, 1981, vol. 55.
- 9 S. Miertuš and J. Tomasi, *Chemical Physics*, 1982, **65**, 239–245.
- 10 C. Adamo and V. Barone, *The Journal of Chemical Physics*, 1999, **110**, 6158–6170.
- 11 F. Weigend, F. Furche and R. Ahlrichs, *Journal of Chemical Physics*, 2003, **119**, 12753–12762.
- 12 F. Weigend and R. Ahlrichs, *Physical Chemistry Chemical Physics*, 2005, **7**, 3297–3305.
- 13 F. Weigend and A. Baldes, *The Journal of Chemical Physics*, 2010, **133**, 174102.
- 14 A. P. Scott and L. Radom, *Harmonic Vibrational Frequencies: An Evaluation of Hartree-Fock, Møller-Plesset, Quadratic Configuration Interaction, Density*

*Functional Theory, and Semiempirical Scale Factors*, 1996.

- 15 M. K. Kesharwani, B. Brauer and J. M. L. Martin, *Journal of Physical Chemistry A*, 2015, **119**, 1701–1714.
- 16 M. L. Laury, M. J. Carlson and A. K. Wilson, *Journal of Computational Chemistry*, 2012, **33**, 2380–2387.
- 17 M. D. Halls, J. Velkovski and H. B. Schlegel, *Theoretical Chemistry Accounts*, 2001, **105**, 413–421.
- 18 K. K. Irikura, R. D. Johnson and R. N. Kacker, *Journal of Physical Chemistry A*, 2005, **109**, 8430–8437.